

NASA CR-152495

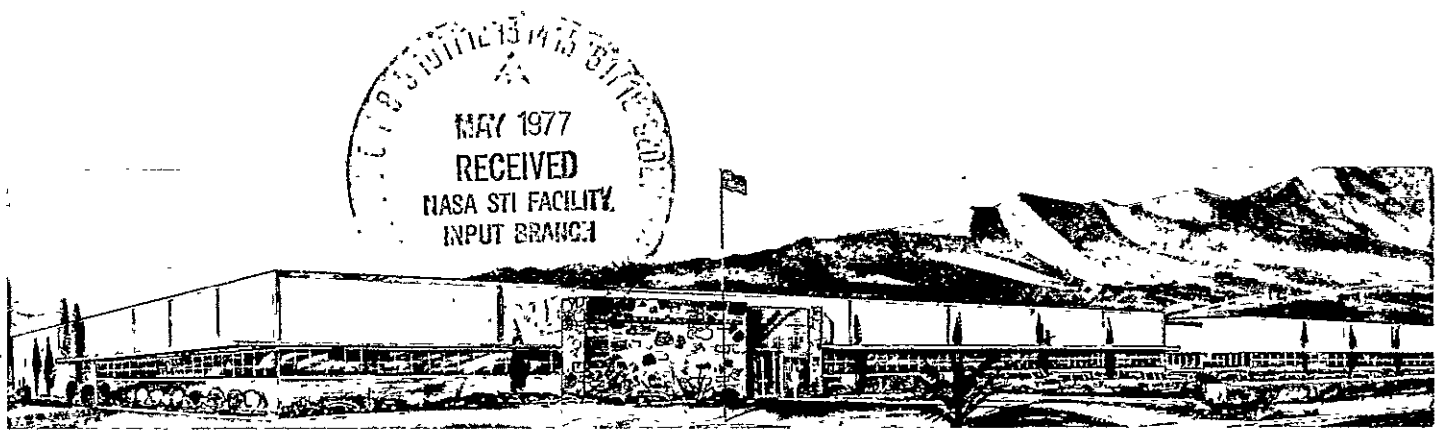
(NASA-CR-152495) ADVANCED ATMOSPHERIC  
SOUNDER AND IMAGING RADIOMETER (AASIR) N77-22451  
Final Report (Santa Barbara Research Center)  
219 p HC A1C/EF AC1 CSCI 14E Unclas  
G3/35 26020

# FINAL REPORT

## ADVANCED ATMOSPHERIC SOUNDER AND IMAGING RADIOMETER (AASIR)

Contract No. NAS 5-20963

For - National Aeronautics and Space Administration  
Goddard Space Flight Center  
Glen Dale Road  
Greenbelt, Maryland 20771



SANTA BARBARA RESEARCH CENTER  
A Subsidiary of Hughes Aircraft Company



**SANTA BARBARA RESEARCH CENTER**

*A Subsidiary of Hughes Aircraft Company*

75 COROMAR DRIVE, GOLETA, CALIFORNIA

**FINAL REPORT**

**ADVANCED ATMOSPHERIC SOUNDER AND  
IMAGING RADIOMETER (AASIR)**

Contract No. NAS 5-20963

National Aeronautics and Space Administration  
Goddard Space Flight Center  
Glen Dale Road  
Greenbelt, Maryland 20771

10 March 1977

CONTENTS

<u>Section</u>	<u>Page</u>
1	INTRODUCTION AND SUMMARY . . . . . 1-1
	Introduction . . . . . 1-1
	Summary of Study Results . . . . . 1-2
	AASIR Specification . . . . . 1-4
2	DESCRIPTION OF THE AASIR . . . . . 2-1
	Scanning Method for IR and Visible Imaging . . . . . 2-7
	System Constraints on Optical Design . . . . . 2-7
	System Constraints on Detector/Radiative Cooler . . . . . 2-9
	System Constraints on Radiometric Calibration . . . . . 2-10
	Data Rates . . . . . 2-11
	AASIR Weight Estimate . . . . . 2-11
	AASIR Power Dissipation Estimate . . . . . 2-12
3	AASIR SYSTEM CONSIDERATIONS . . . . . 3-1
	Noise Equivalent Radiance Calculations . . . . . 3-1
	DC Restore Analysis . . . . . 3-18
	Scan Considerations . . . . . 3-36
	AASIR Modulation Transfer Functions (MTFs) . . . . . 3-70
	Use of the 3.7- $\mu$ m Channels for Wind Velocity Determination . . . . . 3-79
	AASIR Data Rates . . . . . 3-85
	Calculation of D* Values for InSb Channels . . . . . 3-87
	AASIR Commands and Telemetry Monitors . . . . . 3-92
4	OPTICAL DESIGN . . . . . 4-1
	Introduction . . . . . 4-1
	Design Constraints . . . . . 4-1
	Component Optical Design . . . . . 4-2
	Ray Tracing Technique . . . . . 4-2

CONTENTS (Continued)

<u>Section</u>	<u>Page</u>
4	Ritchey Chretien Telescope Design . . . . . 4-4
(Cont)	IR Delay Design . . . . . 4-5
	Step-Scan Mechanism Design . . . . . 4-9
	Scanned IR Fields . . . . . 4-18
	AASIR Image Quality . . . . . 4-23
	AASIR Radiometric Considerations . . . . . 4-29
	AASIR Radiation Baffle Study . . . . . 4-39
5	AASIR RADIATION COOLER . . . . . 5-1
	General . . . . . 5-1
	Design Features . . . . . 5-1
	Design Description . . . . . 5-4
	Analysis and Predicted Performance . . . . . 5-8
	Structural Analyses . . . . . 5-11
	Bench Test Cooling . . . . . 5-19

Appendix A  
AASIR SPECIFICATION

ILLUSTRATIONS

<u>Figure</u>		<u>Page</u>
2-1	Models of the AASIR . . . . .	2-3
2-2	View of Detectors as Projected on Prime Focal Plane . . . . .	2-5
2-3	Optical Schematic of the Quasi Object Plane Scan Mechanism (QOPSM) . . . . .	2-8
3-1	Normalized NEN versus Frame Size . . . . .	3-4
3-2	Normalized NEN versus Scan Efficiency . . . . .	3-5
3-3	Visible Channel Preamplifier Equivalent Circuit . . . . .	3-10
3-4	AASIR Visible Channel Noise Sources (21 $\mu$ rad, 0.55 to 0.75 $\mu$ m, $R_f = 10^8 \Omega$ , scan = 0.386 Hz) . . . . .	3-12
3-5	AASIR Scan Timing Diagram . . . . .	3-19
3-6	DC Restore Equivalent Circuit . . . . .	3-19
3-7	Noise Transfer Function $N_{rms}^2(\omega)$ for AASIR DC Restore . . . . .	3-22
3-8	Noise Transfer Function $N_{pk}^2(\omega)$ for AASIR DC Restore . . . . .	3-23
3-9	DC Restore Sequence . . . . .	3-23
3-10	Equivalent Noise Bandwidth (NBW) versus $T_3/\tau_2$ . . . . .	3-26
3-11	Equivalent Noise Bandwidth (NBW) versus $f_0$ (Sounding Channels); $\rho = T_3/\tau_2 = f_0 = 1/f$ knee . . . . .	3-26
3-12	Equivalent Noise Bandwidth (NBW) versus $f_0$ (IR Imaging Channels) . . . . .	3-27
3-13	Aft Optics Schematic Diagram . . . . .	3-27
3-14	Optimizing Plot for $V_N, V_F$ versus $T_3/\tau_2$ . . . . .	3-29
3-15	AASIR Aft Optics Schematic . . . . .	3-31
3-16	Equivalent Noise Bandwidth (NBW) versus $f_0$ (Sounding Channels); $\rho = T_3/\tau_2, f_0 = 1/f$ knee . . . . .	3-35
3-17	Case 1 Scan Coordinate System . . . . .	3-36
3-18	Case 2 Scan Coordinate System . . . . .	3-37
3-19	Two-Mirror Scan Nonlinearity (Flat Earth Projection) . . . . .	3-45
3-20	AASIR Scan System Block Diagram . . . . .	3-45

ILLUSTRATIONS (Continued)

<u>Figure</u>		<u>Page</u>
3-21	Scan Mirror Reference Pulse Optical Schematic . . . . .	3-51
3-22	Normalized Initialization Pulse - Relative Response versus Scan Angle . . . . .	3-55
3-23	Normalized Initialization Pulse - Relative Response versus Scan Angle . . . . .	3-57
3-24	Normalized Initialization Pulse - Relative Response versus Scan Angle . . . . .	3-59
3-25	Normalized Initialization Pulse - Incandescent Source - Models II and III . . . . .	3-60
3-26	Cross Scan Motion Requirement . . . . .	3-61
3-27	Four-Bar Linkage . . . . .	3-62
3-28	Cross Scan Linkage - End View . . . . .	3-62
3-29	Locus of Geometric Center . . . . .	3-62
3-30	Cross Scan Linkage - Side View . . . . .	3-64
3-31	Ring Detail . . . . .	3-64
3-32	Actuator Scheme . . . . .	3-64
3-33	Vibration Mode . . . . .	3-64
3-34	Stiffness of Ring and Flex Pivots . . . . .	3-65
3-35	Ring Cross Section . . . . .	3-67
3-36	Step Motion . . . . .	3-69
3-37	Detector and Integrator MTF's . . . . .	3-73
3-38	System MTF for 14- $\mu$ m Sounding Channels . . . . .	3-73
3-39	System MTF for IR Imaging Channels . . . . .	3-74
3-40	System MTF for Visible Imaging Channels . . . . .	3-74
3-41	Effects of Bidirectional Scan . . . . .	3-76
3-42	GOES C MTF - Class I $\times$ 21- $\mu$ rad IFOV Specification . . . . .	3-78
3-43	AASIR MTF - Class I Specification $\times$ 16- $\mu$ rad IFOV . . . . .	3-78
3-44	Cloud Velocity Error as a Function of Time (K = 1) . . . . .	3-80
3-45	Normalized Response Function, 125- $\mu$ rad IFOV . . . . .	3-81

ILLUSTRATIONS (Continued)

<u>Figure</u>		<u>Page</u>
3-46	Normalized Response Function, 90- $\mu$ rad IFOV . . . . .	3-81
3-47	Normalized Response Function, 75- $\mu$ rad IFOV . . . . .	3-82
3-48	$\Delta$ SNR versus Cloud Temperature (earth = 300°K, $\overline{\Delta V}_{rms} = 1$ m/sec) . . . . .	3-84
3-49	AASIR Optical Schematic Diagram . . . . .	3-87
3-50	InSb D* versus Instrument Temperature . . . . .	3-91
4-1	AASIR Fields of View as Projected into Object Space (Dimensions refer to Telescope Focal Plane) . . . . .	4-3
4-2	Ritchey Chretien Telescope Image Quality as Related to Field Size . . . . .	4-6
4-3	AASIR Image Quality for Sounding Channels . . . . .	4-6
4-4	Sounding Channels - Variation in Focus with Field Angle . . . . .	4-7
4-5	AASIR Optical Schematic . . . . .	4-10
4-6a	IR Imaging Path . . . . .	4-11
4-6b	Visible Imaging Path . . . . .	4-12
4-7	Scanned Ray Departure from a Straight Line Reverse Scan Configuration . . . . .	4-15
4-8	Scanned Field Departure from Linearity in Scan Direction . . . . .	4-15
4-9	Focus Shift . . . . .	4-16
4-10	AASIR Image Quality Through Telescope, Scan Optics and Relay Optics . . . . .	4-21
4-11	AASIR Focus Shift of Cooled Detectors with Wavelength . . . . .	4-22
4-12	AASIR Focus Shift Through Telescope, Scan Optics and Relay Optics . . . . .	4-22
4-13	VISSR Energy Spread Function (ESF) Actual (Class II) . . . . .	4-24
4-14	ESF Addition Root Sum Square . . . . .	4-24

ILLUSTRATIONS (Continued)

<u>Figure</u>		<u>Page</u>
4-15	Image Degradation Component - VISSR Fabrication . . . . .	4-25
4-16	Case III - Aperture Stop at Relay Lenses . . . . .	4-31
4-17	AASIR Internal Temperature Gradients Thermal Model No. 5 . . . . .	4-32
4-18	Stray Radiation Due to Multiple Reflection Occurring Between the Lens Elements . . . . .	4-40
4-19	Stray Radiation Due to Internal Reflection Occurring within a Lens Element . . . . .	4-40
4-20	Reflection Off $S_1$ of $RL_1$ . . . . .	4-42
4-21	Reflection Off $S_1$ of $RL_2$ . . . . .	4-42
4-22	Internal Reflection within FL . . . . .	4-43
4-23	Internal Reflection within $RL_1$ . . . . .	4-43
4-24	Stray Radiation Directly Entering the Instrument, Bypassing Main Telescope . . . . .	4-46
4-25	Internal Reflection within the Field Lens when $\theta = 6.87^\circ$ . . . . .	4-47
4-26	Internal Reflection within the Field Lens when $\theta = 8.0^\circ$ . . . . .	4-47
4-27	Internal Reflection within the Field Lens when $\theta = 10^\circ$ . . . . .	4-48
4-28	Internal Reflection within the Field Lens when $\theta = 12^\circ$ . . . . .	4-48
4-29	Correction Factor Due to Minor Axis Blockage . . . . .	4-49
5-1	AASIR Cooler Schematic . . . . .	5-2
5-2	AASIR Radiation Cooler Layout Flight Configuration (Mod II) . . . . .	5-3
5-3	AASIR Cooler Flight Configuration Cold Stage Layout (Mod II) . . . . .	5-7
5-4	AASIR Radiation Cooler, Cold Stage Temperature Versus Bias Dissipation . . . . .	5-10
5-5	Cooler Performance Versus Shield Temperature . . . . .	5-11

ILLUSTRATIONS (Continued)

<u>Figure</u>		<u>Page</u>
5-6	Combined Spring Rate for 6 Bands, Either Stage . . . . .	5-15
5-7	Thrust Axis Lumped Mass Model of AASIR Cooler . . . . .	5-17
5-8	AASIR Radiation Cooler Layout Bench Test Configuration (Mod II) . . . . .	5-21
5-9	AASIR Cooler Bench Test Configuration Cold Stage Layout (Mod II) . . . . .	5-22
5-10	AASIR Dewar Test Assembly . . . . .	5-24

TABLES

<u>Table</u>		<u>Page</u>
2-1	AASIR Functional Characteristics . . . . .	2-1
2-2	AASIR Spectral Band Assignments . . . . .	2-4
3-1	Values of NBW and $\delta$ , One Restore per Scan Line ( $20^\circ \times 20^\circ$ frame) . . . . .	3-5
3-2	AASIR NEN Values Obtained from System Equation . . . . .	3-6
3-3	AASIR Visible Channel Signal-to-Noise Ratios . . . . .	3-16
3-4	Visible Channel SNR; $R_f = 10^9 \Omega$ , albedo = 1 (with boost) . . .	3-17
3-5	Restore Error $\delta = \sum_{n=1}^N V_o e^{-nT_3/\tau_2}$ . . . . .	3-24
3-6	VAS Filter Characteristics . . . . .	3-31
3-7	$\Delta N$ Sequence . . . . .	3-34
3-8	Case 1 Scan Overlap . . . . .	3-39
3-9	Overlap ("Shearing") in E-W Direction . . . . .	3-41
3-10	Overlap in N-S Direction . . . . .	3-42
3-11	Reference Pulse Interferometer Components . . . . .	3-52
3-12	Summary of Parameters Used in Reference Pulse Calculations . . . . .	3-53
3-13	Equivalent Resolution . . . . .	3-75
3-14	Values of K . . . . .	3-83
3-15	AASIR Average Data Rates for $20^\circ \times 20^\circ$ Frame . . . . .	3-86
3-16	Maximum Instantaneous Data Rates . . . . .	3-86
3-17	Background Photon Flux for InSb Channels . . . . .	3-89
4-1	AASIR Primary Optics - Basic Lens Data . . . . .	4-4
4-2	AASIR with 1 Aspheric Relay F/1.13 - Basic Lens Data . . . . .	4-8
4-3	AASIR Internal Scan Reversed - Basic Lens Data . . . . .	4-14
4-4	AASIR with Refractive in Scan - Basic Lens Data . . . . .	4-17
4-5	AASIR with Scan and IR Relay - Basic Lens Data . . . . .	4-19

T A B L E S (Continued)

<u>Table</u>		<u>Page</u>
4-6	Summary of AASIR Telescope Energy Spread Function (ESF) Using Variables 'a' and 'b' . . . . .	4-28
4-7	Image Quality - IR Imaging Bands . . . . .	4-29
4-8	AASIR Internal Temperature Gradients Thermal Model - Model 5 . . . . .	4-31
4-9	Radiometric Equation Parameters . . . . .	4-33
4-10	AASIR Signal Noise Ratio and Noise Equivalent Radiance . . . . .	4-36
4-11	Zonal Areas in the Primary Mirror . . . . .	4-40
4-12	Stray Light Induced by Direct Radiation . . . . .	4-45
5-1	AASIR Cooler Design Features . . . . .	5-5
5-2	Radiation Coolers, Physical and Thermal Characteristics . . . . .	5-9
5-3	AASIR Radiation Cooler, Nominal Heat Load Comparison . . . . .	5-9
5-4	VISSR - AASIR Thrust Axis Stiffness-to-Weight Summary Values given as Stiffness (lb/in. )/ Weight (lb) . . . . .	5-14
5-5	VISSR - AASIR Lateral Stiffness and Resonant Frequency . . . . .	5-16
5-6	Peak Response to 1g Sinusoidal Base Motion (Thrust Axis) . . . . .	5-18
5-7	Maximum Alternating Band Stress Due to 1g Base Motion . . . . .	5-18

Section 1  
INTRODUCTION AND SUMMARY

INTRODUCTION

This report contains design information developed for the Advanced Atmospheric Sounder and Imaging Radiometer (AASIR) over the period 6 March 1975 to 31 January 1977 under GSFC contract NAS 5-20963. Only the material generated since the Design Review held in November 1975 is presented except where significant changes have been made or where the earlier data are needed for clarity.

The purpose of the AASIR Design Study is to develop the configuration of a sensor which satisfies the GSFC requirements for sounding, and both IR and visible imaging. \*

The AASIR draws much of its technology from previous SBRC Programs, principally the Visible Infrared Spin Scan Radiometer (VISSR) and the VISSR Sounder (VAS). Therefore, only those areas were studied which clearly departed from existing technology or where performance improvements were needed. These areas were as follows:

Systems Design

- Noise Equivalent Radiance (NEN) Calculations
- Scan Considerations
- Noise Analysis
- Data Rate Considerations
- Radiometric Calibration
- Revision of AASIR Specification (See Appendix A)

Optics

- Optical Design
- Image Quality, MTF
- Quasi-Object Plane Scan Mechanism
- Baffling Design
- Thermal Effects

---

\*The GSFC AASIR Specification is contained in Appendix A.

Mechanics

Composite Material Considerations  
Step-Axis Mechanism  
Weight Analysis  
~~Thermal Analysis~~

Electronics

Resonant Scan Breadboard Test Results  
Resolver Requirements  
Optical Encoder Requirements  
Power Profile

Detectors

Calculation of InSb D\*  
Presentation of latest HgCdTe Detector D\* Data

Radiative Cooler

Structural Design  
Performance Calculations  
Dewar Design  
Results of Dewar Breadboard Testing

Radiometric Calibration

Laboratory  
In-Flight

Miscellaneous

Use of 3.7- $\mu$ m channels for cloud velocity determination

SUMMARY OF STUDY RESULTS

The following statements summarize the results of the study and indicate the status of the current design.

System Design

1. The sensitivity (NEN) requirements of the AASIR Requirements have been met for the  $1.2^\circ \times 1.2^\circ$  frame size except for two of the 14- $\mu\text{m}$  sounding channels. To obtain full sounding accuracy in the larger frame sizes will require averaging of several frames.
2. The use of the Quasi-Object Plane Scan Mechanism (QOPSM) appears to be feasible from the mechanization, image quality and image distortion points of view, but it is strictly a trade off with detector array and radiative cooler complexity.
3. The resonant scan system was breadboarded using a 16-bit two-speed resolver. Repeatability of 2.5 arc-sec was demonstrated, a value about equal to the precision of the measurement technique. Absolute errors, while not so critical, were several times larger. To meet system requirements, a position transducer having 21 bits (2.7- $\mu\text{rad}$ ) would be needed. This appears to be close to the limit of the state of the art for either multispeed resolvers or optical digital shaft encoders. The final solution may require use of a laser interferometer measurement technique.

The resonant scan technique, while simple in terms of mechanization and requiring very low power compared to linear scan systems, may have problems associated with position readout to the required accuracy and later data transmission and picture rectification. These problems were not explored during one study but should be addressed to evaluate the possible need of a linear scan.

4. The first radiative cooler dewar designed for the AASIR (Mod I) appears to have marginal cooling capability in the ground test cryostat mode. Laboratory tests of a dewar model gave  $100^\circ\text{K}$  and subsequent design changes were predicted to give about  $90^\circ\text{K}$ . Since colder temperatures are desired another design was selected (Mod II) in which a longer dewar eliminates the thermal drop across the metal-to-metal friction interface between the cold finger and cryostat. This is essentially the approach taken for the Thematic Mapper for which the minimum cooler temperature is predicted to be less than  $83^\circ\text{K}$ .

**AASIR SPECIFICATION**

The NASA GSFC AASIR Specification is contained in Appendix A. Suggested changes which are consistent with the results of the study are included.

Section 2  
DESCRIPTION OF THE AASIR

The AASIR is a third generation meteorological sensor scheduled to be flown on STORMSAT. AASIR is based on the Visible Infrared Spin-Scan Radiometer (VISSR) first flown on SMS-1 in May 1974 and the VISSR Atmospheric Sounder (VAS), scheduled to fly on GOES-D in 1980. AASIR functional characteristics are shown in Table 2-1.

Table 2-1. AASIR Functional Characteristics

Frame Size	Continuously Variable from 1.2° × 1.2° to 20° × 20°
Frame Time	1.4 to 24 Minutes
Frame Positioning	Anywhere on Earth Disk
Visible Imagery	0.021 mr (0.4 nmi) Resolution
Infrared Imagery	0.125 mr (2.44 nmi) Resolution
Sounding	0.375 mr (7.3 nmi) Resolution
Jitter	< 4 μrad in 8 Seconds
Stability	< 11 μrad in 20 Minutes
Pointing	0.03° Absolute
Date Encoding	8 Bits per Visible Sample 10 Bits per IR Sample
Scan Type	North-South Resonant Sine Scan (0.388 Hz) 60% Scan Efficiency East-West Step by Rotating entire AASIR
Telescope	40.6-cm Cassegrain, f/1 Effective Focal Ratio
Detectors	Si Photodiodes - Visible, Radiation Cooled HgCdTe and InSb for IR Imaging and Sounding
Weight	250 lb includes Electronics
Power	52.2 Watts (average)

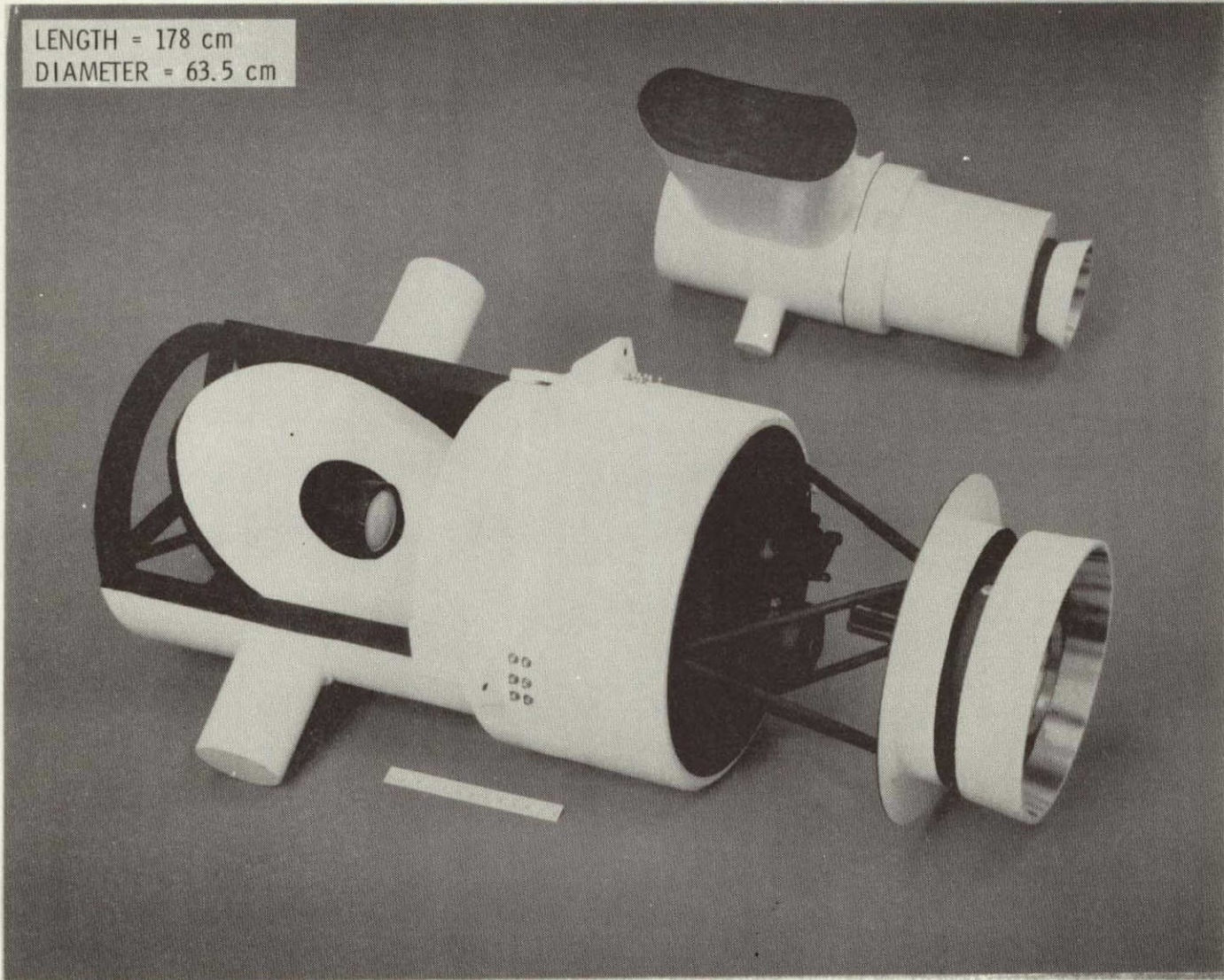
These earlier systems were spin-stabilized which provided good scan stability and allowed the use of a single-axis step-scan sensor. However, the need for higher resolution (both spatially and radiometrically) and the ability to track individual storms dictated the use of a three-axis stabilized spacecraft and a two-axis scan having high pointing precision and tight registration of sounding channels. Increased scan efficiency of the AASIR afforded by the three-axis stabilized STORMSAT and variable frame size gives significant dwell time advantages compared to the VAS.

In general terms the system noise equivalent radiance (NEN), the advantage when comparing full earth frames ( $20^\circ \times 20^\circ$ ) is a factor of about four, but when smaller frame sizes are considered, the advantage is greater. The  $1.2^\circ \times 1.2^\circ$  frame, used primarily for high accuracy sounding, will give a NEN advantage of about fifteen compared to VAS. This dwell time advantage also allows use of silicon photodiodes for visible imaging instead of photomultipliers, as in VAS.

The current AASIR configuration consists of a resonant object plane scan mirror operating in a north-south plane. The east-west step will be provided by the spacecraft via a bearing at the mounting interface. Figure 2-1, a photograph of an AASIR model, shows the scan mirror with covers and sunshade removed.

Table 2-2 gives the spectral band characteristics and radiometric performance expected for the AASIR. The stringent radiometric accuracy (NEN) requirements arise from the need to produce usable temperature-humidity profiles. For example, in the  $15\text{-}\mu\text{m}$   $\text{CO}_2$  band, radiance errors  $\leq 0.25 \text{ erg/sec-cm}^2\text{-sr-cm}^{-1}$  are required to generate temperature profiles with an accuracy of  $\pm 1^\circ\text{K}$ .

Figure 2-2 shows the latest detector array configuration as projected on the telescope focal plane or as it would appear projected on the earth since the detectors define the fields of view (FOV). The figure shows one three-element detector array each for  $11\text{-}\mu\text{m}$  and  $3.7\text{-}\mu\text{m}$  imaging and one



REPRODUCIBILITY OF THE  
ORIGINAL PAGE IS POOR

SBR C

Figure 2-1. Models of the AASIR

Table 2-2. AASIR Spectral Band Assignments

BAND	FUNCTION	NUMBER OF CHANNELS	SPECTRAL BAND CENTER		SPECTRAL BAND WIDTH		IFOV (μrad)	AASIR SPECIFICATION NEN (1.2° × 1.2°) (ergs/sec-cm <sup>2</sup> -st-cm <sup>-1</sup> )	AASIR CALCULATED NEN (1.2° × 1.2°) (ergs/sec-cm <sup>2</sup> -st-cm <sup>-1</sup> )
			(μm)	cm <sup>-1</sup>	(μm)	(cm <sup>-1</sup> )			
1	CO <sub>2</sub> Sounding	1	14.96	668.5	0.112	5	375 × 375	2.45	2.51
2	CO <sub>2</sub> Sounding	1	14.71	680	0.324	15	375 × 375	0.25	0.45
3	CO <sub>2</sub> Sounding	1	14.50	690	0.336	16	375 × 375	0.25	0.255
4	CO <sub>2</sub> Sounding	1	14.22	703	0.324	16	375 × 375	0.25	0.214
5	CO <sub>2</sub> Sounding	1	13.97	716	0.390	20	375 × 375	0.25	0.152
6	CO <sub>2</sub> Sounding	1	13.64	733	0.372	20	375 × 375	0.25	0.154
7	CO <sub>2</sub> Sounding	1	13.33	750	0.355	20	375 × 375	0.25	0.152
7a	CO <sub>2</sub> Sounding	1	12.50	800	0.625	40	375 × 375	0.25	0.07
11	CO <sub>2</sub> Sounding	1	4.24	2360	0.090	50	375 × 375	0.005	0.0033
11a	CO <sub>2</sub> Sounding	1	4.39	2275	0.068	35	375 × 375	0.004	0.0047
11b	CO <sub>2</sub> Sounding	1	4.44	2250	0.079	40	375 × 375	0.004	0.0042
11c	CO <sub>2</sub> Sounding	1	4.52	2210	0.082	40	375 × 375	0.004	0.004
11d	CO <sub>2</sub> Sounding	1	4.57	2190	0.048	40	375 × 375	0.004	0.0042
12	CO <sub>2</sub> Sounding	1	3.94	2535	0.218	140	375 × 375	0.004	0.0011
9a	H <sub>2</sub> O Absorption	1	7.25	1380	0.315	60	375 × 375	0.06	0.065
10	H <sub>2</sub> O Absorption	1	6.71	1490	0.630	140	375 × 375	0.05	0.022
8	IR Imaging	3	11.11	900	1.728	140	125 × 125	0.10	0.067
13	IR Imaging	3	3.70	2700	0.603	440	125 × 125	0.004	0.004
14	VIS Imaging	15	0.55 - 0.75	-	-	-	21 × 21	-	-

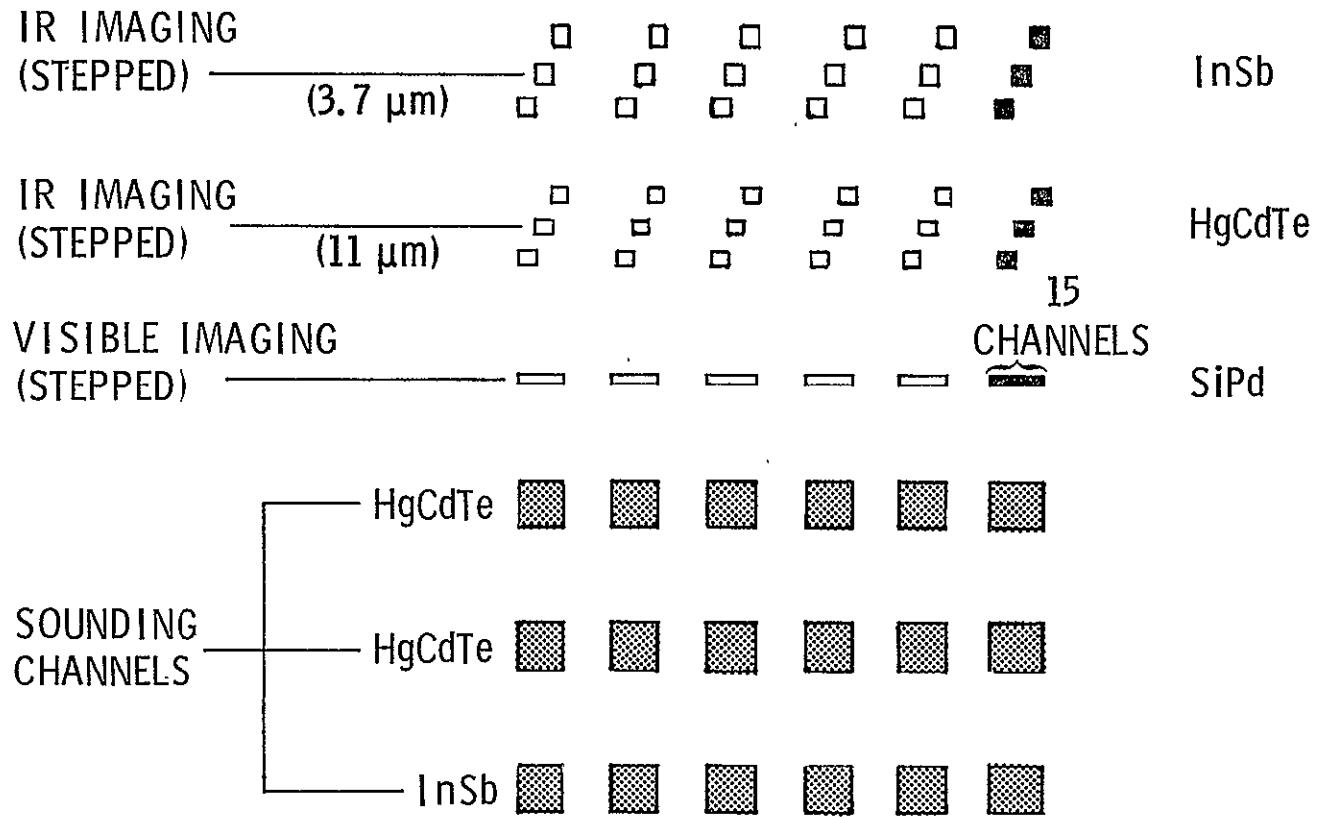


Figure 2-2. View of Detectors as Projected on Prime Focal Plane

15-element array for visible imaging. This is made possible by a step scan mechanism behind the telescope focal plane which steps the FOVs of the imaging detectors sequentially to the positions indicated by the empty outlines. Without this mechanism, known as the quasi object plane scan mechanism (QOPSM), a full complement of imaging detectors would be required, thereby increasing the heat load on the radiative cooler and increasing the complexity of the detector plane. Another alternative to the use of the QOPSM is to fill out the array of imaging detectors, but reduce the number of N-S columns in the array. The scan frequency would have to be increased in order to maintain the same frame time, and channel sensitivity (NEN) would be degraded. In effect there is a tradeoff between detector array complexity, optical/mechanical complexity and performance.

In either case a filter wheel containing three annular bands each with six bandpass filters is positioned such that the outer annulus covers the top row of HgCdTe detectors, the second annulus the middle row, and the inner annulus the bottom row of InSb detectors. The outer two annuli will each contain a  $900 \text{ cm}^{-1}$  (11- $\mu\text{m}$ ) filter and five other channels, the latter being different in the two annuli. The inner annuli will contain filters for short-wavelength  $\text{CO}_2$  sounding and 3.7- $\mu\text{m}$  window channels.

Scanning proceeds as follows: six bidirectional scans are made over the same north-south line, stepping the filter wheel at each mirror turn-around. During the turn-around following the sixth scan, the AASIR is stepped one sounding IGFOV (0.375 mr) in an easterly or westerly direction and the six-scan sequence is repeated. Thus, after 12 scans of  $12 \times 1.29 = 15.48$  seconds, 12 contiguous lines of data will have been scanned and each line will include all spectral channels. More importantly, each HgCdTe detector will have viewed the same spot on earth with a window channel and five other sounding channels ensuring the best possible registration for these channels. Following this, the spacecraft steps the AASIR over eleven steps and the process is repeated. Since the scanner is mechanically resonant, the line time is constant at 1.29 sec, independent of frame size.

## SCANNING METHOD FOR IR AND VISIBLE IMAGING

Figure 2-3 shows schematically the imaging scanning method. The filter wheel, represented by filter annuli A, B, and C, lies close to the telescope prime focal plane. In the figure, the telescope lies to the left. In this system, there is only one array of IR and visible detectors, each subtending  $375 \mu\text{rad}$  (3 to  $125 \mu\text{rad}$  for the IR and 15 to  $21 \mu\text{rad}^*$  for the visible). The three IR imaging detectors are mounted with the sounding detectors on a common substrate at the radiation cooler.

Energy for the IR imaging IFOVs is picked off behind the focal plane by a plane foldout mirror and is directed to a collimating mirror, and then to the step scan mirror. The energy is then sent back to the collimator mirror and then to an fold-in mirror which sends the energy back to the detectors in the radiative cooler via the field and relay lenses. For each step of the scan mirror, the array image is moved over  $750 \mu\text{rad}$ . Thus, the entire sounding array is scanned out in 12 scans.

The step-scan procedure is similar for the visible imaging except that the energy is picked off ahead of the focal plane (see Figure 2-3) and is returned to a silicon photodiode array out of the beam.

The angular step size of the stepping scan mirror depends on the ratio of focal lengths of collimating lens (15.2 cm) and the telescope (325 cm). Therefore, the stepper accuracy is a factor of 20 less critical than for the resonant scanner (assuming the same repeatability requirements).

## SYSTEM CONSTRAINTS ON OPTICAL DESIGN

The STORMSAT mission places stringent requirements on the image quality of the AASIR, mainly for imaging. This in turn places stringent requirements on the thermal design of the AASIR, principally because the three-axis stabilized spacecraft allows prolonged solar heating of the telescope aperture during every orbit. On a spinning spacecraft, solar heating is not so much of a problem because the rapid spin averages out the heat

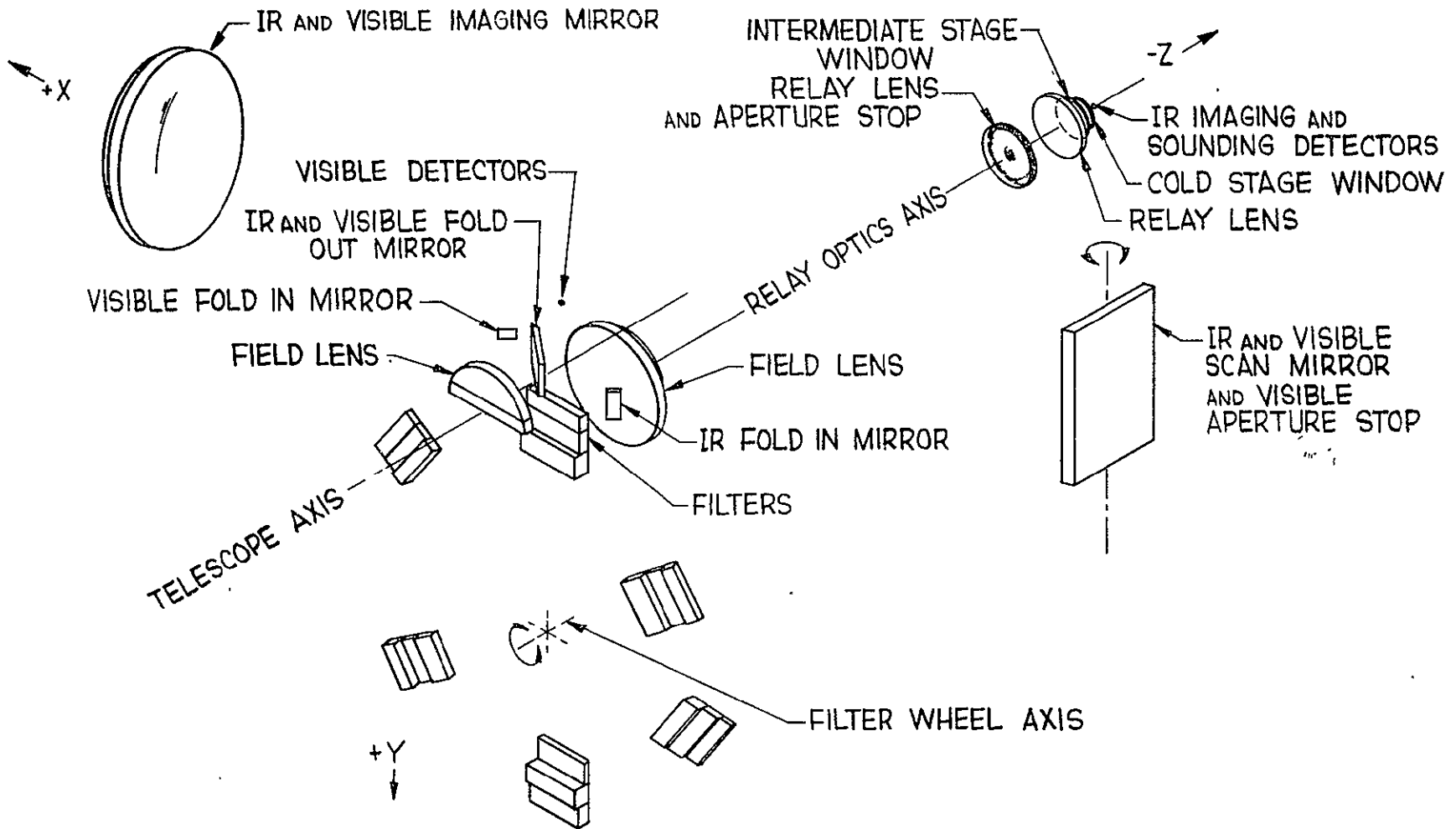


Figure 2-3. Optical Schematic of the Quasi Object Plane Scan Mechanism (QOPSM)

input over the entire orbit. While the AASIR telescope design is superficially similar to VISSR/VAS (40.6-cm diameter, Ritchey-Chretien), defocussing of the VISSR/VAS design due to thermal expansion of the VISSR/VAS design because of the thermal expansion of the all-beryllium VISSR telescope would be excessive. Therefore, the AASIR telescope will use fused-silica primary-secondary mirrors and a graphite filament composite telescope tube. In any case, active focus control will be provided for both the visible and IR channels so that refocussing can be done as required.

#### SYSTEM CONSTRAINTS ON DETECTOR/RADIATIVE COOLER

As shown in Figure 2-1, a passive radiative cooler is used to cool the array of IR detectors consisting of fifteen HgCdTe and six InSb elements (see Figure 2-2). The AASIR design is similar to the VISSR/VAS cooler except that more detectors, and hence, higher heat loads, are involved (two detectors for VISSR, six for VAS). The design consists of an ambient housing earth shield, intermediate stage, and cold stage. The cold stage contains the dewar and detector array, with the intermediate stage serving as a heat shield, isolating the cold stage from the warm surroundings. Unlike the VISSR/VAS cooler, solar loading is not a problem since the STORMSAT spacecraft will be rotated 180° out of the equatorial plane at the equinoxes keeping the sun below the plane of the cooler.

A feature of the AASIR cooler is a pumpable dewar which allows easy assembly, disassembly, and maintainability of the detector/dewar. The dewar is evacuated only during flight, thermal-vacuum tests, or cryostat bench tests. Otherwise, the dewar is vented through a particle filter to the environment and ambient pressure.

## SYSTEM CONSTRAINTS ON RADIOMETRIC CALIBRATION

The stringent radiometric calibration requirements for the IR channels derive from the high radiometric accuracy needed to produce usable temperature and humidity profiles.

In the 15- $\mu\text{m}$   $\text{CO}_2$  temperature sounding band, for example, radiance errors  $\leq 0.25 \text{ erg/sec-cm}^2\text{-sr-cm}^{-1}$  are required to generate temperature profiles with an accuracy of  $\pm 1^\circ\text{K}$ . Relative accuracy between channels is even more important, due to the strong interaction between spectrally adjacent sounding channels in the inversion programs. The calibration specification on the AASIR sensor requires channel-to-channel errors less than sensor NEN corresponding to an absolute calibration of  $\pm 0.5^\circ$  and drift between calibration within  $\pm 0.1\%$ . Translating these errors into radiance errors by assuming a  $250^\circ\text{K}$  scene observed at  $15 \mu\text{m}$  with a sensor NEN of  $0.15 \text{ erg/sec-cm}^{-1}$  results in the following calibration requirements:

$$\begin{aligned} \Delta N_{\text{relative}} &\leq 0.15 \text{ erg/sec-cm}^2\text{-sr-cm}^{-1} \\ \Delta N_{\text{absolute}} &\leq 0.61 \text{ erg/sec-cm}^2\text{-sr-cm}^{-1} \\ \Delta N_{\text{drift}} &\leq 0.977 \text{ erg/sec-cm}^2\text{-sr}^{-1}\text{-cm}^{-1} \end{aligned}$$

Both  $\Delta N_{\text{rel}}$  and  $\Delta N_{\text{drift}}$  are relative errors and are consistent with a total channel-to-channel radiance error  $\leq 0.25 \text{ erg/sec-cm}^2\text{-sr-cm}^{-1}$ .

AASIR in-flight calibration will be done by dc restoring all IR channels on an internal blackbody reference during each scan mirror turn-around and by viewing space periodically. The frequency of space views will depend on system thermal stability and viewing constraints.

A method for correction of ground measured mirror reflectivities and system gains has been developed which depends on measuring the temperatures of various optical elements while the AASIR views space. Solutions to a set of simultaneous equations give new values for those parameters that might have changed after launch. Visible channels will be calibrated in flight by a solar pickoff prism located such that a portion of the solar input

is directed to the silicon photodiodes at least once per day. Additional electrical calibration of signal processing channels will be provided by ramp inputs to the preamplifiers.

**DATA RATES**

The maximum data rate for the AASIR is  $7.0 \times 10^6$  bits/sec which is due mainly to the visible imaging channels. The maximum rate occurs for the  $20^\circ \times 20^\circ$  frame at center scan where the scan rate is maximum. Averaged over a full frame, the data rate is about one-half the maximum rate.

**AASIR WEIGHT ESTIMATE**

The following weight estimate is based on the use of graphite/epoxy for the telescope tube with invar reinforcing rings and invar interfaces for the primary mirror, secondary mirror, and scan mirror.

Scan Mechanism	30 lb
Primary Mirror Assembly	18
Secondary Mirror Assembly	6
Aft Optics and Blackbody	8
Step, Restore, Filter, and Focus Mechanisms	12
Radiation Cooler	8
Main Frame (Structure)	120
Covers and Sunshade	20
Electrical Components	8
Electronics Module	<u>20</u>
Total	250 lb

The Main Frame is made up of the following:

Graphite Telescope Tube	12
Reinforcing Rings (3)	26
Secondary Mirror Support	26
Scan Mirror Support	20
Flex Supports for Telescope Tube (3)	16
Aft Optics and Mounting Ring	<u>20</u>
Total	120 lb

### AASIR POWER DISSIPATION ESTIMATE

The power dissipation estimates given below are based on the VAS where in most cases close similarities exist.

<u>Subsystem</u>	<u>Power (watts)</u>
IR Channel Amplifier (24)	13.7
VIS Channel Amplifiers (15)	6
Processor	3.5
Calibrate Flag Driver	0.45
Filter Wheel Drive	0.45
Temperature Monitors	0.24
Focus Drivers	0.24
Calibrate Ramp	0.10
Imaging Stepper Drive	1.0
Detector Temperature Control Servo	0.1
Calibrate Blackbody Heater	2.0
Power Regulator Losses	<u>5.0</u>
Total Converter Load	32.78
Converter Input at 80% Efficiency	40.98
Resonant Scan Motor	8.0
Calibrate Flag Motor	0.22
Imaging Step Torquer	0.50
Filter Wheel Motor	<u>2.5</u>
Total Average AASIR Power	52.2

Section 3

AASIR SYSTEM CONSIDERATIONS

NOISE EQUIVALENT RADIANCE CALCULATIONS

Infrared System Equation

Fundamental to defining system performance is a method for determining noise equivalent radiance (NEN) which is the radiance needed at the AASIR aperture to produce an output signal equal to the noise. The following system equation was derived from the specific case of a resonant sine, bidirectional scan.

The basic expression for system NEN is given by:

$$NEN = \frac{\gamma(A_d \times NBW)^{\frac{1}{2}} \times 10^7}{A_o \tau_{\Delta\nu} \Omega D^* \Delta\nu} \text{ ergs-sec}^{-1}\text{-cm}^{-2}\text{-sr}^{-1}(\text{-cm}^{-1})^{-1} \quad (1)$$

where:  $\gamma$  = preamplifier noise factor = 1.05

$A_d$  = detector area ( $\text{cm}^2$ )

NBW = equivalent noise bandwidth (Hz)

$A_o$  = effective area of aperture ( $\text{cm}^2$ )

$\tau_{\Delta\nu}$  = transmittance of optics in spectral bandpass  $\Delta\nu$

$\Omega$  = solid angle of view (sr)

$D^*$  = detectivity of detector ( $\text{cm-Hz}^{\frac{1}{2}}\text{-watt}^{-1}$ )

$\Delta\nu$  = spectral bandpass ( $\text{cm}^{-1}$ )

Now, the NBW must be expressed in terms of other known parameters. The equation of motion of the resonant scan is:

$$\phi = \phi_o \sin \omega t^*$$

---

\*Where angles (given in radians) refer to object space, not mirror motion.

where:  $\phi_o$  = the peak scan angle

$\omega t = 2\pi f$  = the scan frequency

$t$  = time, where  $t = 0$  occurs at the zero crossing

$$\phi_m = \phi_o \sin \left( E \frac{\pi}{2} \right)$$

where  $\phi_m$  is the maximum scan angle required. For example, the  $20^\circ$  frame size requires that  $\phi_m = 10.268^\circ = 0.179$  rad including overscan for the  $0.536^\circ$  array size.

$$E = \text{scan efficiency} = \frac{\text{active scan time}}{\text{scan period}}$$

$$\dot{\phi} = \omega \phi_o \cos \omega t$$

So, dwell time  $t_d$

$$t_d = \frac{\alpha}{\dot{\phi}} = \frac{\alpha}{\omega \phi_o \cos \omega t} = \frac{\alpha \sin \left( E \frac{\pi}{2} \right)}{\phi_m \cos \omega t}$$

where  $\alpha$  is the instantaneous field of view (IFOV).

However, the dwell time  $t_d$  will be modified by the ratio of detectors to spectral channels  $N/M$ . Thus,

$$t_d = \frac{N \alpha \sin \left( E \frac{\pi}{2} \right)}{M \phi_m \omega \cos \omega t}$$

The system information bandwidth,  $\Delta f$ , is given by:

$$\Delta f = \frac{1}{2 t_d} = \frac{M \phi_m \omega \cos \omega t}{2 N \alpha \sin \left( E \frac{\pi}{2} \right)} \quad (2)$$

and the equivalent noise bandwidth, NBW, can be expressed as:

$$\text{NBW} = \delta \Delta f \quad (3)$$

Substituting (2) and (3) into (1)

$$NEN = \frac{\gamma A_d^{\frac{1}{2}} \left[ \frac{\delta M \phi_m \omega \cos \omega t}{2 N \alpha \sin \left( \frac{E \pi}{2} \right)} \right]^{\frac{1}{2}} \times 10^7}{A_o \tau_{\Delta\nu} \Omega D^* (\Delta\nu)}$$

making the following substitutions:

$A_d^{\frac{1}{2}} = \alpha D$  (f/No. aft) where f/No. aft is the focal ratio of the beam at the detector and D is aperture diameter in cm. f/No. = 1.0 or 1.4 depending on design of relay optics.

$A_o = \frac{\pi D^2}{4} K$  where K is the area obscuration caused by the secondary mirror

$\Omega = \alpha^2$  = the solid angle of view (sr)

$\omega = 2\pi f_s$ ;  $f_s$  = scan frequency

For bidirectional scan, a scan cycle will take

$$T_s = 2T_F \frac{\alpha}{\theta_h}$$

where  $\theta_h$  is the angular size of the frame, assuming the frame is square.

Thus, for a  $20^\circ \times 20^\circ$  frame,  $\theta_h = 0.349$  rad.  $T_F$  is frame time in seconds.

Thus,

$$\omega = \frac{\pi \theta_h}{T_F \alpha}$$

and

$$NEN = \frac{4 \gamma (f/No.) \left[ \delta M \phi_m \theta_h \cos \left( \frac{\pi \theta_h}{T_F \alpha} t \right) \right]^{\frac{1}{2}} \times 10^7}{D K \alpha^2 \tau_{\Delta\nu} (\Delta\nu) D_s^* \left[ 2 N \pi T_F \sin \left( \frac{E \pi}{2} \right) \right]^{\frac{1}{2}}} \text{ ergs/sec-cm}^2\text{-sr-cm}^{-1}$$

The above equation can be used to show the effect on NEN of varying parameters as follows:

1. Varying the frame size affects the NEN as shown in Figure 3-1. When compared with a single detector, the fixed array size causes a larger degradation for the small frame sizes than the larger ones.

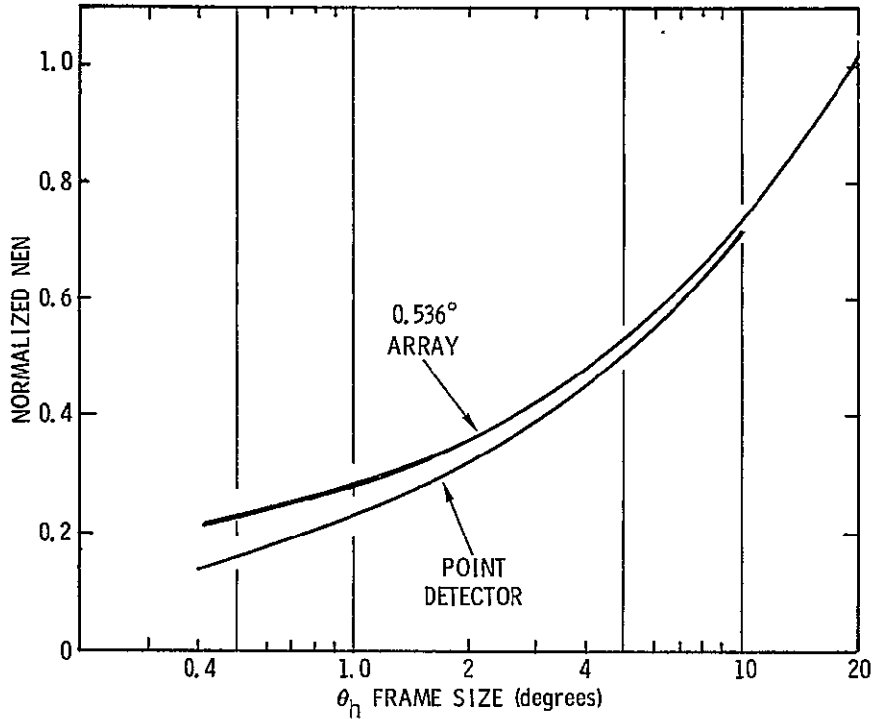


Figure 3-1. Normalized NEN versus Frame Size

2. Varying the scan efficiency,  $E = \frac{\text{active scan time}}{\text{scan period}}$ , has a relatively small effect on NEN as shown in Figure 3-2. DC restore constraints limit scan efficiency to 60% or less.
3. In the case of the present AASIR design, the ratio  $(M/N)^{\frac{1}{2}} = 1$  since there are 18 sounding channels and 18 detectors. It would clearly be difficult and costly to increase N enough to gain a significant improvement in NEN. On the other hand, a small increase in M does not degrade NEN much. For example, if it were desired to increase the number of spectral channels from 18 to 21, the NEN would be degraded by 8%.
4. The value of  $\delta$  depends on the scan frequency and the dc restore parameters selected. Table 3-1 gives values of NBW and  $\delta$  for several scan frequencies.

Table 3-2 gives the NEN values for the nominal AASIR parameters and frame sizes.

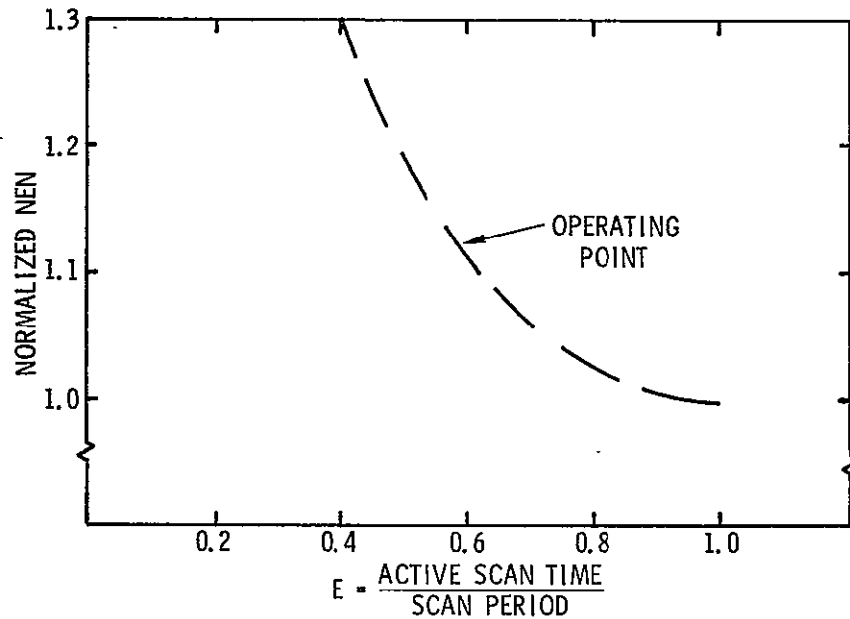


Figure 3-2. Normalized NEN versus Scan Efficiency

Table 3-1. Values of NBW and  $\delta$ , One Restore per Scan Line ( $20^\circ \times 20^\circ$  frame)

SCAN FREQUENCY (Hz)	$\tau_2$ (msec)	NBW (kHz)				$\delta$				$\Delta f$ (kHz)
		$F_0 = 750$	500	250	100	750	500	250	100	
$0.77^1$	36	12.8	10.1	7.33	5.60	2.98	2.35	1.7	1.32	4.3
$0.77^2$	36	8.89	6.44	3.99	2.52	6.17	4.47	2.77	1.75	1.44
$0.385^3$	105.3	9.98	7.42	4.86	3.32	4.64	3.45	2.26	1.54	2.15
$0.385^4$	105.3	7.58	5.31	3.04	1.67	10.54	7.39	4.22	2.32	0.72

WHERE:  $\tau_2$  IS THE RESTORE CIRCUIT TIME CONSTANT IN SECONDS

$\tau_3$  IS THE RESTORE TIME IN SECONDS

$$\rho = \tau_3 / \tau_2 = 3$$

$F_0$  IS THE HgCdTe DETECTOR  $1/f$  NOISE BREAK FREQUENCY

NOTES:

<sup>1</sup>IR IMAGING, BIDIRECTIONAL SCAN - 10-MINUTE FRAME

<sup>2</sup>SOUNDING CHANNELS, BIDIRECTIONAL SCAN - 10-MINUTE FRAME

<sup>3</sup>IR IMAGING CHANNELS, BIDIRECTIONAL SCAN - CURRENT AASIR CONFIGURATION - 20-MINUTE FRAME

<sup>4</sup>SOUNDING CHANNELS, BIDIRECTIONAL SCAN - CURRENT AASIR CONFIGURATION - 20-MINUTE FRAME

Table 3-2. AASIR NEN Values Obtained from System Equation

BAND	$\nu_c$ ( $\text{cm}^{-1}$ )	$\Delta\nu_c$ ( $\text{cm}^{-1}$ )	$\tau_{\Delta\lambda}$	$\delta$	$D^* \times 10^{10}$ ( $\text{cm-Hz}^{\frac{1}{2}}\text{-watt}^{-1}$ )	NEN ( $\text{ergs-sec}^{-1}\text{-cm}^{-2}\text{-sr}^{-1}\text{-cm}^{-1}$ )			
						$20^\circ \times 20^\circ$	$4^\circ \times 4^\circ$	$1.2^\circ \times 1.2^\circ$	$0.4^\circ \times 0.4^\circ$
1	668.5	5	0.094	3.59	1.3	8.68	4.08	2.53	1.85
2	680	15	0.154	3.59	1.48	1.55	0.73	0.451	0.331
3	690	16	0.229	3.59	1.64	0.88	0.415	0.257	0.188
4	703	16	0.244	3.59	1.84	0.738	0.347	0.214	0.156
5	716	20	0.253	3.59	2.0	0.524	0.246	0.152	0.111
6	733	20	0.249	3.59	2.0	0.536	0.25	0.154	0.112
7	750	20	0.253	3.59	2.0	0.524	0.246	0.152	0.111
7a	800	40	0.277	3.59	2.0	0.241	0.113	0.07	0.051
8	900	140	0.300	2.02	2.09	0.235	0.109	0.067	0.049
9a	1380	60	0.321	3.59	1.23	0.224	0.105	0.065	0.047
10	1490	140	0.404	3.59	1.23	0.076	0.036	0.022	0.016
11	2360	50	0.322	3.59	28.6	0.0115	0.0054	0.0033	0.0024
11a	2275	35	0.322	3.59	28.6	0.0164	0.0077	0.0047	0.0035
11b	2250	40	0.322	3.59	28.6	0.0145	0.0068	0.0042	0.0031
11c	2210	40	0.322	3.59	28.6	0.014	0.0065	0.004	0.0029
11d	2190	40	0.322	3.59	28.6	0.014	0.0068	0.0042	0.0031
12	2535	140	0.375	3.59	25.0	0.0038	0.0018	0.0011	0.0008
13	2700	440	0.375	2.02	25.0	0.014	0.0065	0.004	0.0029

NOTES: (f/NO. AFT) = 1;  $F_0 = 200$  Hz

Performance of 3.7- $\mu\text{m}$  Imaging Channels

One of the assigned tasks during the study was to determine the feasibility of adding 3.7- $\mu\text{m}$  imaging channels for the purpose of night viewing of clouds. The task involved exploring the trade-offs between IFOV size and NEN. To help establish a baseline for image quality, VAS design data were used. From the VAS Phase II Design Review Report, Volume 1, pages 3-46, the 11- $\mu\text{m}$  blur diameter containing 90% energy is the RSS sum of the following factors:

Geometric Aberrations (0.9 mr off-axis)	0.096 mr
Diffraction	0.179
Fabrication Tolerance	0.090
In-Orbit Thermal Variations	<u>0.136</u>
	0.260 mr

Since this is the blur diameter enclosing 90% of the point source energy, the geometrical field of view (FOV) of 0.192 mr will still contain a significant fraction of the energy.

Applying the above argument to the AASIR 3.7- $\mu$ m channels, a factor must be added which accounts for the chromatic aberration in the germanium field and relay lenses. This was calculated for the best focus condition at 2.3 mr off-axis which corresponds to the detector position in the array.

3.7- $\mu$ m blur - chromatic plus geometric aberrations

<u>Percent Enclosed Energy</u>	<u>Blur Diameter (mr)</u>
10	0.011
20	0.016
30	0.022
40	0.030
50	0.041
60	0.049
70	0.058
80	0.067
90	0.076
100	0.148

At the 90% level, the RSS blur is:

Chromatic and Geometric Blur	0.075 mr
Diffraction	0.040
Fabrication Tolerance	0.090
In-Orbit Thermal Variations	<u>0.136</u>
RSS Blur	0.184 mr

In-orbit thermal variation is seen to be the dominating factor. Assuming that active focus during every orbit can be provided, the blur becomes 0.124 mr. Applying the ratio of FOV to blur diameter occurring in VAS for the conditions with and without in-orbit thermal variations gives the following FOVs:

With in-orbit thermal variations	0.134 mr
Without in-orbit thermal variations	0.090 mr

It appears from the discussion above that the minimum FOV giving reasonable values of enclosed energy would be close to the size currently planned for AASIR IR imaging, namely 0.125 mr. It is also clear that improvements in the optics fabrication and active in-orbit focussing can improve the 3.7- $\mu\text{m}$  resolution significantly.

3.7- $\mu\text{m}$  Channel NEN - The system NEN can be calculated using the expression derived in the previous subsection:

$$\text{NEN} = \frac{4\gamma(f/\text{No.}) \left[ \delta \phi_m \theta_h \cos \left( \frac{\pi \theta_h}{\alpha T_F} t \right) \right]^{\frac{1}{2}} \times 10^7}{DK\alpha^2 \tau_{\Delta\nu} D^*(\Delta\nu) \left[ 2N\pi T_F \sin \left( E \frac{\pi}{2} \right) \right]^{\frac{1}{2}}}$$

where:  $\gamma$  = preamplifier noise factor = 1.05

$f/\text{No.} = 1$

$\delta = \text{NBW}/\Delta f = 3.6$

$\phi_m$  = maximum scan angle for  $20^\circ \times 20^\circ$  frame = 0.179 rad

$\theta_h$  = angular size of frame = 0.349 rad

$\cos ( ) = 1$  worst-case value

$D$  = aperture diameter = 40.64 cm

$K$  = secondary mirror obscuration ration = 0.87

$\alpha$  = FOV = variable

$\tau_{\Delta\nu}$  = optical transmittance = 0.375

$D^* = 2.5 \times 10^{11} \text{ cm-Hz}^{\frac{1}{2}}\text{-watt}^{-1}$

$\Delta\nu = 440 \text{ cm}^{-1}$

$N$  = number of detectors - related to  $\alpha$

If  $\alpha = 0.125 \text{ mr}$ ,  $N = 3$

$\alpha = 0.090 \text{ mr}$ ,  $N = 4$

$\alpha = 0.075 \text{ mr}$ ,  $N = 5$

$T_F$  = frame time = 23.7 min  $\times$  60 = 1422 sec for the  $20^\circ \times 20^\circ$  frame

$E$  = scan efficiency = 0.60

The following NEN values were obtained:

$\alpha$ (mr)	NEN (ergs-etc.) ( $20^\circ \times 20^\circ$ )	NEN (ergs-etc.) ( $1.2^\circ \times 1.2^\circ$ )
0.075	0.013	0.0017
0.090	0.010	0.0029
0.125	0.006	0.0037

Visible Channel Signal-to-Noise Ratios

The performance of the visible channels using silicon photodiodes is calculated in this subsection. Expressions are derived for noise current with and without high frequency boost, and HP-25 programs for their solution are given.

The analysis includes the following:

1. Inclusion of residual dark current noise and loss tangent noise not considered previously.
2. Analytical integration of noise functions.
3. Trade-off using  $10^8 \Omega$  and  $10^9 \Omega$  feedback resistors with high frequency boost.
4. Consideration of two spectral bands: 0.55 to 0.75  $\mu\text{m}$  and 0.8 to 1.1  $\mu\text{m}$ .
5. Consideration of three additional FOVs; namely, 16, 13, and 10  $\mu\text{rad}$ .
6. Consideration of a higher scan frequency (0.58 Hz) to allow use of a smaller IR detector array ( $3 \times 4$ ) and elimination of the imaging channel scan stepping device.

The silicon photodiode is nominally operated at zero bias into a current mode amplifier. However, owing to optimization and temperature drift of the differential amplifier, the diode may have several hundred millivolts across it. Under these conditions, the dark current noise is assumed to be:

$$i_D = 4.5 \times 10^{-15} \text{ amps/Hz}^{\frac{1}{2}}$$

Loss Tangent Noise - A noise mechanism associated with the dielectric losses of the amplifier input capacitance has been observed. It takes the form:

$$i_C = [4KT (2\pi f) C_T \tan \delta]^{1/2}$$

where  $C_T$  is the total input capacitance.

$$C_T = C_{in} + C_f$$

$C_{in}$  = amplifier input capacitance =  $\sim 10$  pf

$C_f$  = distributed capacitance across the feedback resistor  $\cong 0.1$  pf

$\delta = 0.001$  to  $0.01$ , depending on devices

Loss tangent noise is an " $f^{1/2}$ " noise, rising with increasing frequency.

Figure 3-3 shows the signal and noise sources for the diode-preamplifier combination.

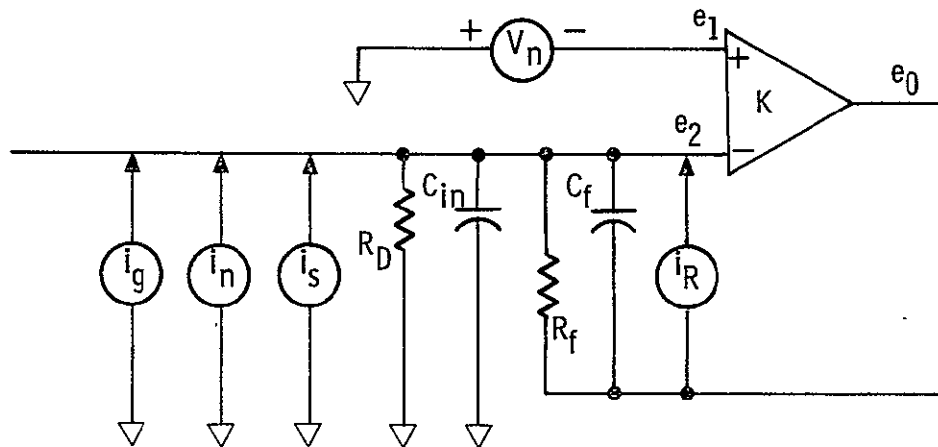


Figure 3-3. Visible Channel Preamplifier Equivalent Circuit

The total noise contributions as a function of frequency can be expressed thus:

$$e_{nt} = \left[ \frac{i_T^2 + V_n^2 (G_T^2 + C_T^2 \omega^2)}{\left(G_f + \frac{G_T}{K_A}\right)^2 + \left(C_f + \frac{C_T}{K_A}\right)^2 \omega^2} \right]^{1/2} \quad (1)$$

where:  $i_T^2 = (4KT C_T \tan \delta \omega) + i_g^2 + i_n^2 + i_D^2 + i_R^2$   
 $i_g^2 =$  shot noise and Johnson diode noise

$$i_g^2 = \frac{4KT}{R_D} + 2 e i_s$$

$i_s =$  signal current

$i_n =$  amplifier noise current =  $6 \times 10^{-16}$  amps/Hz $^{\frac{1}{2}}$

$V_n =$  amplifier noise voltage =  $5.9 \times 10^{-9}$  volts/Hz $^{\frac{1}{2}}$  for two BF 805  
in differential connection (at 1 kHz)

$i_D =$  dark current noise =  $4.5 \times 10^{-15}$  amps/Hz $^{\frac{1}{2}}$

$i_R =$  Johnson noise of the feedback resistance =  $\left(\frac{4KT}{R_f}\right)^{\frac{1}{2}}$

$R_D =$  dynamic diode resistance =  $10^{11} \Omega$

$e =$  charge of electron =  $1.6 \times 10^{-19}$  coul.

$K =$  Boltzmann's constant =  $1.38 \times 10^{-23}$  watts-sec- $^{\circ}K^{-1}$

$K_A =$  amplifier gain  $K_A \gg 1$

Major contributors to system noise are plotted in Figure 3-4 as a function of frequency. It is clear that major contributors are diode shot noise and Johnson noise in the load resistor (curve for  $R_f = 10^8 \Omega$  shown). At high frequency, the signal and all noise components except the amplifier voltage noise  $V_n$  are rolled off by the pole determined by  $R_f$  and  $C_f$ . Therefore, the total noise is asymptotic to a value determined by the  $R_f C_f$  pole and the  $R_T C_T$  zero.

Total system noise is obtained by integrating the square of the noise function over the noise bandwidth of the system.

$$E_{NT} = \left[ \int_0^{\omega_c} e_{nt}^2(\omega) d\omega \right]^{\frac{1}{2}} \quad (2)$$

where

$$\omega_c = 2\pi f_c$$

and

$$f_c = \frac{1}{2T_d}$$

where  $T_d$  is the dwell time associated with a given FOV and the 1.1 factor is the ratio of equivalent noise bandwidth of the output filter and the corner frequency of the information bandwidth determined by the dwell time. That is, without specifying the exact nature of the output low pass filter, we have assumed:

$$2T_d(\Delta f_n) = 1.1$$

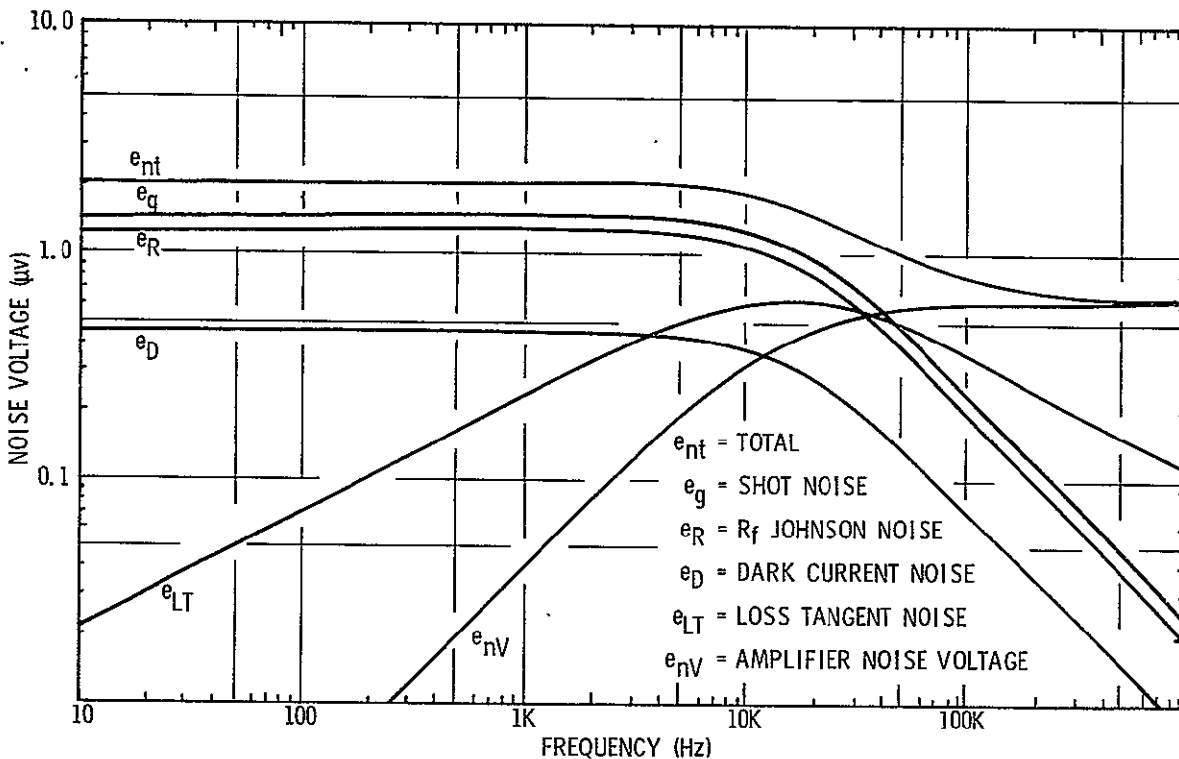


Figure 3-4. AASIR Visible Channel Noise Sources (21  $\mu$ rad, 0.55 to 0.75  $\mu$ m,  $R_f = 10^8 \Omega$ , scan = 0.386 Hz)

The solution to (2) is given by:

$$E_{NT}^2 = E_{N_1}^2 + E_{N_2}^2 + E_{N_3}^2 \quad (3)$$

where:

$$E_{N_1}^2 = \frac{1}{2\pi C_f G_f} (B + V_n^2 G_T^2) \tan^{-1} \frac{2\pi f_c C_f}{G_f} \quad (4)$$

$$B = i_g^2 + i_n^2 + i_D^2 + i_R^2$$

$$E_{N_2}^2 = \frac{A}{4\pi C_f^2} \ln \left[ \left( \frac{2\pi f_c C_f}{G_f} \right)^2 + 1 \right] \quad (5)$$

$$A = 8\pi KTC_T \tan \delta = 5.26 \times 10^{-33}$$

$$E_{N_3}^2 = \left( V_n \frac{C_T}{C_f} \right)^2 \left[ f_c + \frac{G_f}{2\pi C_f} \tan^{-1} \frac{2\pi f_c C_f}{G_f} \right] \quad (6)$$

These functions are easily programmed on an HP-25 or HP-65 calculator as follows:

Program for  $E_{N_1}^2$

C <sub>f</sub>	STO 1	Calculate in radians			
B	STO 2	Enter f <sub>c</sub> in Hz			
V <sub>n</sub> <sup>2</sup>	STO 3				
G <sub>T</sub> <sup>2</sup>	STO 4	Step	Function	Step	Function
G <sub>f</sub>	STO 5	1	↑	13	π
A	STO 6	2	2	14	÷
		3	×	15	RCL 1
		4	π	16	÷
		5	×	17	RCL 5
		6	RCL 1	18	÷
		7	×	19	RCL 3
		8	RCL 5	20	RCL 4
		9	÷	21	×
		10	tan <sup>-1</sup>	22	RCL 2
		11	2	23	+
		12	÷	24	×

Program for  $E_{N_2}^2$  and  $E_{N_3}^2$

$E_{N_2}^2$ :

$f_c$	STO 0	Calculate in radians			
		Enter $f_c$			
$C_f$	STO 1				
B	STO 2	Step	Function	Step	Function
$V_n^2$	STO 3	1	↑	12	+
$G_T^2$	STO 4	2	2	13	ln
$G_f$	STO 5	3	×	14	RCL 6
A	STO 6	4	π	15	×
$C_T^2$	STO 7	5	×	16	4
		6	RCL 1	17	÷
		7	×	18	π
		8	RCL 5	19	÷
		9	÷	20	RCL 1
		10	$\times^2$	21	$\times^2$
		11	1	22	÷

$E_{N_3}^2$ :

		Step	Function	Step	Function
		1	RCL 0	15	π
		2	2	16	÷
		3	×	17	RCL 1
		4	π	18	÷
		5	×	19	CHS
		6	RCL 1	20	RCL 0
		7	×	21	+
		8	RCL 5	22	RCL 3
		9	÷	23	×
		10	$\tan^{-1}$	24	RCL 7
		11	RCL 5	25	×
		12	×	26	RCL 1
		13	2	27	$\times^2$
		14	÷	28	÷

High frequency boost is needed to give flat response out to frequencies beyond the  $R_f C_f$  pole corner frequency. System FOVs less than  $21 \mu\text{rad}$  and/or scan frequencies higher than the nominal value of  $0.386 \text{ Hz}$  call for boosting from the  $R_f C_f$  corner frequency to  $f_c$ . This is accomplished by multiplying (1) by a "zero" with the same corner frequency as the pole. The resulting expression is then integrated as in (2) giving:

$$E_{N_T}^2 \text{ (boost)} = \frac{B + V_n^2 G_T^2}{G_f^2} f_c + \frac{\pi A f_c^2}{G_f^2} + \frac{4 V_n^2 C_T^2 \pi^2 f_c^3}{3} \quad (7)$$

For signal calculations, the performance data of a UDT PIN-020 photodiode was assumed.

The power falling on the detector is:

$$P_d = N_e A_o \Omega T_o a$$

- where:  $N_e$  = radiance when viewing the earth in the spectral band  $0.55$  to  $0.8 \mu\text{m} = 1.12 \times 10^{-2} \text{ w-cm}^{-2}\text{-sr}^{-1}$   
 $A_o$  = effective aperture area =  $1090 \text{ cm}^2$   
 $\Omega$  = solid angle of view  
 $T_o$  =  $0.39$  average optical transmittance in the spectral passband  
 $a$  = albedo - assumed equal to  $1$  or  $0.01$

The UDT PIN-020 photodiode has an average responsivity of  $0.3 \text{ amp/watt}$  over the range  $0.55$  to  $0.8 \mu\text{m}$ .

$$\text{Signal current } i_s = P_d \text{ (Resp)}$$

Signal-to-noise ratio (SNR)

$$\text{SNR} = \frac{i_s R_f}{E_{NT}}$$

This expression was evaluated for four FOVs, two spectral bands, and two values of  $R_f$ . These data are presented in Table 3-3.

There appears to be a small advantage in using a  $10^9 \Omega$  feedback resistor. This value appears to be practical in terms of circuit performance.

Table 3-3. AASIR Visible Channel Signal-to-Noise Ratios

BAND ( $\mu\text{m}$ )	IFOV ( $\mu\text{rad}$ )	SCAN RATE (Hz)	$\Delta f_n$ (kHz)	$R_f = 10^9 \Omega$				$R_f = 10^8 \Omega$			
				$E_{NT}$ (volts $\times 10^{-3}$ ) $\alpha = 1$	$E_S$ (volts $\times 10^{-3}$ ) $\alpha = 1$	SNR ALBEDO $\alpha = 1$	SNR ALBEDO $\alpha = 0.01$	$E_{NT}$ (volts $\times 10^{-4}$ ) $\alpha = 1$	$E_S$ (volts $\times 10^{-4}$ ) $\alpha = 1$	SNR ALBEDO $\alpha = 1$	SNR ALBEDO $\alpha = 0.01$
0.55 - 0.75	21	0.386	14.1	2.61	673	258	3.45	0.30	67.3	224	2.77
0.55 - 0.75	16	0.386	18.5	2.93	391	133	1.56	0.34	39.1	116	1.3
0.55 - 0.75	13	0.386	22.7	3.39	258	76	0.84	0.38	25.8	68	0.73
0.55 - 0.75	10	0.386	29.6	4.10	153	37	0.39	0.46	15.3	33.3	0.34
0.55 - 0.75	21	0.579	21.2	3.56	673	189	2.35	0.40	67.3	168	2.0
0.55 - 0.75	16	0.579	27.8	4.0	391	98	1.06	0.46	39.1	84.6	0.93
0.55 - 0.75	13	0.579	34.1	4.86	258	53	0.57	0.53	25.8	48.7	0.51
0.55 - 0.75	10	0.579	44.4	6.0	153	25	0.26	0.65	15.3	23.5	0.24
0.8 - 1.1	21	0.386	14.1	2.32	365	157	1.9	0.27	36.5	133	1.5
0.8 - 1.1	16	0.386	18.5	2.74	212	77	0.84	0.32	21.2	66	0.7
0.8 - 1.1	13	0.386	22.7	3.21	140	44	0.46	0.37	14.0	38	0.39
0.8 - 1.1	10	0.386	29.6	4.02	83	21	0.21	0.45	8.3	18.4	0.19
0.8 - 1.1	21	0.519	21.2	3.26	365	112	1.3	0.37	36.5	98.4	1.1
0.8 - 1.1	16	0.519	27.8	3.94	212	54	0.57	0.44	21.2	47.7	0.5
0.8 - 1.1	13	0.519	34.1	4.67	140	30	0.31	0.52	14	27	0.28
0.8 - 1.1	10	0.519	44.4	5.92	83	14	0.14	0.65	8.3	12.8	1.13

Selection of the minimum FOV depends on the SNR achievable at the lowest expected albedo as well as other factors. SNR values are given for 100% and 1% albedo values.

Table 3-4 contains data pertaining only to the full frame size ( $20^\circ \times 20^\circ$ ). The various IFOVs were evaluated to see the trade-off with SNR. The two wavelength regions were evaluated in response to interest by GSFC and the two scan speeds relate to two possible system configurations: one with the QOPSM (nominal speed) and without the QOPSM but with  $3 \times 4$  rather than  $3 \times 6$  sounding array ( $\times 1.5$  speed).

Using a  $10^9 \Omega$  feedback resistor gives a  $R_f C_f$  pole at 1590 Hz. Therefore, high frequency boost was used to give flat response.

Table 3-4. Visible Channel SNR;  $R_f = 10^9 \Omega$ , albedo = 1 (with boost)

$\lambda$ ( $\mu\text{m}$ )	IFOV <sup>2</sup> ( $\mu\text{rad}$ ) <sup>2</sup>	SCAN RATE	FRAME SIZE	$E_{NT}$ $\times 10^{-3}$ (volts)	$E_S$ $\times 10^{-3}$ (volts)	SNR
0.5 - 0.75	21	NOMINAL	4 x 4	0.976	673	690
0.5 - 0.75	16	NOMINAL	4 x 4	0.97	391	403
0.5 - 0.75	13	NOMINAL	4 x 4	1.05	258	246
0.5 - 0.75	10	NOMINAL	4 x 4	1.13	153	135
0.5 - 0.75	21	x 1.5	4 x 4	1.24	673	543
0.5 - 0.75	16	x 1.5	4 x 4	1.27	391	308
0.5 - 0.75	13	x 1.5	4 x 4	1.4	258	184
0.5 - 0.75	10	x 1.5	4 x 4	1.56	153	98
0.5 - 0.75	21	NOMINAL	1.2 x 1.2	0.57	673	1181
0.5 - 0.75	16	NOMINAL	1.2 x 1.2	0.55	391	711
0.5 - 0.75	13	NOMINAL	1.2 x 1.2	0.572	258	451
0.5 - 0.75	10	NOMINAL	1.2 x 1.2	0.57	153	268
0.5 - 0.75	21	x 1.5	1.2 x 1.2	0.72	673	935
0.5 - 0.75	16	x 1.5	1.2 x 1.2	0.69	391	567
0.5 - 0.75	13	x 1.5	1.2 x 1.2	0.73	258	353
0.5 - 0.75	10	x 1.5	1.2 x 1.2	0.75	153	204
0.5 - 0.75	21	NOMINAL	4 x 4	0.80	365	456
0.5 - 0.75	16	NOMINAL	4 x 4	0.841	212	252
0.5 - 0.75	13	NOMINAL	4 x 4	0.913	140	153
0.5 - 0.75	10	NOMINAL	4 x 4	1.06	83	78
0.5 - 0.75	21	x 1.5	4 x 4	1.04	365	351
0.5 - 0.75	16	x 1.5	4 x 4	1.13	212	188
0.5 - 0.75	13	x 1.5	4 x 4	1.25	140	112
0.5 - 0.75	10	x 1.5	4 x 4	1.49	83	56
0.5 - 0.75	21	NOMINAL	1.2 x 1.2	0.46	365	794
0.5 - 0.75	16	NOMINAL	1.2 x 1.2	0.458	212	463
0.5 - 0.75	13	NOMINAL	1.2 x 1.2	0.473	140	296
0.5 - 0.75	10	NOMINAL	1.2 x 1.2	0.519	83	159
0.5 - 0.75	21	x 1.5	1.2 x 1.2	0.58	365	629
0.5 - 0.75	16	x 1.5	1.2 x 1.2	0.588	212	361
0.5 - 0.75	13	x 1.5	1.2 x 1.2	0.618	140	226
0.5 - 0.75	10	x 1.5	1.2 x 1.2	0.69	83	120

DC RESTORE ANALYSIS

In the foregoing analyses of system NEN noise bandwidth, values were used but not derived. Noise bandwidth, however, is a function of dc restore parameters and detector 1/f noise corner frequency. This subsection analyzes the effects of dc restore on noise bandwidth and the effect of filter offset which must be restored out by the dc restorer.

The present configuration of the AASIR uses a resonant sinusoidal scanner in which 60% of the period is used for active data collection in both forward and back scans. During each turnaround, 20% of the period is used for dc restoration on an internal blackbody.

The AASIR has the following operational characteristics which have necessitated inclusion of the following two factors:

1. The restore time constant  $\tau_2$  is not negligibly small compared to the restore time  $T_3$ . Typical range of values of  $T_3/\tau_2$  is 2 to 10.
2. The detector sees a different filter each scan so that the effect of a dc offset term must be considered.

This analysis derives expressions for both the equivalent noise bandwidth (NBW) and the filter offset error  $V_F$ . An optimum value of  $T_3/\tau_2$  is determined which minimizes total system restore error.

From Figure 3-5 it can be seen that the timing of the system is relatively fixed except for the restore time constant  $\tau_2$ . Therefore, system performance will be evaluated with  $T_3/\tau_2$  as a parameter.

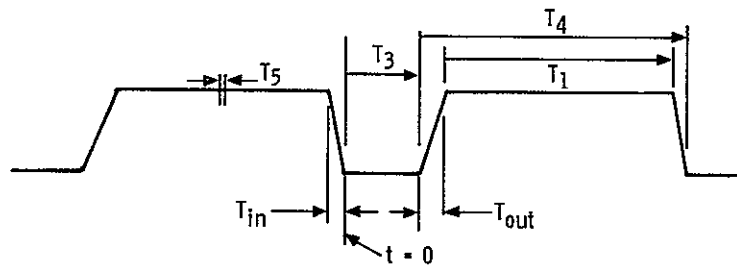
Figure 3-6 shows a simplified schematic diagram of the restore circuit. In the figure, the restore switch is assumed to close at  $t = 0$ . The input noise voltage is represented by a sinusoid of slowly varying but random phase and a dc term  $V_0$  for the offset produced when viewing a different filter each scan. The voltage  $e_2$  is fed back to the subtractor at the input after the switch is closed at  $t = 0$ . At  $t = T_3$ , the switch is opened and the output voltage  $e_0$  thereafter is equal to the difference between  $e_{in}$  and the

voltage stored on the capacitor. The time constant of the restore circuit is shown as RC, but it is understood that the time constant is really RC/K where K >> 1.

$$e_{in}(\omega, t, \theta) = V_0 + \sin(\omega t + \theta) = V_0 + \sin \omega t \cos \theta + \cos \omega t \sin \theta \quad (1)$$

$$E_{in}(s) = \frac{V_0}{s} + \frac{\omega \cos \theta}{s^2 + \omega^2} + \frac{s \sin \theta}{s^2 + \omega^2}$$

$$E_2(s) = \frac{V_0}{s\tau_2(s + 1/\tau_2)} + \frac{\cos \theta}{\tau_2(s^2 + \omega^2)(s + 1/\tau_2)} + \frac{s \sin \theta}{\tau_2(s^2 + \omega^2)(s + 1/\tau_2)}$$



- WHERE: T<sub>2</sub> = SCAN PERIOD = 2.58 sec  
 T<sub>1</sub> = ACTIVE SCAN TIME = 0.774 sec  
 T<sub>3</sub> = RESTORE TIME = 0.4 x 1.29 - T<sub>in</sub> - T<sub>out</sub> = 0.316 sec  
 T<sub>in</sub> = T<sub>out</sub> = 0.10 sec SHUTTER INSERTION - REMOVAL TIME  
 T<sub>4</sub> = RESTORE HOLD TIME = TIME BETWEEN DC RESTORE SWITCH OPENING AND CLOSING  
 T<sub>5</sub> = INTEGRATION TIME OR DWELL TIME PER IFOV. IN THIS ANALYSIS, THE MINIMUM DWELL TIME WHICH OCCURS AT CENTER SCAN IS ASSUMED. THUS, FOR SOUNDING, T<sub>5</sub> = 700 μsec AND FOR IR IMAGING, T<sub>5</sub> = 233 μsec.

Figure 3-5. AASIR Scan Timing Diagram

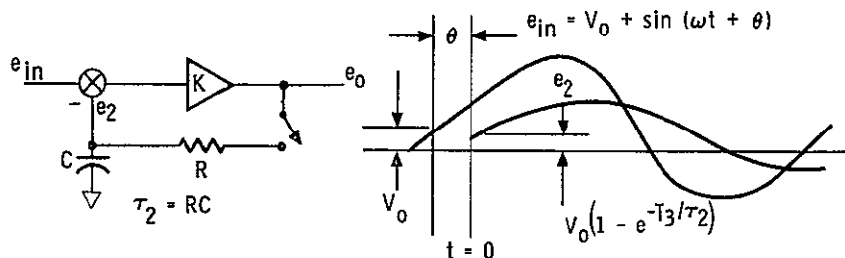


Figure 3-6. DC Restore Equivalent Circuit

Taking the inverse transform

$$e_2(t) = V_o \left( 1 - e^{-T_3/\tau_2} \right) + A \cos \theta + B \sin \theta \quad (2)$$

where

$$A = \frac{\omega \tau_2}{1 + \omega^2 \tau_2^2} \left( 1 - e^{-T_3/\tau_2} \right)$$

$$B = \frac{1}{1 + \omega^2 \tau_2^2} \left( 1 - e^{-T_3/\tau_2} \right)$$

When  $t = T_3$ , the restore switch is opened and the output noise power transfer function is:

$$N^2(\omega, t, \theta) = 2 \left\{ V_o + \sin(\omega t + \theta) - \left[ V_o \left( 1 - e^{-T_3/\tau_2} \right) + A \cos \theta + B \sin \theta \right] \right\}^2$$

Averaging over all values of  $\theta$  gives:

$$N^2(\omega, t) = \frac{1}{2\pi} \int_0^{2\pi} N^2(\omega, t, \theta) d\theta =$$

$$N^2(\omega, t) = 1 + K^2 + A^2 + B^2 + 2A \sin \omega t - 2B \cos \omega t \quad (3)$$

where

$$K = V_o e^{-T_3/\tau_2}$$

Now, to obtain the rms value of  $N^2$  averaged over  $T_1$ , the data taking period:

$$N^2_{\text{rms}}(\omega) = \frac{1}{T_1} \int_0^{T_1} N^2(\omega t) dt$$

and,

$$N^2_{\text{rms}}(\omega) = 1 + K^2 + A^2 + B^2 - \frac{2A}{\omega T_1} (\cos \omega T_1 - 1) - \frac{2B}{\omega T_1} \sin \omega T_1 \quad (4)$$

where A, B, and K are the same as in equations (2) and (3).

As a check, let  $T_3 \gg \tau_2$  in equation (4). The resulting expression is:

$$N_{\text{rms}}^2 = 1 + \frac{1}{\omega^2 \tau_2^2 + 1} - \frac{2[\omega \tau_2 (\cos \omega T_1 - 1) + \sin \omega T_1]}{\omega T_1 (1 + \omega^2 \tau_2^2)} \quad (5)$$

$$T_3 \gg \tau_2$$

which is the same expression developed in Reference 1.

The noise transfer function [equation (4)] is plotted in Figure 3-7. For the smaller values of  $T_3/\tau_2$ , response continues to very low frequencies where  $1/f$  contributions could be significant. This is particularly true in the AASIR since the detector coupling circuit which determines the low frequency rolloff of the system must have a time constant such that the sag over the line time (1.2 sec) must be less than 0.25% (VAS specification). Thus,

$$e^{-1.29\tau} = 0.9975$$

$$\tau = 515 \text{ sec}$$

and

$$f_{3 \text{ db}} = \frac{1}{2\pi\tau} = 0.003 \text{ Hz}$$

In general, small values of  $\tau_2$  (i.e.,  $T_3/\tau_2 > 1$ ) give good attenuation at the low-frequency end but extended response at the high end. Large values, on the other hand, give the opposite effect. Therefore, for a given  $1/f$  noise characteristic, there can be an optimum value of  $\tau_2$  which can give minimum noise.

Before an evaluation of the system noise can be made, however, another source of noise must be considered. This is the noise voltage which develops during the time  $T_4$  (time between switch opening and closing). When the switch closes at  $t = T_4$ , the restore circuit attempts to restore out this voltage. The noise uncertainty left after the next restore interval  $T_3$  will depend

---

<sup>1</sup>J. Bremer and R. Prince, "Noise Characteristics of the AASIR DC Restore Circuit," TM 118-75 for GSFC, September 1975.

on the original peak value, the ratio of  $T_3/\tau_2$ , and the number of restore sequences preceding the present measurement. The peak noise is determined by evaluating equation (3) at  $t = T_4$ . Thus,

$$N_{pk}^2(\omega) = N^2(\omega, t)_{t = T_4} \tag{6}$$

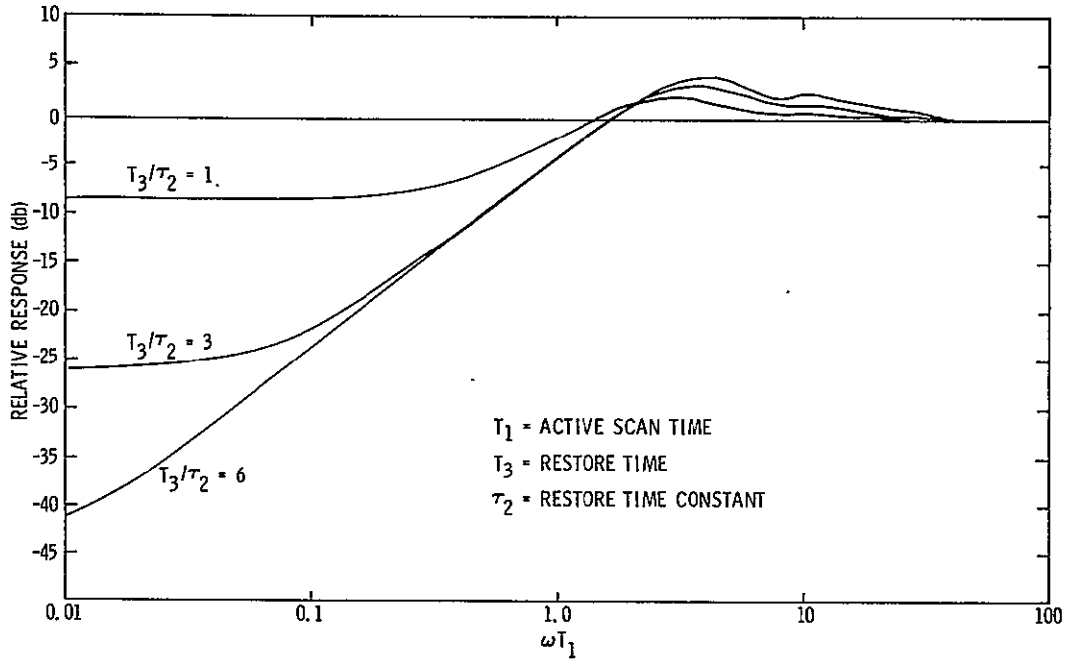


Figure 3-7. Noise Transfer Function  $N_{rms}^2(\omega)$  for AASIR DC Restore

Equation (6) has been plotted in Figure 3-8 with  $T_3/\tau_2$  as a parameter. Again, small values of  $T_3/\tau_2$  give enhanced response to low frequencies.

On successive restores, the dc restore circuit will approach a final value. This is depicted in Figure 3-9 in which  $V_0$  represents the offset presented to the dc restorer initially and  $V_1, V_2, V_n$  represent subsequent offsets. These values of  $V$  are the sum of dc offsets produced when the detector views a different filter at the beginning of each restore sequence and  $N_{pk}(\omega)$ . However, the effect of the filter offset will be treated later when noise optimization is considered.

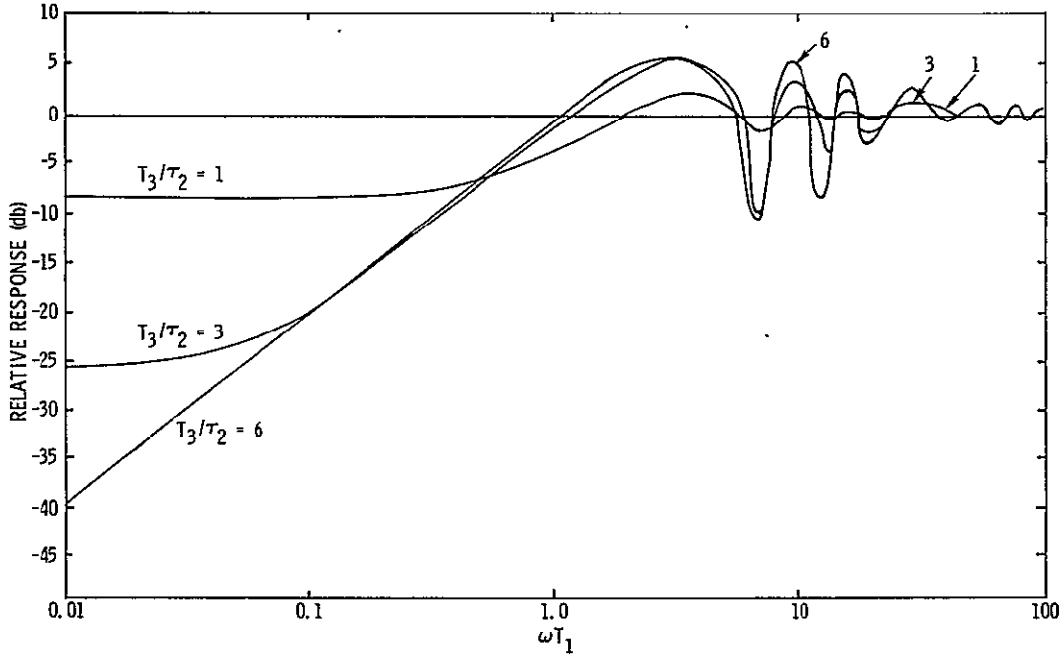


Figure 3-8. Noise Transfer Function  $N^2_{pk}(\omega)$  for AASIR DC Restore

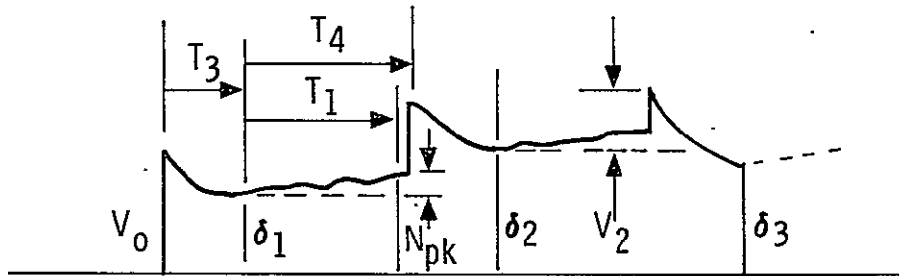


Figure 3-9. DC Restore Sequence

Thus,

$$\delta_1 = V_0 e^{-T_3/\tau_2}$$

$$\delta_2 = (\delta_1 + V_1) e^{-T_3/\tau_2} = V_1 e^{-T_3/\tau_2} + V_0 e^{-2T_3/\tau_2}$$

$$\delta_3 = (\delta_2 + V_2) e^{-T_3/\tau_2} = V_2 e^{-T_3/\tau_2} + V_1 e^{-2T_3/\tau_2} + V_0 e^{-3T_3/\tau_2}$$

$$\delta_n = V_n e^{-T_3/\tau_2} + \dots + V_0 e^{-nT_3/\tau_2} \tag{7}$$

From this it is clear that the voltage that the dc restorer must restore out is dependent on the most recent offset voltage  $V_n$  and to a lesser extent those that preceded it. If

$$V_o = V_1 = \dots V_n$$

then the restore error after an infinite number of restores would be given by:

$$\delta = V_n \frac{e^{-T_3/\tau_2}}{1 - e^{-T_3/\tau_2}} = V_n \frac{K}{1 - K} \tag{8}$$

Table 3-5 shows how equation (7) converges to (8) as a function of  $T_3/\tau_2$  and the number of restores, N. It is clear that even for values of  $T_3/\tau_2$  approaching 1, the restore error reaches final value in only a few restores. Also, the initial offset can be essentially restored out in the first restore if  $T_3/\tau_2 > 5$ . For example, if  $T_3/\tau_2 = 6$ , the error is only 0.25% after the first restore. The optimum value of  $T_3/\tau_2$  depends on the total noise, not the restore error alone.

Table 3-5. Restore Error  $\delta = \sum_{n=1}^N V_o e^{-nT_3/\tau_2}$

$T_3/\tau_2$	N						$\frac{K}{1 - K}$
	1	2	3	4	5	6	
1	0.368	0.503	0.553	0.571	0.578	0.581	0.582
2	0.135	0.154	0.156				0.156
3	0.0498	0.0523	0.0524				0.0524
4	0.0183	0.0187					0.0187
5	0.0067	0.0068					0.0068
6	0.0025						0.0025
7	$9.1 \times 10^{-4}$						$9.1 \times 10^{-4}$
8	$3.3 \times 10^{-4}$						$3.3 \times 10^{-4}$
9	$1.2 \times 10^{-4}$						$1.2 \times 10^{-4}$
10	$4.5 \times 10^{-5}$						$4.5 \times 10^{-5}$

Equivalent Noise Bandwidth

The equivalent noise bandwidth (NBW) of the system is obtained by integrating over frequency the product of the noise power transfer function, the system filter transfer function (in this case, an integrator), and the 1/f noise characteristic.

That is,

$$NBW = \int_{0.0003}^{\infty} \left[ N_{rms}^2(f) + K^2 N_{pk}^2(f) \right] \frac{\sin^2 \pi f T_5}{(\pi f T_5)^2} \left( 1 + \frac{f_0}{f} \right) df \quad (9)$$

where for convenience of integration the integral can be broken down into:

$$NBW = \int_{0.01}^{\infty} \left[ N_{rms}^2(f) + K^2 N_{pk}^2(f) \right] df + e^{-2T_3/\tau_2} \int_{0.003}^{0.01} \frac{f_0}{f} df$$

The second term integrates the 1/f noise over the frequency range where both the instrument response and the noise power transfer function are flat.

Figure 3-10 shows NBW plotted as a function of  $T_3/\tau_2$  with the 1/f knee frequency  $f_0$  as a parameter. The curves show that a broad range of  $T_3/\tau_2$  can be selected without affecting NBW significantly. As will be shown, however, the filter offset error dictates that a value of  $T_3/\tau_2 > 8.5$  be used to reduce the offset to a level comparable to the noise.

Figures 3-11 and 3-12 show the dependence of NBW on 1/f noise break frequency,  $f_0$ . It is clear that NBW is strongly dependent on  $f_0$  and that the optimum value of  $T_3/\tau_2$  is about 2.

Filter Offset Error

At the end of each scan line, during the time that the restore mirror is inserted and the filter wheel has stepped to a new position, an offset error is produced owing to the difference in optical properties of the various bandpass filters. This subsection estimates the magnitude of the error and indicates a value of  $T_3/\tau_2$  required to reduce it to a level comparable to the restore noise.

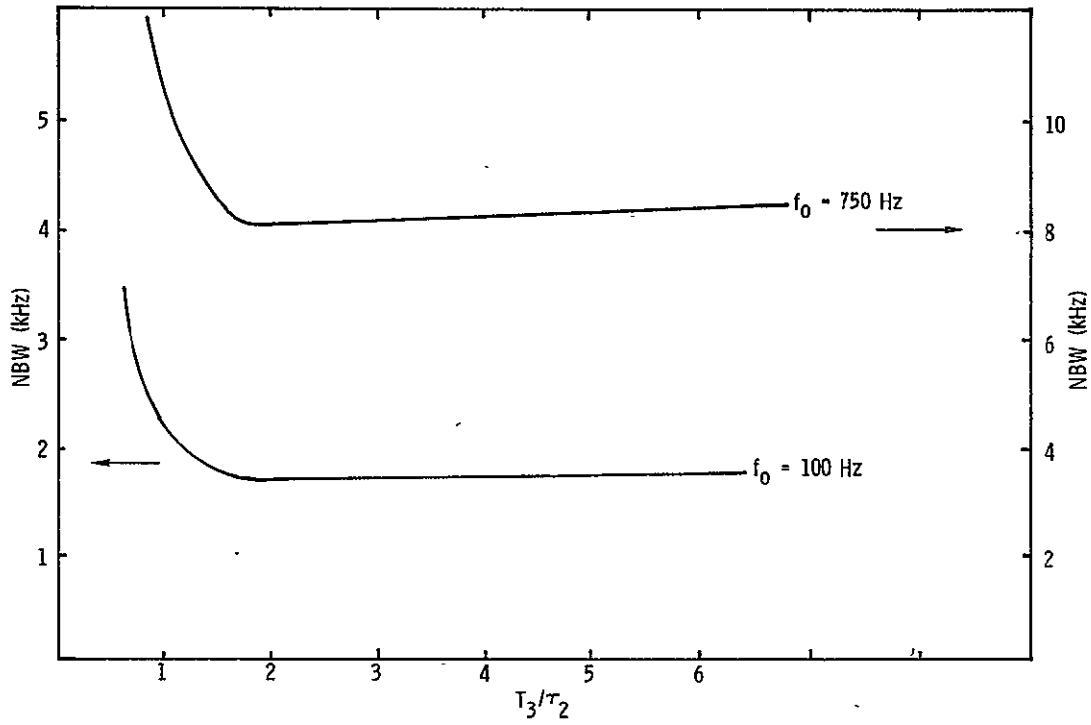


Figure 3-10. Equivalent Noise Bandwidth (NBW) versus  $T_3/\tau_2$

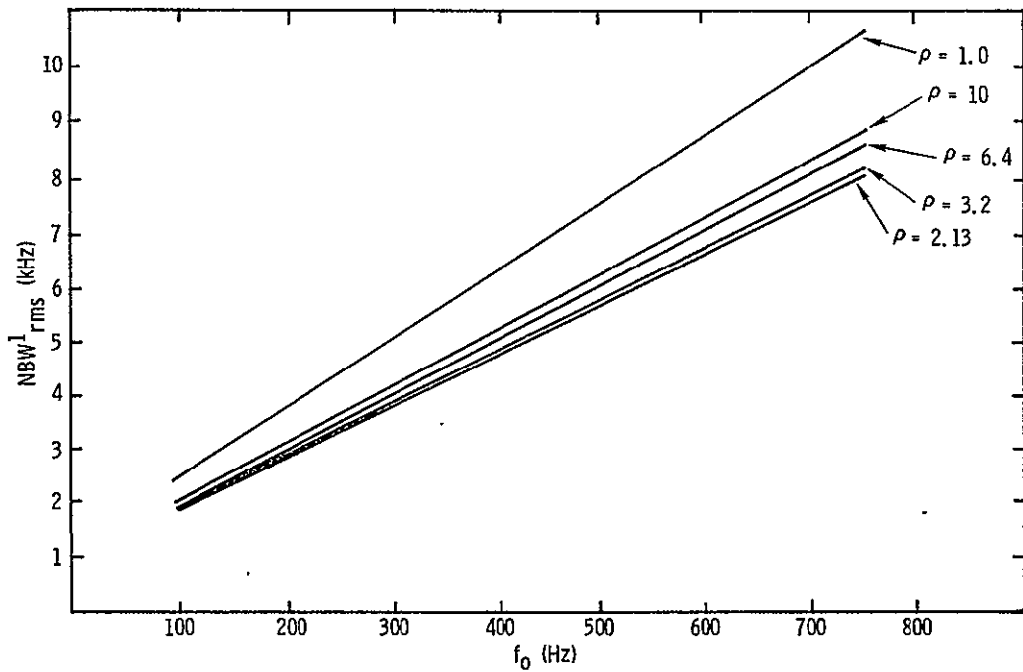


Figure 3-11. Equivalent Noise Bandwidth (NBW) versus  $f_0$  (Sounding Channels);  $\rho = T_3/\tau_2$ ,  $f_0 = 1/f$  knee

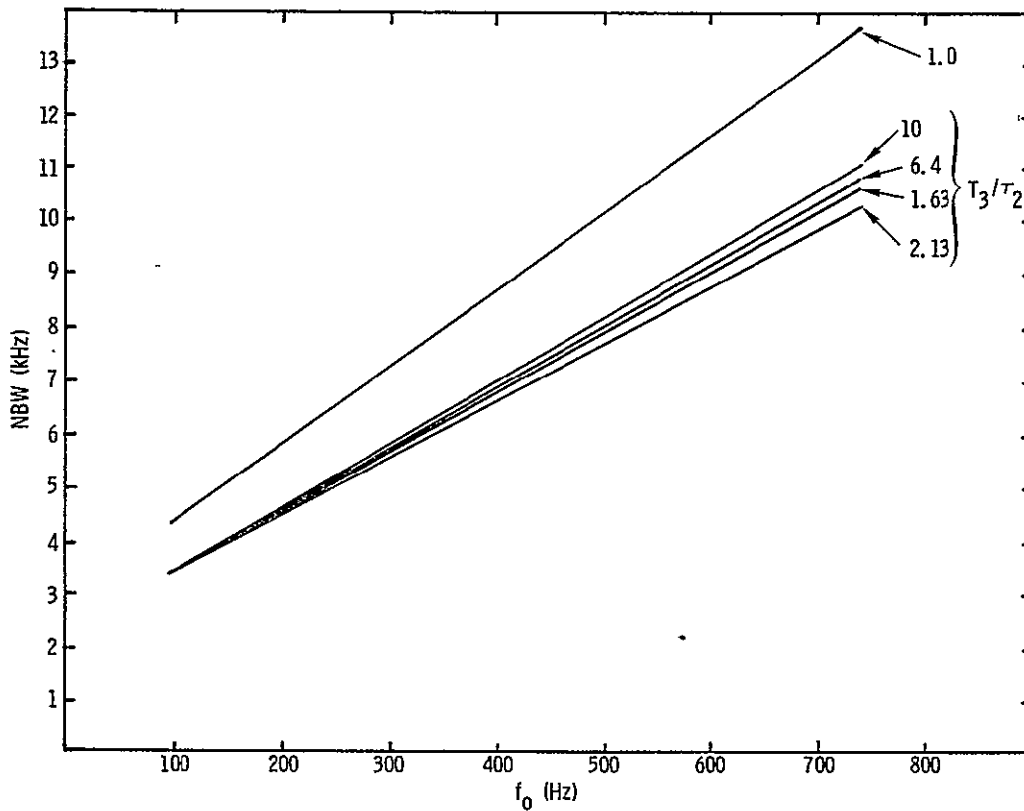


Figure 3-12. Equivalent Noise Bandwidth (NBW) versus  $f_0$  (IR Imaging Channels)

Figure 3-13 shows schematically the aft optics portion of the AASIR.

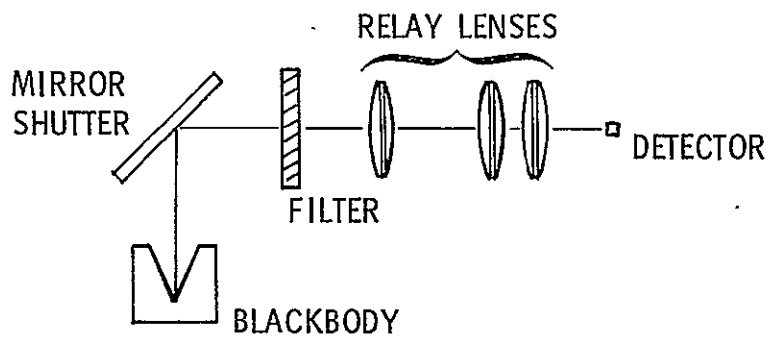


Figure 3-13. Aft Optics Schematic Diagram

The radiance seen by the detector is:

$$N_D = N_{BB} \rho_m \tau_F \tau_R + N_F \epsilon_F \tau_R + \rho_F N_R (1 - \tau_R) \tau_R + N_R \epsilon_R.$$

where:  $N_{BB}$  = radiance of blackbody through bandpass of filter  
 $N_F$  = emitted radiance from back of filter  
 $N_R$  = radiance from front of relay lenses  
 $\rho_m$  = reflectance of shutter mirror  
 $\rho_F$  = reflectance from rear of filter  
 $\tau_F$  = in-band transmittance of filter  
 $\tau_R$  = transmittance of relay  
 $\epsilon_R$  = emissivity of relay  
 $\epsilon_F$  = emissivity of filter

We will assume that  $\rho_m \cong 1$  and  $T_{BB} = T_F \cong 330^\circ\text{K}$ ,  $T_R \cong 300^\circ\text{K}$ . This means that both the blackbody and filter wheel will be heated to a higher than ambient temperature to ensure temperature stability. Therefore,

$$N_{F_1} = \tau_R (N_{BB_1} \tau_{F_1} + N_{F_1} \epsilon_{F_1}) + \rho_{F_1} N_R \epsilon_R \tau_R$$

for a given filter.

Letting  $\bar{N}_{BB_1} = N_{BB_1} \tau_{F_1} + N_{F_1} \epsilon_{F_1}$ , the radiance difference between two consecutive filters is

$$\Delta N = \tau_R (\bar{N}_{BB_1} - \bar{N}_{BB_2}) + (\rho_{F_1} - \rho_{F_2}) N_R \epsilon_R \tau_R \quad (10)$$

The filter wheel offset error voltage is given by:

$$V_F = \Delta N A_d \Omega_d \tau_R R G e^{-T_3/\tau_2} \quad (11)$$

where:  $A_d$  = the area of the detector  
 $\Omega_d$  = the solid angle viewed by the detector  
 $R$  = the detector responsivity  
 $G$  = the amplifier gain

The restore noise output voltage is:

$$V_N = \frac{\sqrt{A_d}}{D^*} (NBW)^{\frac{1}{2}} R G \quad (12)$$

The system noise is minimum when  $T_3/\tau_2$  is selected to make  $V_F + V_N$  minimum.

This can be seen in Figure 3-14 where a representative value has been assumed for  $\Delta N$  and the ordinate has been normalized in terms of  $(NBW)^{\frac{1}{2}}$ . The minimum value of  $V_F + V_N$  lies to the right of the intersection of the two curves, and the optimum value of  $T_3/\tau_2$  is about 10 for the filter parameters assumed. It is clear that although the minimum restore noise occurs for  $T_3/\tau_2 \cong 2$ , the filter offset error requires much larger values.

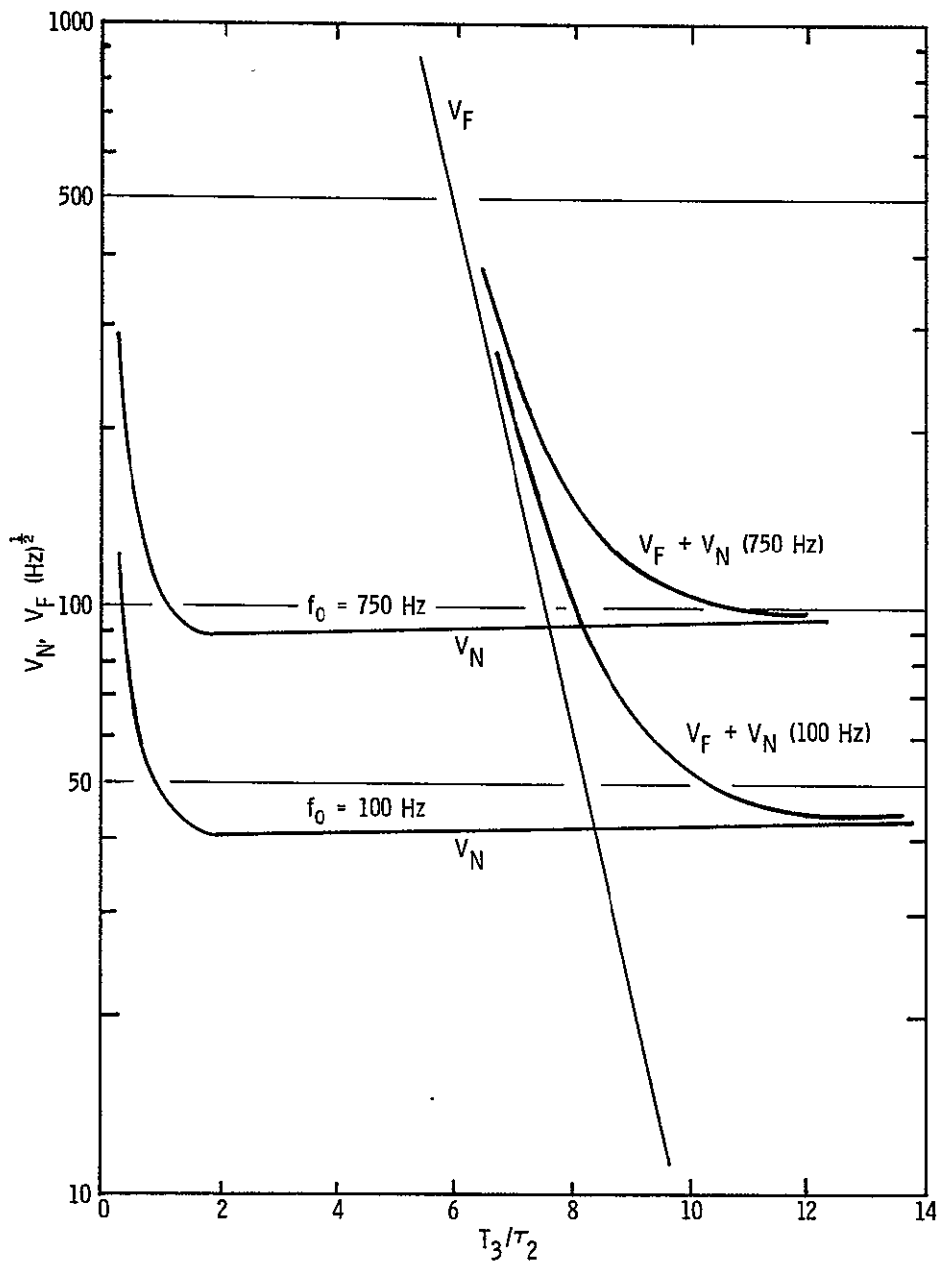


Figure 3-14. Optimizing Plot for  $V_N, V_F$  versus  $T_3/\tau_2$

The value of  $T_3/\tau_2$  giving the minimum value of  $V_N + V_T$  is given by:

$$\rho_{opt} = \ln \frac{\Delta N A_D^{\frac{1}{2}} \Omega_d \tau_R D^*}{\frac{\partial}{\partial \rho} (NBW)^{\frac{1}{2}}}$$

where  $\rho = T_3/\tau_2$ .

In the next subsection, this expression is used, together with measured parameters of the VAS filters, to determine the magnitude of the filter offset error and whether ordering of the filters is necessary to reduce it.

### IR Imaging Channels

Since the IR imaging detectors view through a single filter, there is no offset error. As a result, the curves of Figure 3-12 can be used to determine the optimum value of  $T_3/\tau_2$  ( $\approx 2$ ).

### Conclusion

The results of this analysis are generally applicable to most dc restore systems. In the special case of the AASIR, however, the condition  $1 \leq T_3/\tau_2 \leq 10$  has been treated. Also, the effect of filter offset error has been considered and an expression for the optimum value of  $T_3/\tau_2$  giving minimum total error has been derived.

### Filter Offset Error Revisited

The foregoing dc restore analysis treats the filter offset error in a superficial way. However, a more detailed treatment is needed to account for the characteristics of the different filters used in the AASIR. Also, the optical system is, in fact, more complex than that shown in Figure 3-13. The reflectance and transmittance was measured for each of the filters selected for use on the VAS. Transmittances for these filters are shown in Table 3-6.

The aft optics portion of the AASIR appears schematically in Figure 3-15. The dc restore mirror is shown in position and the detector sees the blackbody through the filter, blocker if used, field lens, relay lenses, and three dewar windows.

Table 3-6. VAS Filter Characteristics

OPTICAL FILTER DESIGNATION	CENTER WAVELENGTH ( $\mu\text{m}$ )	HALF RESPONSE BANDWIDTH ( $\mu\text{m}$ )	ASSUMED IN-BAND TRANSMITTANCE
-1	14.706	0.216	0.50
-5	13.423	0.360	0.55
-6	13.158	0.346	0.55
-7	12.658	0.321	0.55
-8	11.173	1.76	0.65
-9	7.246	0.210	0.60
-10	6.711	0.677	0.70
-11	4.283	0.092	0.60
-12	3.731	0.617	0.75

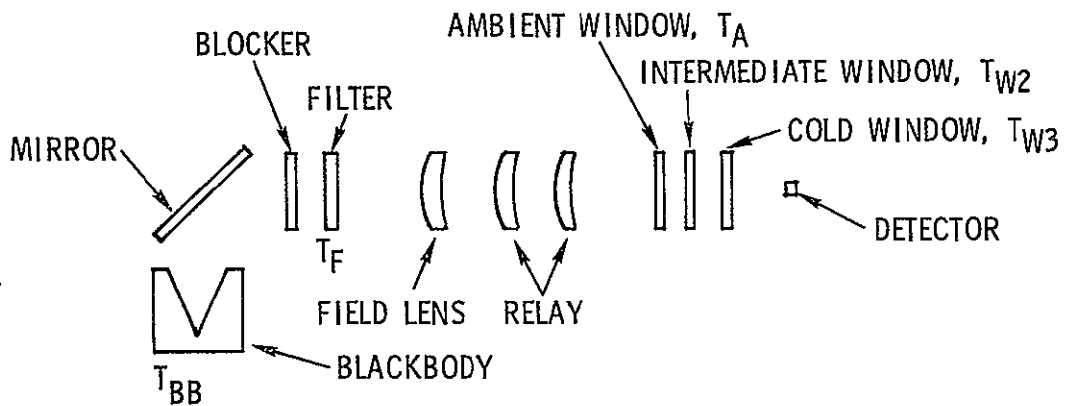


Figure 3-15. AASIR Aft Optics Schematic

Equation (1) gives the radiance difference as seen by the detector when switching from one filter to another:

$$\begin{aligned}
 \Delta N = \int_{\Delta\lambda} [ & N_{BB} (\tau_{Bj} \tau_{Fj} - \tau_{Bk} \tau_{Fk}) + N_A (\rho_{Bj} \tau_{Fj}^2 - \rho_{Bk} \tau_{Fk}^2) \\
 & + N_F (\epsilon_{Bj} \tau_{Fj} - \epsilon_{Bk} \tau_{Fk}) \\
 & + N_F (\epsilon_{Fj} \tau_{Fj} \rho_{Bj} - \epsilon_{Fk} \tau_{Fk} \rho_{Bk}) ] \tau_L^6 D^*_\lambda d\lambda \\
 & + \int_{\lambda=2}^{\lambda=16} [ N_A (1 - \tau_L) (\rho_{Fj} - \rho_{Fk}) (\tau_L^6 + \tau_L^7 + \tau_L^8 + \tau_L^9) \\
 & + (N_{W2} \epsilon_L + N_A \rho_L) (\rho_{Fj} - \rho_{Fk}) \tau_L^{10} \\
 & + (N_{W3} \epsilon_L + N_A \rho_L) (\rho_{Fj} - \rho_{Fk}) \tau_L^{11} ] D^*_\lambda d\lambda \quad (1)
 \end{aligned}$$

where:

- $N_{BB}$  = blackbody reference at  $T_{BB}$  ( $w\text{-cm}^{-2}\text{-st}^{-1}\text{-}\mu\text{m}^{-1}$ )
- $N_A$  = ambient surroundings at  $T_A$
- $N_F$  = filter wheel at  $T_F$
- $N_{W2}$  = intermediate dewar window at  $T_{W2} = 150^\circ\text{K}$
- $N_{W3}$  = cold dewar window at  $T_{W3} = 85^\circ\text{K}$
- $\tau_{Fj}$  = transmittance of the jth filter
- $\tau_{Bj}$  = transmittance of the blocker associated with the jth filter<sup>(1)</sup>
- $\rho_{Fj}$  = reflectance of jth filter<sup>(2)</sup>
- $\rho_{Bj}$  = reflectance of jth blocker (side facing the detector)
- $\epsilon_{Bj}$  = emissivity of jth blocker element
- $\epsilon_{Fj}$  = emissivity of jth filter element
- $\tau_L$  = transmittance of any lens or window element<sup>(3)</sup>
- $\rho_L$  = reflectance of any lens or window element<sup>(3)</sup>
- $\epsilon_L$  = emissivity of any lens or window element<sup>(3)</sup>
- $D^*_\lambda$  = normalized spectral detectivity

Notes:

- (1) Not all filters have an associated blocker element. Where it is not used

$$\tau_B = 1, \rho_B = \epsilon_B = 0$$

- (2) Reflectance of filters and blockers was obtained by measurement. It is not necessarily the same on both sides.
- (3) The field lens, relay lenses, and windows are AR coated Ge. All are assumed to have the same optical properties.

The first integral gives the in-band radiance contributions and the second wide-band radiances obtained by reflectance off the back of the filter.

A computer program was written which computed the radiance differences ( $\Delta N$ ) for all filter orientations and combinations. For each filter pair combination, the minimum  $\Delta N$  was determined. Thus, it is possible to calculate the  $\Delta N$ s for any desired filter sequence although there is a preferred sequence which gives minimum  $\Delta N$ s. One typical sequence is given in Table 3-7. From this it is seen that a  $\Delta N$  value of about  $2.76 \times 10^{-4}$  w-cm<sup>-2</sup>-st<sup>-1</sup> is the largest  $\Delta N$  that must be restored out. The optimum value of  $T_3/\tau_2$  for this  $\Delta N$  is given by:

$$T_3/\tau_2(\text{opt}) \quad \ln \left[ \frac{\Delta N A_o^{\frac{1}{2}} \Omega_o D^*}{\frac{\partial(\text{NBW})^{\frac{1}{2}}}{\partial(T_3/\tau_2)}} \right] = 5.26$$

where:  $A_o = 1090 \text{ cm}^2$  = area of aperture  
 $\Omega_o = (375 \times 10^{-6}) = 1.41 \times 10^{-7}$  ster  
 $D^* = 3 \times 10^{10} \text{ cm-Hz}^{\frac{1}{2}}\text{-watt}^{-1}$   
 $\frac{\partial(\text{NBW})^{\frac{1}{2}}}{\partial(T_3/\tau_2)} = 0.2$

For this set of temperatures, the worst case  $\Delta N = 6.4 \times 10^{-4}$  occurs when switching from filter -12 to -8 (or vice-versa). The corresponding optimum value of  $T_3/\tau_2$  is 6.1. Therefore, it can be concluded that the ordering of the filters is relatively unimportant and that the optimum value

of  $T_3/T_2$  lies between 5 and 6. Corresponding values of NBW are shown in Figure 3-16.

In practice the blackbody and filter wheel will be operated above ambient temperature as in VAS to ensure stability of filter properties and to simplify the decalibration. Calculations were made with  $T_{BB} = T_F = 310^\circ\text{K}$ ,  $T_A = 300^\circ\text{K}$ , but the  $\Delta N$  difference between this and the  $T_{BB} = T_F = T_A = 300^\circ\text{K}$  case was insignificant.

Table 3-7.  $\Delta N$  Sequence\*

FILTER SEQUENCE	$\Delta N$ ( $\text{W}\cdot\text{cm}^{-2}\cdot\text{st}^{-1} \times 10^{-4}$ )
8 TO 6	+2.76
6 TO 5	+0.34
5 TO 1	+0.26
1 TO 7	-0.85
7 TO 9	-0.0075
9 TO 11	+2.7
11 TO 10	-0.96
10 TO 12	+1.68
$T_{BB} = 300^\circ\text{K}$ , $T_F = 300^\circ\text{K}$ , $T_A = 300^\circ\text{K}$ , $T_2 = 150^\circ\text{K}$ , $T_3 = 85^\circ\text{K}$	

---

\*The sequence shown is typical but not necessarily optimum.

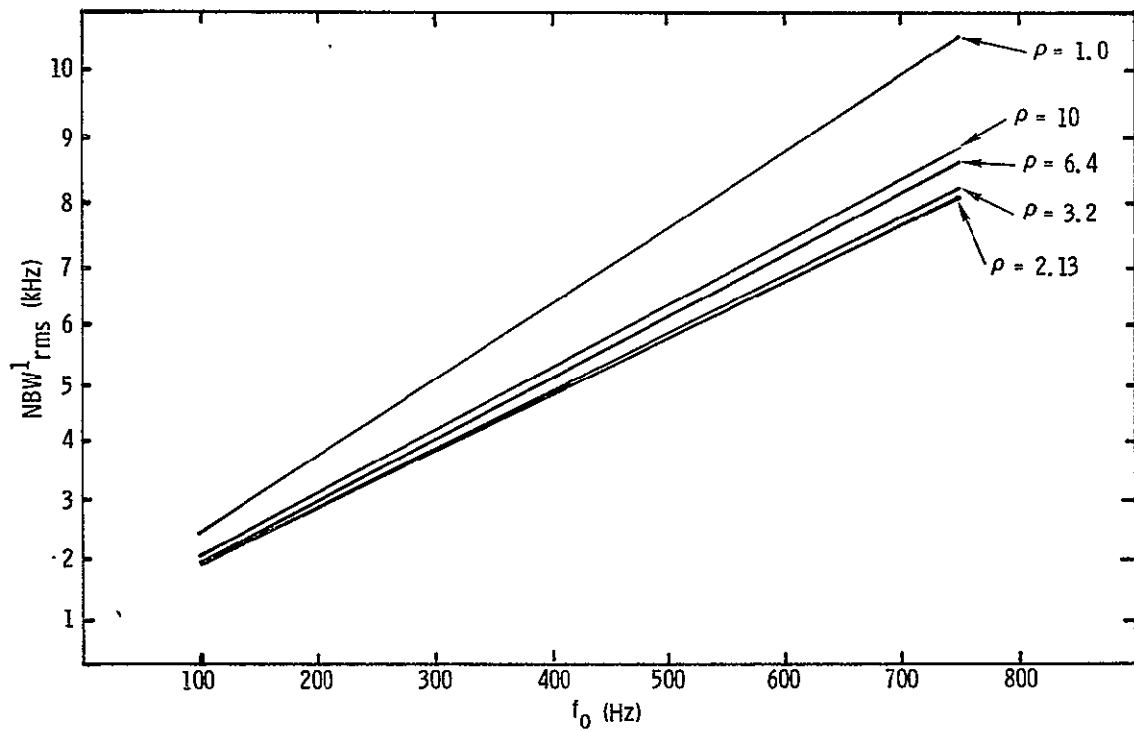


Figure 3-16. Equivalent Noise Bandwidth (NBW) versus  $f_0$  (Sounding Channels);  $\rho = T_3/\tau_2$ ,  $f_0 = 1/f$  knee

SCAN CONSIDERATIONS

The current AASIR design uses a single-axis N-S resonant scan object space mirror. The E-W step axis gimbal is a large bearing supporting a ring in which the entire AASIR is rotated. Other types of two-axis scan systems have been examined during the course of the study. These include two types of single-mirror, two-axis scan system and a two-mirror scan system. Each of these will be discussed.

AASIR Scan Overlap

In the AASIR baseline design (see Figure 3-17), the inner gimbal carries the resonant scan mirror (N-S) and the outer gimbal carrying the entire AASIR is stepped E-W by the spacecraft. When the AASIR is stepped the dimension of the detector array ( $0.2363^\circ$ ), the edges of the array when projected into object space are contiguous at the equator but overlap an amount which is proportional to the latitude of scan. At  $8^\circ$ , corresponding roughly to the limb of the earth, this amounts to  $40 \mu\text{rad}$  or two visible IFOV.

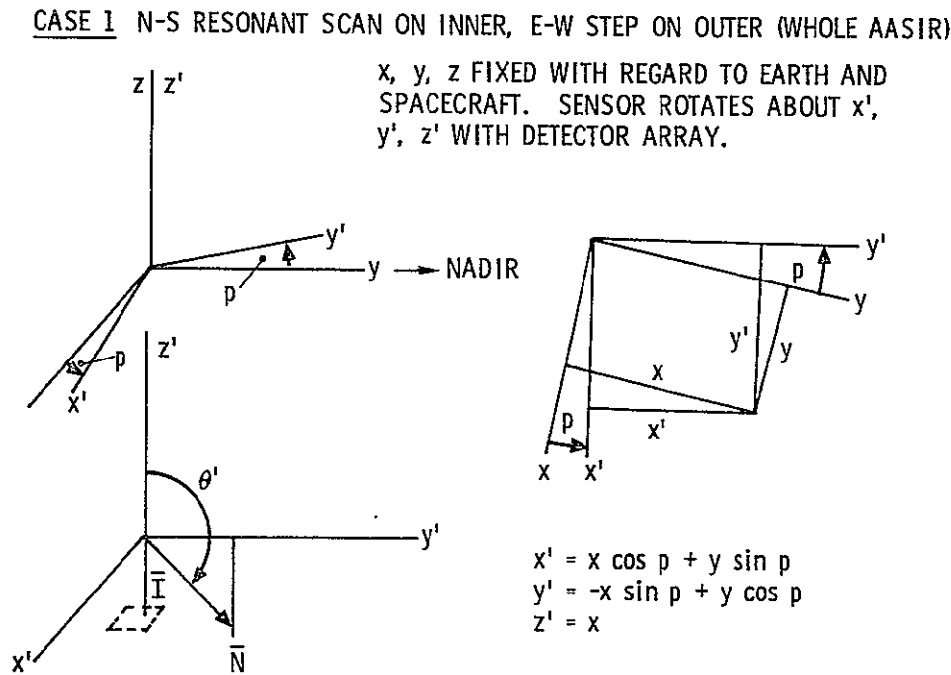


Figure 3-17. Case 1 Scan Coordinate System

Another type of two-axis scan, first proposed by Hughes Aircraft Company, Culver City, was also treated (see Figure 3-18). In this case, inner gimbal axis is parallel to the plane of the resonant scan mirror which scans E-W. The outer gimbal steps N-S. Both overlap and "shear" exist in this design. In addition, the scan lines are curved and the image is rotated. However, the image is rotated an amount equal to the scan line curvature so that registration of corresponding sounding IFOVs is maintained over the scan line.

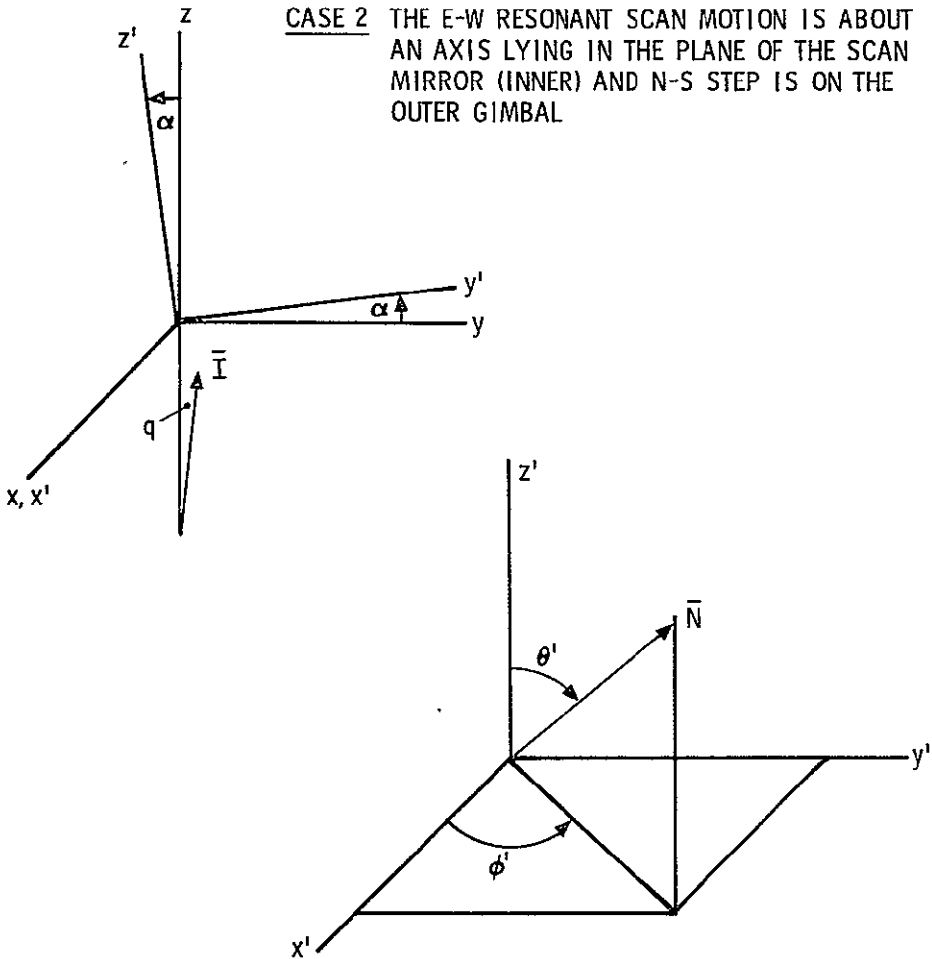


Figure 3-18. Case 2 Scan Coordinate System

$$\begin{vmatrix} x' \\ y' \\ z' \end{vmatrix} = \begin{vmatrix} x \\ y \\ z \end{vmatrix} \begin{vmatrix} \cos p & \sin p & 0 \\ -\sin p & \cos p & 0 \\ 0 & 0 & 1 \end{vmatrix}$$

and the inverse

$$\begin{vmatrix} x \\ y \\ z \end{vmatrix} = \begin{vmatrix} x' \\ y' \\ z' \end{vmatrix} \begin{vmatrix} \cos p & -\sin p & 0 \\ \sin p & \cos p & 0 \\ 0 & 0 & 1 \end{vmatrix}$$

Direction cosines of unit vector  $\bar{N}$  are:

$$x' = 0$$

$$y' = \sin \theta'$$

$$z' = \cos \theta'$$

$$x = x' \cos p - y' \sin p = -\sin \theta' \sin p$$

$$y = x' \sin p + y' \cos p = \sin \theta' \cos p$$

$$z = z' = \cos \theta'$$

The mirror normal unit vector is:

$$\bar{N} = -\sin \theta' \sin p \hat{i} + \sin \theta' \cos p \hat{j} + \cos \theta' \hat{k}$$

The reflected ray  $\bar{R}$  is given by:

$$\bar{R} = \bar{I} - 2(\bar{N} \cdot \bar{I})\bar{N} \text{ in the } x, y, z \text{ system}$$

and  $\bar{I} = a' \hat{i} + b' \hat{j} + c' \hat{k}$  is the incident ray unit vector originating in the detector array.  $\bar{I}$  is constrained for this analysis to lie only in the  $x', z'$  plane.

Then,

$$a' = \sin \gamma$$

$$b' = 0$$

$$c' = \cos \gamma$$

$$\begin{vmatrix} a \\ b \\ c \end{vmatrix} = \begin{vmatrix} a' \\ b' \\ c' \end{vmatrix} \begin{vmatrix} \cos p & -\sin p & 0 \\ \sin p & \cos p & 0 \\ 0 & 0 & 1 \end{vmatrix}$$

$$a = a' \cos p - b' \sin p = \sin \gamma \cos p$$

$$b = a' \sin p + b' \cos p = \sin \gamma \sin p$$

$$c = c' = \cos \gamma$$

To calculate the overlap, we need only to find  $r_1$  which is the direction cosine along the x axis.

$$r_1 = \cos \alpha$$

$$r_1 = a - 2N_1 (aN_1 + bN_2 + cN_3)$$

$$r_1 = a - 2a(\sin^2 \theta' \sin^2 p) + 2b \sin^2 \theta' \sin p \cos p$$

For the case where  $\bar{I}$  is "on axis":

$$a = b = 0, c = 1$$

and

$$r_1 = 2 \sin \theta' \cos \theta' \sin p$$

When the mirror is aligned to view along the N-S line through the nadir, then

$$p = 0 \text{ and } r_1 = 0$$

When the mirror is rotated  $11 \times 375 \mu\text{rad} = 4125 \mu\text{rad} = 0.2363^\circ$

$$\alpha = \cos^{-1} (2 \sin \theta' \cos \theta' \sin 0.2363)$$

and the overlap is given by:

$$\Delta = \alpha_{135} - \alpha_{\theta'}$$

The overlap as a function of scan angle is given in Table 3-8.

Table 3-8. Case 1 Scan Overlap

DEFLECTION IN OBJECT-SPACE (degrees)	$\theta'$ (degrees)	$\alpha$ (degrees)	$\Delta$ ( $\mu\text{rad}$ )	$\Delta$ (VIS IFOV)
0	135	90.2363	0	0
1	134.5	90.23626	0.6283	0.03
2	134	90.23616	2.5133	0.1197
3	133.5	90.23598	5.653	0.269
4	133	90.23572	10.048	0.478
5	132.5	90.23540	15.695	0.747
6	132	90.23501	22.594	1.076
7	131.5	90.23454	30.742	1.464
8	131	90.23400	40.137	1.911
9	130.5	90.23339	50.776	2.418
10	130	90.23271	62.65749	2.984

In the arrangement shown in Figure 3-18, the vector  $\bar{I}$  is in the x, y, z system,  $\theta'$  is fixed at  $90^\circ$ , and  $q = -45^\circ$  for the nadir view but is stepped N-S by outer gimbal.  $\phi'$  is scanned to give E-W scan.

Similar analysis yields:

$$r_1 = a - 2N_1 (N_1 a + N_2 b + N_3 c)$$

$$N_1 = \sin \theta' \cos \phi'$$

$$N_2 = \sin \theta' \sin \phi' \cos q - \cos \theta' \sin q$$

$$N_3 = \sin \theta' \sin \phi' \sin q + \cos \theta' \cos q$$

where  $\bar{I}$  lies in x, z plane.

For  $\bar{I}$  along optic axis  $a = b = 0, c = 1$

$$N_1 = \cos \phi'$$

$$N_2 = \sin \phi' \cos q$$

$$N_3 = \sin \phi' \sin q$$

$$r_1 = -2 \cos \phi' \sin \phi' \sin q$$

$$\alpha = \cos^{-1} r_1$$

$$\Delta = \alpha_{-45^\circ} - \alpha_q$$

$$\alpha = \cos^{-1} (-\sin 2 \phi' \sin q)$$

The angular displacement from the x axis is not a direct function of  $\phi'$ . Therefore, solving for  $\phi'$ , which gives a displacement of one array width ( $0.2363^\circ$ ), gives:

$$\phi_0 = 90.16709^\circ$$

Table 3-9 shows the overlap as a function of the scan angle  $q$  with  $\phi' = \phi'_0$ .

This effect is seen as a "shear" rather than overlap. Therefore, there is a continuous misalignment of corresponding IFOVs as a function of latitude.

Table 3-9. Overlap ("Shearing") in E-W Direction

OBJECT-SPACE DEFLECTION (degrees)	q (degrees)	Δ (μrad)	Δ (VIS IFOV)
0	-45	0	
1	-44.5	36.1	1.72
2	-44	72.6	3.45
3	-43.5	109.4	5.21
4	-43	146.4	6.97
5	-42.5	183.82	8.75
6	-42	221.5	10.55
7	-41.5	259.5	12.35
8	-41	297.73	14.18
9	-40.5	336.29	16.01
10	-40	375.14	17.86

Other effects can be seen by evaluating  $r_3$ , the direction cosine with respect to the z axis. Thus,

$$r_3 = c - 2N_3^2 c \quad \text{where } a = b = 0, c = 1$$

$$r_3 = \cos \gamma = 1 - 2 \sin^2 \phi' \sin^2 q$$

$$\gamma = \cos^{-1} r_3$$

Overlap in the N-S direction can be determined by evaluating  $\gamma$  for several E-W angles ( $\phi'$ ). Table 3-10 shows several effects present in this scan arrangement. The N-S angle ( $q$ ) is stepped in increments of  $0.11815^\circ = 2062.5 \mu\text{rad}$  which gives  $4125 \mu\text{rad}$  or one array dimension in object space.

1. By comparing corresponding values of  $q$  for  $\phi' = 94^\circ$  and  $\phi' = 98^\circ$ , the scan lines are found to have curvature. At the earth limb  $\phi' = 98^\circ$ , the scan line departs from the horizontal by  $19,370 \mu\text{rad}$ .
2. The amount of overlap is a function of  $\phi'$  and to a lesser extent  $q$ .

Conclusion - Both systems analyzed have an overlap problem. In terms of sorting out the effects, Case 1 would appear to require the least ground data processing since only one correction is required.

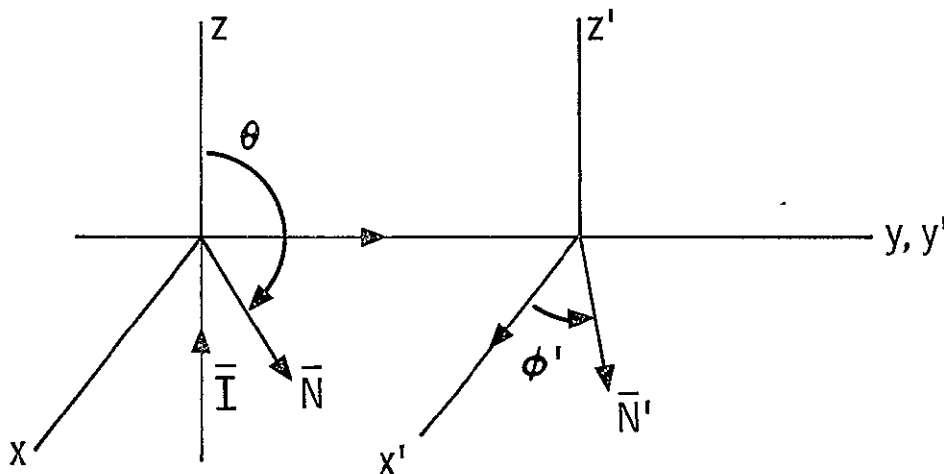
Table 3-10. Overlap in N-S Direction

q (N-S) (degrees)	$\phi' = 94^\circ$			$\phi' = 98^\circ$		
	$\gamma$ (degrees)	$\Delta$ ( $\mu$ rad)	OVERLAP ( $\mu$ rad)	$\gamma$ (degrees)	$\Delta$ ( $\mu$ rad)	OVERLAP ( $\mu$ rad)
-45	89.7212	4865.9	0	88.8902	19370.4	0
-44.88185	89.4860	4104.2	20.76	88.6584	4045.2	79.75
-44.76370	89.2251	8208.5	20.68	88.4266	8090.8	79.39
-44.64555	89.0157	12312.9	20.6	88.1948	12136.7	79.13
AT TOP OF FRAME						
-40.1558	79.8411	172440	--	79.1416	170144.9	--
-40.0377	80.0764	168333	18.838	79.3739	166088.6	68.677

Analysis of a Two-Mirror System

Scan overlap problems associated with the AASIR baseline and Hughes two-axis scan systems prompted consideration of a two-mirror scan system. In this arrangement, the inner mirror would step N-S much like the VISSR/VAS and the outer mirror would scan E-W in a resonant mode. The following analysis will show that even this apparently orthogonal system is not free of scan distortion.

In the figure, the x, y, z system carries the inner N-S step mirror and the x', y', z' system carries the outer E-W scan mirror.



The mirror normal in the x, y, z system is given by:

$$\bar{N} = \sin \theta \hat{j} + \cos \theta \hat{k}$$

The detector ray ( $\bar{I}$ ) is assumed to travel up the z axis. Thus,

$$\bar{I} = a \hat{i} + b \hat{j} + c \hat{k}, \quad a = b = 0, \quad c = 1$$

The reflected ray  $\bar{R}$  is the same as the incident ray ( $\bar{I}$ ) in the primed system. Thus,

$$\begin{aligned} \bar{R} &= \bar{I} - 2(\bar{N} \cdot \bar{I})\bar{N} = \bar{I}' \\ r_1 &= -2N_1N_3 = 0 = a' \\ r_2 &= -2N_2N_3 = -\sin 2\theta = b' \\ r_3 &= 1 - 2N_3 = -\cos 2\theta = c' \end{aligned}$$

In the primed system

$$\begin{aligned} N_1' &= \cos \phi' \\ N_2' &= \sin \phi' \\ N_3' &= 0 \\ \bar{R}' &= \bar{I}' - 2(\bar{N}' \cdot \bar{I}')\bar{N}' \end{aligned}$$

and the direction cosines for the reflected ray are:

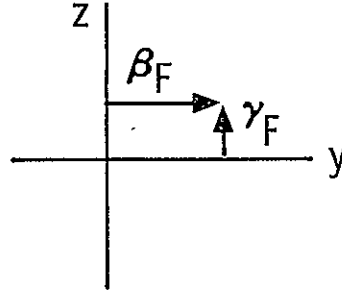
$$\begin{aligned} r_1' &= \sin 2\phi' \sin 2\theta = \cos \alpha \\ r_2' &= -\sin 2\theta \cos 2\phi' = \cos \beta \\ r_3' &= -\cos 2\theta = \cos \gamma \end{aligned}$$

where  $\alpha$  is the angle between the unit vector  $\bar{R}'$  and the x axis;  $\beta$  and  $\gamma$  apply similarly to the y and z axis, respectively.

The direction cosines above would describe the scan motion if the detector line-of-sight were projected on the inside of a unit sphere with the AASIR in the center. When projected on a flat earth, however, the angles to the line-of-sight are given by:

$$\beta_F = \frac{r_2'}{r_1'} = -\frac{1}{\tan 2\phi'}$$

$$\gamma_F = \frac{r_3'}{r_1'} = -\frac{1}{\sin 2\phi' \tan 2\theta}$$



In Figure 3-19, the angular differences between the mirror angle  $\gamma$  and the deflections in the earth plane ( $\Delta\gamma_F$ ) are plotted on the ordinate. Thus,

$$\Delta\beta_F = \beta_F - 2(45 + \phi)$$

$$\Delta\gamma_F = \gamma_F - 2(135 - \theta) \text{ (in } \mu\text{rad)}$$

The dotted lines in the figure indicate that N-S stepping produces straight lines. However, the displacement in the N-S direction is a function of both  $\phi'$  and  $\theta$ . Values of  $\Delta\beta_F$  give the difference between the scan position and integer values of  $\phi'$ .

### Scan System

The scan system studied during the AASIR study was described in the AASIR Design Review Report published in November 1975. At that time, however, the system had not been tested and evaluated. Subsequently, the system was tested to the extent permitted by the equipment. The results are presented here.

The AASIR resonant scan system consists of the elements shown schematically in Figure 3-20. The rotating components are the mirror and the rotors of the angle sensing transducer and the motor. They form one rigid body which is suspended at its two ends by two flex pivots to form a mechanical resonant system with a natural frequency of 0.388 Hz.

The angle sensing transducer provides continuously refreshed angular data. The scan control logic uses these data to derive the scan size and scan center. These two outputs are then compared with the commanded scan

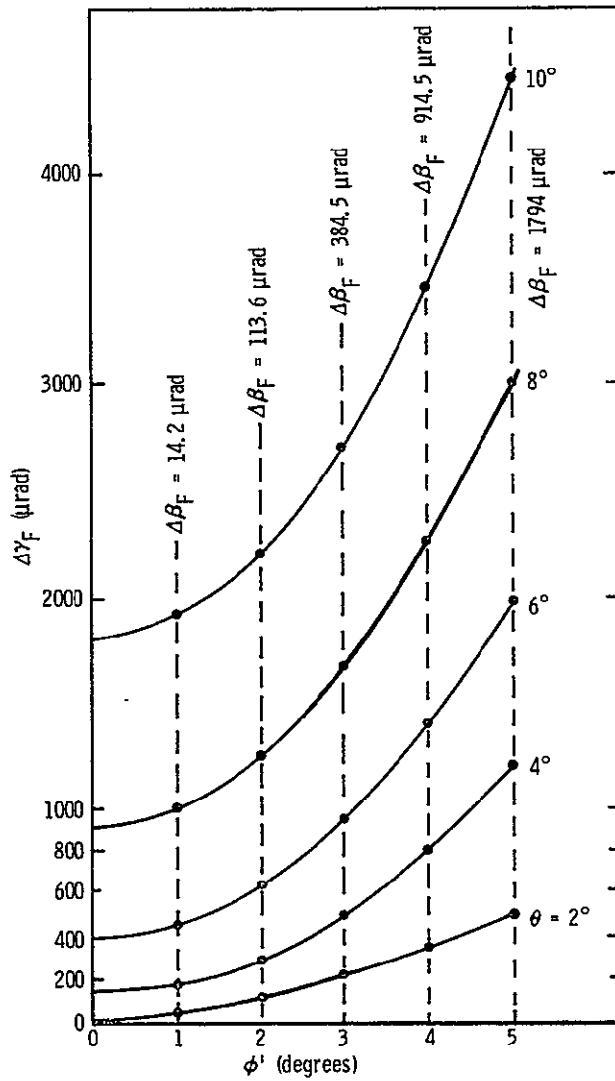


Figure 3-19. Two-Mirror Scan Nonlinearity (Flat Earth Projection)

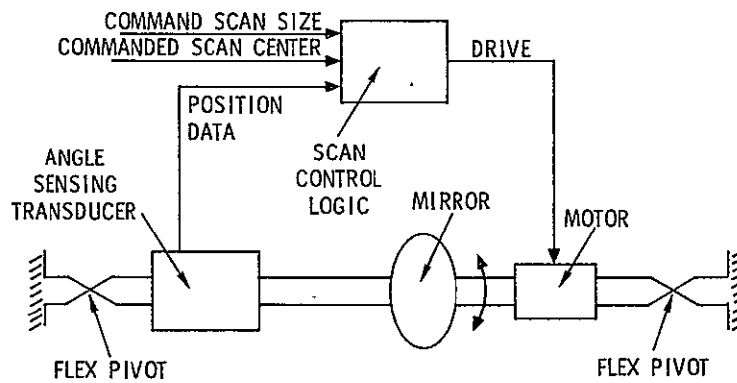


Figure 3-20. AASIR Scan System Block Diagram

size and scan center to generate the necessary drive to the motor that will maintain the smallest difference between the commanded data and the measured data.

AASIR preliminary specifications called for an IFOV registration of less than  $\pm 1\%$  of the sounding IFOV or  $\pm 3.75 \mu\text{rad}$  on the scene. This translates to a short-term repeatability requirement of  $\pm 1.875 \mu\text{rad}$  on the angle sensing transducer (AST). A report prepared by EOD and dated December 1974 provided some analytical background for the design of a scan mirror assembly (SMA) for use on the AASIR. This part of this report deals with the choice of gimballed angle sensors. Here various AST approaches were examined and the resolver/resolver-to-digital converter (RDC) was chosen as the most applicable candidate. Based on this conclusion, the resolver/RDC approach was selected.

A 1:72 speed American Electronics resolver was obtained on loan from Hughes, Division 72. However, no specifications or other form of documentation was available for this resolver. Data Devices Corporation, which built the original RDC for this resolver, was contacted and a duplicated RDC was ordered. The specifications for the device are as follows:

Model No. :	3484-CM
Description:	1:72 speed resolver-to-digital converter
Input:	1:72 speed resolver; 2000-Hz resolver reference provided by Data Devices Corporation (DDC)
Output:	20-bit binary angle data converter busy line Outputs DTL/TTL compatible
Resolution:	20-bit binary
Accuracy:	$\pm 2$ arc seconds at tracking rates from $0^\circ/\text{sec}$ to $22^\circ/\text{sec}$
Power Supplies:	+5 vdc at 900 ma +15 vdc at 200 ma -15 vdc at 200 ma

Mechanical:           Five printed circuit boards  
                          5.38 × 5.26 × 0.75 inch thick

Temperature:         0°C to 70°C operating

Test Evaluation - The resolver was built into the SMA and the system was driven at resonant frequency. The scan motion is defined by:

$$\theta = \theta_m \sin \omega t$$

where:      $\omega = 2.44$  radians/sec  
            $\theta_m = 6.35^\circ$

A digital comparator which triggers a short-arc flash lamp used as an autocollimation source for a Wild T3 theodolite comprised the basic setup for dynamic testing.

Dynamic repeatability, the single most important specification for the successful performance of the AASIR, received special attention. Since no repeatability specification was available on the RDC, it was assumed to be within the  $\pm 2$  arc seconds accuracy limits. However, our test data show a dynamic repeatability error of  $\pm 9$  arc seconds, which is far in excess of what was anticipated. On discussing these results with DDC, it became apparent that the Type II loop within the RDC is dynamically limited. DDC suggested replacing the error processor module with a faster version to improve the dynamic response. When the RDC was tested with the new error processor, within the limits of  $10^\circ/\text{sec}^2$  acceleration specified by DDC, \* the following results were obtained:

Static Hysteresis	= $\pm 1.3$ arc seconds
Dynamic Repeatability	= $\pm 2.5$ arc seconds
Static Accuracy	= +3 to -16 arc seconds
Dynamic Accuracy	= +5 to -13 arc seconds

---

\*This necessitated reducing the resonant frequency of the SMA by about a factor of two by increasing the mass of the simulated mirror.

These test results reveal the following:

1. The static hysteresis of  $\pm 1.3$  arc seconds is about double of what can be expected from a 20-bit RDC.
2. When the static hysteresis is subtracted from the dynamic repeatability, we get  $\pm 1.2$  arc second error. This may be due to the dynamic response of the Type II loop in the RDC.
3. It is logical to assume that very little if any of the static hysteresis and dynamic repeatability errors were contributed by the resolver. However, there is insufficient information to predict how the resolver contributed to the accuracy figures.

Conclusion -

1. The measured static hysteresis error is far in excess of what is thought to be possible using state-of-the-art design.
2. The dynamic response of the Type II loop directly affects the dynamic repeatability error. Careful design can reduce this error.
3. DDC did not provide any circuit detail of their RDC. All circuit components were epoxy potted. In any future negotiations with a RDC vendor, we should explicitly demand that all circuit details be made available to us for evaluation and upgrading if necessary, and that all circuit components be accessible.
4. Since both the resolver and the RDC contribute to the overall error, it is desirable to have one party, the RDC manufacturer, take full responsibility for the resolver/RDC package. Another approach is for the RDC vendor to write the specifications for the resolver and guarantee package performance when the specified resolver is used.
5. DDC has displayed a lack of interest in our application. The reason may be the fact that the RDC related department is understaffed and thus more emphasis is placed on the high-volume low-resolution and accuracy converters.
6. The test setup (mostly reading the theodolite) limited dynamic resolution to about 1 to 2 arc seconds. This would be inadequate to measure the desired repeatability of 0.3 arc second. A Hewlett-Packard laser interferometer transducer Model 5501A would be the logical replacement. Data storage with a minimum capability of 1000 points to store data from the transducer would also be needed.

Optical Encoders

As a result of the test evaluation described above, the decision was made to stop hardware development until a better potential source of ASTs could be found.

In this connection, discussions with Baldwin Electronics of Little Rock, Arkansas, were held to determine whether an optical encoder could be provided to meet our requirements. A tentative specification for a suitable optical encoder was written and is excerpted below.

Repeatability - The angular position at which a detector channel is sampled must repeat to better than  $\pm 3.75 \mu\text{rad}$  on the scene or  $\pm 1.875 \mu\text{rad}$  on the encoder.

Accuracy - The encoder must allow registration of one detector in the array to any other detector in the array along the line of scan. This means that the accuracy over the angular subtense of the array must be at least as good as the relative placement accuracy of the detectors in the array. This is the equivalent of about  $\pm 6.25 \mu\text{rad}$ . Therefore, accuracy can be expressed as an error slope of  $6.25 \mu\text{rad}/0.54^\circ = 11.6 \mu\text{rad}/^\circ$ . On this basis, the absolute accuracy must be  $\pm 74 \mu\text{rad}$  at the edges of the frame.

Resolution - 16 bits - The basic resolution of the encoder can be 16 bits. However, the angle between least significant bits (LSB) ( $95.873 \mu\text{rad}$ ) will be divided into a number of equal angular intervals either by a further refinement of the optical encoder (optical resolver) or by purely electronic means. The division will have a value between 9 and 12 depending on the visible channel IFOV which sets the basic sampling factor for the system. That is, if the elemental angular interval is

$$\alpha = \frac{95.873}{k} \mu\text{rad} \quad \begin{array}{l} 9 \leq k \leq 12 \\ k \text{ an integer} \end{array}$$

then visible channel sampling is done every  $\alpha \mu\text{rad}$ .

IR imaging channels are sampled every  $m\alpha \mu\text{rad}$ ,  $m$  an integer. IR sounding channels are sampled every  $n\alpha \mu\text{rad}$ ,  $n$  an integer.

Field-of-view sizes and spacing between FOVs in object space, determined by the sizes and spacings of detectors, will be integral multiples of  $\alpha$   $\mu$ rad.

Readout Delay - It is recognized that an unavoidable readout delay will exist due to the time constant of the detector and propagation times of the electronics. Due to the variable scan rate (bidirectional sine scan), this delay must be minimized and known to a first order. Maximum delays of 1  $\mu$ sec should be a design goal.

Output Format - Output data format can be either binary or grey code.

Mounting Configuration - The optical encoder will be mounted in an assembly containing a dc torquer and two flex pivots. Two such identical assemblies will be used in the AASIR, one on each side of the mirror.

Torquer to be Used - The dc torquer found to be adequate to drive the scan mirror is an Aeroflex TQ52W-1. The load to be driven weighs 26 pounds and has an angular momentum of 900 in. -lb.

Flex Pivots - Bendix flex pivots, type 5032, shall be used.

Subsequent discussions with Baldwin indicated that they were confident that an encoder satisfying our requirements could be built. A two-phase program was proposed which would consist of a paper study phase and a breadboard phase. However, when the costs of such a program were revealed, it did not appear attractive. The costs would have been about \$50K for the program and approximately \$40K for an appropriate laser transducer to provide dynamic mirror measurements.

Conclusion - The conclusion to be drawn from the study of the resonant scanner is that the method used for mirror drive would be adequate provided that a suitable resolver/encoder could be found. It appears that either the resolver/RDC or optical encoder can be made to work. Perhaps a more important consideration is finding a cooperative vendor. In this regard, Baldwin Electronics would be an excellent vendor.

The use of a laser interferometer for in-flight mirror positioning and readout was not explored during the current study. However, the method appears feasible and worthy of further study.

Precise Angular Measurements

High accuracy angular monitoring is required for tracking in-flight high resolution sensor scan mirror motion. One method for accomplishing this is through the use of interferometric fringe counting. A reference pulse is desirable if interferometric techniques are used to measure scan mirror motion as a function of time. The reference pulse would serve as a periodic initialization function for the fringe counting process. This reference pulse must have a unique relationship with the scan mirror and its scan angle.

Schematically the relationship of the reference pulse interferometer components is illustrated in Figure 3-21. Information concerning radiant energy source, detector, and interferometer end mirrors for the three models considered is tabulated in Table 3-11.

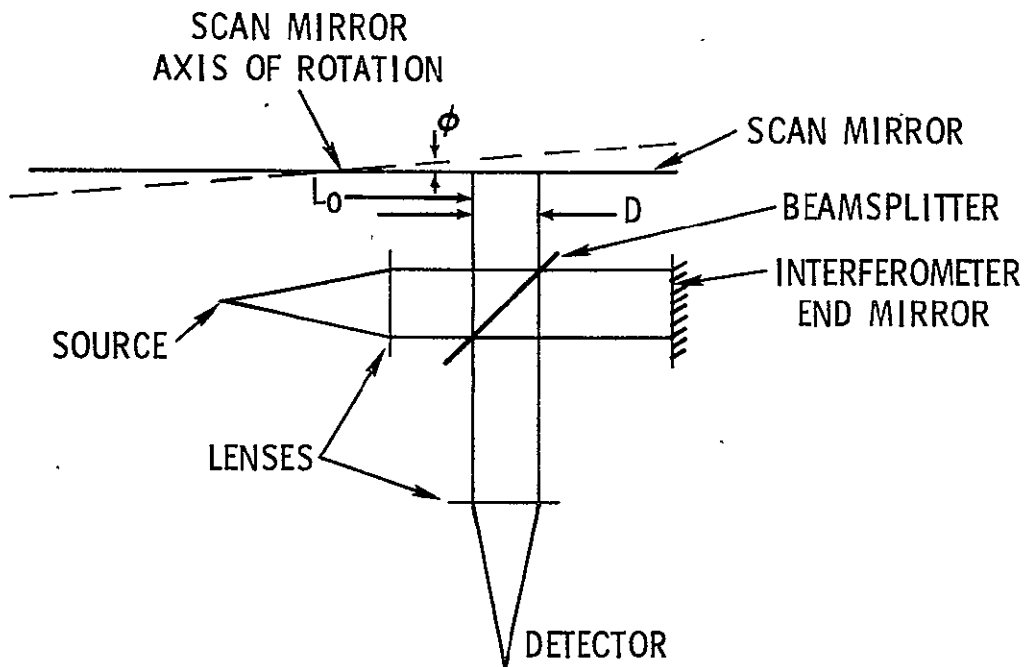


Figure 3-21. Scan Mirror Reference Pulse Optical Schematic

Table 3-11. Reference Pulse Interferometer Components

ELEMENT	MODEL		
	I	II	III
RADIANT ENERGY SOURCE	MONOCHROMATIC LASER	INCANDESCENT LAMP	INCANDESCENT LAMP
DETECTOR	SiPd	SiPd	SiPd
END MIRRORS	PLANE	PLANE	CORNER CUBES

Analytical expressions have been derived describing the three models. The expressions are based on the interference produced by superposition of two beams.

$$N = N_1 + N_2 + 2\sqrt{N_1 N_2} \cos \delta \tag{1}$$

where:  $N_1$  = beam 1 radiance function  
 $N_2$  = beam 2 radiance function  
 $\delta$  = phase difference

The derived expressions are:

Model I "Monochromatic" Source - Plane Mirrors

$$P_D = \frac{\Omega W}{4} \left[ DN_s \Delta\nu + \frac{N_s \Delta\nu}{4\pi\nu\phi} \{ \sin 4\pi\nu [(L_o + D)\phi + \Delta] - \sin 4\pi\nu(L_o\phi + \Delta) \} \right] \tag{2}$$

Model II "Broadband" Source - Plane Mirrors

$$P_D = \frac{\Omega W}{4} \left[ D \int_{\nu} N_s d\nu + \int_{\nu} \frac{N_s}{4\pi\nu\phi} \{ \sin 4\pi\nu [(L_o + D)\phi + \Delta] - \sin 4\pi\nu(L_o\phi + \Delta) \} d\nu \right] \tag{3}$$

Model III "Broadband" Source - Corner Cube Reflectors

$$P_D = \frac{\Omega WD}{4} \int_{\nu} N_s [1 + \cos 4\pi\nu (L_o\phi + \Delta)] d\nu \tag{4}$$

where:  $P_D$  = radiant power at detector  
 $\Omega$  = system solid angle  
 $W, D$  = beam dimensions  
 $N_s$  = radiance  
 $\nu$  = wavenumber  
 $\phi$  = scan angle  
 $L_0$  = distance from axis of rotation to beam edge (see Figure 3-21)  
 $\Delta$  = "residual" phase difference

Some physical interpretation in connection with the above equations is: Scan mirror angle  $\phi$  is assumed to be zero when scan mirror and interferometer fixed end mirror are perpendicular. As scan mirror angle  $\phi$  deviates from zero, the reference signal rapidly approaches 1/2 of the peak signal. Peak signal occurs at  $\phi = 0, \Delta = 0$ .

The normalized power at the detector  $(P_D)_N$  has been calculated for each model. Table 3-12 lists the parameters used.

Table 3-12. Summary of Parameters Used in Reference Pulse Calculations

MODEL	$L_0$ (inch)	$D$ (inch)	$\Delta$ (inch)	FIGURE NUMBER
I	0.00	0.50	$0 \times 10^{-6}$	3-22a
I	0.00	0.50	$3 \times 10^{-6}$	3-22b
I	0.00	0.50	$6 \times 10^{-6}$	3-22c
I	0.00	0.50	$9 \times 10^{-6}$	3-22d
I	5.00	0.50	$0 \times 10^{-6}$	3-24a
I	5.00	0.50	$3 \times 10^{-6}$	3-24b
I	-0.25	0.50	$0 \times 10^{-6}$	3-23a
I	-0.25	0.50	$3 \times 10^{-6}$	3-23b
I	-0.25	0.50	$6 \times 10^{-6}$	3-23c
I	-0.25	0.50	$9 \times 10^{-6}$	3-23d
II	5.00	0.40	$0 \times 10^{-6}$	3-25
III	5.00	0.40	$0 \times 10^{-6}$	3-25

As seen in Figures 3-22 and 3-23, the output pulse of Model I is drastically modified by  $\Delta$  for small  $L_0$  values. For  $L_0 = 5$  inches, Figure 3-24, the residual phase  $\Delta$  does not alter the output pulse materially. However, the pulse shape is not ideal for a well-defined initialization pulse. Figure 3-25 illustrates both Models II and III. The output pulses for both models are very similar. The stringent alignment requirements for Model II, with its flat end mirrors, probably preclude its use on a space sensor. The use of corner cubes in Model III should reduce its alignment sensitivity significantly with respect to Model II.

Model I has been set up and experimentally demonstrated. Models II and III have not been demonstrated experimentally.

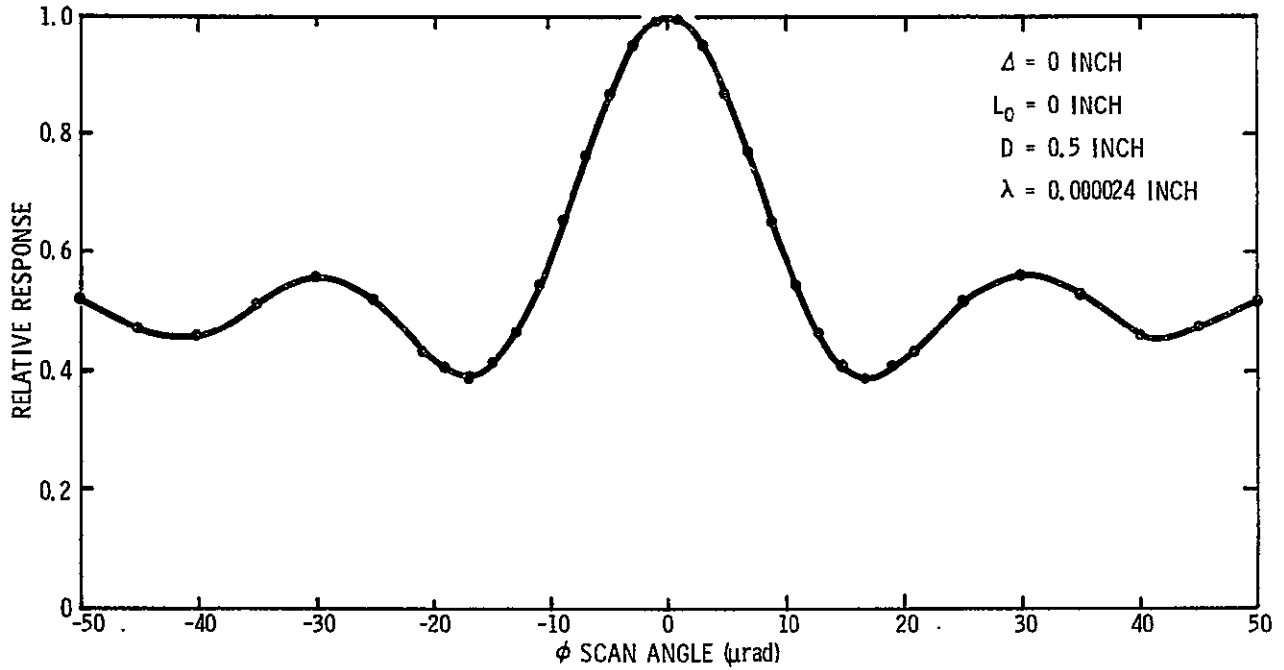


Figure 3-22a. Normalized Initialization Pulse - Relative Response versus Scan Angle

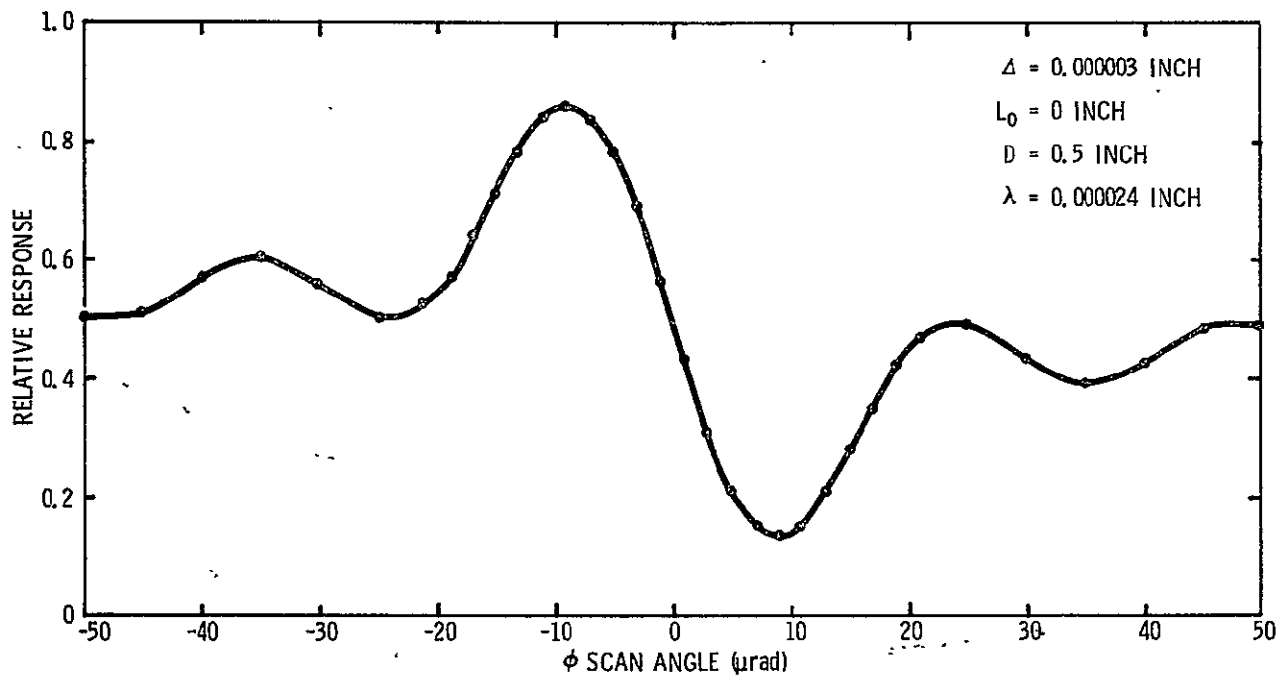


Figure 3-22b. Normalized Initialization Pulse - Relative Response versus Scan Angle

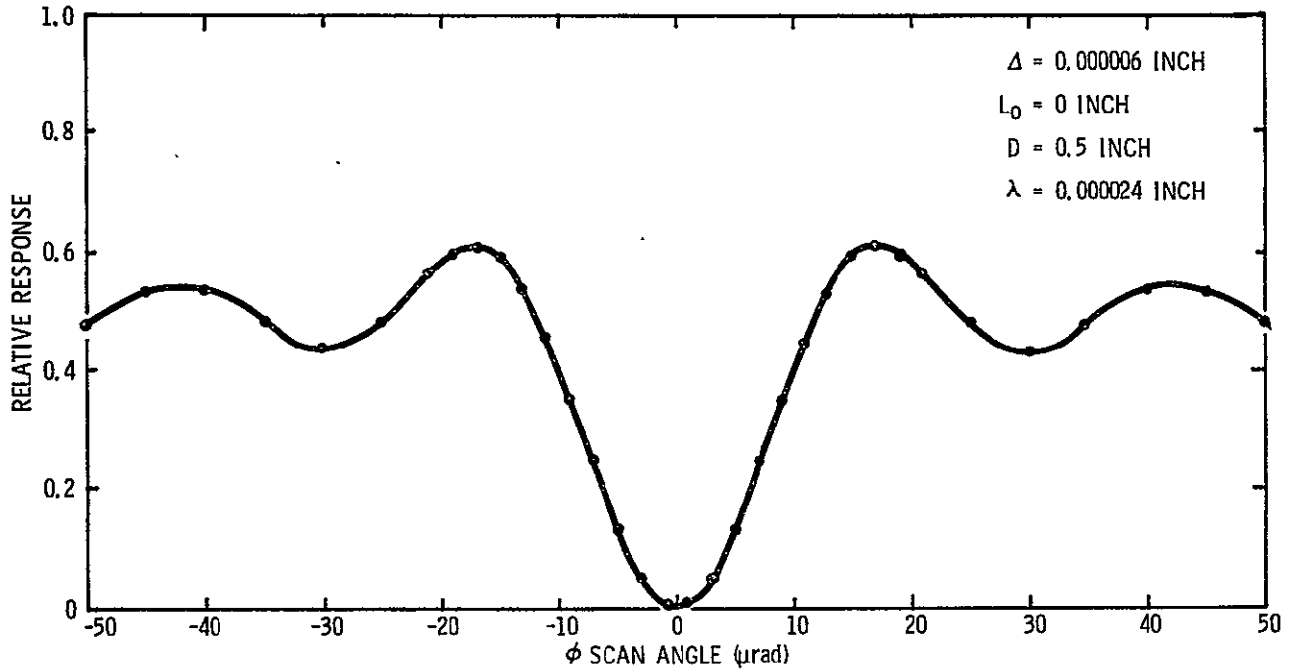


Figure 3-22c. Normalized Initialization Pulse - Relative Response versus Scan Angle

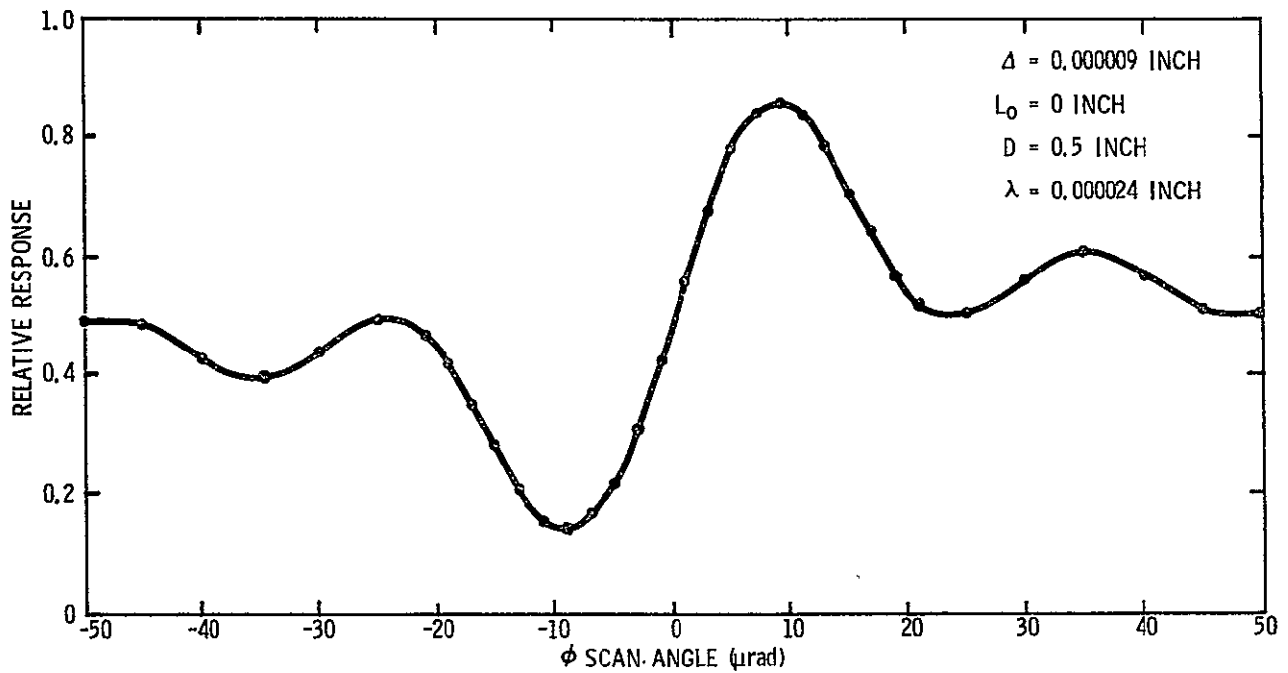


Figure 3-22d. Normalized Initialization Pulse - Relative Response versus Scan Angle

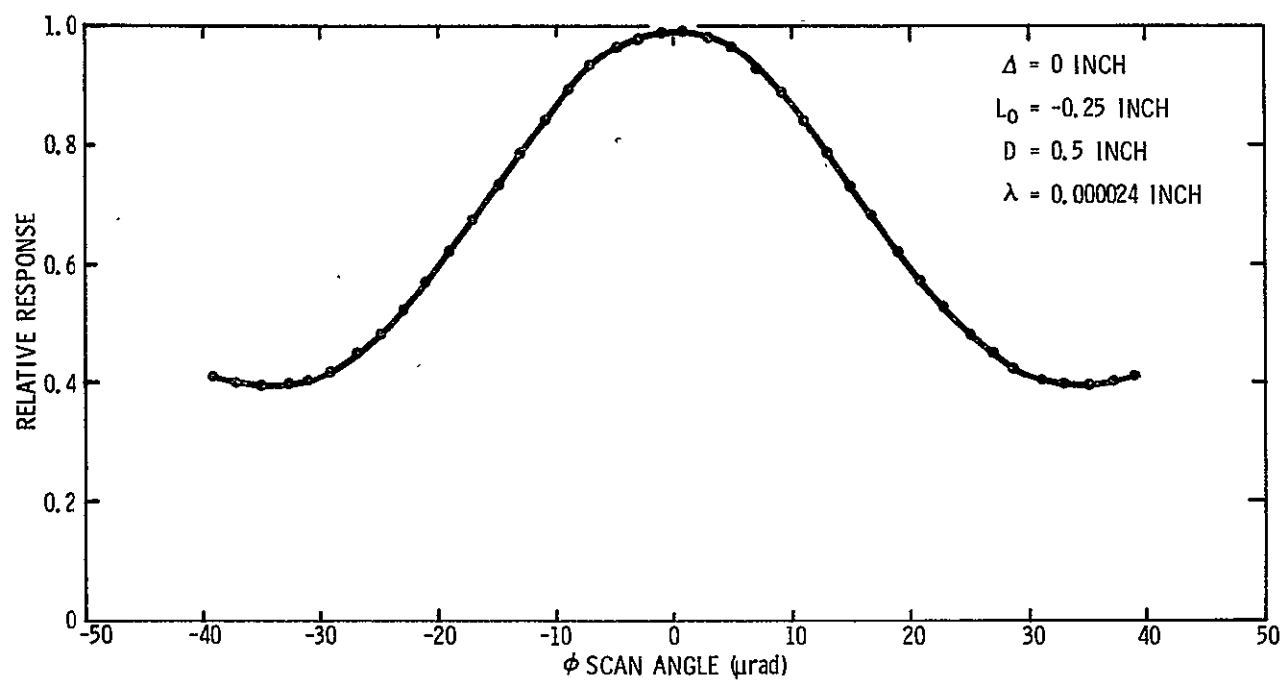


Figure 3-23a. Normalized Initialization Pulse - Relative Response versus Scan Angle

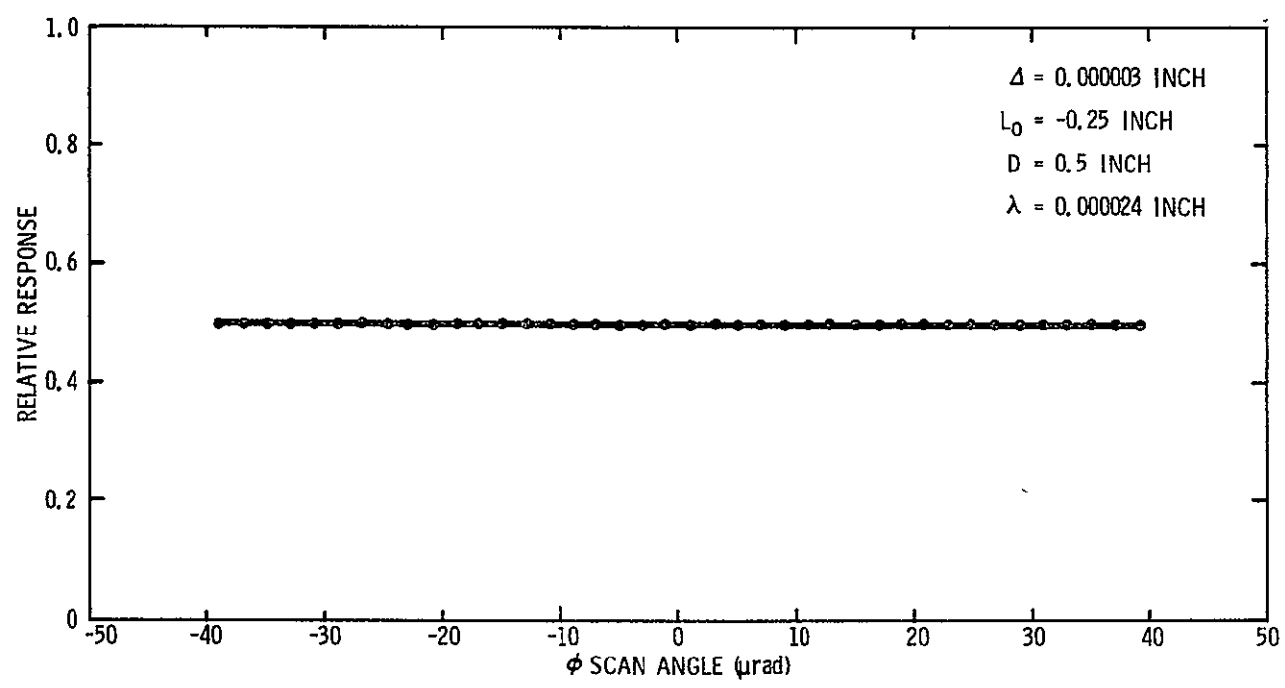


Figure 3-23b. Normalized Initialization Pulse - Relative Response versus Scan Angle

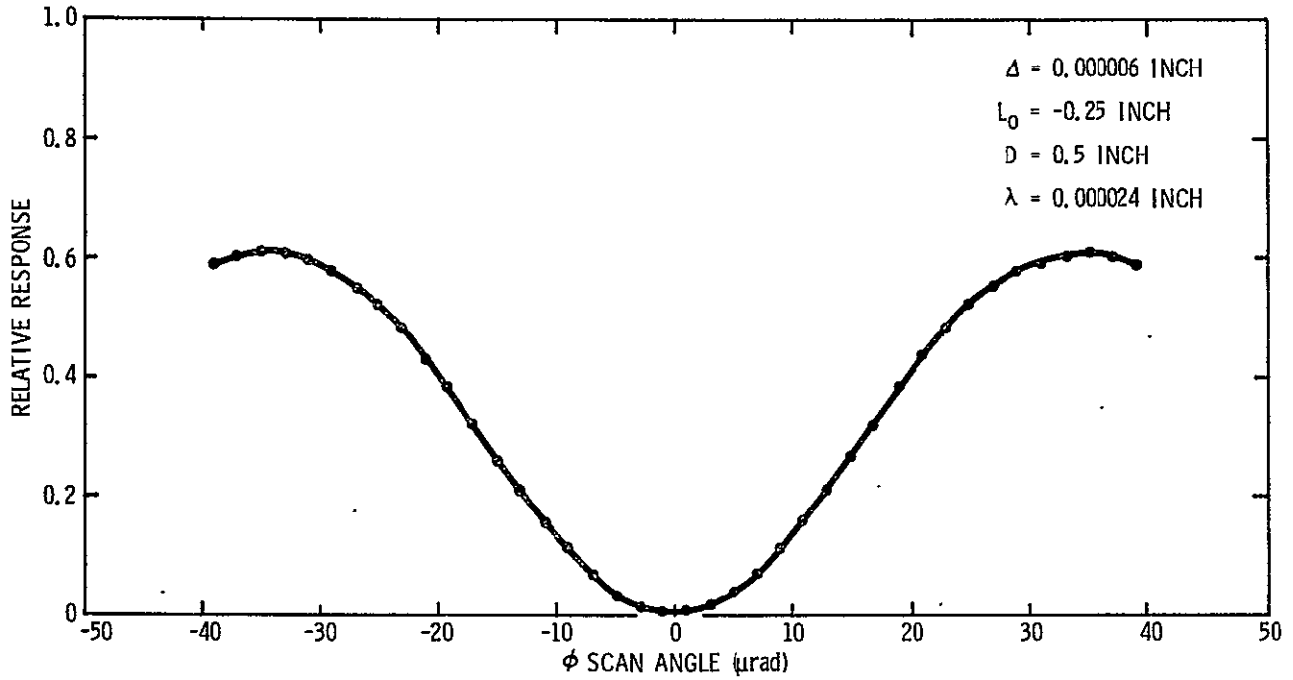


Figure 3-23c. Normalized Initialization Pulse - Relative Response versus Scan Angle

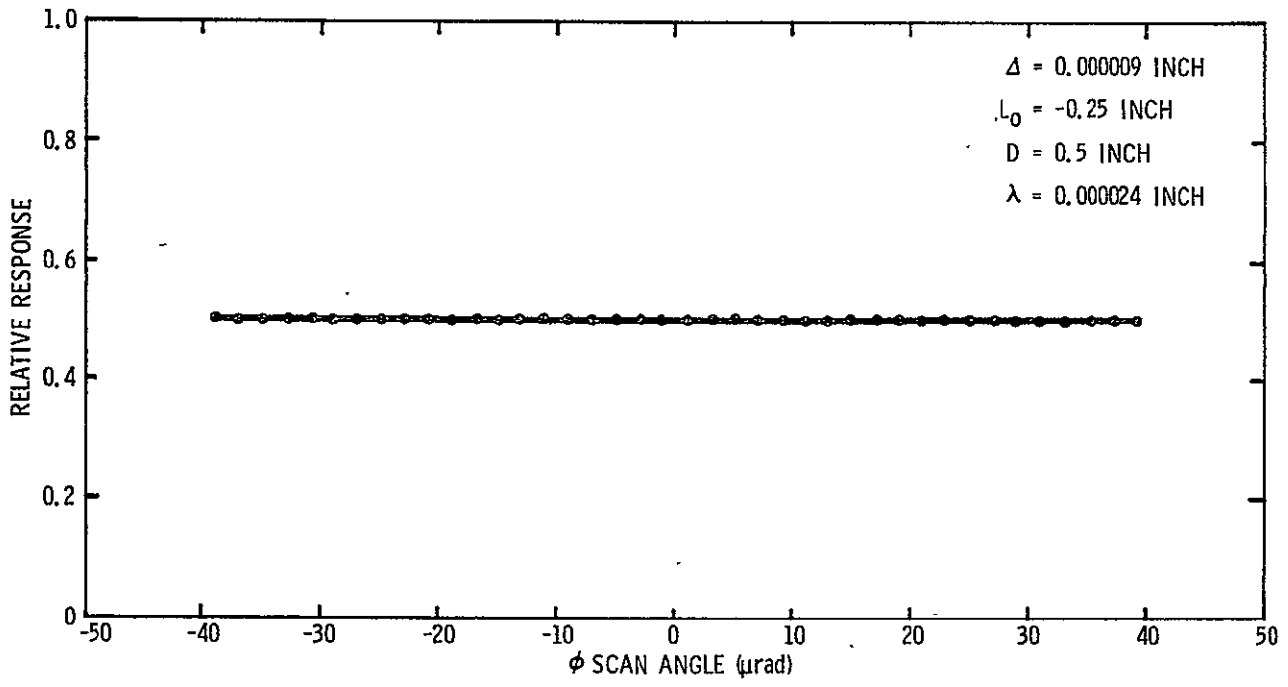


Figure 3-23d. Normalized Initialization Pulse - Relative Response versus Scan Angle

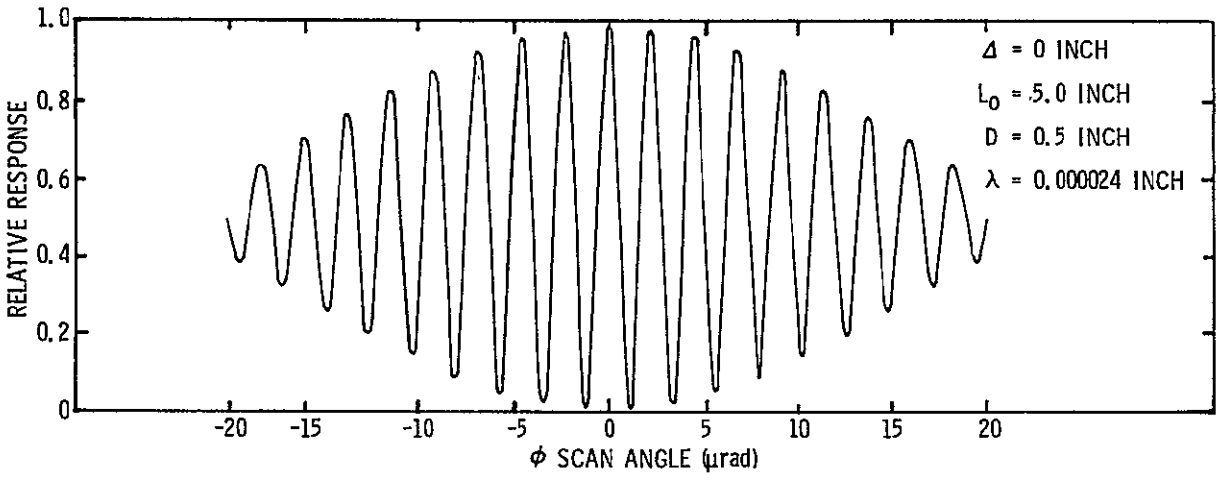


Figure 3-24a. Normalized Initialization Pulse - Relative Response versus Scan Angle

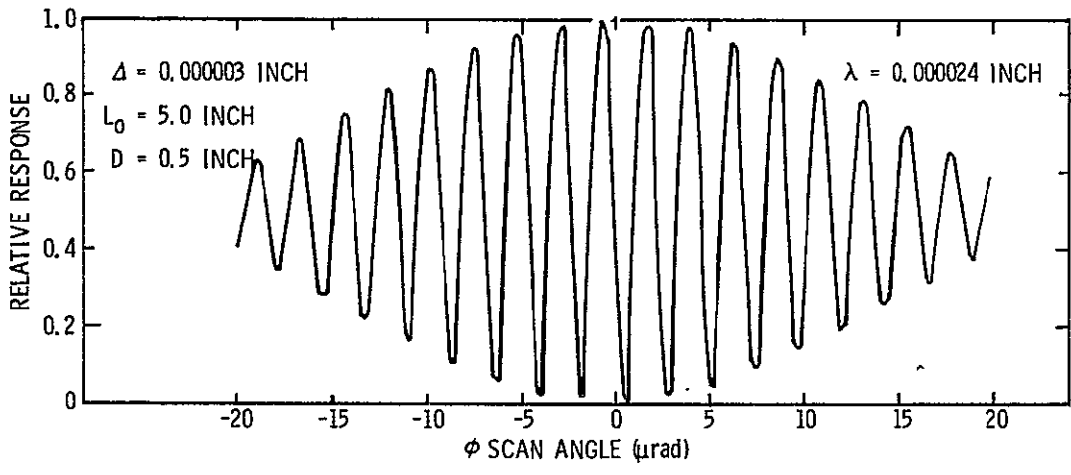


Figure 3-24b. Normalized Initialization Pulse - Relative Response versus Scan Angle

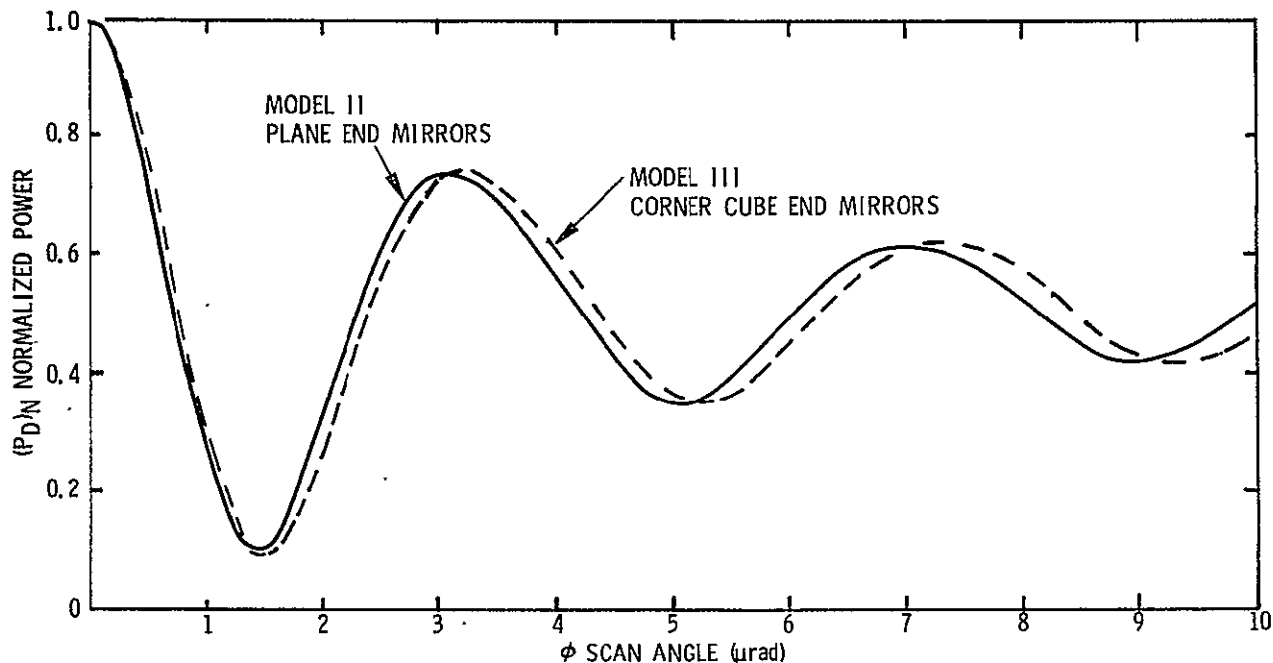


Figure 3-25. Normalized Initialization Pulse - Incandescent Source - Models II and III

Linkage for East-West Step Scan of the AASIR

Past discussions with GSFC have indicated that the cross scan motion of the AASIR will be accomplished by rotating the entire instrument about an axis parallel to the axis of the telescope. To reduce the reaction forces transmitted to the spacecraft, GSFC has further specified that the CG of the instrument will lie on the axis of rotation which will be located on or about the axis of the telescope (see Figure 3-26). Since the cooler view of space may not be obstructed, at least one of the bearings would have to be large (24- to 26-inch diameter). The cross scan motion consists of alternating steps of 375 μrad and 11 × 375 μrad over ±10° total. The resolution requirement is about 1 μrad. The major problems associated with a large, rolling element bearing are lubrication and friction. The oscillating motion over relatively small angles could cause lubricant build-up over the life of the instrument, changing the stick/slip characteristics of the bearing.

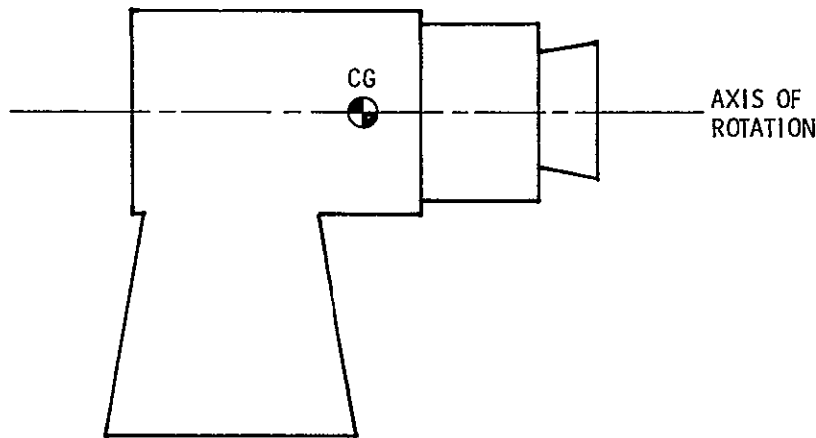


Figure 3-26. Cross Scan Motion Requirement

An investigation was made to try to eliminate the large bearing from the design. Figure 3-27 shows a four-bar linkage whose motion characteristics are desirable for this application. Link 1 is fixed. Links 2 and 4 are connecting links, and link 3 is the coupler. As the coupler is moved back and forth, its instantaneous center of rotation is located at the point where links 2 and 4 cross. Now, if link 1 is the spacecraft and link 3 is the instrument, point "O" would be the center of rotation for small angles of motion. Since point "O" has to be on the axis of the telescope, links 2 and 4 must take the shape of rings rather than straight bars. Figure 3-28 depicts this configuration. The rectangular portion at the bottom of the instrument represents the sunshade, and "O" is the axis of the telescope. Link 4 is connected to the spacecraft at the upper left pivot and connected to the AASIR at the lower right pivot. Similarly, line 2 is connected at the upper right and lower left. As the AASIR rotates through  $\pm 10^\circ$ , each of the four pivots moves  $\pm 5^\circ$ . Since this is well within the rotational limits of a "Bendix type" flex pivot, the large ball bearing is now replaced by four flex pivots. The locus of the telescope axis is shown in Figure 3-29. The maximum displacement "r", which occurs at  $\pm 10^\circ$  rotation, is about 0.16 inch.

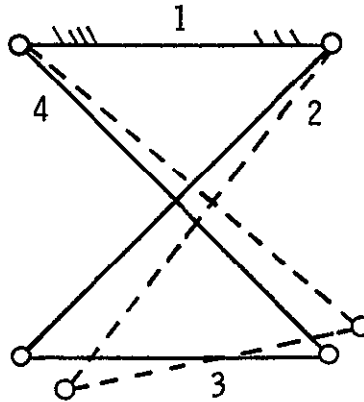


Figure 3-27. Four-Bar Linkage

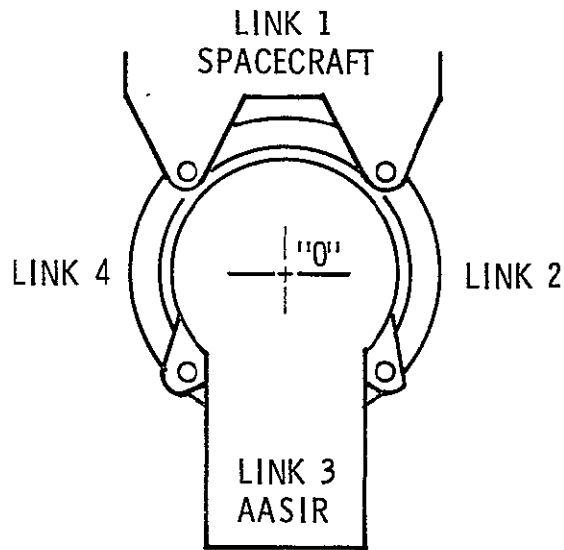


Figure 3-28. Cross Scan Linkage - End View

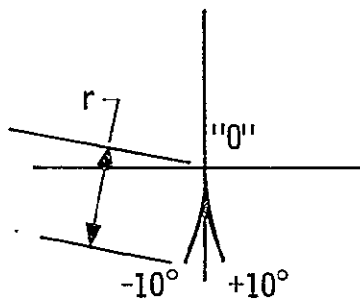


Figure 3-29. Locus of Geometric Center

☛ To carry the design one step further, see Figure 3-30, which shows how the rings could be spaced along the instrument. Note that link 2 is split into two pieces to provide rigidity. As the AASIR rotates, the optical axis translates slightly but does not tilt. Thus, the optical performance of the instrument is not affected by the fact that the rotation is not perfect. Now, in the three-dimensional case, flex pivots would be used on both sides of the rings, and since link 2 has been split, a total of four flex pivots would be used for each ring (see Figure 3-31). Referring back to Figures 3-27 and 3-28, the linkage can be driven by rotating or pushing on any of the three movable links. An example of a drive system is shown in Figure 3-32. One end of a linear actuator is attached to the spacecraft and the other end to a lever arm on the AASIR. This subsection will not discuss the drive system further because the problems associated with the drive system are present regardless of the technique used to support the instrument.

A preliminary stiffness analysis was done to determine if the linkage method of support could be built with enough rigidity to support the AASIR. Assuming a 230-pound instrument as depicted by the AASIR model, the required radial and axial stiffness can be calculated for a given natural frequency.

$$f = \frac{1}{2\pi} \sqrt{\frac{K}{M}}$$

$$K = m(2\pi f)^2$$

for:  $m = 230 \text{ lb}$  and  $f = 150 \text{ cps}$

$$K = \frac{230}{386} 2\pi(150)^2$$

$$K = 530,000 \text{ lb/in.}$$

where K is the total radial or axial stiffness that needs to be provided by the rings and flex pivots. If the mode of vibration is radial, as shown in Figure 3-33, all of the stiffness must be provided by the two sections of link 2. The required stiffness for each section would be:

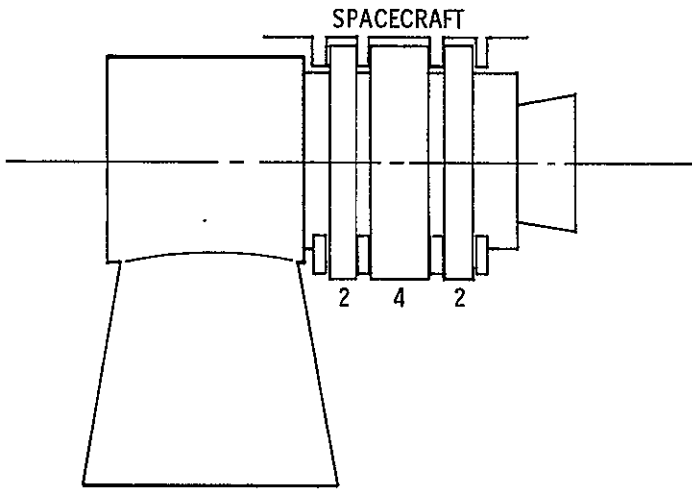


Figure 3-30. Cross Scan Linkage - Side View

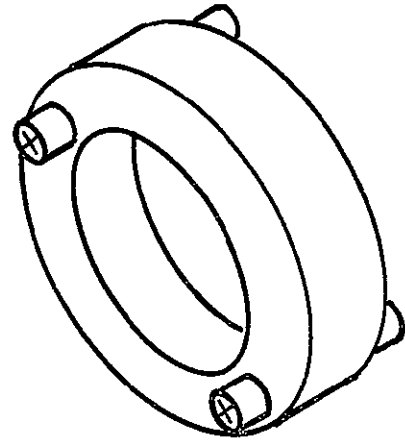


Figure 3-31. Ring Detail

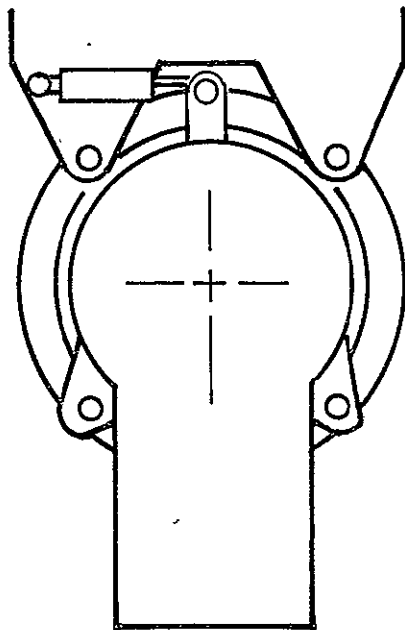


Figure 3-32. Actuator Scheme

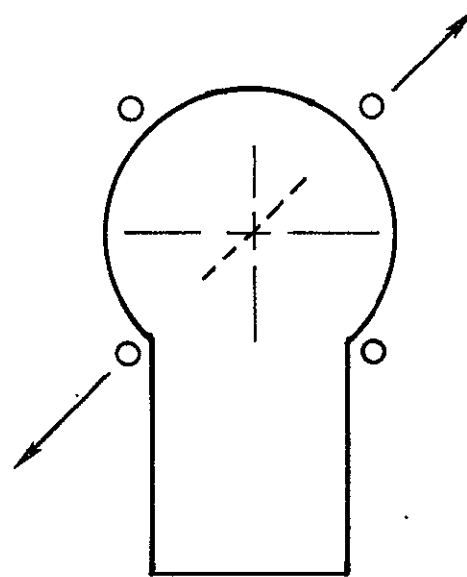


Figure 3-33. Vibration Mode

$$K_s = \frac{K}{2} = \frac{530,000}{2}$$

$$K_s = 265,000 \text{ lb/in.}$$

Referring back to Figure 3-31, there are four pivots per section. Figure 3-34 shows a stiffness model of a section of link 2. Note that link 4 does not provide any stiffness in this mode.  $K_p$  is the radial stiffness of each flex pivot and  $K_R$  is the stiffness of the ring itself.

$$K_s = \frac{1}{\frac{1}{K_R} + \frac{2}{2K_p}} = \frac{1}{\frac{1}{K_R} + \frac{1}{K_p}}$$

Assume that  $K_R = K_p$

For  $K_s = 265,000 \text{ lb/in.}$

$$K_R = K_p = 530,000 \text{ lb/in.}$$

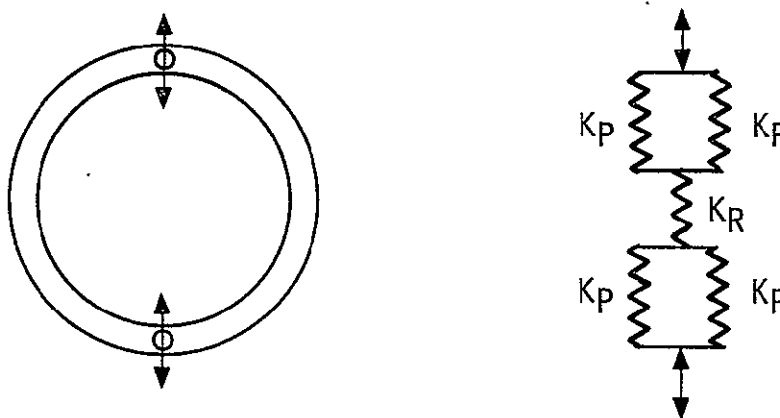


Figure 3-34. Stiffness of Ring and Flex Pivots

A standard 1-inch diameter Bendix flex pivot has a radial stiffness of about 100,000 lb/in. According to Bendix, the stiffness is proportional to the diameter squared, so a 2.3-inch diameter pivot should have the required radial stiffness. In any case, assume that a flex pivot about 2.0- to 2.5-inch diameter could be designed for infinite life at  $+5^\circ$  and have a radial stiffness of 530,000 lb/in. Note that the pivots can be oriented in the ring

to take advantage of the fact that the pivots are stronger in one direction than another. This is because regardless of the vibration mode, the direction of loading on the pivots is always colinear, as shown in Figure 3-34 (assuming that the torsional stiffness of the pivots is small compared to the radial stiffness).

Now, the remaining question is whether a ring can be designed to have a stiffness of 530,000 lb/in. when loaded as shown in Figure 3-34. Using a formula from Roarke (Table VIII, page 157)<sup>2</sup>

$$Dy = 0.149 \frac{WR^3}{EI}$$

$$K_R = \frac{W}{Dy} = \frac{EI}{0.15 R^3}$$

- where: R = average radius of ring  
E = modulus of elasticity for given material  
I = moment of inertia of cross section of ring

Assuming that the AASIR telescope tube is 22 inches in diameter, the ring would require an ID of about 24 inches. Using the cross section shown in Figure 3-35, a beryllium ring would have the following properties:

$$R = 13.75 \text{ in.}$$

$$I = 5.5 \text{ in.}^4$$

$$E = 42 \times 10^6 \text{ lb/in.}^2$$

$$A = 2.6 \text{ in.}^2$$

$$K_R = \frac{42 \times 10^6 (5.5)}{0.15 (13.75)^3} = 590,000 \text{ lb/in.}$$

$$\text{Weight of ring} = 0.067(\pi)(27.5)(2.6) = 15 \text{ lb}$$

---

<sup>2</sup>R. J. Roarke, Formulas for Stress and Strain, McGraw-Hill Book Co., Inc. (1943).

Since link 2 is split in two parts and link 4 is twice as wide, the total weight of the rings would be about 60 lb.

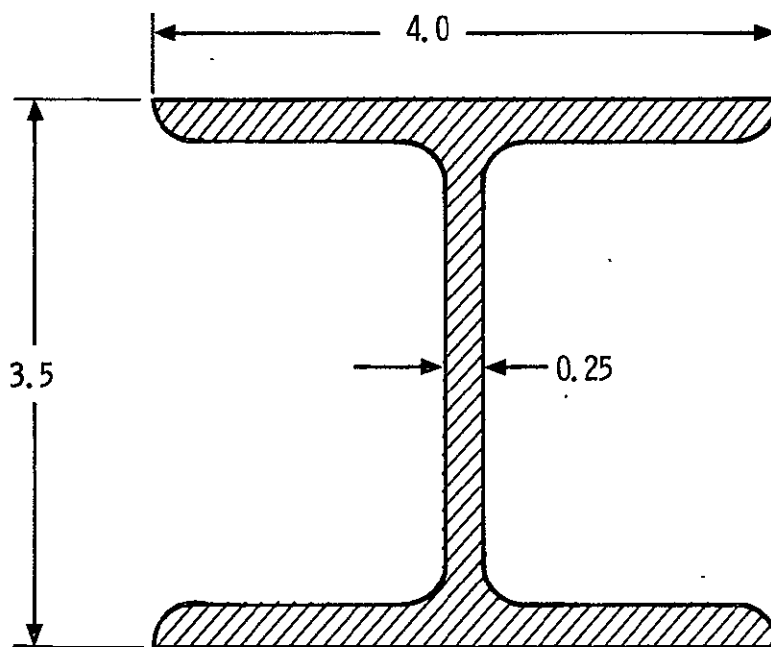


Figure 3-35. Ring Cross Section

As the AASIR rotates through a  $10^\circ$  angle, the rings pivot with respect to the spacecraft. Referring back to Figure 3-28, if the instrument rotates clockwise, both link 2 and link 4 also rotate clockwise. Since the CG of the links is approximately at point "0," a reaction force from the rings will be felt by the spacecraft. However, if the CG of the AASIR were deliberately displaced slightly above point "0," the reaction force from links 2 and 4 could be cancelled by the reaction force from link 3. By choosing the location of the CG carefully, the unbalanced forces due to the center shift shown in Figure 3-29 could also be, at least partially, cancelled.

To drive the AASIR from its nominal  $0^\circ$  position, the pivots must be flexed torsionally. A standard 1-inch diameter Bendix flex pivot has a torsional spring rate of 54 in. -lb/rad. According to Bendix, the torsional spring rate is proportional to the diameter cubed, so a 2.3-inch diameter

pivot should have a torsional spring rate of about 650 in. -lb/rad. The reaction torque at point "0" would be about  $8 \times 650 = 5200$  in. -lb/rad. The maximum torque occurs after the instrument has rotated  $10^\circ$  and the pivots have rotated through  $5^\circ$  (0.09 rad).

$$T_{\max} = 5200(0.09) = 450 \text{ in. -lb}$$

Referring back to Figure 3-32, if the drive system was located 18 inches from point "0," the maximum force required by the linear actuator would be 25 lb. A single 375-rad step would require the actuator to move about 0.007 inch, and the average power required to make the last step at the edge of the frame in 0.25 second would be:

$$P = \frac{Fx}{t}$$

$$P = \frac{25(0.007)}{0.25}$$

$$P = 0.7 \text{ in. -lb/sec} = 0.08 \text{ watt}$$

Note that the power is required only while stepping away from the center of the frame. This power will be returned to the system while stepping back toward the center of the frame. Additional power is required to accelerate the instrument during steps. Assume that the inertia of the 230-lb AASIR is 20,000 lb-in.<sup>2</sup> and a cosine step is made as shown in Figure 3-36. Let  $\alpha$  equal the maximum acceleration during a step.

$$\alpha = 375 \times 10^{-6} \left( \frac{\pi}{0.25} \right)^2$$

$$\alpha = 0.03 \text{ rad/sec}^2$$

$$T_{\max} = I\alpha = \frac{20,000(0.03)}{386}$$

$$T_{\max} = 1.5 \text{ in. -lb}$$

$$P_{av} = \frac{T_{av}(\theta)}{t}$$

$$P_{av} = \frac{0.7(1.5)(375 \times 10^{-6})}{0.25}$$

$$P_{av} = 0.0016 \text{ in. -lb/sec} = 0.0002 \text{ watt}$$

For a step of  $11 \times 375$  rad in 0.25 sec, the average power required would be 0.022 watt.

In conclusion, the linkage method of suspending the instrument may be considered as an alternative to a large set of rolling element bearings. Advantages include low friction and hysteresis, no lubrication, and long service life. In addition, the linkage automatically isolates the instrument from the spacecraft thermally and acts as a kinematic mount. The primary disadvantage is the added size, weight, and complexity of the beryllium rings required to obtain adequate radial and axial stiffness.

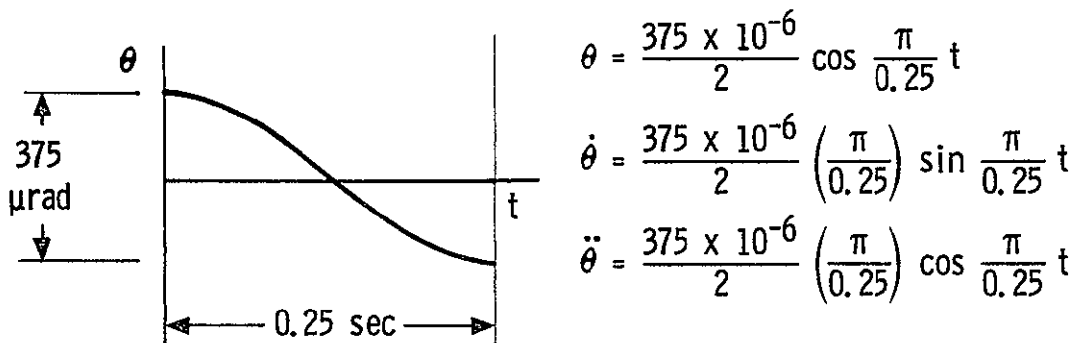


Figure 3-36. Step Motion

AASIR MODULATION TRANSFER FUNCTIONS (MTF)

The AASIR uses bidirectional scanning over the same scan line to obtain registration of IFOVs in each of the spectral bands and to minimize frame time. Owing to phase shifts which are caused by the electrical filter in the output (in this case, an integrator and hold circuit), the registration of spectral IFOVs in the scene will be degraded compared with the unidirectional scan case unless shifting of data is used.

The magnitude of the effect may be evaluated by considering the system MTF consisting of three subsystem MTFs:

1. Centrally obscured telescope
2. Ideal rectangular detector
3. Integrator

The optical transfer function (OTF) of the rectangular detector is the Fourier transform of the ideal detector IFOV and it is real, i. e.,

$$OTF_D = \left| \frac{\sin \alpha \pi \nu}{\alpha \pi \nu} \right| \tag{1}$$

where  $\alpha$  is the width of the IFOV in the scan direction in radians determined by the detector or field stop.  $\nu$  is spatial frequency in cycles/radians.

The electrical transfer function of the output integrator is:

$$F(S) = \frac{1}{T} \left( \frac{1}{S} - \frac{1}{S} e^{-TS} \right) \text{ in Laplace notation or}$$

$$F(\omega) = \frac{1}{T} \left( \frac{1}{j\omega} - \frac{1}{j\omega} e^{-j\omega T} \right) \text{ s = } j\omega$$

where T is the integration time. Separating the real and imaginary parts:

$$F(\omega) = \frac{-\sin \omega T}{\omega T} + \frac{j(1 - \cos \omega T)}{\omega T} \tag{2}$$

For scanning in one direction only, the phase angle of this function is not important since frequencies in corresponding picture elements in succeeding scans will be delayed the same. Therefore, the absolute value of the expression can be used,

$$\begin{aligned}
 |F(\omega)| &= \left[ \frac{(1 - \cos \omega T)^2 + \sin^2 \omega T}{(\omega T)^2} \right]^{\frac{1}{2}} \\
 &= \frac{1}{\omega T} (1 + \cos^2 \omega T - 2 \cos \omega T + \sin^2 \omega T)^{\frac{1}{2}} \\
 &= \left[ \frac{2(1 - \cos \omega T)}{(\omega T)^2} \right]^{\frac{1}{2}} = \left[ \frac{4 \sin^2 \frac{\omega T}{2}}{(\omega T)^2} \right]^{\frac{1}{2}} \\
 &= \frac{\sin \left( \frac{\omega T}{2} \right)}{\left( \frac{\omega T}{2} \right)} = \frac{\sin \pi f T}{\pi f T}
 \end{aligned}$$

Frequency  $f$  can be related to spatial frequency  $\nu$  by means of the scan parameter  $\tau_d/\alpha$  where  $\tau_d$  is the IFOV dwell time. Thus,

$$\nu = f \frac{\tau_d}{\alpha}$$

and

$$\text{MTF} = \frac{\sin \pi \nu \frac{\alpha}{\tau_d} T}{\left( \pi \nu \frac{\alpha}{\tau_d} T \right)}$$

if  $K = \frac{T}{\tau_d}$ , then  $\frac{1}{K}$  is the number of integrations performed per dwell time, or the number of samples per dwell time and,

$$\text{MTF}_I = \frac{\sin (\pi \nu K \alpha)}{(\pi \nu K \alpha)} \tag{3}$$

C-2

When scanning in both directions, the phase angle of the OTF becomes important because it affects the resolution obtainable when combining bidirectional scans. For this case, the MTF of the output filter is given by:<sup>3</sup>

$$MTF = OTF + OTF^* = 2 \operatorname{Re} (OTF)$$

where the asterisk denotes the complex conjugate. Thus, for the integrator:

$$MTF_I' = \frac{\sin \omega T}{\omega T} = \frac{\sin (2\pi \nu K \alpha)}{(2\pi \nu K \alpha)} \quad (4)$$

Equations (1), (3), and (4) are plotted in Figure 3-37 for the sounding IFOV (375  $\mu$ rad).

The degradation in  $MTF_I'$  (curve 3) is due to the phase shift in the integrator which can be corrected by shifting each data point in one scan by an amount equal to twice the phase angle or  $2\pi \nu \alpha$  radians. Note that this phase shift is unaffected by the sinusoidal variation in scan velocity.

Figure 3-38 shows the system sounding channel MTF for the cases where the phase shift is compensated for and where it is not. System MTFs for IR imaging and visible imaging channels are shown in Figures 3-39 and 3-40, respectively.

Since the system is sampled once per dwell time, it is possible that aliasing can occur in the output. This can be seen in Figure 3-38 where the spatial frequencies above the sampling frequency are shown "folded over" the frequencies below the sampling frequency. Sampling at twice the highest spatial frequency in the MTF will satisfy the Nyquist criterion and will improve the system MTF, but the signal-to-noise ratio per sample will be degraded by the square root of two.

On the other hand, it may not be necessary to sample twice per dwell time since the spatial frequency content or MTF of the scene may roll off below that where aliasing could be a problem. Therefore, the optimum value will lie between values of one and two.

---

<sup>3</sup>J. M. Lloyd, Thermal Imaging Systems, p 104, Plenum Press (1975).

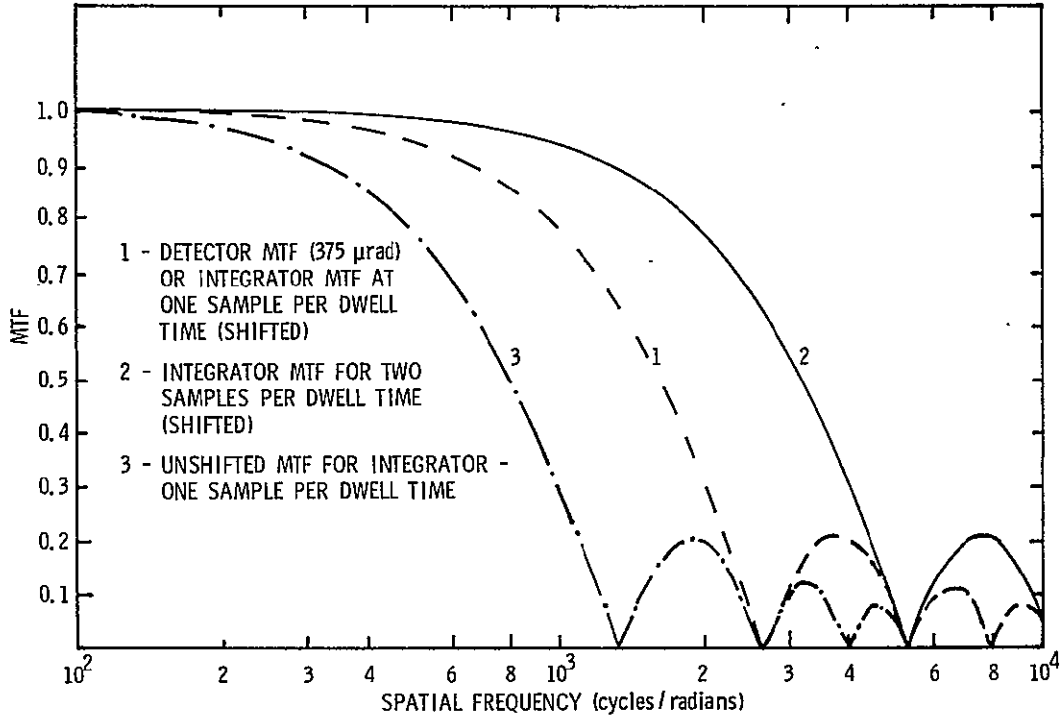


Figure 3-37. Detector and Integrator MTFs

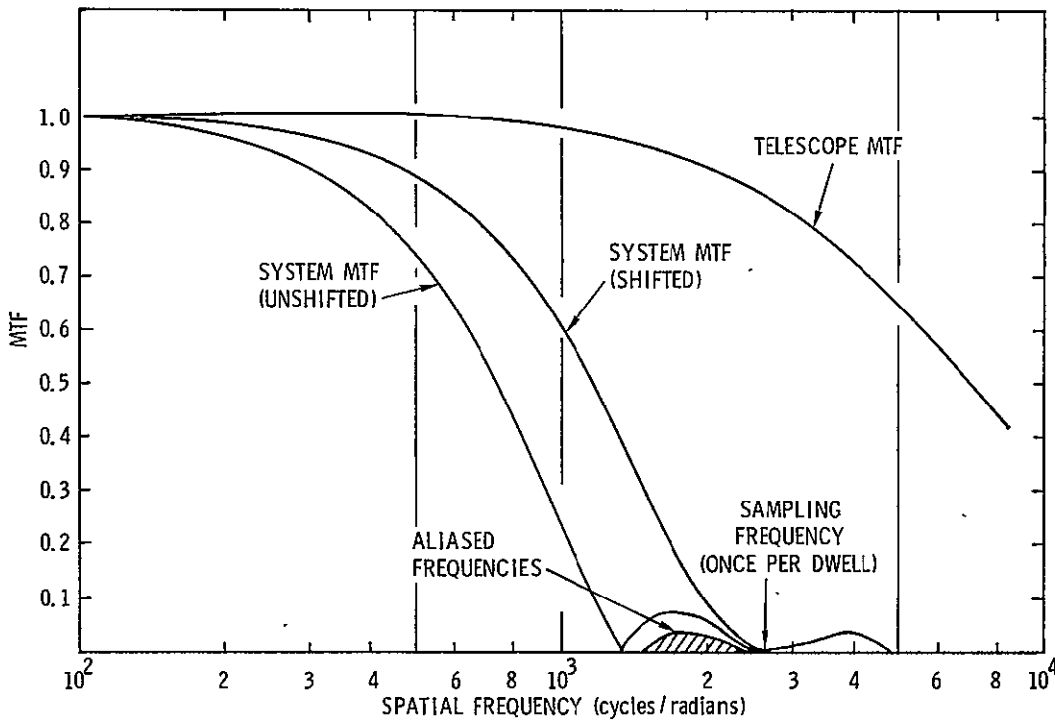


Figure 3-38. System MTF for 14- $\mu$ m Sounding Channels

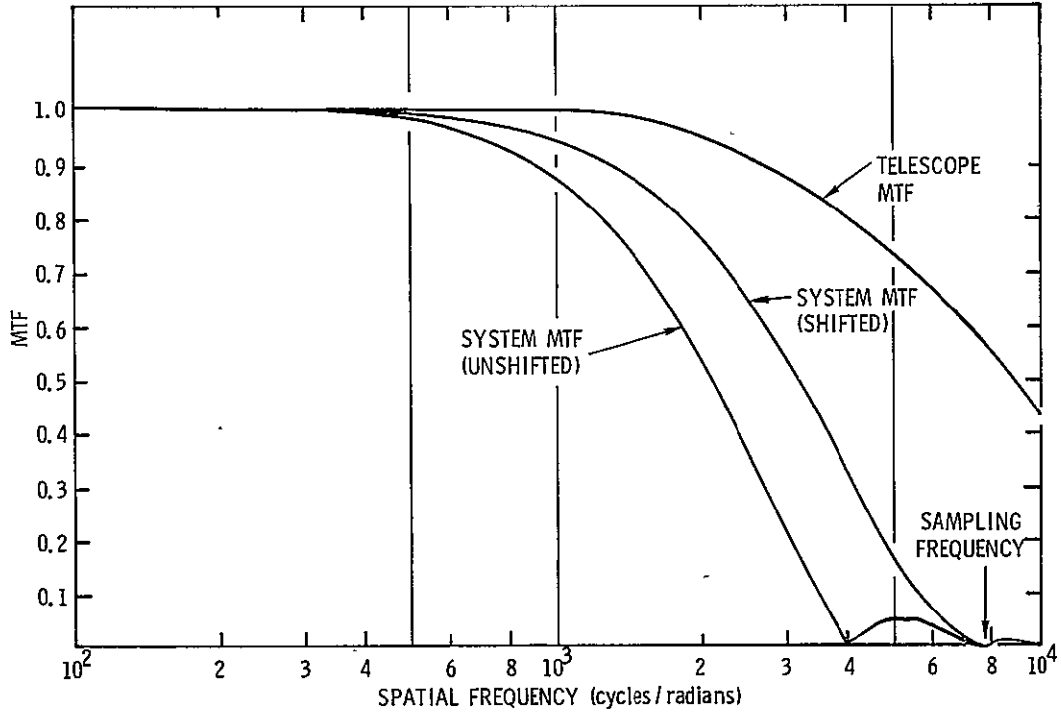


Figure 3-39. System MTF for IR Imaging Channels

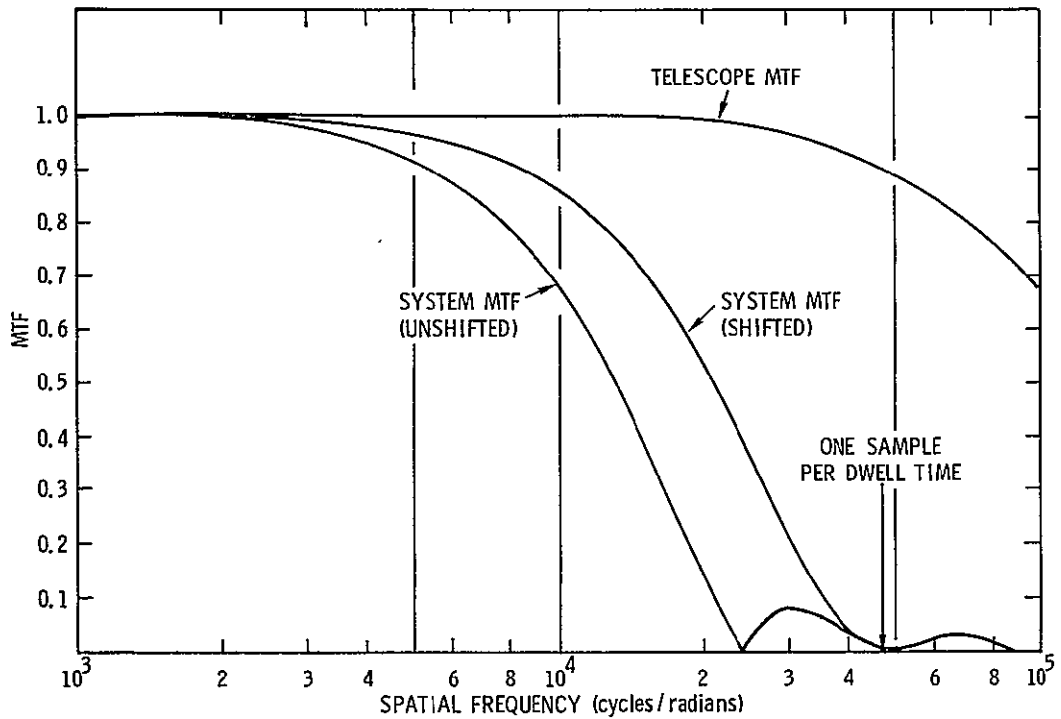


Figure 3-40. System MTF for Visible Imaging Channels

Equivalent Resolution

Lloyd<sup>3</sup> discusses an expression to describe the equivalent resolution,  $\bar{R}$ , of an imaging system:

$$\bar{R} = \frac{1}{2 \int_0^{\infty} (MTF)^2 df}$$

As defined,  $\bar{R}$  is in effect inversely proportional to the equivalent square bandwidth and thus is a function of the area under the MTF curve as well as the cutoff frequency. The equivalent resolution  $\bar{R}$  is equal to  $\alpha$  when the function is rectangular. Values of  $\bar{R}$  are given in Table 3-13 together with the value of  $\alpha = \alpha_0$  corresponding to the first zero in the MTF.

Table 3-13. Equivalent Resolution

	SHIFTED		UNSHIFTED	
	$\bar{R}$ ( $\mu$ rad)	$\alpha_0$ ( $\mu$ rad)	$\bar{R}$ ( $\mu$ rad)	$\alpha_0$ ( $\mu$ rad)
14- $\mu$ m SOUNDING	582	375	938	750
IR IMAGING	210	125	316	250
VISIBLE IMAGING	32	21	51	42

Unsymmetrical Detector Response

The preceding analysis has treated the case of an ideal rectangular detector response. In fact, the response may have roughly a sawtooth shape due to the sweepout effect in HgCdTe. However, it appears clear from Figure 3-41 that so long as an integrate-hold circuit is used, the effects of bi-directional scanning can be corrected by a simple angular shift in the data the equivalent of two IFOVs.

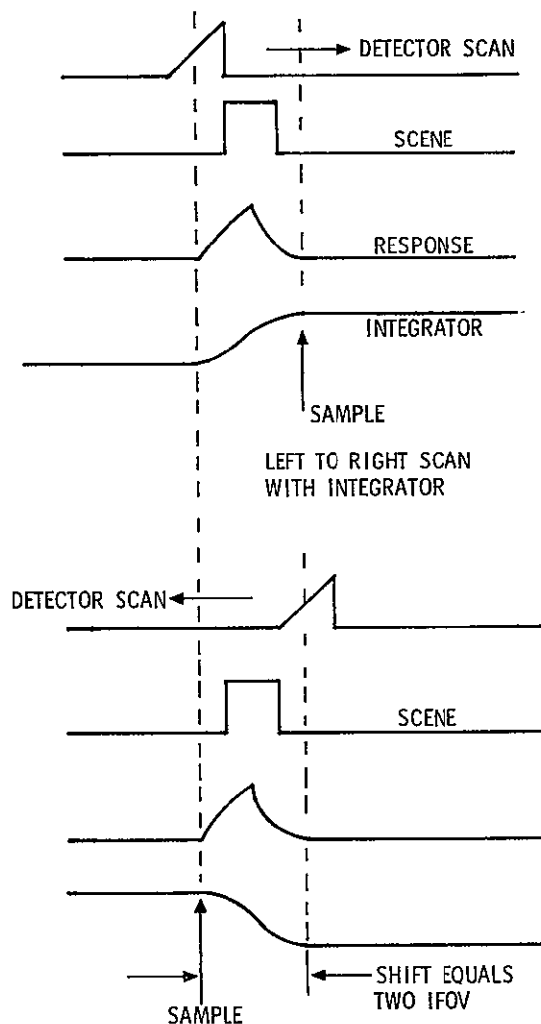


Figure 3-41. Effects of Bidirectional Scan

AASIR VISIBLE IMAGING CHANNEL MTF

This subsection treats the calculated MTF response of the AASIR visible channels based on GOES C (VISSR) telescope parameters. Of interest is the MTF response of the telescope with the IFOV reduced from 21  $\mu$ rad to 16  $\mu$ rad. The anticipated 16- $\mu$ rad MTF response was derived from the GOES C Class I telescope performance specification multiplied by a 21- $\mu$ rad  $\sin x/x$  FOV function.

The Class II optical performance specification is defined as that imposed on optical manufacturers when testing the telescope system consisting of the primary, secondary, and scan mirrors. The Class I specification

used as a baseline here is the Class II specification degraded by an amount consistent with mounting the telescope elements in the final sensor hardware. The Class II specification MTF was derived from the energy spread functions of a diffraction-limited telescope and the combined geometrical aberrations and optical finishing imperfections.

Figure 3-42 shows the Class I specification for both the sine wave and square wave MTF. Actual measurements of the GOES B telescope are also shown in the figure, but it should be noted that this particular telescope was the best ever measured. Also, the Class I specification is not to be confused with the systems level MTF specification which can be satisfied by a much poorer telescope MTF. This was done to account for further degradations which occur in systems tests as a result of test equipment, thermal shifts, and other factors.

During the study, the question of the smallest practical IFOV size was addressed. Two sizes, 21  $\mu$ rad and 16  $\mu$ rad, were compared. The MTF curves for 16  $\mu$ rad shown in Figure 3-43 were obtained by dividing the sine wave response of Figure 3-42 by a 21- $\mu$ rad  $\sin x/x$  function and multiplying the result by a 16- $\mu$ rad  $\sin x/x$  function, i. e.,

$$\text{Class I} \times \text{sinc } 16^* = \text{Class I} \times \text{sinc } 21 \times \frac{\text{sinc } 16}{\text{sinc } 21}$$

The square wave MTF response was obtained from the sine wave MTF by a method described by Coltman.<sup>4</sup>

Comparison of the sine wave MTF of the Class I  $\times$  16- $\mu$ rad curve with the 16- $\mu$ rad IFOV only curve gives a feeling for the degradation to be expected from the "best" GOES B beryllium telescope. The expectation here is that this performance could be equalled by a telescope using fused silica elements. On the other hand, the 16- $\mu$ rad square wave response of Figure 3-43 can be compared with the 21- $\mu$ rad square wave response of Figure 3-42.

---

\*Only sine wave MTFs can be manipulated in this manner.

<sup>4</sup>J. W. Coltman, JOSA, Vol. 44, No. 6, June 1954.

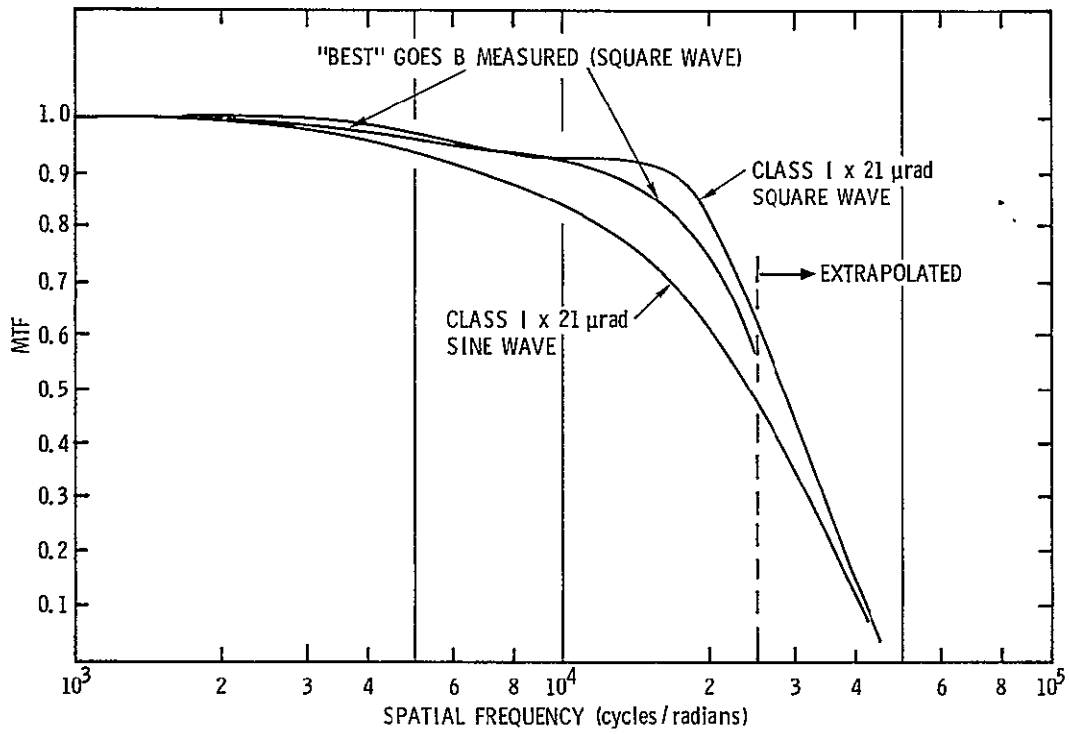


Figure 3-42. GOES C MTF - Class I x 21-μrad IFOV Specification

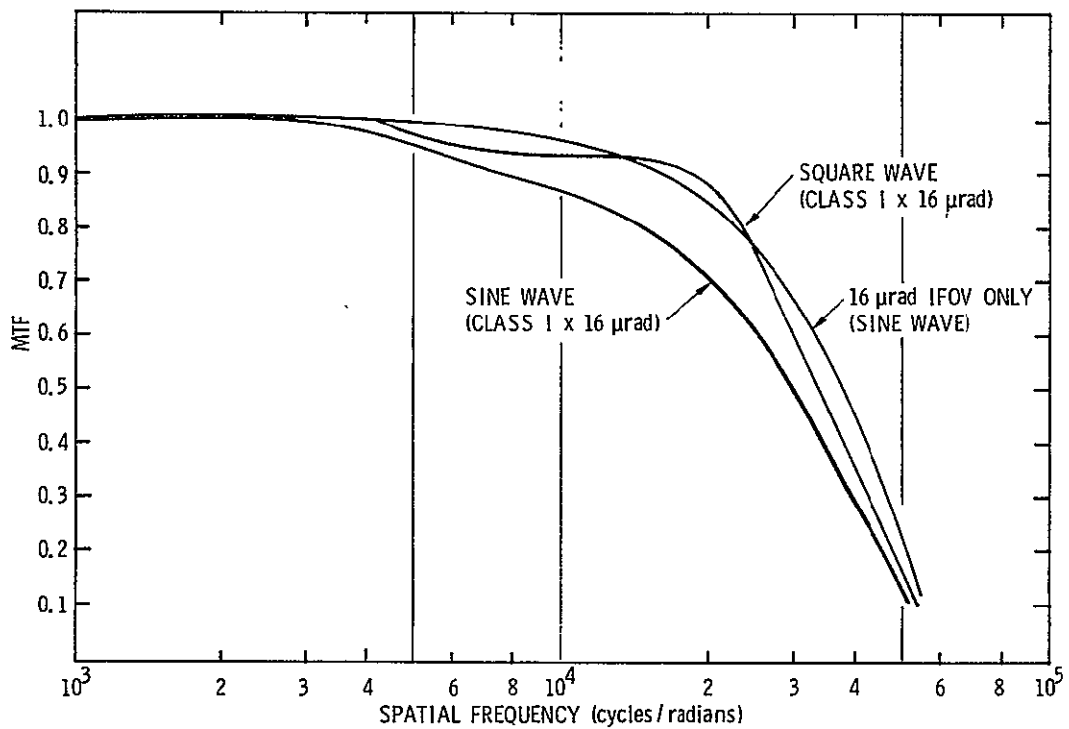


Figure 3-43. AASIR MTF - Class I Specification x 16-μrad IFOV

USE OF THE 3.7- $\mu$ m CHANNELS FOR WIND VELOCITY DETERMINATION

This subsection of the report discusses the use of 3.7- $\mu$ m channels for wind determination at night by time lapse imaging of clouds.

Basically, the velocity measurement error is a function of pixel size and frame time. That is, for a given pixel size, the error decreases with increasing number of frames. This can be expressed as:

$$\overline{\Delta V}_{\text{rms}} = \frac{[(\Delta X_1)^2 + (\Delta X_2)^2 + (\Delta Y_1)^2 + (\Delta Y_2)^2]^{\frac{1}{2}}}{t_2 - t_1} \quad (1)$$

where:  $\Delta X_1$  = uncertainty of cloud location in E-W direction at  $t_1$   
 $\Delta X_2$  = uncertainty of cloud location in E-W direction at  $t_2$   
 $\Delta Y_1$  = uncertainty of cloud location in N-S direction at  $t_1$   
 $\Delta Y_2$  = uncertainty of cloud location in N-S direction at  $t_2$

Assuming that  $\Delta X_1 = \Delta X_2 = \Delta Y_1 = \Delta Y_2 = \Delta$  and that by a method to be described  $\Delta$  can be reduced to  $K\Delta$  of a pixel,  $K < 1$ . The velocity error due to pixel size will be:

$$\overline{\Delta V}_{\text{rms}} = \frac{2\Delta}{t_2 - t_1} = \frac{2K(\text{pixel})}{t_2 - t_1} \quad (2)$$

The velocity error  $\overline{\Delta V}_{\text{rms}}$  due to finite pixel size is shown in Figure 3-44 for three representative pixel sizes, 75  $\mu$ rad, 90  $\mu$ rad, and 125  $\mu$ rad, and  $K = 1$ . From the figure, it is clear that even for the smallest IFOV, the error is greater than 4 m/sec for a single frame time of 24 minutes. The figure shows that given sufficient time  $\overline{\Delta V}_{\text{rms}}$  values below the single frame time minimum can be obtained. However, the lifetimes of clouds are limited so that determination of  $\overline{\Delta V}_{\text{rms}}$  in minimum time (which is a single frame time) is desirable. To measure cloud velocities smaller than 4 m/sec in a single frame time,  $K$  must be less than unity and oversampling must be used to resolve less than one IFOV. The value of  $K$  is the fraction of the full scale response that must be resolved to give the desired cloud velocity error,  $\overline{\Delta V}_{\text{rms}}$ .

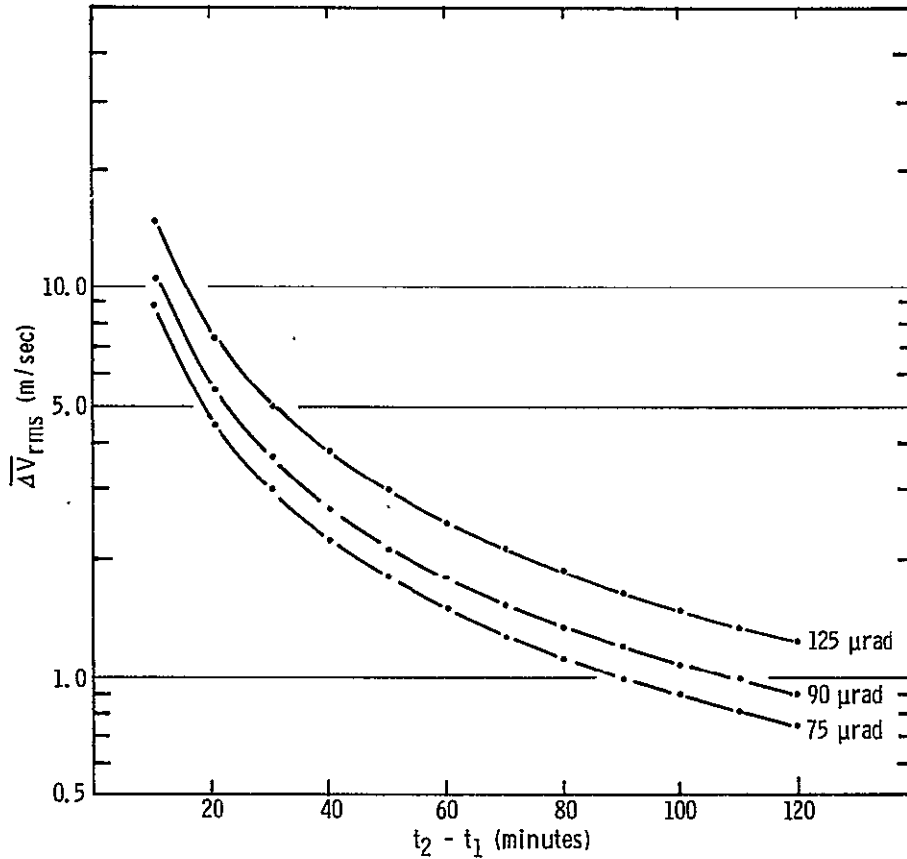


Figure 3-44. Cloud Velocity Error as a Function of Time (K = 1)

The value of K was determined knowing system image quality and noise performance as follows:

1. The telescope image quality was evaluated considering diffraction, geometrical aberrations including color, and fabrication tolerances. Using these factors, the energy spread function (ESF) was generated.
2. The ESF was differentiated to give the point spread function (PSF).
3. The PSF was convolved with a thin slit to give the line spread function (LSF).
4. The LSF was then convolved with a semi-infinite step which represents a cloud edge.
5. Various IFOVs (75, 90, and 125 μrad) were convolved with the result of Step 4. These are shown in Figures 3-45, 3-46, and 3-47.

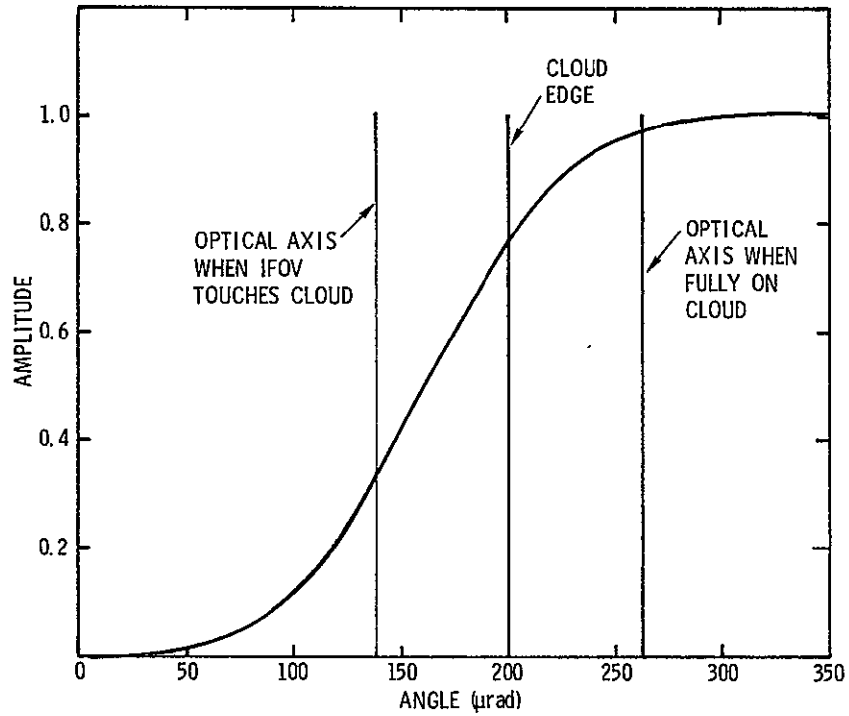


Figure 3-45. Normalized Response Function, 125-μrad IFOV

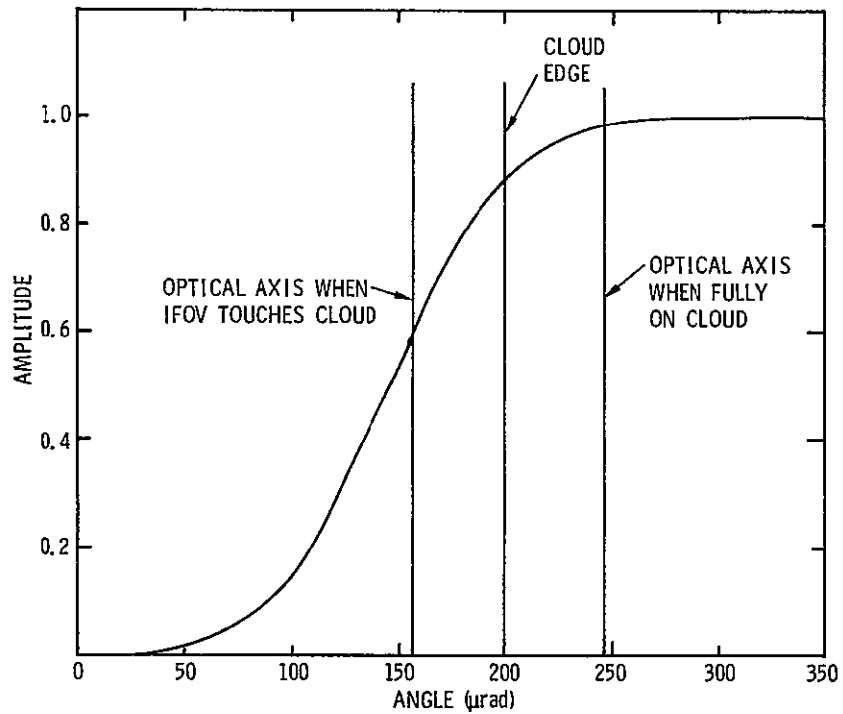


Figure 3-46. Normalized Response Function, 90-μrad IFOV

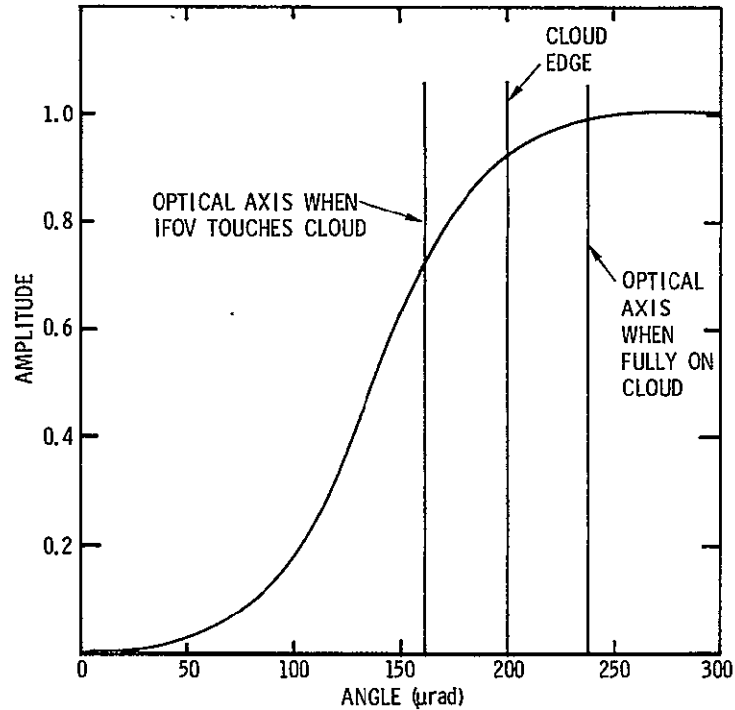


Figure 3-47. Normalized Response Function, 75-μrad IFOV

The value of K in the absence of noise can be given by:

$$K = \left( \frac{\partial F}{\partial \phi} \right) \frac{T_F \overline{\Delta V}_{rms}}{36} \tag{3}$$

where:  $\left( \frac{\partial F}{\partial \phi} \right)$  = the slope of the normalized response function shown in Figures 3-45, 3-46, and 3-47 (per μrad)

$T_F$  = the observing time in seconds

$\overline{\Delta V}_{rms}$  = the maximum permissible cloud velocity error in m/sec

Typical values are given in Table 3-14 for one and two frame times. Values of  $K > 1$  have no significance.

Using the 125-μrad IFOV to get  $\overline{\Delta V}_{rms} = 1$  m/sec, for example, we would need to resolve 0.276 of the amplitude step output when viewing from the earth to a cloud. If a larger value of  $\overline{\Delta V}_{rms}$  or more frame times can be tolerated, the amplitude fraction can be larger (in the absence of noise).

Table 3-14. Values of K

$\overline{\Delta V}_{rms}$ (m/sec)	125 $\mu$ rad		90 $\mu$ rad		75 $\mu$ rad	
	$T_F$	$2T_F$	$T_F$	$2T_F$	$T_F$	$2T_F$
1	0.2763	0.552	0.332	0.665	0.355	0.71
2	0.5525	1.10	0.665	1.33	0.71	1.421
3	0.829	--	0.997	--	1.07	--
4	1.10	--	1.33	--	--	--

To bring noise into the picture, let

$$\Delta N = N_E - N_C$$

where  $\Delta N$  is the radiance difference between the earth and cloud. Since it is desired to resolve  $\overline{\Delta V}_{rms}$ , a radiance difference must be detected which is equal to

$$K\Delta N = K(N_E - N_C)$$

The signal-to-noise ratio (SNR) associated with this change in radiance depends on the system NEN. Thus,

$$\Delta SNR = \frac{K\Delta N}{NEN} \tag{4}$$

where NEN has been previously calculated and is indicated below.

<u>IFOV</u> ( $\mu$ rad)	<u>NEN</u> (ergs/etc.)
125	0.006
90	0.010
75	0.013

Equation (4) has been plotted in Figure 3-48 for the case of  $\overline{\Delta V}_{rms} = 1$  m/sec. The SNR for any IFOV is in direct proportion to the values of  $\overline{\Delta V}_{rms}$  or  $T_F$  assumed.

The results indicate that because the image blur is a large fraction of the FOV, the SNR advantage of the large FOVs overpowers the resolution advantage of the smaller IFOVs. Therefore, in this application, the 125- $\mu$ rad FOV is better for cloud velocity determination than smaller sizes. However, the optimum value may be larger than 125  $\mu$ rad.

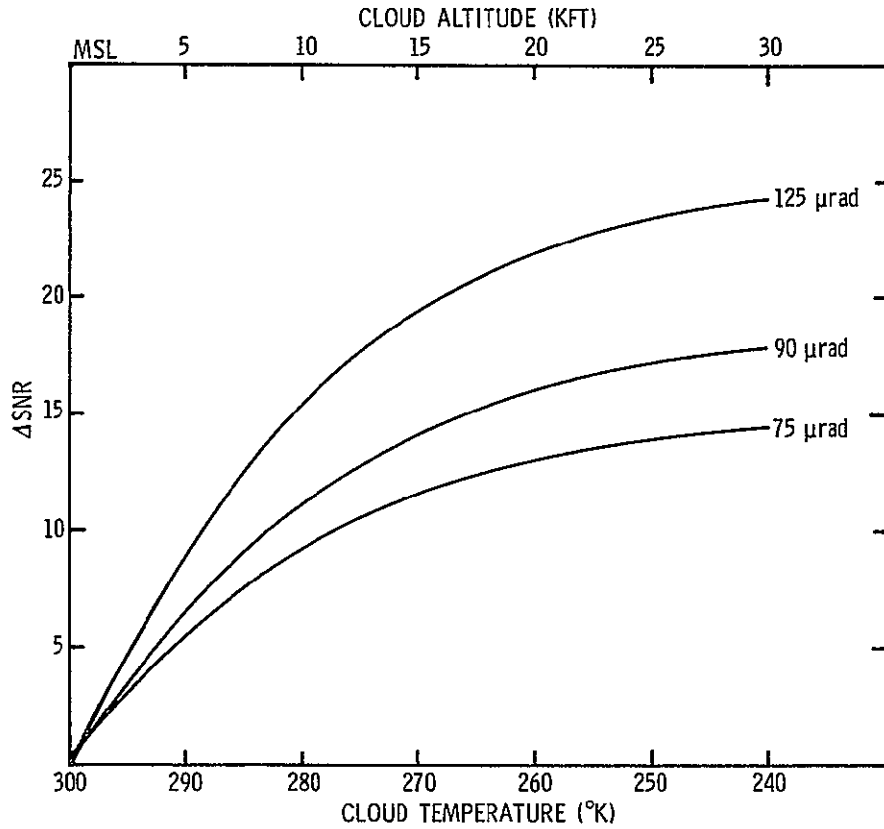


Figure 3-48.  $\Delta$ SNR versus Cloud Temperature (earth = 300 $^{\circ}$ K,  $\overline{\Delta V}_{rms} = 1$  m/sec)

## AASIR DATA RATES

The average data rates for the AASIR are given in Table 3-15 for the  $20^\circ \times 20^\circ$  frame size. The maximum instantaneous data rates obtained at center scan are given in Table 3-16.

Assuming that sample-and-hold circuits will be used for all channels, the digitizer must be capable of sampling at a maximum rate of 1 MHz. That is, at center scan where the maximum data rate occurs for every  $375 \mu\text{rad}$  of scan (in  $695.1 \mu\text{sec}$ ), there are 18 sounding channels,  $18 \times 15 = 270$  visible channels, and  $2 \times 3 \times 3 = 18$  IR imaging channels. Each channel is sampled twice so that 612 samples are taken every  $695.1 \mu\text{sec}$ ; the sampling rate is therefore 0.88 MHz. This rate is appropriate for currently available A/D converters.

Table 3-15. AASIR Average Data Rates for 20° x 20° Frame

CHANNEL	IFOV (μrad)	NUMBER OF IFOVs PER LINE	NUMBER OF SAMPLES PER IFOV	BITS PER SAMPLE	BITS PER LINE PER DETECTOR	NUMBER OF DETECTORS PER LINE	NUMBER OF LINES PER FRAME	TOTAL BITS PER FRAME	AVERAGE DATA RATE BITS/SEC
SOUNDING	375	931	2	10	$1.86 \times 10^4$	3	931	$5.2 \times 10^7$	$3.61 \times 10^4$
IR (11-μm) IMAGING	125	2,793	2	10	$5.59 \times 10^4$	1	2,793	$1.56 \times 10^8$	$1.08 \times 10^5$
IR (3.7-μm) IMAGING	125	2,793	2	10	$5.59 \times 10^4$	1	2,793	$1.56 \times 10^8$	$1.08 \times 10^5$
VISIBLE	21	16,620	2	8	$2.66 \times 10^5$	1	16,620	$4.42 \times 10^9$	$3.07 \times 10^6$
TOTAL								$4.78 \times 10^9$	$3.32 \times 10^6$

NOTES: FRAME TIME OF 24 MINUTES ASSUMED; DATA ARE TAKEN TWO SAMPLES PER IFOV, BUT NOT AT A CONSTANT RATE.

Table 3-16. Maximum Instantaneous Data Rates

CHANNEL	DWELL TIME <sup>1</sup> PER IFOV (μsec)	SAMPLES PER SEC PER DETECTOR	NUMBER OF DETECTORS	BITS PER SAMPLE	BITS PER SECOND	
SOUNDING	695.1	2,877	18	10	$5.18 \times 10^5$	
IR (11-μm) IMAGING	231.7	8,632	3	10	$2.6 \times 10^5$	
IR (3.7-μm) IMAGING	231.7	8,632	3	10	$2.6 \times 10^5$	
VISIBLE	38.9	51,414	15	8	$6.17 \times 10^6$	TOTAL $7.21 \times 10^6$ BPS

<sup>1</sup>MINIMUM DWELL TIME AT CENTER SCAN WHICH WILL GIVE MAXIMUM INSTANTANEOUS DATA RATE IS ASSUMED.

CALCULATION OF D\* VALUES FOR InSb CHANNELS

The D\* achieved from the AASIR detector depends primarily on the photon flux in the background and, therefore, on the temperature of the instrument. In this case, the detectors are background limited except for thermal noise contributions at lower instrument temperatures.

Figure 3-49 shows the optical schematic used to determine the photon flux falling on the detector from the telescope background.

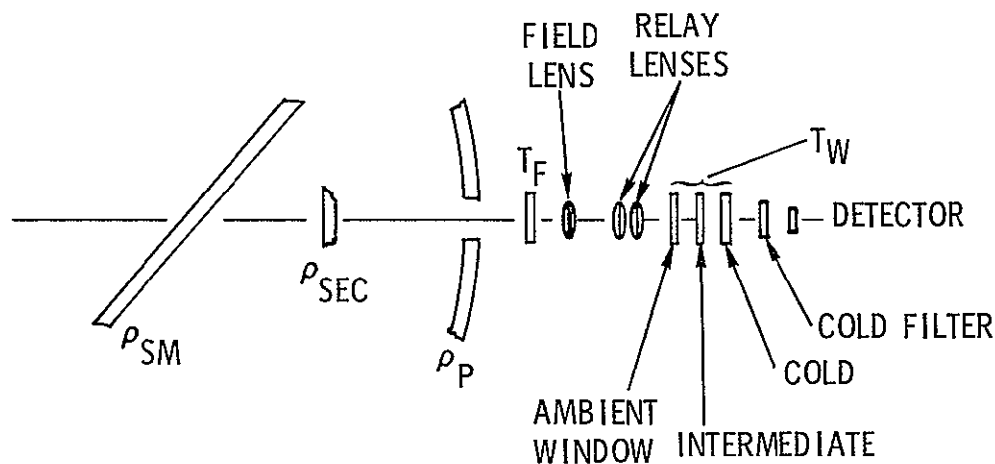


Figure 3-49. AASIR Optical Schematic Diagram

$\rho_{SM}, \rho_P, \rho_{SEC} = 0.94$  = reflectances of the scan mirror, primary mirror, and secondary mirror, respectively

$T_F$  = transmittance of bandpass filter = 0.6

$T_R$  = transmittance of relay = 0.804

$T_W$  = transmittance of windows (ambient, intermediate, and cold windows) = 0.93 each

$A_s$  = area of cold stop, located at the intermediate window =  $0.33 \text{ cm}^2$

$A_d$  = area of detector ( $\text{cm}^2$ ) =  $2.32 \times 10^{-4} \text{ cm}^2$

$B(T)_F$  = blackbody function in bandpass defined by  $T_F$  associated with each optical element between bandpass filter and aperture

$B(T)_{CF}$  = blackbody function in bandpass 1.8 to 4.7  $\mu\text{m}$  defined by cold filter

$\epsilon_F$  = emissivity of surface =  $(1 - \rho)$

$\Omega_d$  = solid angle of cold stop viewed by detector = 1.52 sr

$T_{CF}$  = transmittance of cold filter = 0.85

$$Q_{BG} = \left[ (1 - \rho_{SM})B(T)\rho_{SEC}\rho_P T_F T_R T_W + (1 - \rho_P)B(T)_F \rho_{SEC} T_F T_R T_W + (1 - \rho_{SEC})B(T)_F T_F T_R T_W + \epsilon_F B(T)_{CF} T_R T_W + \epsilon_R B(T)_{CF} T_W + \epsilon_W B(T)_{CF} \right] \Omega_d T_{CF}$$

For this simple analysis, we shall let:

1)  $\rho_{SM} = \rho_P = \rho_{SEC} = 0.94$

2) All optical elements are at temperature T

Then, the photon flux from the telescope is:

$$Q_{BG} = \left[ B(T)_F T_F T_R T_W (1 - \rho^3) + \epsilon_F B(T)_{CF} T_R T_W + \epsilon_R B(T)_{CF} T_W + \epsilon_W B(T)_{CF} \right] \Omega_d$$

The photon flux from the scene is given by:

$$Q_S = B(T)_s A_o \Omega_o \rho^3 T_F T_R T_W T_{CF}$$

but is negligible compared to  $Q_{BG}$ .

Total photon flux falling on the detector is:

$$Q_T = Q_{BG} + Q_S$$

Total noise current is:

$$I_{NS} = (I_{NSD}^2 + I_{NRF}^2 + I_{NRD}^2)^{\frac{1}{2}}$$

Shot noise current is given by:

$$I_{NSD} = (2\eta e^2 Q_T A_d)^{\frac{1}{2}} \quad (\text{see Table 3-17})$$

- where:  $\eta$  = quantum efficiency  $\approx 0.6$   
 $e$  = electronic charge =  $1.6 \times 10^{-19}$   
 $Q_T$  = see Table 3-17  
 $A_d$  =  $2.32 \times 10^{-4} \text{ cm}^2$

Table 3-17. Background Photon Flux for InSb Channels

	BAND					
	11	11a	11b	11c	11d	12
$\nu_c$ (cm <sup>-1</sup> )	2360	2275	2242.5	2212	2190	2700
$\Delta\nu$ (cm <sup>-1</sup> )	50	35	23	23	440	440
$\lambda_c$ (μm)	4.24	4.39	4.46	4.52	4.57	3.70
$\Delta\lambda$ (cm x 10 <sup>-4</sup> )	0.089	0.067	0.046	0.047	0.048	0.607
$B(T)_F$ ( $\Delta\lambda$ ) (photons cm <sup>-2</sup> sec <sup>-1</sup> sr <sup>-1</sup> )						
(x 10 <sup>14</sup> ) AT 263°K	0.397	0.405	0.322	0.360	0.397	0.715
(x 10 <sup>14</sup> ) AT 273°K	0.597	0.632	0.467	0.546	0.592	1.150
(x 10 <sup>14</sup> ) AT 310°K	2.86	2.69	2.05	2.32	2.52	6.75
$B(T)_{CF}$ (1.8 x 4.71) μm (photons cm <sup>-2</sup> sec <sup>-1</sup> sr <sup>-1</sup> )						
(x 10 <sup>14</sup> ) AT 263°K	4.78	4.78	4.78	4.78	4.78	4.78
(x 10 <sup>15</sup> ) AT 273°K	7.79	7.79	7.79	7.79	7.79	7.79
(x 10 <sup>15</sup> ) AT 310°K	3.58	3.58	3.58	3.58	3.58	3.58
$Q_{BG}$ (photons cm <sup>-2</sup> sec <sup>-1</sup> )						
(x 10 <sup>14</sup> ) AT 263°K	5.1	5.1	5.1	5.1	5.1	5.1
(x 10 <sup>14</sup> ) AT 273°K	7.36	7.36	7.36	7.36	7.36	7.36
(x 10 <sup>15</sup> ) AT 310°K	2.77	2.77	2.77	2.77	2.77	2.77
$I_{NSD}$ (amps Hz <sup>-1/2</sup> )						
(x10 <sup>-14</sup> ) AT 263°K	6.05	6.05	6.05	6.05	6.05	6.05
(x10 <sup>-14</sup> ) AT 273°K	7.24	7.24	7.24	7.24	7.24	7.24
(x10 <sup>-13</sup> ) AT 310°K	1.4	1.4	1.4	1.4	1.4	1.4
$D^{\#}$ (cm Hz <sup>1/2</sup> watt <sup>-1</sup> )						
(x 10 <sup>11</sup> ) AT 263°K	4.7	5.3	5.4	5.44	5.5	4.4
(x 10 <sup>11</sup> ) AT 273°K	4.24	4.4	4.5	4.5	4.5	3.7
(x 10 <sup>11</sup> ) AT 310°K	2.2	2.3	2.3	2.3	2.4	1.9
$I_{NS}$ (amps Hz <sup>-1/2</sup> )						
(x10 <sup>-14</sup> ) AT 263°K	6.1	6.1	6.1	6.1	6.1	6.1
(x10 <sup>-14</sup> ) AT 273°K	7.3	7.3	7.3	7.3	7.3	7.3
(x10 <sup>-13</sup> ) AT 310°K	1.4	1.4	1.4	1.4	1.4	1.4

The Johnson noise in the load resistor is:

$$I_{NRF} = \left( \frac{4KT}{R_f} \right)^{\frac{1}{2}} = 7.43 \times 10^{-16} \text{ amps}/\sqrt{\text{Hz}} \text{ for } R_f = 9 \times 10^9 \Omega, T = 90^\circ\text{K}$$

where, for bias voltages of -0.025 volts or less, the noise will be flat above 25 Hz.

Detector Johnson noise at 0-volt bias:

$$I_{NRD} = \left( \frac{4KTA_{dj}}{R \times A} \right)^{\frac{1}{2}} = 1 \times 10^{-14} \text{ amp}/\text{Hz}^{\frac{1}{2}}$$

where:  $A_{dj}$  = detector junction area =  $2 \times 10^{-4} \text{ cm}^2$   
 $R \times A$  = resistance area product =  $10^4 \Omega\text{-cm}^2$   
 $T = 90^\circ\text{K}$

$$D^* = \frac{e A_d^{\frac{1}{2}} \lambda}{hc \eta I_{NS}}$$

where:  $\eta$  = quantum efficiency = 0.6  
 $e$  = electronic charge =  $1.6 \times 10^{-19}$   
 $A_d = 2.32 \times 10^{-4} \text{ cm}^2$   
           = see Table 3-17  
 $hc = 2 \times 10^{-23}$

Table 3-17 summarizes the values of detector  $D^*$  anticipated for the AASIR InSb channels.

The  $D^*$  values shown are a function of instrument temperature as shown in Figure 3-50. A value of  $2.86 \times 10^{10} \text{ cm-Hz}^{\frac{1}{2}} \text{ watt}^{-1}$  used in previous system NEN calculations is not achieved above an instrument temperature of about  $26^\circ\text{C}$ .

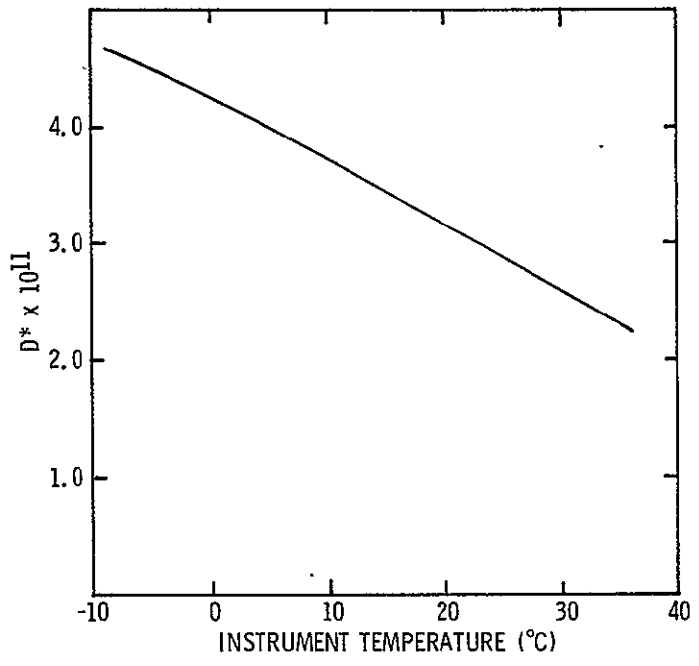


Figure 3-50. InSb  $D^*$  versus Instrument Temperature

**AASIR COMMANDS AND TELEMETRY MONITORS**

The following is a tentative listing of AASIR commands and digital and analog telemetry monitors.

Command List

1. Scan Mirror Stow, LATCH
2. Scan Mirror Stow, UNLATCH
3. Radiative Cooler Heater No. 1, ON
4. Radiative Cooler Heater No. 2, ON
5. All Heaters, OFF
6. Primary Power Supply, ON
7. Redundant Power Supply, ON
8. Power Supplies, OFF
9. Detector Temperature Control Heater, ON
10. IR Sounding Channels Gain, STEP
11. IR Imaging Channels Gain, STEP
12. Visible Channels Gain, STEP
13. Visible Channel Focus, FORWARD
14. Blackbody Heater, ON, STEP 1
15. Blackbody Heater, ON, STEP 2
16. Blackbody Heater, OFF
17. Electronic Calibration Waveform, ENABLE
18. Electronic Calibration Waveform, INHIBIT
19. Scan Drive Primary, ON
20. Scan Drive Redundant, ON
21. Scan Drive, OFF
22. VIS and IR Imaging Step Scan, ON
23. VIS and IR Imaging Step Scan, OFF
24. Processor, ON
25. Processor, OFF
26. Filter Wheel, FORWARD STEP
27. Filter Wheel, REVERSE STEP

28. Filter Wheel Heater, ON
29. Filter Wheel Heater, OFF
30. Frame Size Increase, STEP
31. Frame Size Decrease, STEP
32. Frame Center Up, STEP
33. Frame Center Down, STEP
34. Detector Temperature Control Heater, OFF

AASIR Digital Telemetry Monitors

1. Primary Power Supply, ON/OFF
2. Redundant Power Supply, ON/OFF
3. Radiative Cooler Heater No. 1, ON/OFF
4. Radiative Cooler Heater No. 2, ON/OFF
5. Detector Temperature Control Heater, ON/OFF
6. IR Channels Gain, LINE 1 (MSB)
7. IR Sounding Channels Gain, LINE 2 (LSB)
8. IR Imaging Channels Gain, LINE 1 (MSB)
9. IR Imaging Channels Gain, LINE 2 (LSB)
10. Visible Channels Gain, LINE 1 (MSB)
11. Visible Channels Gain, LINE 2 (LSB)
12. Blackbody Heater Step 1, ON/OFF
13. Blackbody Heater Step 2, ON/OFF
14. Visible Channel Focus, FORWARD/OFF
15. Visible Channel Focus, REVERSE/OFF
16. Infrared Channel Focus, FORWARD/OFF
17. Infrared Channel Focus, REVERSE/OFF
18. Mirror Stow Command, ON/OFF
19. Scan Mirror Stow Position, UNLATCH/LATCH
20. Scan Drive, PRIMARY/REDUNDANT
21. Scan Drive, ON/OFF
22. VIS and IR Step Scan, ON/OFF
23. Processor, ON/OFF
24. Filter Wheel, FWD/REV

25. Filter Wheel Position, BIT 1
26. Filter Wheel Position, BIT 2
27. Filter Wheel Position, BIT 3
28. Filter Wheel Heater, ON/OFF
29. Frame Size, BIT 1 (MSB)
30. Frame Size, BIT 2 (LSB)
31. Frame Center, BIT 1 (MSB)
32. Frame Center, BIT 2
33. Frame Center, BIT 3
34. Frame Center, BIT 4
35. Frame Center, BIT 5
36. Frame Center, BIT 6
37. Frame Center, BIT 7

#### Analog Telemetry Monitors

1. +15V Signal Power Supply
- \*2. +15V Auxiliary (TM Reference) Power Supply
3. +5V Motor Power Supply
4. +5V Auxiliary Power Supply
- \*5. Primary Mirror Temperature
- \*6. Secondary Mirror Temperature
- \*7. Primary Encoder Temperature
- \*8. Redundant Encoder Temperature
- \*9. Blackbody Temperature No. 1
- \*10. Blackbody Temperature No. 2
- \*11. Radiative Cooler Stage No. 1 Temperature
- \*12. Radiative Cooler Stage No. 2 Temperature
- \*13. Electronics Module Temperature
- \*14. Infrared Detector Temperature Control Voltage
- \*15. Scan Mirror Temperature

---

\*Telemetry signals shall be available when the AASIR is OFF and the satellite  $\pm 15$  vdc secondary power is ON.

- \*16. Baffle Tube Forward End Temperature
- \*17. Baffle Tube Aft End Temperature
- \*18. Shutter Cavity Temperature
- 19. Infrared Channel Focus Drive Position
- 20. Visible Channel Focus Drive Position
- 21. 29V DC Current Level
- 22. Primary Scan Drive Torque
- 23. Redundant Scan Drive Torque
- \*24. Radiative Cooler Earth Shield Temperature
- \*25. Radiative Cooler Ambient Stage Temperature
- \*26. Primary Mirror Aperture Stop Temperature
- \*27. Secondary Mirror Shield Temperature
- \*28. Filter Wheel Heater Temperature No. 1
- \*29. Filter Wheel Heater Temperature No. 2

---

\*Telemetry signals shall be available when the AASIR is OFF and the satellite  $\pm 15$  vdc secondary power is ON.

Section 4  
OPTICAL DESIGN

INTRODUCTION

This section of the AASIR Final Report treats the optical design of the AASIR primary optics, step-scan mechanism and IR relay. Computer ray tracing techniques were used to determine geometric image blur. Effects of diffraction, fabrication tolerances and environmental degradation are not included, but it is clear that these effects are dominant and that geometric image blur causes little degradation to the system MTF.

Of particular importance in the design of the step-scan mechanism was elimination of scan distortion, i. e. , tilting or bending of scan lines, rotation of the image and defocussing as a function of scan or field angle. The design must also minimize scan modulation by careful attention to the exit pupil location.

DESIGN CONSTRAINTS

Since it is practical to use only a single radiative cooler and a single optical path into the cooler, to minimize heat load both IR imaging and IR sounding detectors were located on a common detector substrate. Although the sounding channels and IR scanning channels enter the cooler together, they must at some point in the optical path be separated so that step scanning of the IR imaging channels can be imposed. Another constraint involves the visible imaging channels which use detectors separate from the cooler, but for simplicity and economy are scanned by the same step-scan mechanism used for the IR imaging channels.

## COMPONENT OPTICAL DESIGN

Three essential parts must be designed. The primary optics, the scanning optics, and the IR relay optics. These sections will be discussed separately; however, the design of the scanning optics is accomplished with the primary optics included, and the design of the relay is accomplished with the primary optics included.

## RAY TRACING TECHNIQUE

Evaluation of the optical performance has been accomplished by ray tracing using the Accos V Design Program. Spot diagrams of 100 rays have been generated for each field angle. The spot diagram is examined to find the plane of best focus and the radial energy distribution is printed for the plane of best focus. The plane of best focus is determined by the computer to be the plane with minimum diameter blur circle. For curves showing the blur circle as a function of field angle, each blur diameter is based on its own plane of best focus.

If an attempt is made to correlate the lens prescription information with the optical layouts, it is apparent that there is a coordinate difference. The y and z axes both have a sign reversal.

The x-y coordinates of the centroid of energy for the spot diagram are used in determining the scan linearity and the scan straightness.

The fields of view, if projected on the ground would have a relationship as shown in Figure 4-1. The dimensional values shown are applicable to the spacing if all the field stops existed at the telescope focal plane.

Note that the telescope optical axis is coincident with the center of the scanned field of the visible band detectors. Figure 4-1 shows that the visible field is contained within 2.1 mrad, the IR scanning channels within 5.35 mrad and the IR sounding channels with 7.06 mrad. Ray tracing for the optical system must demonstrate that the image blur as a function of field angle is consistent with the IFOV.

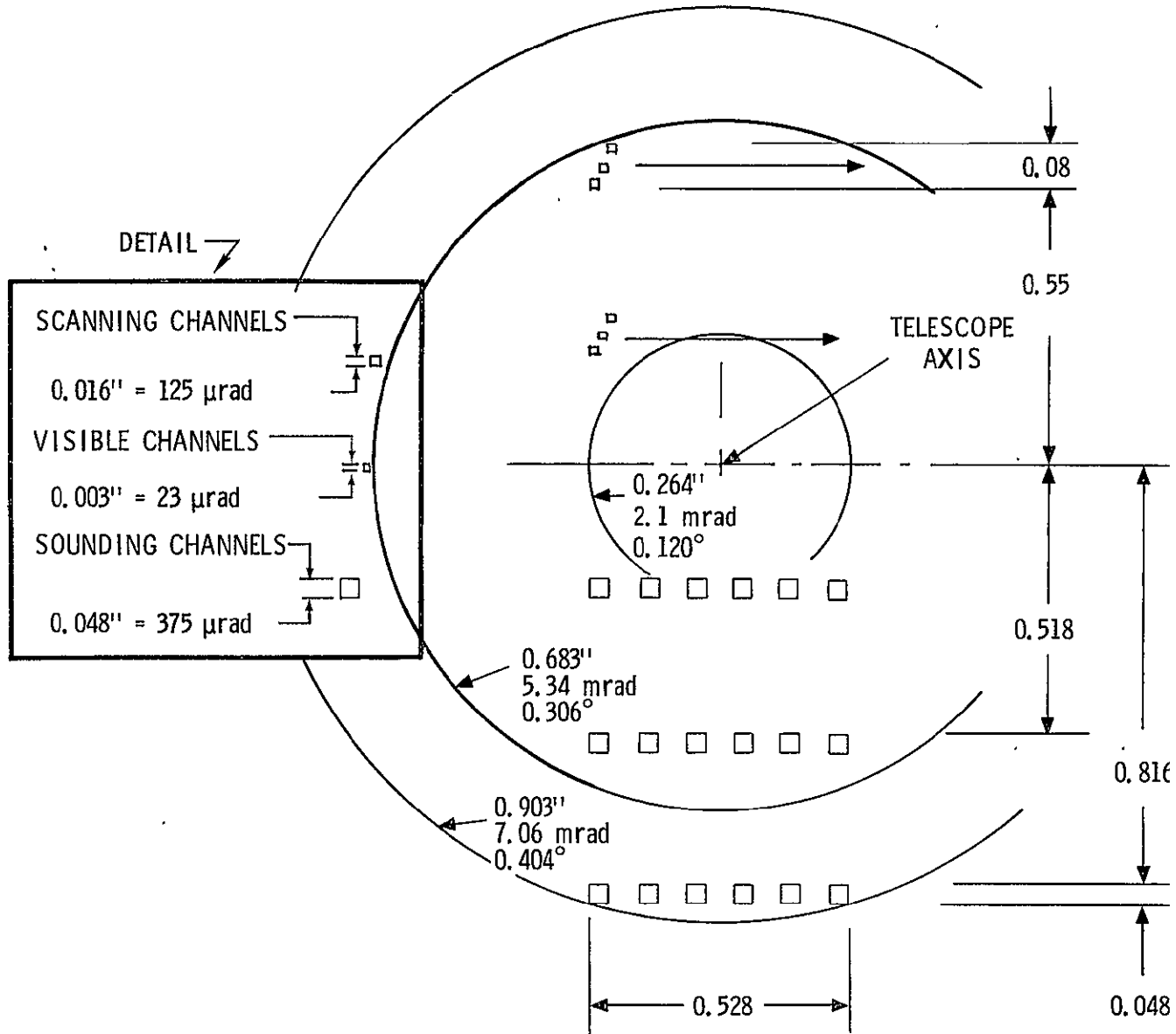


Figure 4-1. AASIR Fields of View as Projected into Object Space (Dimensions refer to Telescope Focal Plane)

RITCHEY CHRETIEN TELESCOPE DESIGN

The primary optics are a Ritchey Chretien configuration, similar to that used in the VISSR instruments. The design of the telescope presents no great mystery, but data are included here as an aid in building the entire optical design.

The computer data shown below in Table 4-1 gives the design parameters of the primary telescope. The computer printout is self explanatory.

Table 4-1. AASIR Primary Optics - Basic Lens Data

SURF	RD	TH	MEDIUM	RM	DF
0	0.0	0.100000D+11	AIR		
1	0.0	0.0	AIR		
2	-64.000000	-24.400000	PEFL		
3	-20.266000	30.396700	REFL		
4	0.0	0.0	AIR		
5	0.0	0.0	AIR		

CC AND ASPHERIC DATA

SURF	CC	AD	AE	AF	AG
2	-1.03900D+00				
3	-3.16600D+00				

REF OBJ HT	REF AP HT	OBJ SURF	REF SURF	IMG SURF	
-0.418881D+08 (	8.00000	0	1	5	
	0.24 DS)				
EFL	BF	F/NBR	LENGTH	GIH	
128.0126	0.0	8.00	30.3967	0.5361	
WAVL NBR	1	2	3	4	5
WAVELENGTH	0.58756	0.48613	0.65627	0.43584	0.70652
SPECTRAL WT	1.0000	1.0000	1.0000	1.0000	1.0000

APERTURE STOP AT SURF 2

LENS UNITS ARE INCHES

Figure 4-2 shows the image blur of the Ritchey Chretien telescope as a function of field angle. Two curves drawn show the diameter of a circle containing 100% of the energy and the diameter containing 90% of the energy. Note from Figure 4-1 that the visible channel detectors of 23- $\mu$ rad angular subtense are within  $0.12^\circ$  of the optical axis. Hence a 1.0  $\mu$ rad blur is expected, a blur very small in comparison to the detector size. The scanning channels subtending 125  $\mu$ rad are all within a field of  $0.306^\circ$ . The sounding channels subtending 375  $\mu$ rad are within a  $0.404^\circ$  field. Clearly, in each case the telescope geometrical blur circle is extremely small in comparison to IFOV size.

#### IR DELAY DESIGN

Energy used for sounding is collected by the Ritchey Chretien telescope, passed through the prime focal plane where filtering occurs, and relayed to the cooled detectors by a three-element infrared relay. The relay optics include germanium condenser lenses.

Suitable image quality is achieved only with an aspheric surface in the condenser optics. An initial design used aspheric surfaces on the convex surfaces of both the condenser elements. More recently the design was modified to put the aspheric shape on the concave side of each surface. The present configuration uses an aspheric surface only on the concave side of the first condenser element.

The image quality shown in Figure 4-3 is for the sounding channels as they are brought to focus at the IR image plane within the radiative cooler. One curve indicates the diameter of a circle containing 100% of the energy, while the second curve shows the diameter containing 90% of the energy. The extreme rays through the sounding channels would be at  $0.1^\circ$  and  $0.404^\circ$  off-axis. The data here represent the image for the combination of the telescope and the relay optics.

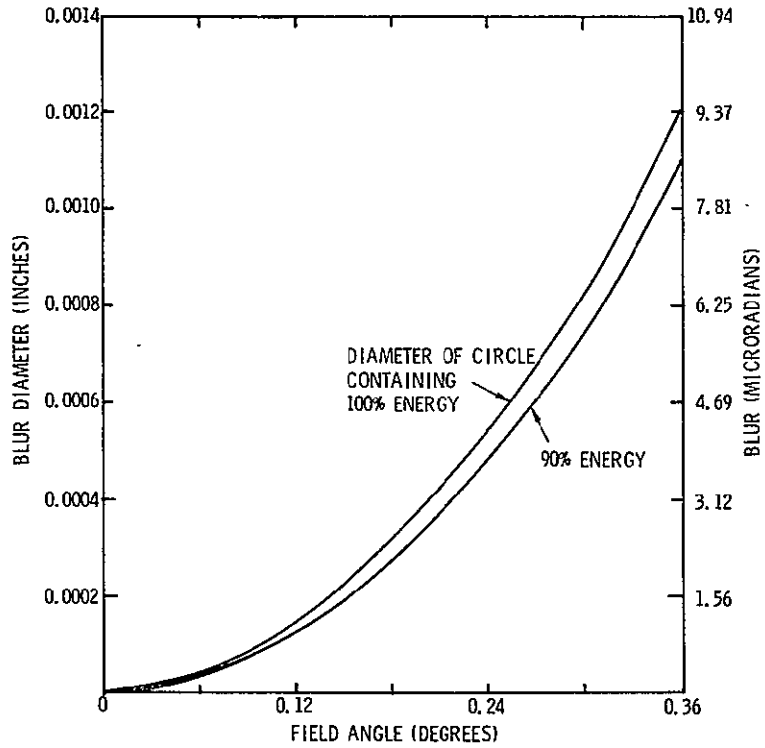


Figure 4-2. Ritchey Chretien Telescope Image Quality as Related to Field Size

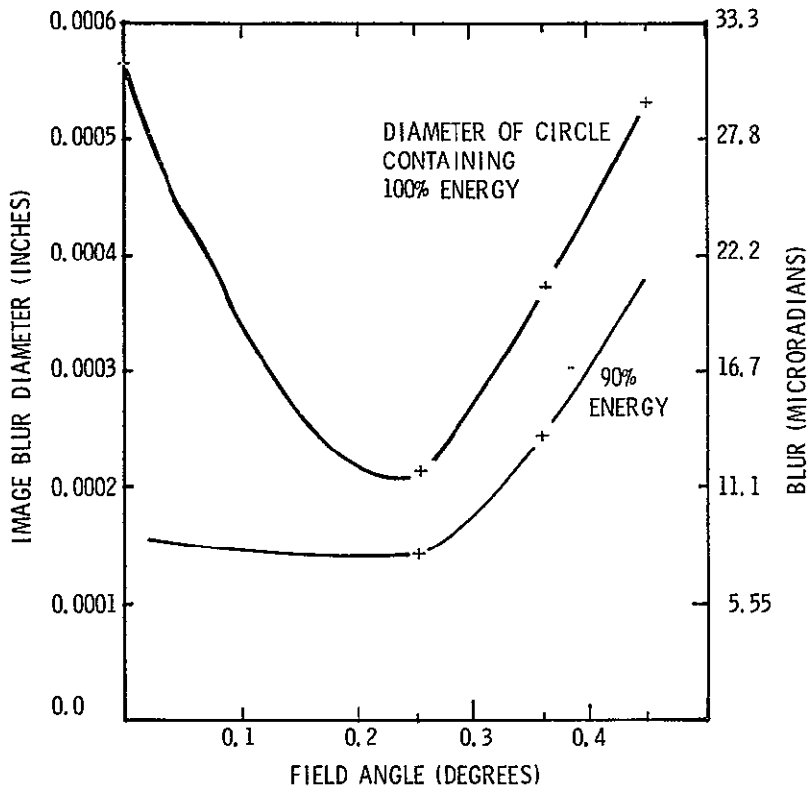


Figure 4-3. AASIR Image Quality for Sounding Channels

Figure 4-4 shows the variation of focus with field angle for rays used in the sounding channels. The sounding channels use fields that range from  $0.1^\circ$  to  $0.4^\circ$  off-axis. Thus, it may be seen that the extreme focus variation is about 0.0015 inch across the field. A flat focal plane positioned midway between these extremes will see a defocus of  $\pm 0.00075$ . This defocus on a 0.006-inch detector will not cause a significant MTF change.

The computer printout of the lens prescription is shown as Table 4-2.

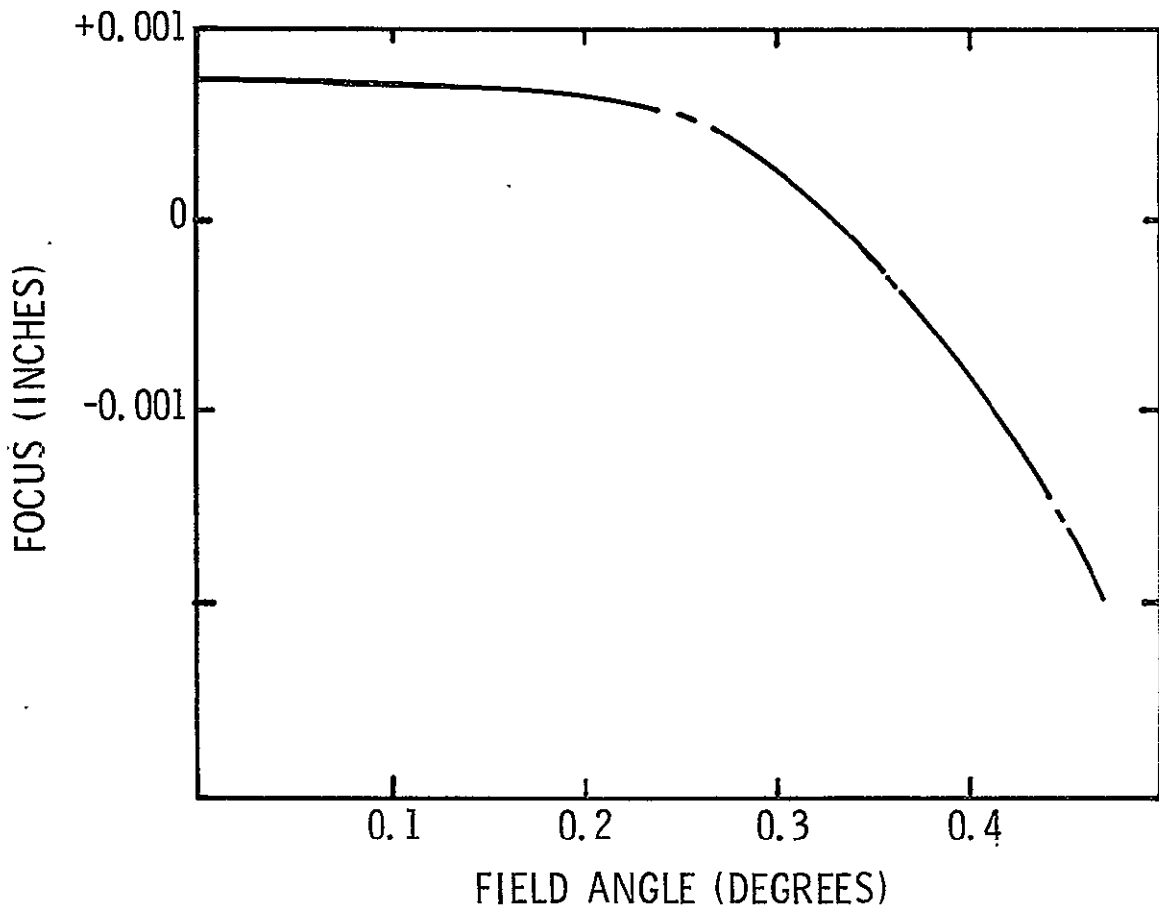


Figure 4-4. Sounding Channels - Variation in Focus with Field Angle

Table 4-2. AASIR with 1 Aspheric Relay F/1.13 -  
Basic Lens Data

SURF	PD	TH	MEDIUM	PM	DF	
0	0.0	0.900000D+11	AIR			
1	-64.000000	-24.400000	PEFL			
2	-20.266000	30.403000	PEFL			
3	0.0	1.000000	AIR			
4	6.666666	0.150000	MATL	GERM	4.002271	0.904
5	10.000000	7.200000	AIR			
6	2.507367	0.150000	MATL	GERM	4.002271	0.904
7	3.439986	1.350000	AIR			
8	1.183428	0.150000	MATL	GERM	4.002271	0.904
9	1.970497	0.060000	AIR			
10	0.0	0.040000	MATL	GERM	4.002271	0.904
11	0.0	0.500000	AIR			
12	0.0	0.0	AIR			

REFRACTIVE INDICES

SURF	N1	N2	N3	N4	N5
4	4.002271	4.002748	4.001945	4.019524	1.000000
6	4.002271	4.002748	4.001945	4.019524	1.000000
8	4.002271	4.002748	4.001945	4.019524	1.000000
10	4.002271	4.002748	4.001945	4.019524	1.000000

CC AND ASPHERIC DATA

SURF	CC	AD	AE	AF	AG
1	-1.03900D+00				
2	-3.16600D+00				
7	0.0	1.34374D-02	6.12886D-03	0.0	0.0

TILT AND DEC DATA

SURF	TYPE	TD	XD	ALPHA	BETA	GAMMA
4	DEC	0.44000	-0.30000			
REF OBJ HT		REF AP HT	OBJ SURF	REF SURF	IMG SURF	
-0.563923D+09	0.36 DG	8.00000	0	1	12	
EFL	BF	F NBP	LENGTH	GIH		
-18.0081	0.5000	-1.13	40.5030	-0.1129		
WAVL NBP	1	2	3	4	5	
WAVELENGTH	11.50000	10.50000	12.50000	4.50000	15.00000	
SPECTRAL WT	1.0000	1.0000	1.0000	1.0000	1.0000	

NO APERTURE STOP

LENS UNITS ARE INCHES

## STEP-SCAN MECHANISM DESIGN

Numerous configurations for the scan mechanism have been explored. In most, it was found that the scanning action created a field motion that was not orthogonal to the detector array. The design study selected the configuration as shown in Figure 4-5 which provides excellent orthogonal motion, reasonably linear scan, and creates a flat image field.

The optical path for the IR imaging channels shown in Figure 4-6a folds energy out of its original path, collimates and then scans the energy. Refocusing is accomplished in a manner to displace the beam only slightly from its initial path. The IR energy is then folded back into the beam ahead of the IR relay. The location of the scanned channels on the detector plane is displaced from the apparent position projected into object space such that the actual detector array (including sounding detectors) is more compact than the object space array. That is, the InSb imaging detectors are grouped with the InSb sounding detectors and the HgCdTe imaging detectors are similarly grouped with the HgCdTe sounding detectors. This arrangement facilitates fabrication of the detector array and reduces radiative losses through the cooler window since the array area is reduced.

Figure 4-6b illustrates the optical path taken by the visible channels. The optical beam passes over the top of the filter wheel and through the top portion of the zinc selenide lens. The beam is then folded out and into the step scanner where it is scanned with the IR imaging channels. The visible channels are then directed to a detector package out of the IR beam.

Note, particularly the IR and visible field lens in Figure 4-5 which is used to help image the entrance aperture on the scanning mirror. By careful selection of material it appears possible to use a single piece of zinc selenide to cover the entire spectral range from the visible to 11- $\mu$ m. Antireflection coatings will be applied in bands to optimize transmittance for the three spectral regions.

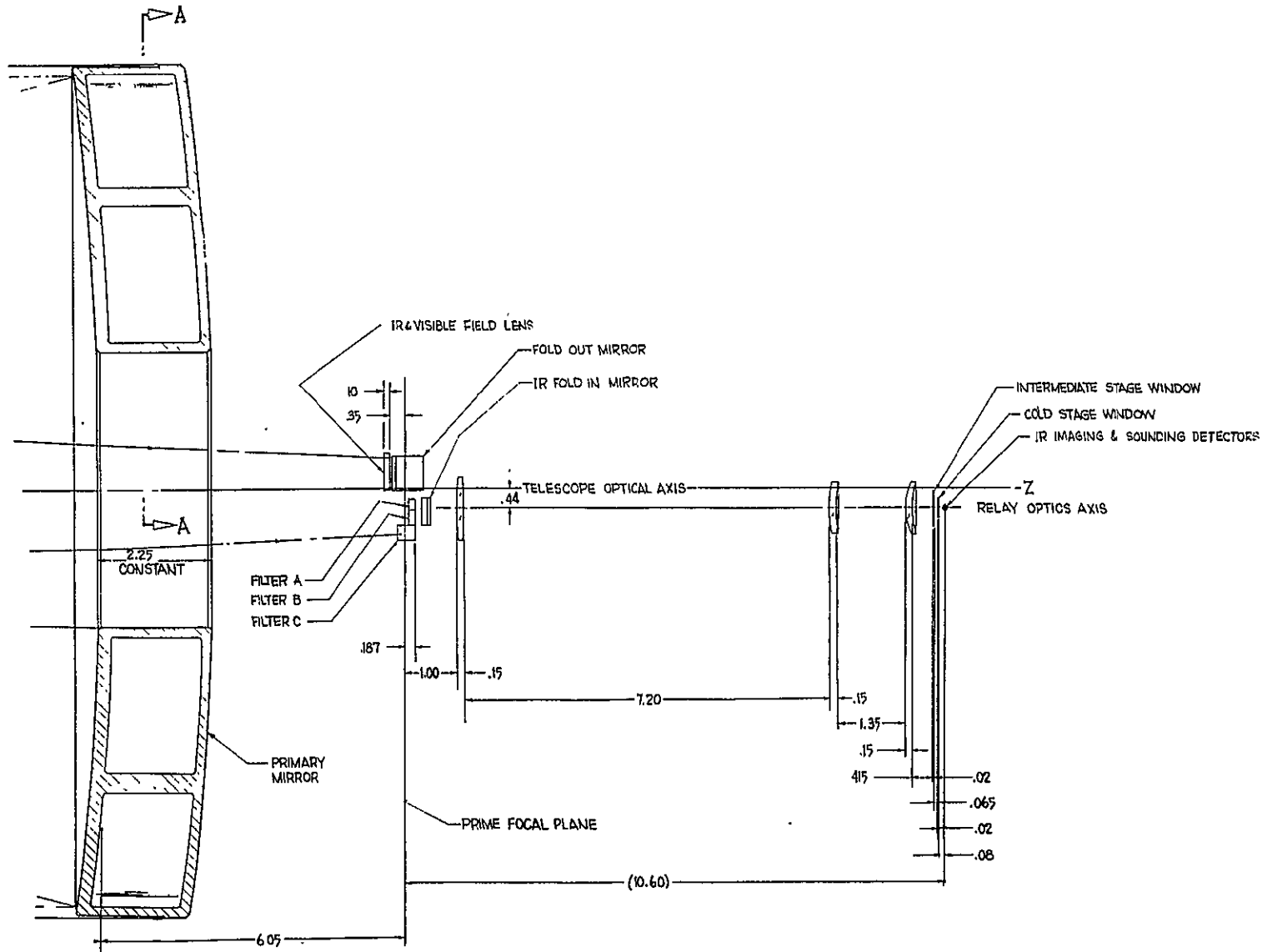


Figure 4-5. AASIR Optical Schematic

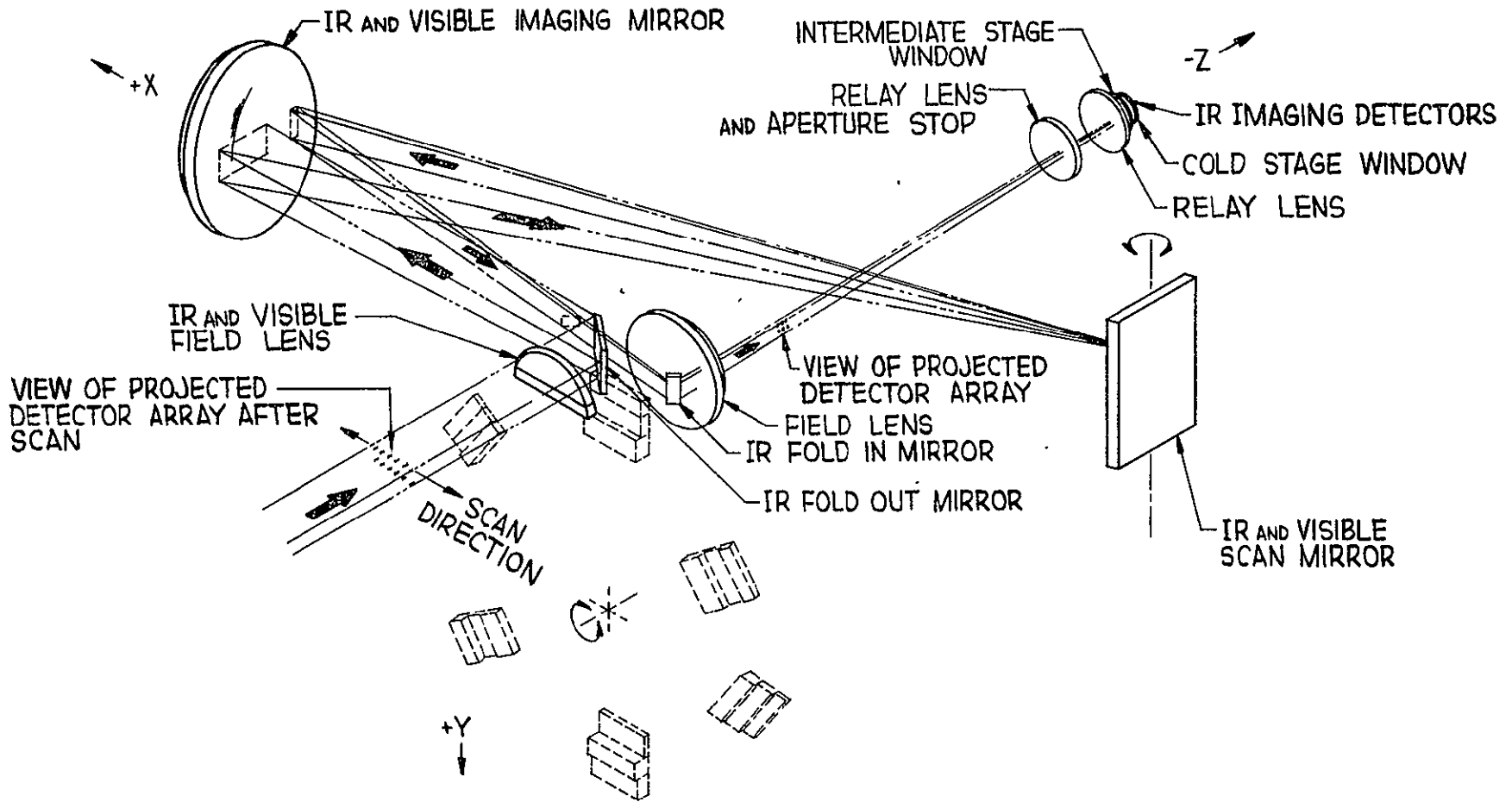


Figure 4-6a. IR Imaging Path

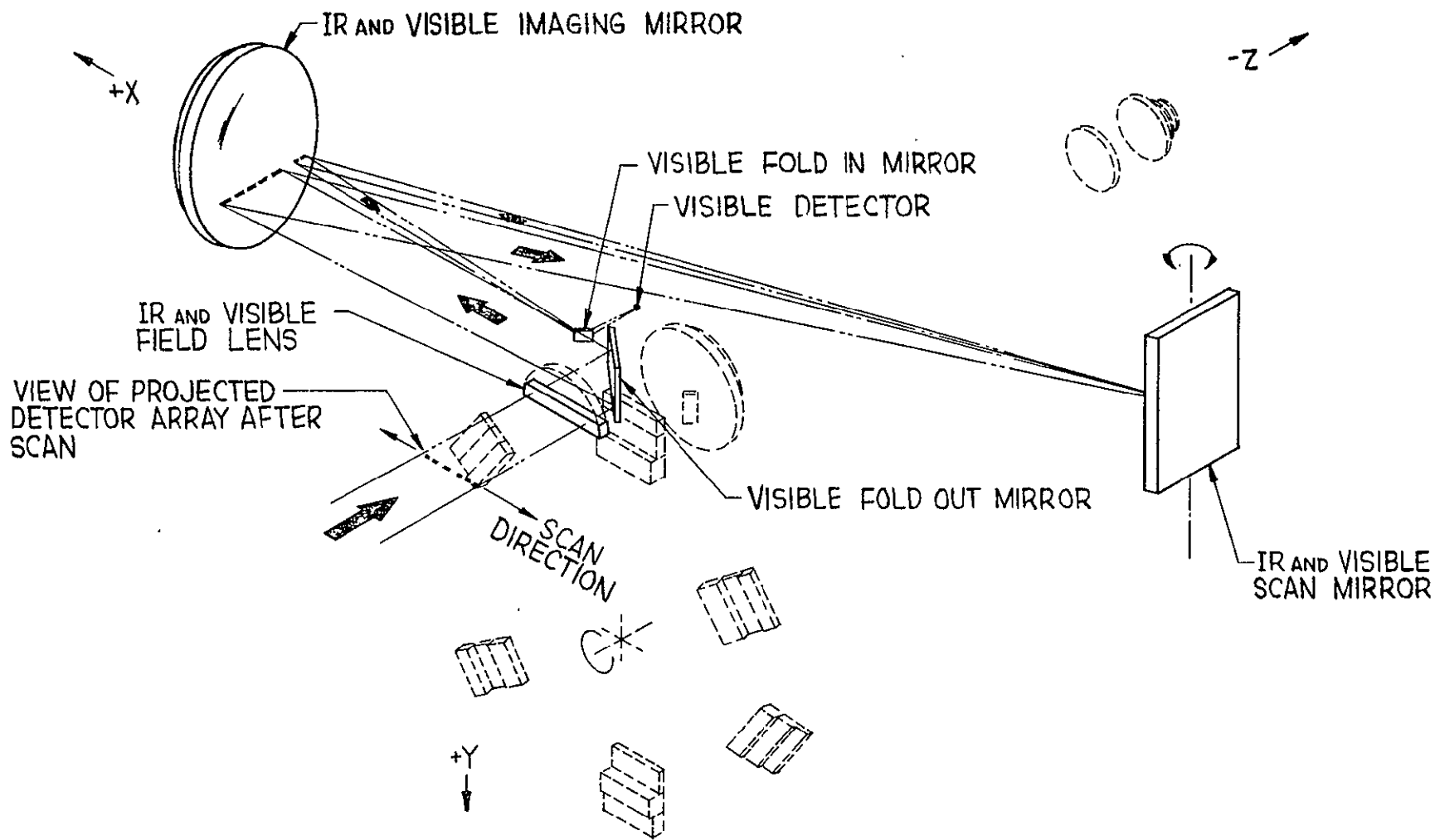


Figure 4-6b. Visible Imaging Path

The scan mechanism was initially evaluated by using a finite object distance and running light rays backward through the optics. In this fashion it is possible to make equal increment changes in the angle of the internal scan mirror and observe the position of the rays at the other end of the scan mechanism. Table 4-3 is a computer printout of the elements used for this evaluation.

In Figure 4-7 it is shown that the variation in ray height is small throughout the scan. For rays near the optical axis, there is a height change of about 0.0007 inch through the scan, and near the field edge (0.627 inch off-axis) the height change is about 0.0003. In terms of the effect on the system performance it means that the separation between the sounding channels and the scanning channels will change by 5  $\mu$ rad during a scan, or about 20% of a visible channel field of view.

Figure 4-8 shows the departure from linearity of scan in the scan direction. It shows that the image displacement is almost exactly proportional to angular mirror rotation and that no compensating mechanisms are required to achieve a rectilinear scan geometry.

Figure 4-9 shows the focus shift of the telescope and of the scan optics as a function of field angle. Note that the curved field of the Ritchey Chretien telescope is nicely balanced against the curved field of the scan optics for a net flat field.

The absolute value of focal position is mostly the result of an arbitrary choice of spacing in the design. However, the variation in focus must be kept small. The surface of best focus is curved for a Ritchey Chretien telescope. However, after passing through the scan optics, the surface is very flat. Table 4-4 is a printout of the surface data for the telescope and the scan mechanism.

Table 4-3. AASIR Internal Scan Reversed -- Basic Lens Data

SURF	RD	TH	MEDIUM	RN	DF
0	0.0	37.575000	AIR		
1	0.0	-37.555000	AIR		
2	0.0	-3.578740	AIR		
3	6.595260	3.578740	REFL		
4	0.0	15.901740	AIR		
5	-16.000000	0.0	REFL		
6	0.0	-16.000000	AIR		
7	0.0	0.0	REFL		
8	0.0	16.000000	AIR		
9	-16.000000	0.0	PEFL		
10	0.0	-7.901740	AIR		
11	0.0	0.0	PEFL		
12	0.0	0.350000	AIR		
13	-14.232000	0.100000	GL1	2.401000	-0.514
14	0.0	-0.450000	AIR		
15	0.0	0.0	AIR		

REFRACTIVE INDICES

SURF	N1	N2	N3	N4	N5
13	2.401000	2.407000	2.394000	2.437000	2.435000

CC AND ASPHERIC DATA

SURF	CC	AD	AE	AF	AG
3	-7.104800-01				
7	0.0	-6.000000-05	0.0	0.0	0.0

SPECIAL CONDITIONS

SURF	CONDITION
5	ASI
9	ASI
13	ASI

TILT AND DEC DATA

SURF	TYPE	TD	XD	ALPHA	BETA	GAMMA
2	TILT	0.0	8.000000	0.0	12.0239	0.0
4	RTILT	0.0	0.0	0.0	-77.9761	0.0
5	TILT	-1.25000	0.0	-8.9893	0.0	0.0
6	PTILT	0.0	0.0	0.0	0.0	0.0
7	PTILT	0.0	0.0	0.0	-1.6000	0.0
8	TILT	0.0	0.0	0.0	-1.6000	0.0
10	PTILT	-1.25000	0.0	-8.9893	0.0	0.0
11	TILT	0.0	0.0	0.0	-45.0000	0.0
12	RTILT	0.0	0.0	0.0	45.0000	0.0

PICKUPS

SURF	TYPE	J	A	B
8	BETA	7	1.0000	0.0
8	GAMMA	7	1.0000	0.0

PEF OBJ HT	PEF RP HT	OBJ SURF	PEF SURF	IMG SURF
0.6000000+00 (-0.91 DG)	2.34840	0	1	15

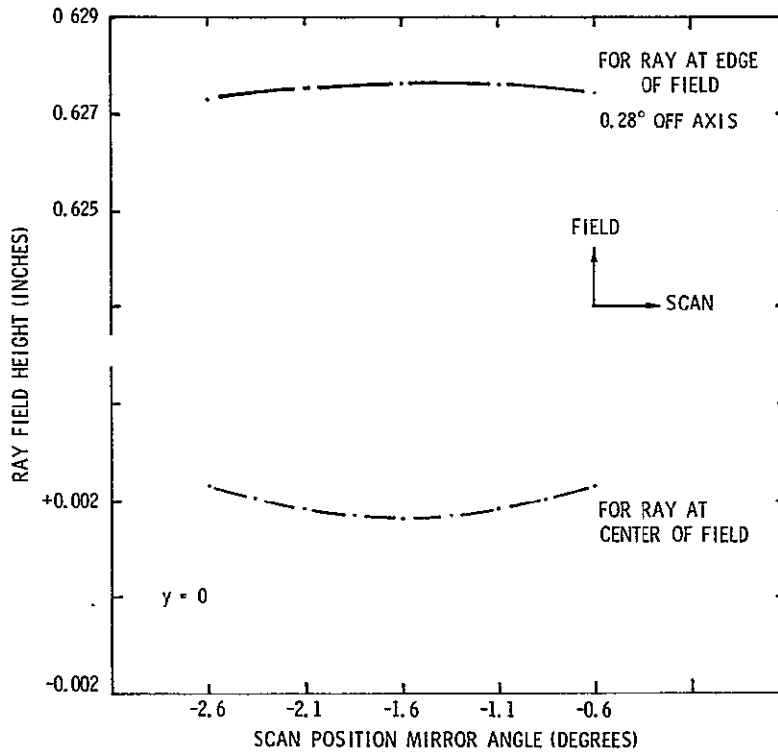


Figure 4-7. Scanned Ray Departure from a Straight Line Reverse Scan Configuration

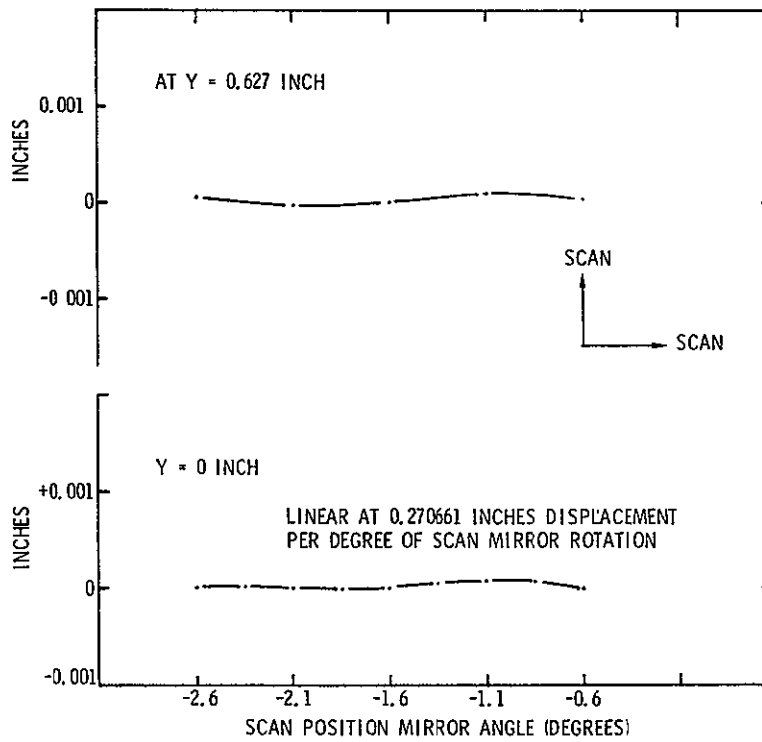


Figure 4-8. Scanned Field Departure from Linearity in Scan Direction

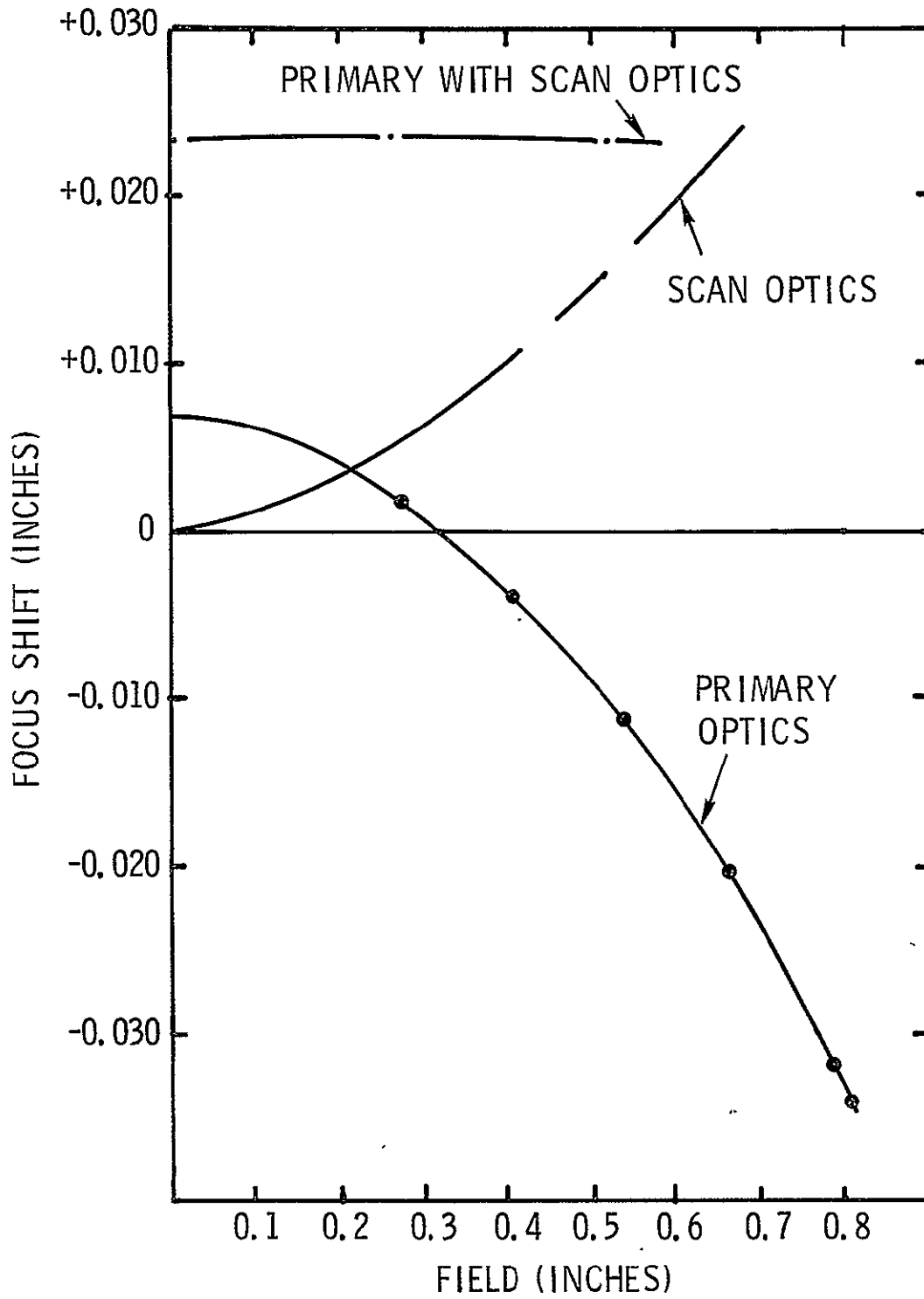


Figure 4-9. Focus Shift

Table 4-4. AASIR with Refractive in Scan - Basic Lens Data

SURF	RD	TH	MEDIUM	RN	DF
0	0.0	0.100000D+11	AIR		
1	0.0	0.0	AIR		
2	-64.000000	-24.400000	REFL		
3	-20.266000	30.000000	REFL		
4	0.0	0.100000	GL1	2.401000	-0.514
5	13.600000	0.350000		1.000000	-0.419
6	0.0	0.0	PEFL		
7	0.0	-7.301740	AIR		
8	16.000000	0.0	REFL		
9	0.0	16.000000	AIR		
10	0.0	0.0	REFL		
11	0.0	-16.000000	AIR		
12	16.000000	0.0	REFL		
13	0.0	15.301740	AIR		
14	0.0	3.573740	AIR		
15	-6.595260	-3.573740	REFL		
16	0.0	-37.555000	AIR		
17	0.0	37.575000	AIR		
18	0.0	0.0	AIR		

REFRACTIVE INDICES

SURF	N1	NE	N2	N4	N5
4	2.401000	2.407000	2.374000	2.437000	2.435000
5	1.000000	1.000000	1.000000	1.000000	1.000000

CC AND ASPHERIC DATA

SURF	CC	AD	AE	AF	AG
2	-1.03900D+00				
3	-3.16600D+00				
10	0.0	6.00000D-05	0.0	0.0	0.0
15	-7.10480D-01				

SPECIAL CONDITIONS

SURF	CONDITION
15	ASI

TILT AND DEC DATA

SURF	TYPE	TD	AD	ALPHA	BETA	GAMMA
6	TILT	0.0	0.0	0.0	45.0000	0.0
7	TILT	0.0	0.0	0.0	45.0000	0.0
8	TILT	-1.25000	0.0	8.3893	0.0	0.0
10	TILT	0.0	0.0	0.0	1.6000	0.0
11	TILT	0.0	0.0	0.0	-1.6000	0.0
13	RTILT	-1.25000	0.0	8.9893	0.0	0.0
14	TILT	0.0	0.0	0.0	-77.9761	0.0
16	RTILT	0.0	-8.00000	0.0	12.0239	0.0

PICKUPS

SURF	TYPE	J	A	B
11	BETA	10	-1.0000	0.0
11	GAMMA	10	1.0000	0.0

REF OBJ HT	REF SURF	HT	OBJ SURF	REF SURF	IMG SURF
-0.418881D+02	0	0.24 DG	3.00000	1	18

## SCANNED IR FIELDS

The optical properties of the entire system are shown in Table 4-5. Figure 4-10 shows the image quality for rays passing through the telescope, the scan mechanism, and the relay optics. Curves are plotted to show the diameter of the circle containing 100% of the energy and the diameter containing 90% of the energy. Data are included for the central scan position as well as both extremes.

From the data shown, it is clear that the image quality is unchanged through the scan. The scanned infrared channels use detectors of about 0.002 inch in the cooled focal plane. The field edge of  $0.3^\circ$  has a blur of 0.00054 inch with 90% of the energy in 0.00022 inch diameter.

Figure 4-11 shows the shift in focus with wavelength. This concludes that the focal difference in the long-wavelength channels is not significant, but the 4.5- $\mu\text{m}$  channels will require some fixed offset.

Figure 4-12 shows the focus shift of energy passing through the primary optics, the scan mechanism, and the relay optics. Data are shown for the center scan position as well as both ends of scan.\* The data show about a 0.0006-inch shift in the plane of best focus depending on field height but almost no shift in focus due to the scan. Thus, the imaging properties of the instrument should not contribute scan modulation.

---

\*The three curves representing different scan positions fall so closely on top of each other that they blend into one curve.

Table 4-5. AASIR with Scan and IR Relay -  
Basic Lens Data

SURF	PD	TH	MEDIUM	PH	DF	
0	0.0	0.100000D+11	AIR			
1	0.0	0.0	AIP			
2	-64.000000	-24.400000	PEFL			
3	-20.266000	30.000000	PEFL			
4	0.0	0.100000	GL1	2.401000	0.971	
5	13.600000	0.350000		1.000000	13.041	
6	0.0	0.0	PEFL			
7	0.0	-7.901740	AIP			
8	16.000000	0.0	REFL			
9	0.0	16.000000	AIP			
10	0.0	0.0	PEFL			
11	0.0	-16.000000	AIP			
12	16.000000	0.0	PEFL			
13	0.0	15.901740	AIP			
14	0.0	3.578740	AIP			
15	-6.585260	-3.578740	PEFL			
16	0.0	-37.555000	AIP			
17	0.0	38.655000	AIP			
18	6.666666	0.150000	MATL	GEPM	4.002271	0.904
19	10.000000	7.200000	AIP			
20	2.507367	0.150000	MATL	GEPM	4.002271	0.904
21	3.439986	1.350000	AIP			
22	1.183428	0.150000	MATL	GEPM	4.002271	0.904
23	1.970497	0.060000	AIP			
24	0.0	0.040000	MATL	GEPM	4.002271	0.904
25	0.0	0.500000	AIP			
26	0.0	0.0	AIP			

Table 4-5. AASIR with Scan and IR Relay -  
Basic Lens Data (Cont)

REFRACTIVE INDICES

SURF	N1	N2	N3	N4	N5
4	2.401000	2.407000	2.394000	2.437000	2.435000
5	1.000000	1.000000	1.000000	1.000000	1.000000
18	4.002271	4.002748	4.001945	4.019524	1.000000
20	4.002271	4.002748	4.001945	4.019524	1.000000
22	4.002271	4.002748	4.001945	4.019524	1.000000
24	4.002271	4.002748	4.001945	4.019524	1.000000

CC AND ASPHERIC DATA

SURF	CC	AD	AE	AF	AG
2	-1.03900D+00				
3	-3.16600D+00				
10	0.0	6.00000D-05	0.0	0.0	0.0
15	-7.10480D-01				
21	0.0	1.34374D-02	6.12886D-03	0.0	0.0
23	0.0	0.0	0.0	0.0	0.0

SPECIAL CONDITIONS

SURF	CONDITION
15	ACI
18	ACI
19	ACI
20	ACI
22	ACI

TILT AND DEC DATA

SURF	TYPE	YD	XD	ALPHA	BETA	GAMMA
6	TILT	0.0	0.0	0.0	45.0000	0.0
7	TILT	0.0	0.0	0.0	45.0000	0.0
8	TILT	-1.25000	0.0	8.9893	0.0	0.0
10	TILT	0.0	0.0	0.0	1.6000	0.0
11	TILT	0.0	0.0	0.0	-1.6000	0.0
13	PTILT	-1.25000	0.0	8.9893	0.0	0.0
14	TILT	0.0	0.0	0.0	-77.9761	0.0
16	PTILT	0.0	-8.00000	0.0	12.0239	0.0
18	DEC	-0.44000	-0.30000			

PICKUP:

SURF	TYPE	J	A	B
11	BETA	10	-1.0000	0.0
11	GAMMA	10	1.0000	0.0

REF OBJ HT	REF AP HT	OBJ SURF	REF SURF	IMG SURF
-0.418881D+08	8.00000	0	1	26

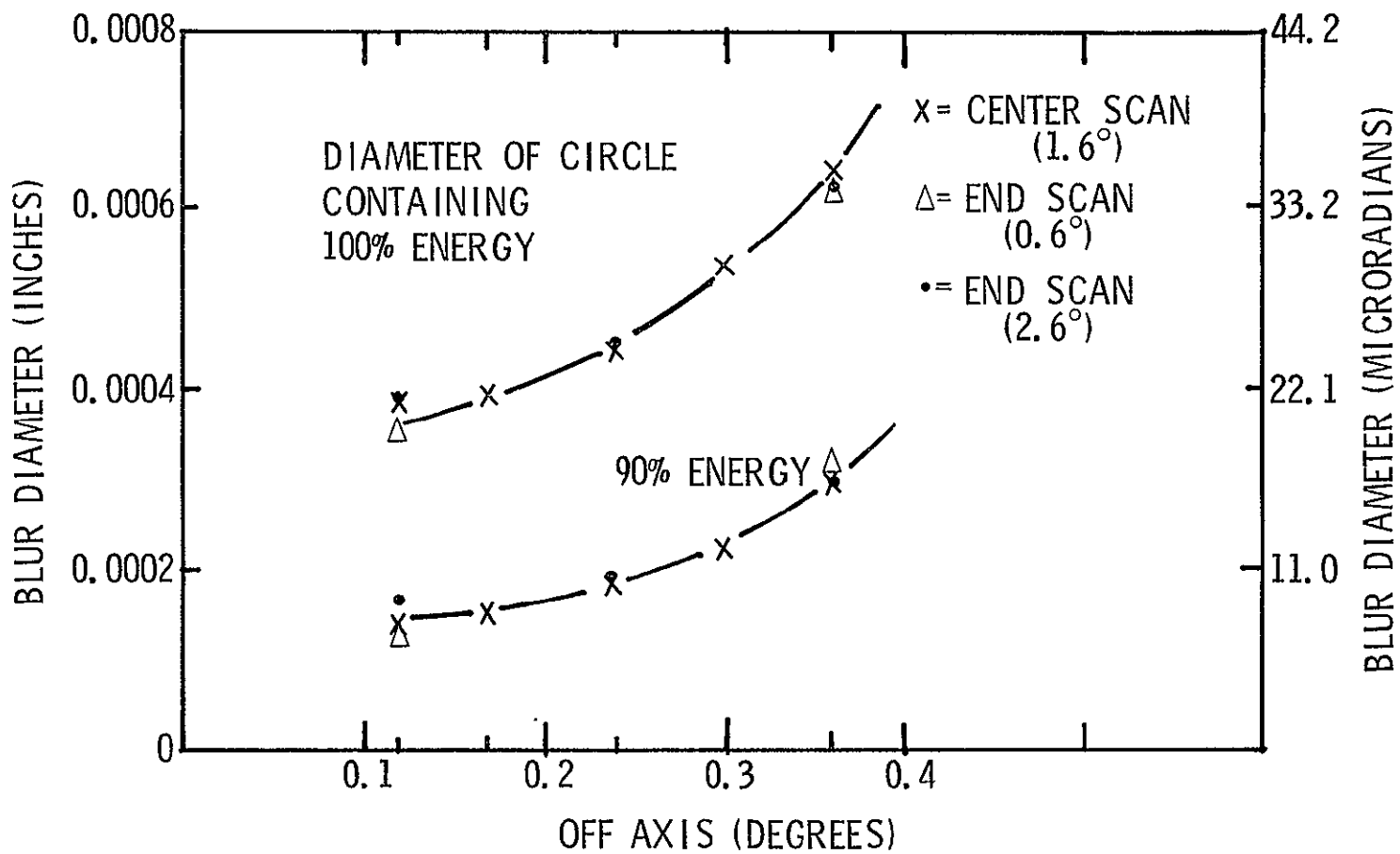


Figure 4-10. AASIR Image Quality Through Telescope, Scan Optics and Relay Optics

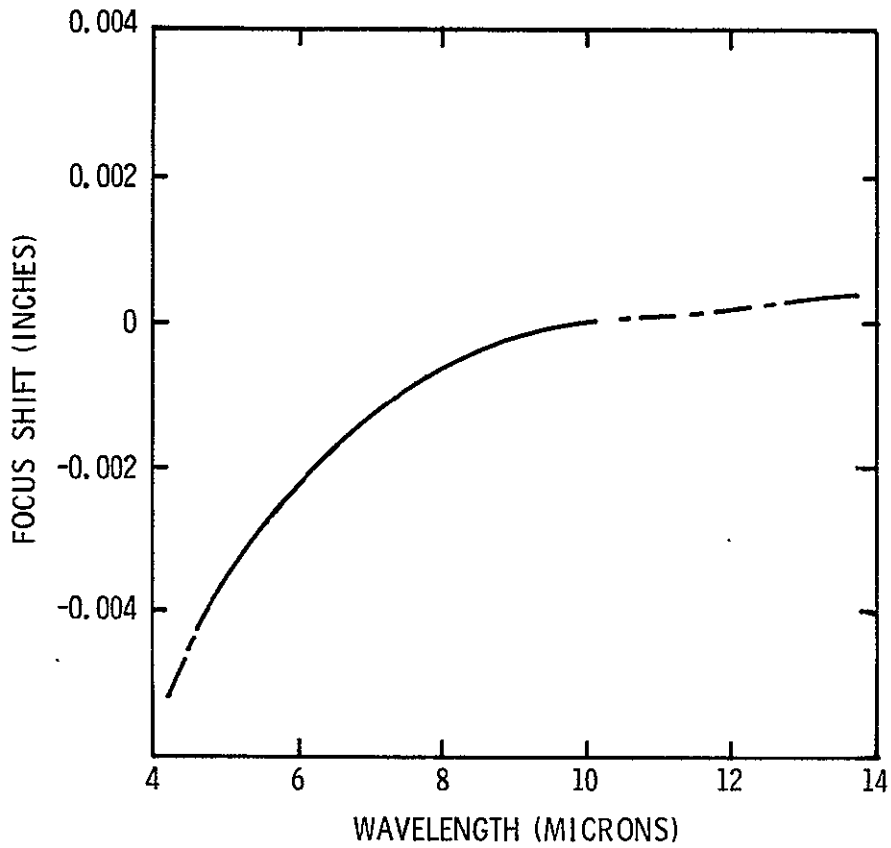


Figure 4-11. AASIR Focus Shift of Cooled Detectors with Wavelength

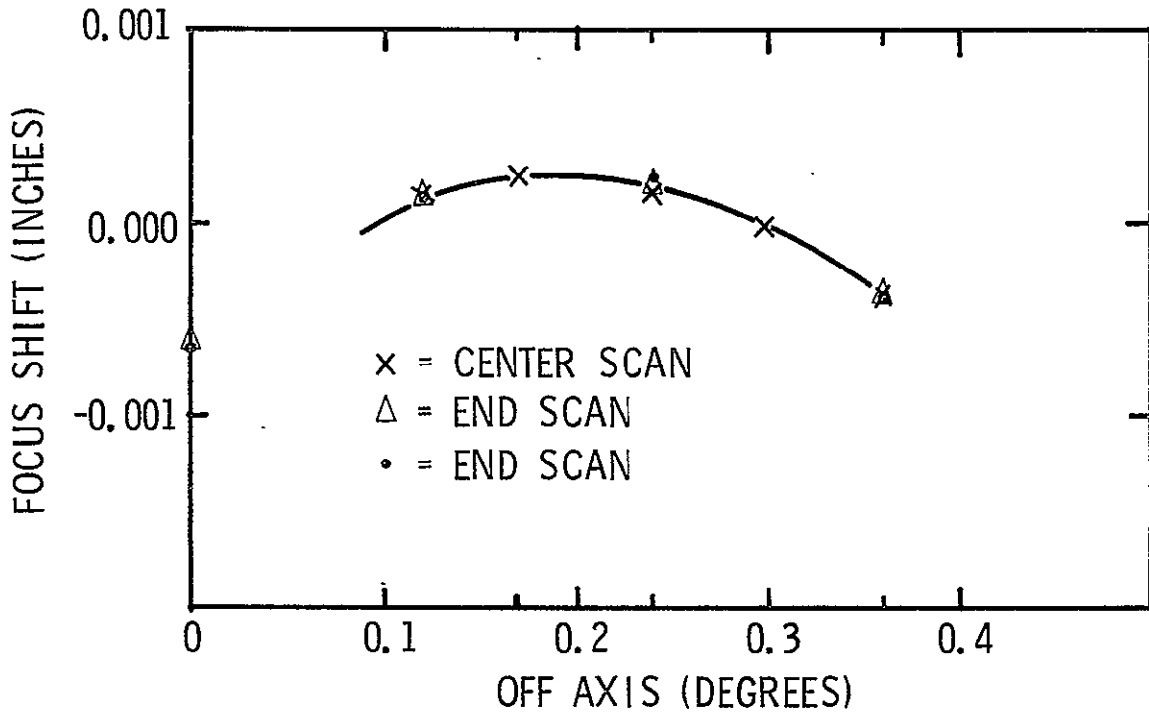


Figure 4-12. AASIR Focus Shift Through Telescope, Scan Optics and Relay Optics

AASIR IMAGE QUALITY

The estimated AASIR image quality is based on residual geometrical design aberrations, diffraction effects, and fabrication and mounting tolerances. Image quality of three manufactured VISSR optical systems are used as a basis for extrapolation to AASIR system. The extrapolation methods are given below.

Figure 4-13 illustrates the Energy Spread Functions\* (ESF) for the three VISSR/SMS optical systems used in the Engineering Model, Proto-flight Model, and Flight Model No. 1. The fourth curve represents the initial VISSR optical system specification.

Energy spread functions can be manipulated using root sum square techniques. Figure 4-14 illustrates the principle. If we have two ESFs with corresponding angular dimension functions of  $\phi_1$  and  $\phi_2$ , the angular dimension functions,  $\phi_T$ , associated with the combination is given by

$$\phi_T = \sqrt{\phi_1^2 + \phi_2^2} \tag{1}$$

The Figure 4-13 ESFs include image degradation components, such as: diffraction (D), residual design aberrations (A), mounting (M), and fabrication (F) variations. These can be expressed by:

$$\phi_T = \sqrt{\phi_D^2 + \phi_A^2 + \phi_M^2 + \phi_F^2} \tag{2}$$

The VISSR design has  $\phi_A \approx 0$  for the field angles used. Furthermore, the data given in Figure 4-13 are for laboratory measurements in which mounting stresses were (assumed) small  $\phi_M \approx 0$ . Thus equation (2) reduces to

$$\phi_T = \sqrt{\phi_D^2 + \phi_F^2} \tag{3}$$

Solving for  $\phi_F$  and taking a representative compromise for the three curves gives Figure 4-15. Also plotted on Figure 4-15 is the allotted VISSR fabrication component.

\*Also known as "radial energy distribution."

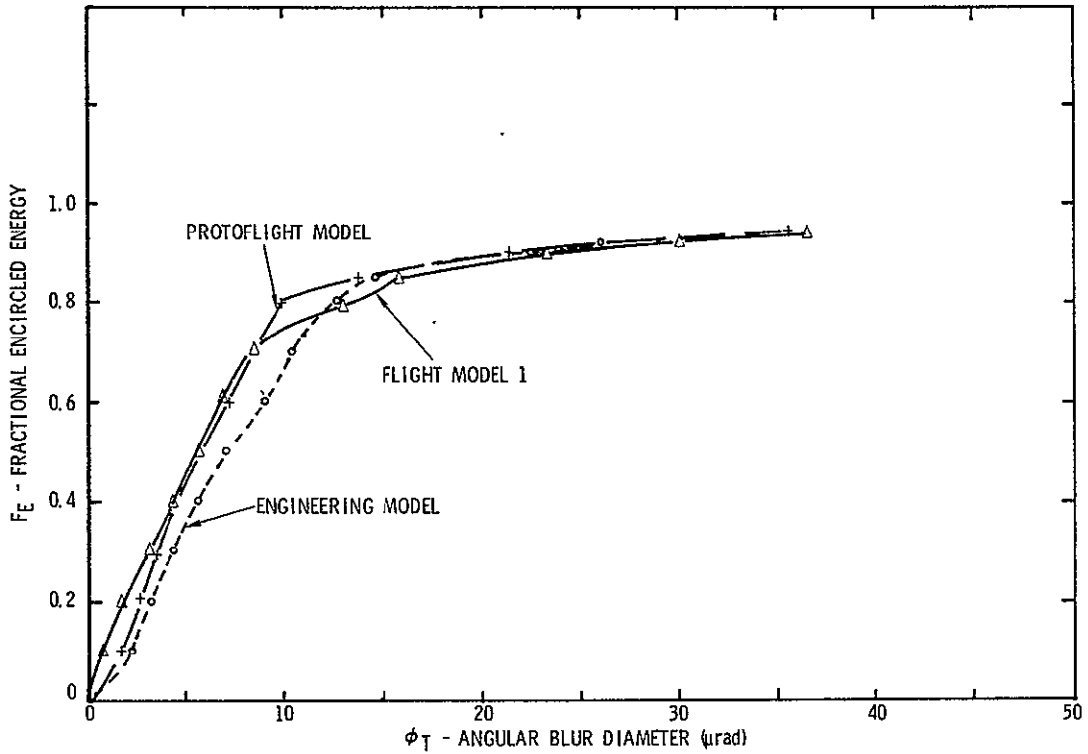


Figure 4-13. VISSR Energy Spread Function (ESF) Actual (Class II)

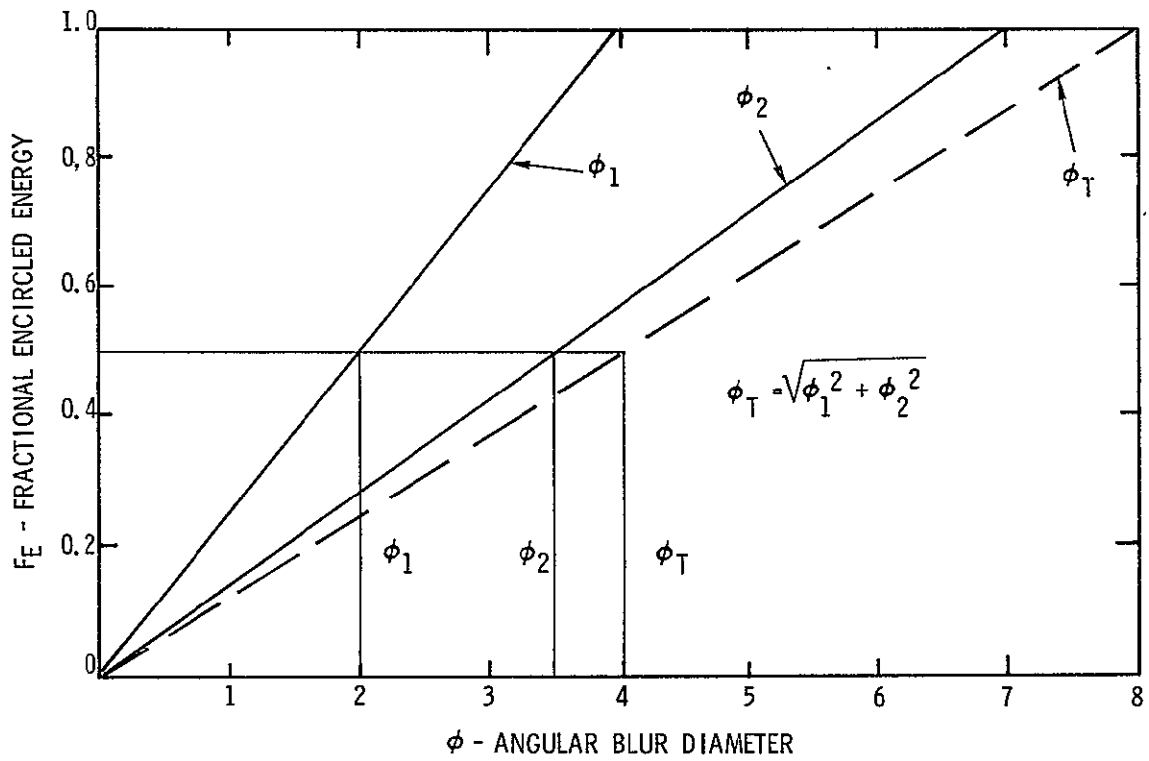


Figure 4-14. ESF Addition Root Sum Square

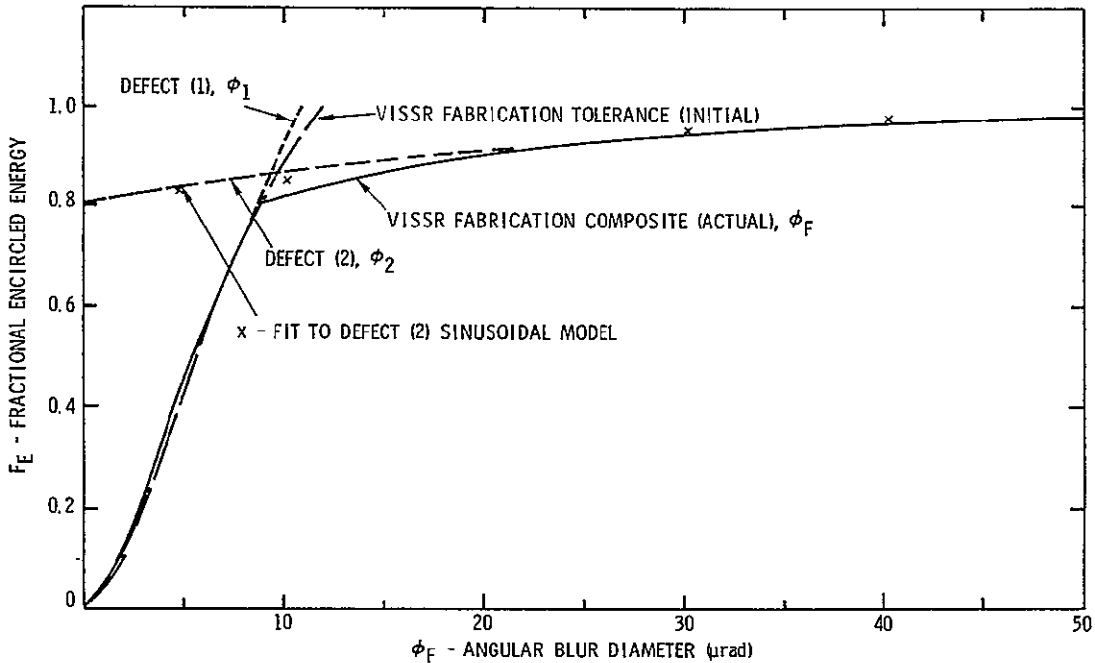


Figure 4-15. Image Degradation Component - VISSR Fabrication

It is interesting to note that the actual fabrication component follows the allotted component for the fractional energy region of 0 to 0.8. However, above a value of 0.8 the curve has a sharp break and flattens out. This is believed to be caused by surface roughness (ripple) with a small spatial period, perhaps of the order of 0.1 to 0.3 inch.

In an attempt to understand Figure 4-15 more fully and to associate some quantitative values with it, the following model was used. The fabrication function,  $\phi_F$ , was assumed to be caused by two types of defects. Defect (1) affects the whole aperture and is equivalent to a slowly varying wavefront deformation. The associated curve is  $\phi_1$ . Defect (2) affects only a fraction of the aperture (20% in this case) and has a wavefront deformation resulting in the curve labelled  $\phi_2$ . Where

$$\phi_2 = \sqrt{\phi_F^2 - \phi_1^2} \tag{4}$$

It is desired to determine quantitatively what character of ripple would produce curve  $\phi_2$ . Presumably a variety of mathematical expressions could be found to fit the data. The model used below is a simple sinusoidal function. The effective surface deviation,  $\Delta z$ , from the ideal is given by

$$\Delta z = \frac{\Delta z_0}{2} \sin \frac{2\pi y}{y_0} \quad (5)$$

where  $\Delta z_0$  is peak-to-peak surface deviation. The surface slope deviation is

$$\frac{\partial \Delta z}{\partial y} = \frac{\Delta z_0}{2} \frac{2\pi}{y_0} \cos \frac{2\pi y}{y_0} \quad (6)$$

and of course the ray deviation is twice this. Fitting the equation to the experimental curve gives

$$60 \times 10^{-6} = \frac{\Delta z_0 2\pi}{y_0} \quad (7)$$

or

$$\frac{\Delta z_0}{y_0} = 9.6 \times 10^{-6} \quad (8)$$

where, as above,  $\Delta z_0$  is the peak-to-peak surface variation and  $y_0$  is the period of the sinusoidal function.

If it is assumed  $y_0 \cong 0.2$  inch.

$$\Delta z_0 = 1.9 \times 10^{-6} \text{ inch} = \frac{\lambda}{12.6} \text{ surface deviation}$$

The fit of this model to the experimental data is shown in Figure 4-15.

Four optical suppliers have manufactured VISSR optical systems. All systems have the above phenomenon. In some, the effect was significantly more pronounced than that shown in Figure 4-13. Therefore it can be concluded that it is very difficult to polish, without ripples, VISSR nickel-plated beryllium aspheric surfaces.

The above data can be extrapolated to predict the ESF for AASIR configurations. The expression used is

$$\phi_T = \sqrt{\phi_D^2 + \phi_A^2 + (a \phi_M)^2 + (b \phi_F)^2} \quad (9)$$

the above expression results in VISSR performance characteristics if we let  $\phi_A \approx 0$  and  $a = b = 1.0$ .

Table 4-6 gives several cases where "a" and "b" are varied. A realistic achievable case is believed to be  $a = 0.7$  and  $b = 0.5$ . The parameter  $b = 0.5$  is considered realistic if the primary-secondary mirrors are made from fused silica or CER-VIT material.

The above equation (9) is for use with the AASIR telescope system. A more complete model would include the quasi object space scan (QOSS) and IR relay (IRR) optical systems. Quantities for residual geometrical aberrations and fabrication tolerances are required.

Computer ray tracing through the complete system gives a single term,  $\phi_A$ , which can include all residual design aberrations. However, the nature of the fabrication tolerances will probably be different and thus,

$$\phi_F(\text{total}) = \sqrt{(b\phi_F/\text{VISSR})^2 + (\phi_F/\text{QOSS})^2 + (\phi_F/\text{IRR})^2} \quad (10)$$

Table 4-7 is a tabulation of values used in estimating the image quality for the two imaging IR bands. The resultant image quality for 3.5- to 4.0- $\mu\text{m}$  and 10.5- to 12.5- $\mu\text{m}$  spectral bands are given in columns 7 and 8, respectively.

Table 4-6. Summary of AASIR Telescope Energy Spread Function (ESF)  
Using Variables "a" and "b"

FRACTIONAL ENCIRCLED ENERGY $F_E$	IMAGE DEGRADATION COMPONENTS				$\phi_T$ - EQUATION (9)					
	DIFFRACTION EFFECT $\phi_D$	RESIDUAL DESIGN ABERRATION $\phi_A$	MOUNTING TOLERANCE a = 1 $\phi_M$	FABRICATION TOLERANCE b = 1 $\phi_F$	a = 1.0 b = 1.0	a = 0.7 b = 0.7	a = 0.7 b = 0.5	a = 0.7 b = 0.333	a = 0.5 b = 0.5	a = 0.5 b = 0.333
0	0				0	0	0	0	0	0
0.05	0.55									
0.10	0.70	0.27	1.8	1.8	2.65	1.93	1.72	1.58	1.48	1.32
0.15	0.85									
0.20	1.00	0.32	2.85	2.85	4.17	3.01	2.67	2.45	2.27	2.01
0.25	1.15									
0.30	1.30	0.67	3.75	3.75	5.50	3.99	3.54	3.25	3.03	2.69
0.35	1.40									
0.40	1.55	0.70	4.60	4.60	6.72	4.86	4.31	3.95	3.67	3.25
0.45	1.70									
0.50	2.00	1.09	5.50	5.50	8.10	5.90	5.25	4.83	4.51	4.01
0.55	2.40									
0.60	3.90	1.11	6.50	6.50	10.05	7.61	6.91	6.47	6.13	5.63
0.65	4.35									
0.70	4.75	1.51	7.50	7.50	11.72	8.94	8.15	7.66	7.28	6.72
0.75	5.15									
0.80	5.50	1.54	8.70	8.70	13.55	10.33	9.41	8.84	8.39	7.74
0.85	6.00	(1.74)	9.50	13.00	17.27	12.89	11.20	10.10	10.19	8.96
0.90	10.50	1.93	10.25	20.00	24.38	19.01	16.29	14.49	15.50	13.59
0.92	14.00	(2.03)	10.55	23.00	28.99	22.67	19.67	17.70	18.98	16.93
0.94	17.00	(2.12)	11.00	31.00	37.09	28.70	24.35	21.44	23.75	20.75
0.96	26.00	(2.22)								
0.98	53.00	(2.31)								
1.00		2.41	12.00							

$\phi$  VALUES ARE IN  $\mu$ rad.

Table 4-7. Image Quality - IR Imaging Bands

① F <sub>E</sub>	② ϕ (TELE + DIFF) 3.75 μm	③ ϕ (TELE + DIFF) 11 μm	④ ϕ IR/FAB	⑤ ϕ <sub>A</sub> 3 mrad 3.5-4.0 μm	⑥ ϕ <sub>A</sub> 3 mrad 11.5 μm	⑦ ϕ <sub>T</sub> (② <sup>2</sup> +④ <sup>2</sup> +⑤ <sup>2</sup> ) <sup>1/2</sup> 3.5-4.0 μm	⑧ ϕ <sub>T</sub> (③ <sup>2</sup> +④ <sup>2</sup> +⑥ <sup>2</sup> ) <sup>1/2</sup> 11.5 μm
0	0	0	0	0	0	0	0
0.10	4.45	12.32	9.4	4.9	3.1	11.5	15.8
0.20	6.44	17.63	14.2	7.4	4.4	17.3	23.1
0.30	8.38	22.93	18.7	10.6	5.9	23.1	30.2
0.40	10.04	27.35	23.0	18.9	7.1	31.4	36.4
0.50	12.81	35.24	27.5	28.4	8.1	41.6	45.4
0.60	23.88	68.32	32.5	37.6	8.8	55.1	76.2
0.70	29.00	83.19	37.6	45.3	9.9	65.6	91.8
0.80	33.58	96.32	43.2	52.5	10.9	75.8	106.1
0.85	36.91	105.17	46.8	57.7	11.8	83.0	115.7
0.90	63.70	183.75	50.6	62.9	12.7	102.8	191.0
0.92	84.45	244.83	52.0	69.4	16.4	121.0	250.8
0.94	102.66	277.33	52.5	75.9	20.2	138.0	283.0

ϕ VALUES ARE IN μrad.

#### AASIR RADIOMETRIC CONSIDERATIONS

This analysis is a continuation of radiometric calibration analyses which were summarized in the AASIR Design Review Report, dated November 1975. The feasibility analysis of in-flight calibration, which would permit explicit determination of in-orbit mirror reflectance, offset voltage, and sensor calibration (sensitivity) constants, is summarized below.

The basic AASIR signal equation is

$$V = V_0 + K\tau_{AO}\Omega A\Delta\nu \left[ \rho_{SC}\rho_P\rho_S N(T_{OB}) + (1 - \rho_{SC})\rho_P\rho_S N(T_{SC}) + (1 - \rho_P)\rho_S N(T_P) + (1 - \rho_S) N(T_S) - N(T_{BB}) \right] \quad (1)$$

Henceforth we shall use

$$K_1 = K\tau_{AO}\Omega A\Delta\nu \quad (2)$$

Definition of symbols are:

- V = signal
- $V_o$  = electronic offset
- K = gain - responsivity factor
- $\tau_{AO}$  = aft optics transmittance
- $\Omega$  = solid angle
- A = area
- $\Delta\nu$  = spectral band
- $\rho$  = reflectance
- N = spectral radiance
- T = temperature

Subscripts used are:

- SC = scan mirror
- P = primary mirror
- S = secondary mirror
- BB = DC restore blackbody
- OB = scene (object)

For this analysis the system aperture stop is located at the IR relay lens system (see Figure 4-16). This corresponds to Case III (Design Review Report).

Thermal Model - Model No. 5 is used in this analysis. Table 4-8 gives a tabulation of mirror temperatures as a function of time of day. Figure 4-17 graphically illustrates the same data. A more detailed thermal analysis model is being worked on but was not available.

In the in-flight calibration mode AASIR will be viewing space, thus  $T_{OB} \approx 0$ . Therefore equation (1) becomes

$$V = V_o + K_1 \left[ (1 - \rho_{SC}) \rho_P \rho_S N(T_{SC}) + (1 - \rho_P) \rho_S N(T_P) + (1 - \rho_S) N(T_S) - N(T_{BB}) \right] \quad (3)$$

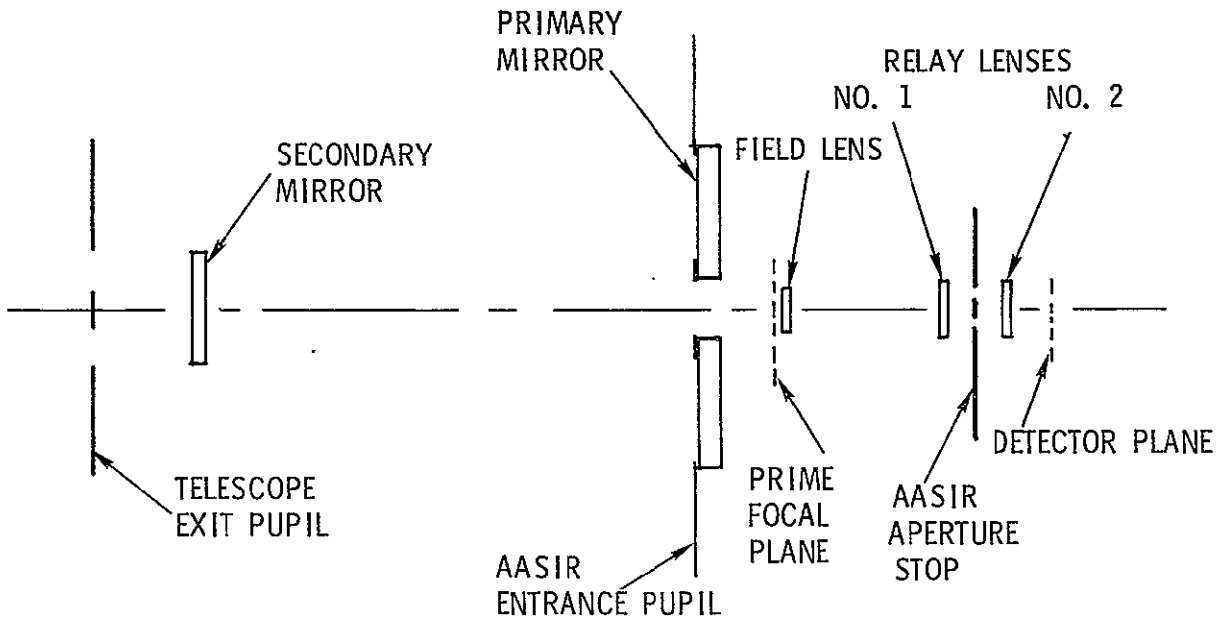


Figure 4-16. Case III - Aperture Stop at Relay Lenses

Table 4-8. AASIR Internal Temperature Gradients  
Thermal Model - Model 5

TIME (sec) $\times 10^5$	TIME (hours)	TEMPERATURE		
		SCAN MIRROR T <sub>SC</sub> (°K)	PRIMARY T <sub>P</sub> (°K)	SECONDARY T <sub>S</sub> (°K)
3.456	00	312.2	318.3	309.4
3.492	01	311.0	318.1	308.2
3.528	02	309.5	317.8	306.5
3.564	03	308.4	317.5	305.2
3.600	04	306.8	317.2	303.4
3.636	05	305.3	316.7	301.5
3.672	06	304.2	316.2	300.1
3.708	07	302.7	315.6	298.2
3.744	08	301.7	315.2	296.8
3.780	09	301.2	314.5	295.5
3.816	10	301.0	314.0	294.9
3.852	11	301.9	313.9	294.9
3.888	12	306.9	314.7	296.2
3.924	13	311.4	315.5	298.0
3.960	14	315.6	316.5	301.6
3.996	15	317.5	317.2	305.3
4.032	16	318.5	317.7	308.0
4.068	17	319.4	318.3	311.3
4.104	18	319.3	318.7	313.0
4.140	19	318.7	319.1	314.3
4.176	20	317.8	319.4	314.8
4.212	21	316.9	319.5	314.5
4.248	22	315.6	319.7	313.8
4.284	23	314.5	319.6	312.9
4.320	24	313.1	319.5	311.5

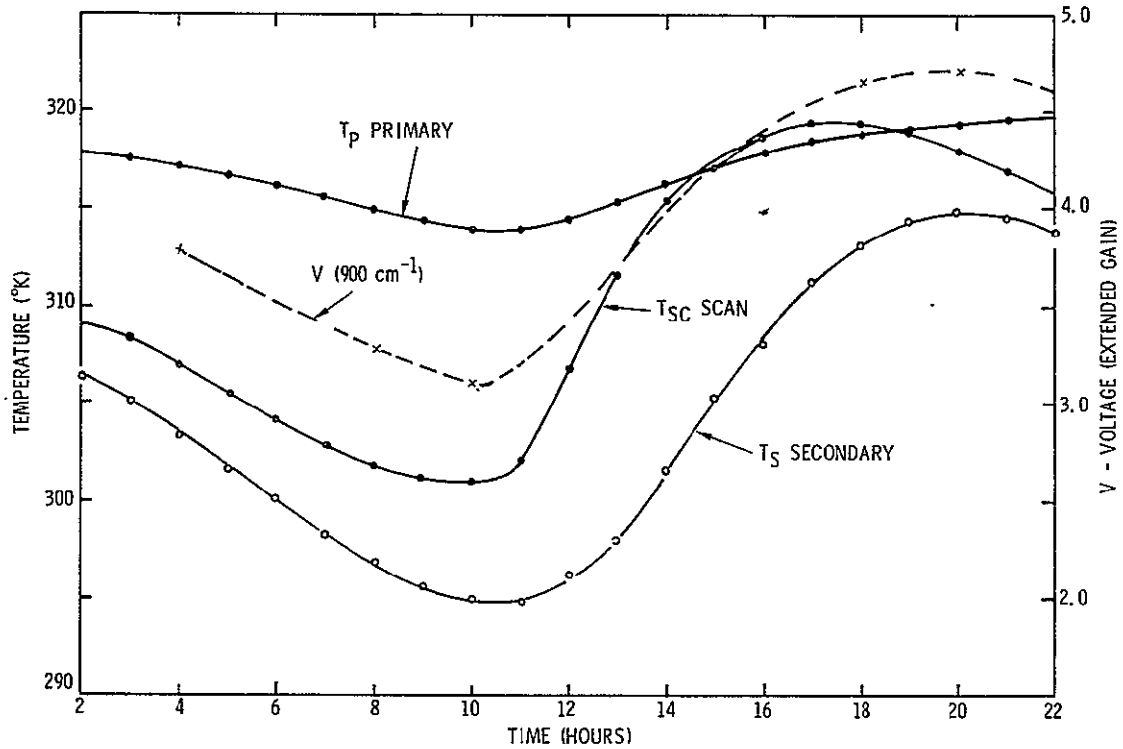


Figure 4-17. AASIR Internal Temperature Gradients  
Thermal Model No. 5

The AASIR internal temperature gradients (Table 4-8) change on a function of time. Therefore AASIR output voltage (v) will vary accordingly. The dc restore blackbody temperature is assumed to be controlled at 330°K.

Offset voltage,  $V_o$ , and sensitivity/gain factor,  $K_1$ , have been calculated for all spectral bands. The calculations are based on the following premises:

1. An "average" AASIR temperature set  
 $T_{SC} = 315.6^\circ K$ ,  $T_P = 316.5^\circ K$ ,  $T_S = 301.6^\circ K$
2.  $T_{BB} = 330^\circ K$
3.  $\rho_{SC} = \rho_P = \rho_S = 0.96$
4.  $V = 4.75$  volts at  $T_{OB} = 320^\circ K$   
 $= 0.25$  volts at  $T_{OB} = 0^\circ K$

Tabulated results are listed in Table 4-9.

Table 4-9. Radiometric Equation Parameters

SPECTRAL BAND (cm <sup>-1</sup> )	V <sub>0</sub>	K <sub>1</sub>
668.5	5.3131699	0.0274579
680	5.3216324	0.0275448
690	5.3290271	0.0276367
703	5.3386896	0.0277787
716	5.3484067	0.0279456
733	5.3611945	0.0282011
750	5.3740715	0.0284982
800	5.4124399	0.0296116
900	5.4912079	0.0329370
1380	5.8974820	0.0803248
1490	5.9956001	0.1047291
2360	6.8234728	1.3190494
2275	6.7386103	1.0047746
2250	6.7138173	0.9282095
2210	6.6743051	0.8182866
2190	6.6546210	0.7685887
2535	7.0009808	2.3377114
2700	7.1718562	4.0628518

Basically the in-flight calibration feasibility question can be stated as:  
 "Are there sufficient temporal temperature gradient changes to permit  
 determination of V<sub>0</sub>, K<sub>1</sub>, ρ<sub>SC</sub>, ρ<sub>P</sub>, and ρ<sub>S</sub> with adequate accuracy when  
 AASIR system sensitivity (NEN), digitization limitations, mirror and dc  
 restoration blackbody temperature readout uncertainties are considered?"

Thus a relationship between temperature readout uncertainty and  
 corresponding uncertainties of fitted values K<sub>1</sub>, ρ<sub>SC</sub>, ρ<sub>P</sub>, and ρ<sub>S</sub> was used.  
 This was developed by noting that the uncertainty of AASIR voltage output, V<sub>u</sub>,  
 due to temperature measurement uncertainty, ΔT, is of the form

$$\Delta V_u = \left[ \left( \frac{\partial V}{\partial T_{SC}} \Delta T_{SC} \right)^2 + \left( \frac{\partial V}{\partial T_P} \Delta T_P \right)^2 + \left( \frac{\partial V}{\partial T_S} \Delta T_S \right)^2 + \left( \frac{\partial V}{\partial T_{BB}} \Delta T_{BB} \right)^2 \right]^{\frac{1}{2}} \quad (4)$$

This assumes random errors between temperature measurements.

Furthermore the voltage uncertainty due to  $\Delta T_{SC}$  uncertainty is denoted as  $\Delta V_u(\Delta T_{SC})$  and is

$$\begin{aligned} \Delta V_u(\Delta T_{SC}) = \frac{\partial V}{\partial T_{SC}} \Delta T_{SC} = & \left( \frac{\partial V}{\partial K_1} \Delta K_1 \right)_{SC} + \left( \frac{\partial V}{\partial \rho_{SC}} \Delta \rho_{SC} \right)_{SC} \\ & + \left( \frac{\partial V}{\partial \rho_P} \Delta \rho_P \right)_{SC} + \left( \frac{\partial V}{\partial \rho_S} \Delta \rho_S \right)_{SC} \end{aligned} \quad (5)$$

continuing in like manner

$$\Delta V_u(\Delta T_P) = \frac{\partial V}{\partial T_P} \Delta T_P = \left( \frac{\partial V}{\partial K_1} \Delta K_1 \right)_P + \left( \frac{\partial V}{\partial \rho_P} \Delta \rho_P \right)_P + \left( \frac{\partial V}{\partial \rho_S} \Delta \rho_S \right)_P \quad (6)$$

$$\Delta V_u(\Delta T_S) = \left( \frac{\partial V}{\partial T_S} \Delta T_S \right)_S = \left( \frac{\partial V}{\partial K_1} \Delta K_1 \right)_S + \left( \frac{\partial V}{\partial \rho_S} \Delta \rho_S \right)_S \quad (7)$$

$$\Delta V_u(\Delta T_{BB}) = \left( \frac{\partial V}{\partial T_{BB}} \Delta T_{BB} \right)_{BB} = \left( \frac{\partial V}{\partial K_1} \Delta K_1 \right)_{BB} \quad (8)$$

Equations (5) and (6) can be simplified by noting  $(1 - \rho) < \rho$  and therefore for equation (5)

$$\left( \frac{\partial V}{\partial \rho_P} \Delta \rho_P \right)_{SC} + \left( \frac{\partial V}{\partial \rho_S} \Delta \rho_S \right)_{SC} < \left( \frac{\partial V}{\partial \rho_{SC}} \Delta \rho_{SC} \right)_{SC} \quad (9)$$

Therefore the smaller two terms are deleted. In a like manner for equation (6)

$$\left( \frac{\partial V}{\partial \rho_S} \Delta \rho_S \right)_P < \left( \frac{\partial V}{\partial \rho_P} \Delta \rho_P \right)_P \quad (10)$$

and the smaller term is deleted.

For purposes of finding equivalent uncertainty, the coherence between  $(\Delta K_1)_x$  and  $(\Delta \rho)_x$  to  $\Delta T_x$  must be maintained. For example, the voltage uncertainty  $\Delta V_u(\Delta T_{SC})$  is distributed equally between  $(\Delta K_1)_{SC}$  and  $(\Delta \rho_{SC})_{SC}$ .

This is equivalent to letting

$$\left(\frac{\partial V}{\partial K_1} \Delta K_1\right)_{SC} = \left(\frac{\partial V}{\partial \rho_{SC}} \Delta \rho_{SC}\right)_{SC} = \frac{1}{2} \frac{\partial V}{\partial T_{SC}} \Delta T_{SC} \quad (11)$$

$$\left(\frac{\partial V}{\partial K_1} \Delta K_1\right)_P = \left(\frac{\partial V}{\partial \rho_P} \Delta \rho_P\right)_P = \frac{1}{2} \frac{\partial V}{\partial T_P} \Delta T_P \quad (12)$$

$$\left(\frac{\partial V}{\partial K_1} \Delta K_1\right)_S = \left(\frac{\partial V}{\partial \rho_S} \Delta \rho_S\right)_S = \frac{1}{2} \frac{\partial V}{\partial T_S} \Delta T_S \quad (13)$$

$$\left(\frac{\partial V}{\partial K_1} \Delta K_1\right)_{BB} = \frac{\partial V}{\partial T_{BB}} \Delta T_{BB} \quad (14)$$

There are several ways of viewing data to develop a "feel" for calibration feasibility. The results are summarized in Table 4-10. Column 1 lists the spectral band being considered. Columns 2 and 3 give assumed mirror and blackbody readout temperature uncertainty. Column 4 lists the extended gain mode multiplier factor.

As previously indicated in the Design Review Report, page 4-73, in the inflight calibration mode the signal could be averaged over a 1.2° frame time. However, for the improvement in SNR to be useful, the effective digitization/telemetry noise must be equal or less than the sensor noise. Practically, this can be achieved by increasing the offset voltage ( $V_o$ ) and electronic gain, which is included in the  $K_1$  term. The value "b" is this multiplication factor.

Column 5 gives the total voltage uncertainty ( $\Delta V_T$ ) due to mirror temperature uncertainty ( $\Delta V_u$ ) and digitization effects. Equation (4) is used to obtain  $\Delta V_u$ . The total,  $\Delta V_T$ , is obtained by

$$\Delta V_T = \left[ (\Delta V_u)^2 + \left( \frac{4.75}{\sqrt{12} \cdot 2^\eta} \right)^2 \right]^{\frac{1}{2}} \quad (15)$$

where  $\eta$  is the A/D converter bit magnitude,  $\eta = 10$ .

Table 4-10. AASIR Signal Noise Ratio and Noise Equivalent Radiance

① $\nu$ ( $\text{cm}^{-1}$ )	② TEMPERATURE READOUT UNCERTAINTY		⑥ EXTENDED GAIN MODE				⑧ NORMAL MODE EQUIVALENT $\Delta N$ (ergs/etc.)	⑨ SNR		⑩ NEN (ergs/etc.)	
	$\Delta T_M$ (°K)	$\Delta T_{BB}$ (°K)	b	$\Delta V_T$ (volts)	$V_{\text{max}}-V_{\text{min}}$ (volts)	$\frac{V_{\text{max}}-V_{\text{min}}}{\Delta V_T}$		MAX	MIN		
668.5	0.1	0.1	16	0.0808	4.557	15.3	0.2079	56.4	41.1	2.45	
	0.4	0.02		0.0256	3.318	48.4		0.0658	178		178
	0.1	0.01		0.0100	(1.239)	124.0		0.0246	456		332
800	0.1	0.1	16	0.0960	4.642	14.8	0.2290	48.4	33.5	0.25	
	0.4	0.02		0.0296	3.220	48.0		0.0707	157		108.8
	0.1	0.01		0.0112	(1.422)	127		0.0267	414		288
900	0.1	0.1	16	0.1082	4.706	14.4	0.232	43.5	29.1	0.10	
	0.4	0.02		0.0328	3.146	47.6		0.0703	143.5		95.9
	0.1	0.01		0.0125	(1.560)	124.8		0.0268	376.5		251.7
1380	0.1	0.1	15	0.1634	4.691	12.6	0.1533	28.7	16.2	0.06	
	0.4	0.02		0.0452	2.647	45.4		0.0424	103.8		58.6
	0.1	0.01		0.0181	(2.054)	113.5		0.0170	259.2		146.0
1490	0.1	0.1	15	0.1790	4.751	12.1	0.1288	26.5	14.4	0.05	
	0.4	0.02		0.0486	2.585	44.6		0.0350	97.8		53.2
	0.1	0.01		0.0197	(2.166)	110		0.0142	241.2		131.2
2210	0.1	0.1	14	0.2735	4.763	9.8	0.0270	17.4	7.7	0.004	
	0.4	0.02		0.0671	2.097	39.7		0.0066	71.0		31.3
	0.1	0.01		0.0290	(2.666)	91.9		0.0029	164.2		72.3
2275	0.1	0.1	13	0.2638	4.447	9.6	0.0228	16.9	7.3	0.001	
	0.4	0.02		0.0643	1.926	39.2		0.0056	69.2		30.0
	0.1	0.01		0.0280	(2.522)	90.1		0.0024	158.8		68.8
2535	0.1	0.1	13	0.3046	4.542	8.9	0.0113	14.9	6.1	0.004	
	0.4	0.02		0.0722	1.845	37.4		0.0027	62.9		25.6
	0.1	0.01		0.0320	(2.697)	84.3		0.0012	141.9		57.7
2700	0.1	0.1	13	0.3318	4.598	8.4	0.0071	13.9	5.4	0.004	
	0.4	0.02		0.0775	1.798	36.1		0.00166	59.3		23.2
	0.1	0.01		0.0347	(2.800)	80.7		0.00074	132.5		51.8

Column 6 lists maximum and minimum output voltage and their differences. These are calculated based on temperature gradients given in Table 4-8. Column 7 is column 6 divided by column 5. Column 8 in the normal gain mode equivalent,  $\Delta N$ , to  $\Delta V_T$ . This is given by

$$\Delta N = \frac{\Delta V_T}{\frac{\partial V}{\partial N(T_{OB})}} = \frac{\Delta V_T}{bK_1 \rho S C \rho P \rho S} \quad (16)$$

Column 9 and 10 are a tabulation of maximum and minimum SNRs which are obtained by dividing column 6 by 5. Column 11 lists the system NEN specification. It should be noted that if the system NEN is larger than normal mode equivalent,  $\Delta N$ , the "SNR" listed in column 9 and 10 are not realized because AASIR system noise dominates and limits usable SNR.

The results tabulated in Table 4-10 do not provide a definitive answer to the question of feasibility of using AASIR internal temperature gradients as an inflight calibration technique. They suggest it may be possible but if so it will be a lengthy process and would be done at infrequent intervals. The equations given below would be used to determine optimum values of  $V_o$ ,  $K_1$ ,  $\rho_{SC}$ ,  $\rho_P$ , and  $\rho_S$ . The method of Least Squares is used to fit the data. The required equations are those labeled as 17a through 17e.

Briefly the data are fit in the following manner.

1. Assume a nominal set of parameters for equation 3 -  $V_o$ ,  $K_1$ ,  $\rho_{SC}$ ,  $\rho_P$ ,  $\rho_S$
2. Measured data sets consist of  $V_i$ ,  $(T_{SC})_i$ ,  $(T_P)_i$ ,  $(T_S)_i$ ,  $(T_{BB})_i$
3. Calculate  $i^{th}$  partial derivatives needed for equations 17a through 17e using  $i^{th}$  temperature sets and equation (3).
4.  $\Delta V_i = V_c - V_i$  where  $V_i$  is measured value,  $V_c$  is calculated value using equation (3) and nominal set of parameters, see item 1.
5. After complete set of "i" measurements have been used in equation 17a through 17e; solve 17a through 17e for  $\Delta V_o$ ,  $\Delta K_1$ ,  $\Delta \rho_{SC}$ ,  $\Delta \rho_P$ ,  $\Delta \rho_S$
6. New set of parameters are given by
 
$$V_o' = V_o + \Delta V_o$$

$$K_1' = K_1 + \Delta K_1$$

$$\rho_{SC}' = \rho_{SC} + \Delta \rho_{SC}$$

$$\rho_P' = \rho_P + \Delta \rho_P$$

$$\rho_S' = \rho_S + \Delta \rho_S$$
7. If equations 17a through 17e are linear enough the prime set of parameters are desired values. If equations are nonlinear it may be necessary to use iteration. Thus, the primed set of parameters would be used as second approximation. The same "i" set of measurements would be used to determine another approximation which would give a set -  $V_o''$ ,  $K_1''$ ,  $\rho_{SC}''$ ,  $\rho_P''$  and  $\rho_S''$

$$\sum_i \left\{ \left[ \left( \frac{\partial V}{\partial V_o} \right)_i \Delta V_o + \left( \frac{\partial V}{\partial K_1} \right)_i \Delta K_1 + \left( \frac{\partial V}{\partial \rho_{SC}} \right)_i \Delta \rho_{SC} + \left( \frac{\partial V}{\partial \rho_P} \right)_i \Delta \rho_P + \left( \frac{\partial V}{\partial \rho_S} \right)_i \Delta \rho_S - \Delta V_i \right] \left( \frac{\partial V}{\partial V_o} \right)_i \right\} = 0 \quad (17a)$$

$$\sum_i \left\{ \left[ \left( \frac{\partial V}{\partial V_o} \right)_i \Delta V_o + \left( \frac{\partial V}{\partial K_1} \right)_i \Delta K_1 + \left( \frac{\partial V}{\partial \rho_{SC}} \right)_i \Delta \rho_{SC} + \left( \frac{\partial V}{\partial \rho_P} \right)_i \Delta \rho_P + \left( \frac{\partial V}{\partial \rho_S} \right)_i \Delta \rho_S - \Delta V_i \right] \left( \frac{\partial V}{\partial K_1} \right)_i \right\} = 0 \quad (17b)$$

$$\sum_i \left\{ \left[ \left( \frac{\partial V}{\partial V_o} \right)_i \Delta V_o + \left( \frac{\partial V}{\partial K_1} \right)_i \Delta K_1 + \left( \frac{\partial V}{\partial \rho_{SC}} \right)_i \Delta \rho_{SC} + \left( \frac{\partial V}{\partial \rho_P} \right)_i \Delta \rho_P + \left( \frac{\partial V}{\partial \rho_S} \right)_i \Delta \rho_S - \Delta V_i \right] \left( \frac{\partial V}{\partial \rho_{SC}} \right)_i \right\} = 0 \quad (17c)$$

$$\sum_i \left\{ \left[ \left( \frac{\partial V}{\partial V_o} \right)_i \Delta V_o + \left( \frac{\partial V}{\partial K_1} \right)_i \Delta K_1 + \left( \frac{\partial V}{\partial \rho_{SC}} \right)_i \Delta \rho_{SC} + \left( \frac{\partial V}{\partial \rho_P} \right)_i \Delta \rho_P + \left( \frac{\partial V}{\partial \rho_S} \right)_i \Delta \rho_S - \Delta V_i \right] \left( \frac{\partial V}{\partial \rho_P} \right)_i \right\} = 0 \quad (17d)$$

$$\sum_i \left\{ \left[ \left( \frac{\partial V}{\partial V_o} \right)_i \Delta V_o + \left( \frac{\partial V}{\partial K_1} \right)_i \Delta K_1 + \left( \frac{\partial V}{\partial \rho_{SC}} \right)_i \Delta \rho_{SC} + \left( \frac{\partial V}{\partial \rho_P} \right)_i \Delta \rho_P + \left( \frac{\partial V}{\partial \rho_S} \right)_i \Delta \rho_S - \Delta V_i \right] \left( \frac{\partial V}{\partial \rho_S} \right)_i \right\} = 0 \quad (17e)$$

In summary, equations have been developed that are useful in evaluating the feasibility of an inflight calibration mode that takes advantage of AASIR internal temperature gradients. The completed analysis indicates possible feasibility, but is not conclusive.

A more definitive assessment can be made with additional computer simulation. The latest detailed thermal model would be used, and noise (temperature uncertainty) superimposed on the thermal model mirror temperature sets. The addition of the temperature measurement uncertainty (noise) would improve the computer simulation validity significantly.

#### AASIR RADIATION BAFFLE STUDY

Results from early AASIR thermal models showed that the thermal performance of the AASIR would be strongly influenced by the presence of the central baffle in the telescope. The effect was that sunlight impinging on the central baffle directly and by reflection off the scan mirror caused heating of the baffle. The thermal model showed that by re-radiation the hot central baffle could cause heating of the telescope tube and thus defocussing of the telescope. It was therefore important to know whether or not adequate suppression of stray radiation could be provided without the central baffle. Two cases were analyzed; one with and one without the central baffle. In both cases, the relationship between scene radiance and spurious radiation falling on the detector is determined. Extensive computer runs were made to ray trace the stray light at various angles.

##### Case I. Telescope with Baffle System Installed

A properly designed central baffle will stop essentially all direct stray radiation coming into the instrument. In this case, the primary source for the spurious radiation comes from the multiple reflections occurring between the lenses of the IR relay system (see Figure 4-18) or from the internal reflection within the lens element itself (see Figure 4-19).

From the ray trace data, various zonal areas can be identified at the primary mirror that contribute to these multiple and internal reflection-induced spurious radiations. Table 4-11 summarizes the data.

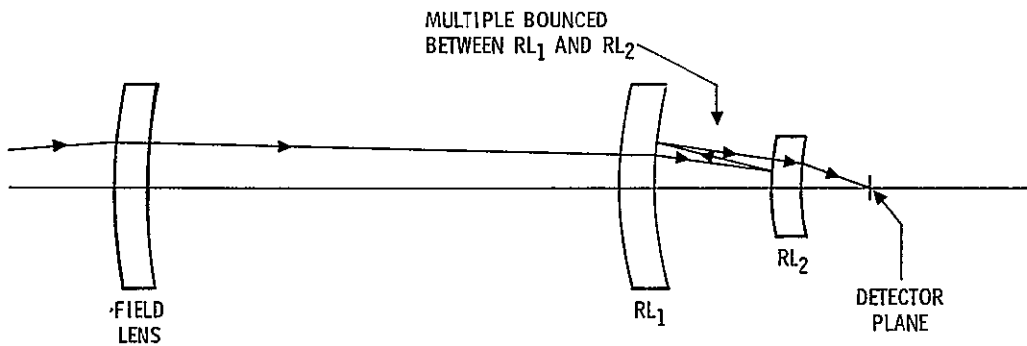


Figure 4-18. Stray Radiation Due to Multiple Reflection Occurring Between the Lens Elements

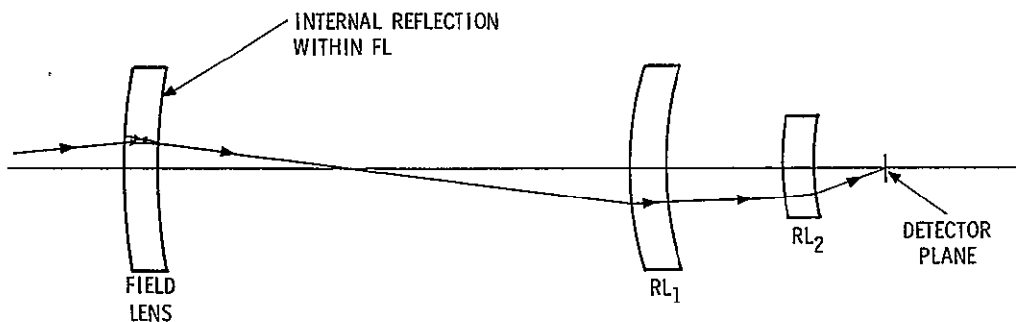


Figure 4-19. Stray Radiation Due to Internal Reflection Occurring within a Lens Element

Table 4-11. Zonal Areas in the Primary Mirror

SOURCE	FIELD ANGLE (mr)			
	6 mr	3 mr	1.5 mr	0 mr
REFLECTION OFF S <sub>1</sub> OF RL <sub>1</sub> AND THEN OFF S <sub>2</sub> OF FL	R = 2:0	3.0	2.7	2.4
REFLECTION OFF S <sub>1</sub> OF RL <sub>2</sub> AND THEN OFF S <sub>2</sub> OF RL <sub>1</sub>	8.0	5.5	4.7	4.0
INTERNAL REFLECTION WITHIN FL	NO TRANSMISSION	NO TRANSMISSION	8.0	8.0
INTERNAL REFLECTION WITHIN RL <sub>1</sub>	2.4	2.4	2.4	2.4
INTERNAL REFLECTION WITHIN RL <sub>2</sub>	NO TRANSMISSION	NO TRANSMISSION	NO TRANSMISSION	NO TRANSMISSION

RL = RELAY LENS      R = RADIAL DISTANCE FROM THE CENTER OF PRIMARY MIRROR IN INCHES  
 FL = FIELD LENS

Figures 4-20 through 4-23 show various zonal areas in the primary mirror at different field angles. It can be seen that the two biggest contributors to spurious radiation are:

- a) Reflection off S<sub>1</sub> of RL<sub>2</sub> and then off S<sub>2</sub> of RL<sub>1</sub>
- b) Internal reflection within FL

Since the remaining cases are not significant, the calculation is made only with the above two cases.

- a) "Reflection off S<sub>1</sub> of RL<sub>2</sub> and then off S<sub>2</sub> of RL<sub>1</sub>" Case

$$\frac{P_{\text{spurious}}}{P_{\text{scene}}} = \frac{N \Sigma (A_{\text{pmz}} \pi \phi^2) \rho^2 (A_{\text{D}}/A_{\text{total}})}{N(\Omega A_{\text{pm}})} \quad (1)$$

- where:
- P<sub>spurious</sub> = power of spurious radiation
  - P<sub>scene</sub> = power of scene radiation
  - A<sub>pmz</sub> = primary mirror zone area
  - A<sub>pm</sub> = primary mirror area
  - φ = field angle
  - ρ = Ge surface reflectance after AR coating (≈4%)
  - A<sub>D</sub> = individual detector area (6 × 10<sup>-3</sup>)<sup>2</sup>
  - A<sub>total</sub> = total detector array area (0.1)<sup>2</sup>
  - (Ω A<sub>pm</sub>) = AASIR solid angle area product (0.000153 cm<sup>2</sup> sr)

From Figure 4-21:

- Between 3 and 6 mr, average primary mirror zone is 7-inch radius
- Between 1.5 and 3 mr, average primary mirror zone is 5.2-inch radius
- Between 0 and 1.5 mr, average primary mirror zone is 4.5-inch radius

Therefore,

$$(\Omega A_{\text{pmz}})_{3 \text{ to } 6 \text{ mr}} = \{\phi^2_{6 \text{ mr}} - \phi^2_{3 \text{ mr}}\} \pi (R^2_{\text{pmz}} - R^2_{\text{sm}})$$

- where:
- R<sub>pmz</sub> = primary mirror zone radius
  - R<sub>sm</sub> = secondary mirror radius

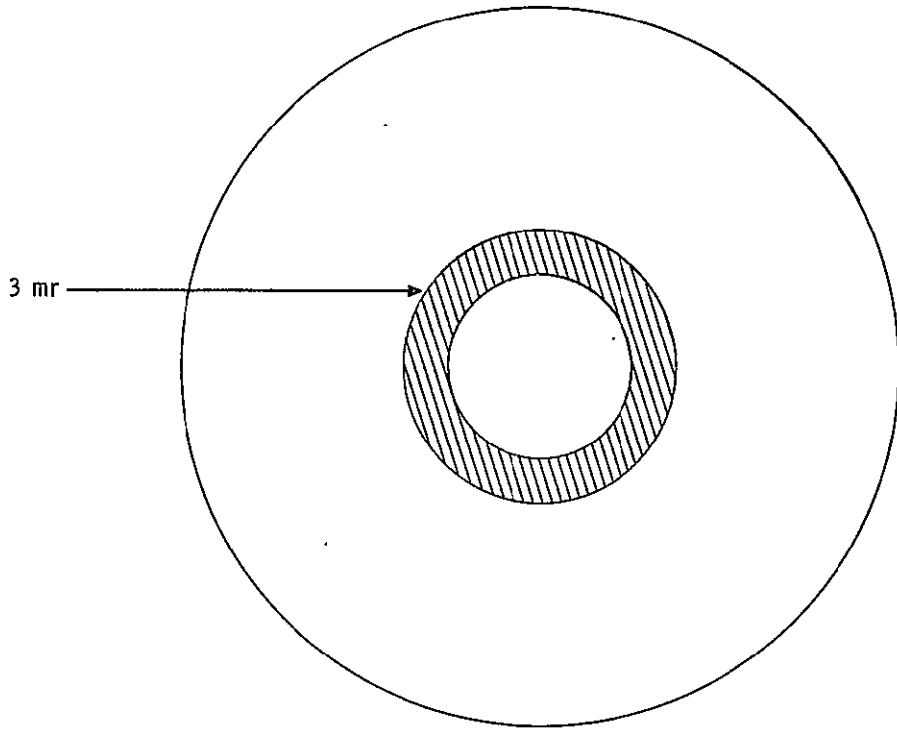


Figure 4-20. Reflection Off  $S_1$  of  $RL_1$

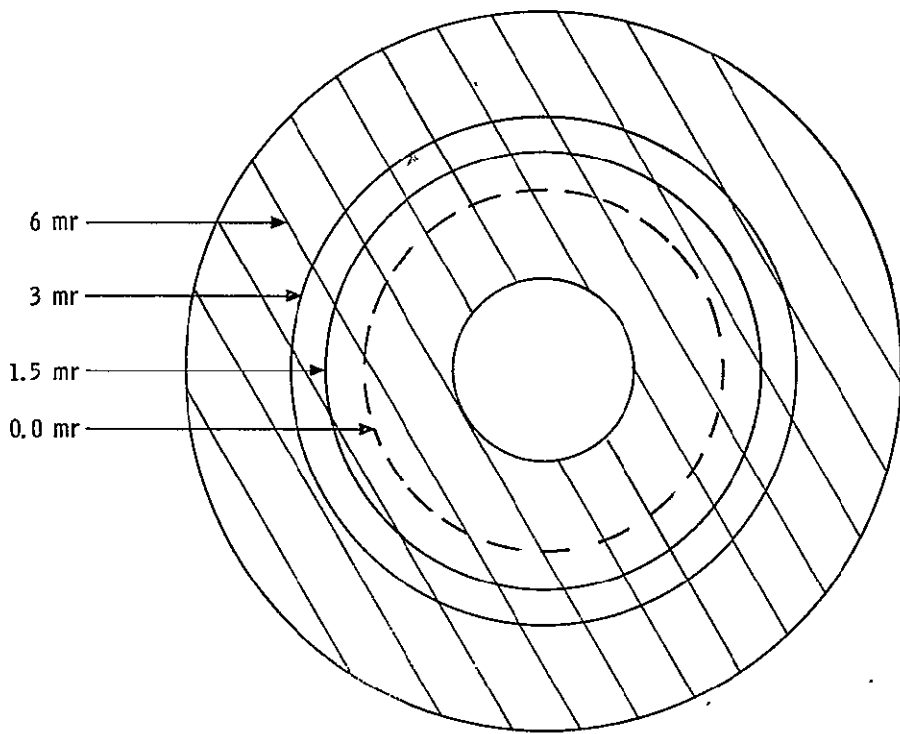


Figure 4-21. Reflection Off  $S_1$  of  $RL_2$

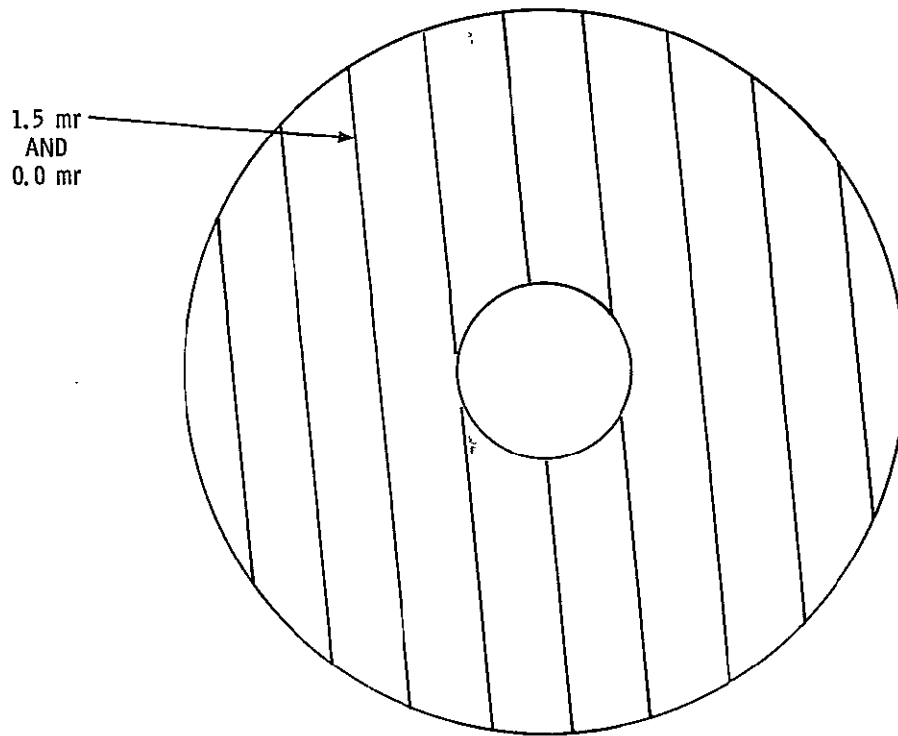


Figure 4-22. Internal Reflection within FL

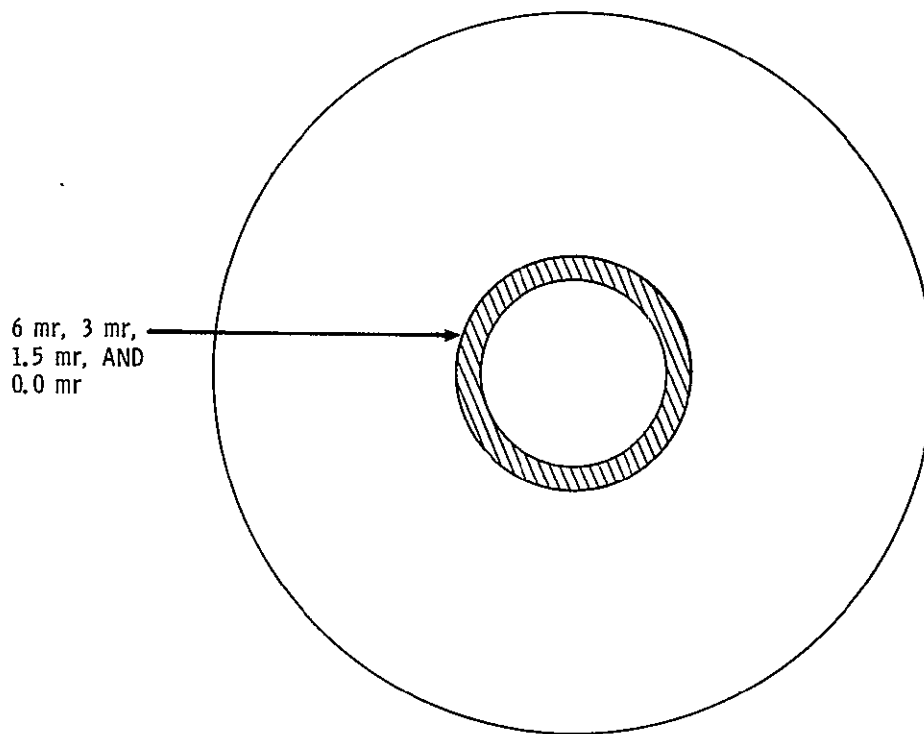


Figure 4-23. Internal Reflection within RL<sub>1</sub>

$$\begin{aligned}
 (\Omega A_{\text{pmz}})_{3 \text{ to } 6 \text{ mr}} &= [(6 \times 10^{-3})^2 - (3 \times 10^{-3})^2] \pi (7^2 - 3.2^2) 6.45 \\
 &= 2.2 \times 10^{-2} \text{ cm}^2 \text{ sr}
 \end{aligned}$$

$$\begin{aligned}
 (\Omega A_{\text{pmz}})_{1.5 \text{ to } 3 \text{ mr}} &= [(3 \times 10^{-3})^2 - (1.5 \times 10^{-3})^2] \pi (5.2^2 - 3.2^2) 6.45 \\
 &= 0.23 \times 10^{-2} \text{ cm}^2 \text{ sr}
 \end{aligned}$$

$$\begin{aligned}
 (\Omega A_{\text{pmz}})_{0 \text{ to } 1.5 \text{ mr}} &= [(1.5 \times 10^{-3})^2 - 0] \pi (4.5^2 - 3.2^2) 6.45 \\
 &= 0.046 \times 10^{-2} \text{ cm}^2 \text{ sr}
 \end{aligned}$$

$$\Sigma(\Omega A_{\text{pmz}})_{\phi} = 2.47 \times 10^{-2} \text{ cm}^2 \text{ sr}$$

Then, equation (1) becomes:

$$\begin{aligned}
 \frac{P_{\text{spurious}}}{P_{\text{scene}}} &= \frac{(3.14)(2.47 \times 10^{-2})(4 \times 10^{-2})^2 \{(6 \times 10^{-3})(6 \times 10^{-3})/10^{-2}\}}{(0.000153)} \\
 &= 2.8 \times 10^{-3}
 \end{aligned}$$

b) "Internal reflection within FL" Case

From Figure 4-22, the average field angle is 2 mr. Again,

$$\begin{aligned}
 \frac{P_{\text{spurious}}}{P_{\text{scene}}} &= \frac{NA_{\text{pm}} \pi \phi^2 \rho^2 (A_D/A_{\text{total}})}{N(\Omega A_{\text{pm}})} \\
 &= \frac{(1089)(3.14)(0.002)^2 (4 \times 10^{-2})^2 (36 \times 10^{-6}/10^{-2})}{(0.000153)} \\
 &= 0.0005 \\
 &= 5 \times 10^{-4}
 \end{aligned}$$

If we add cases a) and b),

$$\begin{aligned}
 \Sigma \frac{P_{\text{spurious}}}{P_{\text{scene}}} &= (2.8 \times 10^{-3}) + (5 \times 10^{-4}) \\
 &= 3.3 \times 10^{-3}
 \end{aligned}$$

This shows that noise equivalent signal due to stray radiation is 0.33% of the scene signal.

Case II. Without Radiation Baffle System

When there is no central baffle, the system must contend with direct stray radiation that is incident upon the field lens, bypassing both primary and secondary mirrors. Therefore, various field angles of direct stray radiation that could enter the instrument through the sun shield and then be reflected off the scan mirror were determined. Then by ray trace, various corresponding zonal areas at the field lens were defined. Figure 4-24 illustrates the mechanics of stray light entering the instrument at various field angles. It should be emphasized that, in this direct stray radiation case, only those rays that are internally reflected within the field lens make it all the way to the detector plane. Table 4-12 summarizes the ray trace data. Figures 4-25 through 4-28 show these zonal areas at the field lens. Figure 4-29 is simply the actual clear aperture of the sun shield and subsequent correction factors due to minor axis blockage (sun shield opening is not a circular but an elliptical area).

Table 4-12. Stray Light Induced by Direct Radiation

SOURCE	FIELD LENS ZONAL AREAS
STRAIGHT THROUGH	ALL STOPPED OUT - NO TRANSMISSION
REFLECTION OFF RL <sub>1</sub>	ALL STOPPED OUT - NO TRANSMISSION
REFLECTION OFF RL <sub>2</sub>	ALL STOPPED OUT - NO TRANSMISSION
INTERNAL REFLECTION WITHIN FL $\theta = 6.87^\circ$ $\theta = 8.0^\circ$ $\theta = 10.0^\circ$	$0.125 < R < 0.45$ inch $0.175 < R < 0.50$ inch $0.25 < R < 0.575$ inch
INTERNAL REFLECTION WITHIN RL <sub>1</sub>	ALL STOPPED OUT - NO TRANSMISSION
INTERNAL REFLECTION WITHIN RL <sub>2</sub>	ALL STOPPED OUT - NO TRANSMISSION

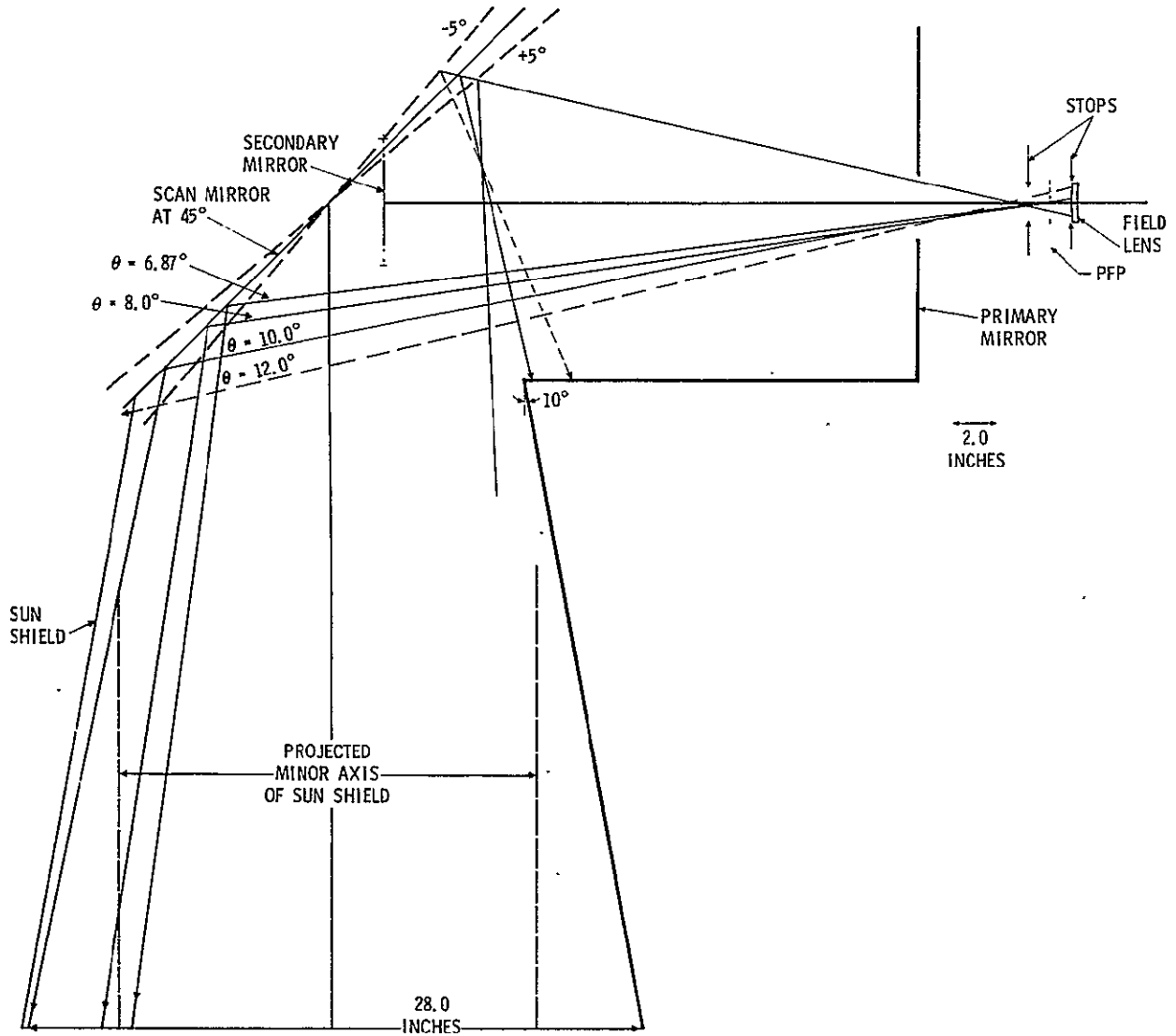


Figure 4-24. Stray Radiation Directly Entering the Instrument, Bypassing Main Telescope

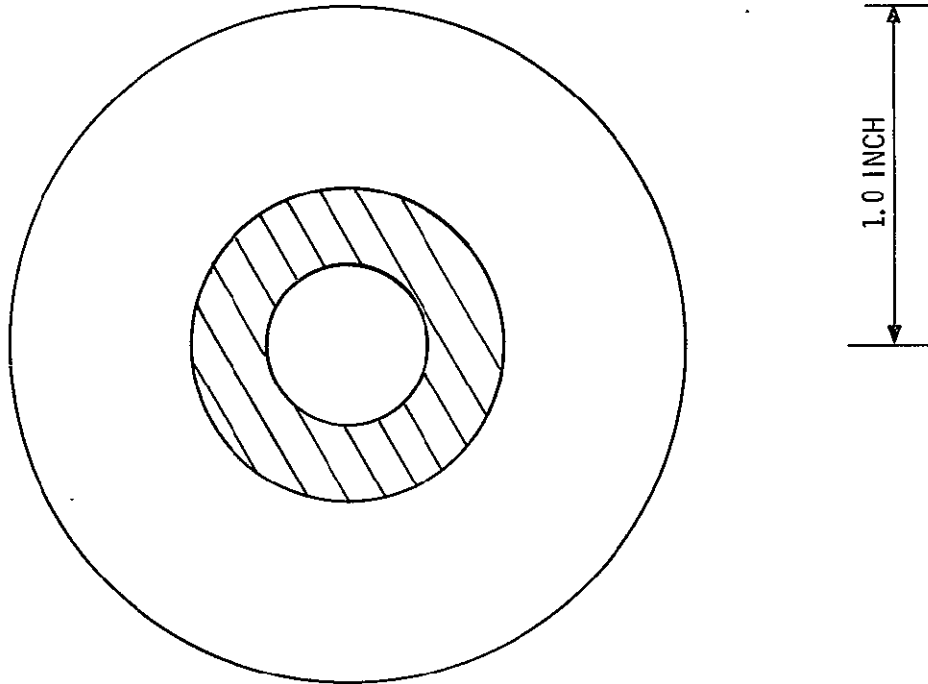


Figure 4-25. Internal Reflection within the Field Lens when  $\theta = 6.87^\circ$

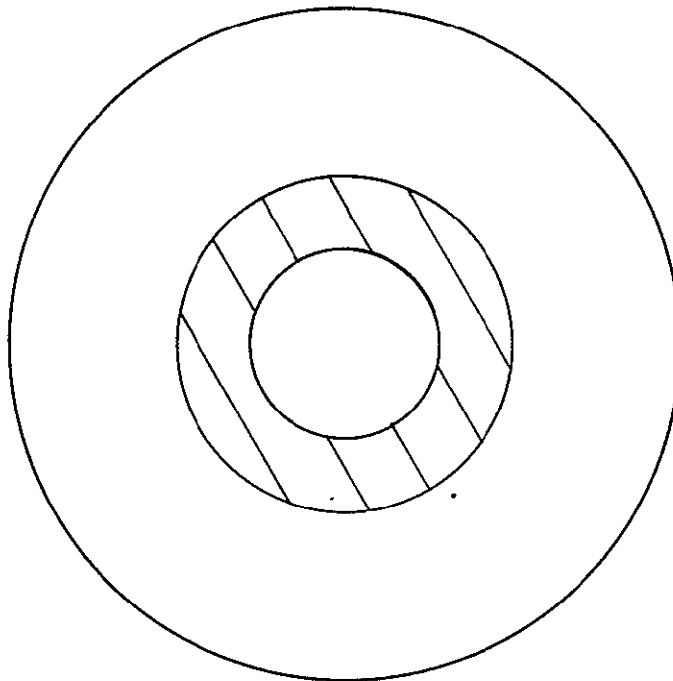


Figure 4-26. Internal Reflection within the Field Lens when  $\theta = 8.0^\circ$

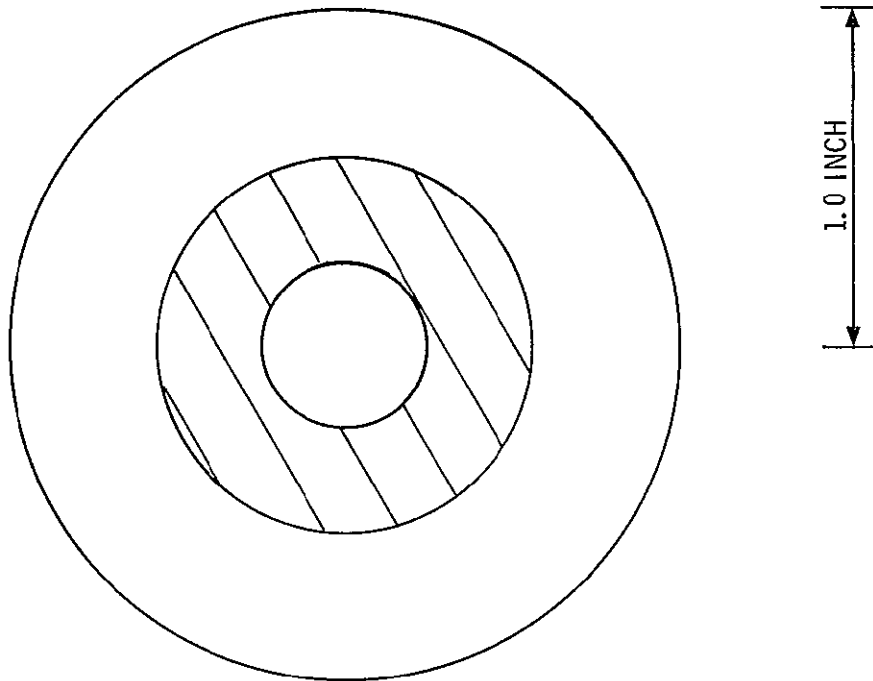


Figure 4-27. Internal Reflection within the Field Lens when  $\theta = 10^\circ$

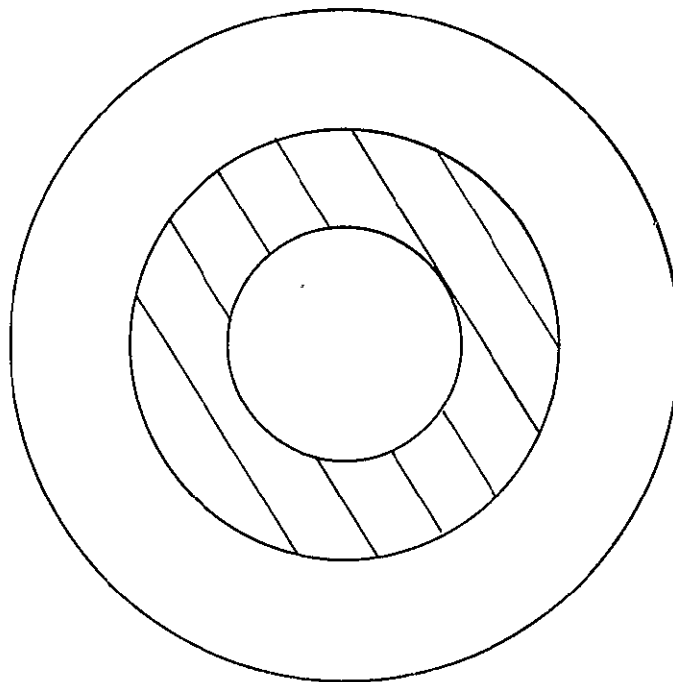


Figure 4-28. Internal Reflection within the Field Lens when  $\theta = 12^\circ$

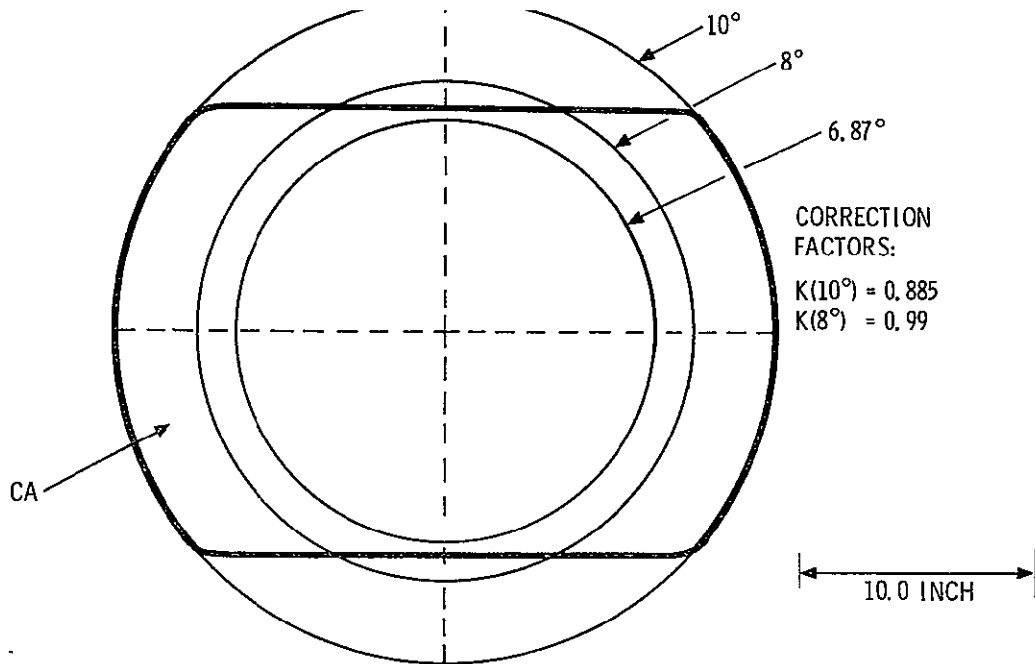


Figure 4-29. Correction Factor Due to Minor Axis Blockage

Therefore,

$$\frac{P_{\text{spurious}}}{P_{\text{scene}}} = \frac{N \sum (\Omega_{\theta} A_z) \rho_{\text{FL}}^2 (A_D / A_{\text{total}})}{N(\Omega A)_{\text{AASIR}} \rho_m^2} \quad (2)$$

where:  $\Omega_{\theta}$  = solid angle of rays incident upon FL

$A_z$  = zonal areas at FL for each  $\theta$

$\rho_{\text{FL}}$  = Ge surface reflectance ( $\approx 4\%$ )

$A_D$  = single detector size

$A_{\text{total}}$  = total detector area

$(\Omega A)_{\text{AASIR}}$  = AASIR solid angle area product

$\rho_m$  = primary mirror and secondary mirror reflectance ( $\approx 97\%$ )

From Figure 4-25, it is assumed that the zone of  $0.24 \text{ inch} < R < 0.45 \text{ inch}$  is the average area for the field angles between  $\theta = 5.3^\circ$  and  $\theta = 7.5^\circ$ . From Figures 4-26 and 4-27, the average zonal area for field angles of  $7.5^\circ$  to  $9.0^\circ$  is  $0.28 \text{ inch} < R < 0.5 \text{ inch}$ ; for field angles of  $9^\circ$  to  $10^\circ$ , it is  $0.25 \text{ inch} < R < 0.55 \text{ inch}$ , where  $R$  is the radial distance from the center of the field lens.

Therefore, when

$$5.3^\circ \leq \theta \leq 7.5^\circ \quad A_{z1} = \pi\{(0.45)^2 - (0.24)^2\} 6.25 = 2.84 \text{ cm}^2$$

$$7.5^\circ \leq \theta \leq 9^\circ \quad A_{z2} = \pi\{(0.5)^2 - (0.28)^2\} 6.25 = 3.37 \text{ cm}^2$$

$$9^\circ \leq \theta \leq 10^\circ \quad A_{z3} = \pi\{(0.55)^2 - (0.25)^2\} 6.25 = 4.71 \text{ cm}^2$$

and

$$\Omega_{\theta=5.3^\circ} = 2\pi(1 - \cos \theta) \text{ rad}$$

$$= 2\pi(1 - \cos 5.3^\circ)$$

$$= 0.027$$

$$\Omega_{\theta=7.5^\circ} = 0.054$$

$$\Omega_{\theta=9^\circ} = 0.077$$

$$\Omega_{\theta=10^\circ} = 0.095$$

So, for

$$\begin{aligned} 5.3^\circ \leq \theta \leq 7.5^\circ \quad (\Omega A)_1 &= (\Omega_{\theta=7.5^\circ} - \Omega_{\theta=5.3^\circ}) A_{z1} \\ &= (0.054 - 0.027) 2.84 \\ &= 0.0767 \text{ cm}^2 \text{ sr} \end{aligned}$$

$$\begin{aligned} 7.5^\circ \leq \theta \leq 9^\circ \quad (\Omega A)_2 &= (\Omega_{\theta=9^\circ} - \Omega_{\theta=7.5^\circ}) A_{z2} \\ &= (0.077 - 0.054) 3.37 \\ &= 0.0775 \text{ cm}^2 \text{ sr} \end{aligned}$$

$$\begin{aligned} 9^\circ \leq \theta \leq 10^\circ \quad (\Omega A)_3 &= (\Omega_{\theta=10^\circ} - \Omega_{\theta=9^\circ}) A_{z3} \\ &= (0.095 - 0.077) 4.71 \\ &= 0.0848 \text{ cm}^2 \text{ sr} \end{aligned}$$

Finally,  $\Sigma(\Omega_{\theta}A_z)$ , with correction factors due to minor axis blockage of the sun shield clear aperture, is:

$$\begin{aligned} \Sigma(\Omega_{\theta}A_z) &= \Sigma(\Omega A)_i K_i \\ &= (0.0767) + (0.0775)(0.99) + (0.0848)(0.885) \\ &= 0.2287 \end{aligned}$$

where  $K_i$  is the correction factor.

If all these values are substituted into equation (2),

$$\begin{aligned} \frac{P_{\text{spurious}}}{P_{\text{scene}}} &= \frac{N(0.2287)(0.04)^2 \{(6 \times 10^{-3})^2 / (0.1)^2\}}{N(0.000153)(0.97)^2} \\ &= 0.00914 \end{aligned}$$

This means 0.9% of the signal is the noise attributable to direct spurious radiation alone. However, in this case, the noise is generated not only by the direct stray radiation, but also by the multiple reflections that already have been discussed in Case I. So, in this case of no central baffle system, the multiple reflection effect has to be added. Then,

$$\frac{P_{\text{spurious}}}{P_{\text{scene}}} = 0.0124 \quad \text{for "No Central Radiation Baffle" Case}$$

$$\frac{P_{\text{spurious}}}{P_{\text{scene}}} = 0.0033 \quad \text{for "With Central Radiation Baffle" Case}$$

### Conclusion

The spurious radiation contribution shown for the telescope with no central baffle would generally be considered excessive for a radiometric system viewing an extended source. When viewing a point source, the telescope image quality (not including spurious radiation analyzed above) will allow about 90% of the energy from the point source to be contained within the geometrical FOV. On this basis, an additional 1% due to spurious radiation would not be significant. However, when viewing an extended source, the percentage of energy contained within the geometrical FOV is much higher, and the spurious radiation represents a larger fraction of the radiation originating outside the FOV.

The overall effect of spurious radiation has not been evaluated for the AASIR but should be considered in connection with the thermal analysis and image quality.

Section 5  
AASIR RADIATION COOLER

GENERAL

The design selected for the AASIR Radiation Cooler is a shielded two-stage configuration, schematically shown in Figure 5-1. The design consists of an ambient housing and earth shield, intermediate stage, and cold stage. The cold stage houses the detector array, with the intermediate stage serving as a heat shield, isolating the cold stage from the warm surroundings. The earth shield provides a similar barrier from earth and spacecraft energy which would otherwise be incident on the intermediate stage.

The earth and intermediate stage shields have outline configurations similar to sections of a parabola. The intermediate and cold stage radiator designs are of the open-faced honeycomb structure coated with a high emittance thermal paint. The cold stage assembly houses the "pumpable" detector dewar package which eases dewar disassembly and maintainability. The cooler design presented herein (MOD II) has been altered from that proposed in the November '75 Design Review Report (MOD I). The redesigned cooler has increased in overall diameter by 29%; and is 44% deeper. "Parabolic" shields have been added for improved cooling capacity and the cold stage has been modified to improve bench test cooling. The details of these changes and their effect on performance are detailed in the following sections.

DESIGN FEATURES

Figure 5-2 shows a schematic representation of the AASIR Radiation Cooler; its outline dimensions and orientation. The overall cooler diameter is 18.0 inches and has an overall depth of 7.5 inches. The cooler clear FOV is  $160^\circ\text{K}$  with an intermediate stage radiating area of  $188.9 \text{ inch}^2$  and a cold stage area of  $35.8 \text{ inch}^2$ .

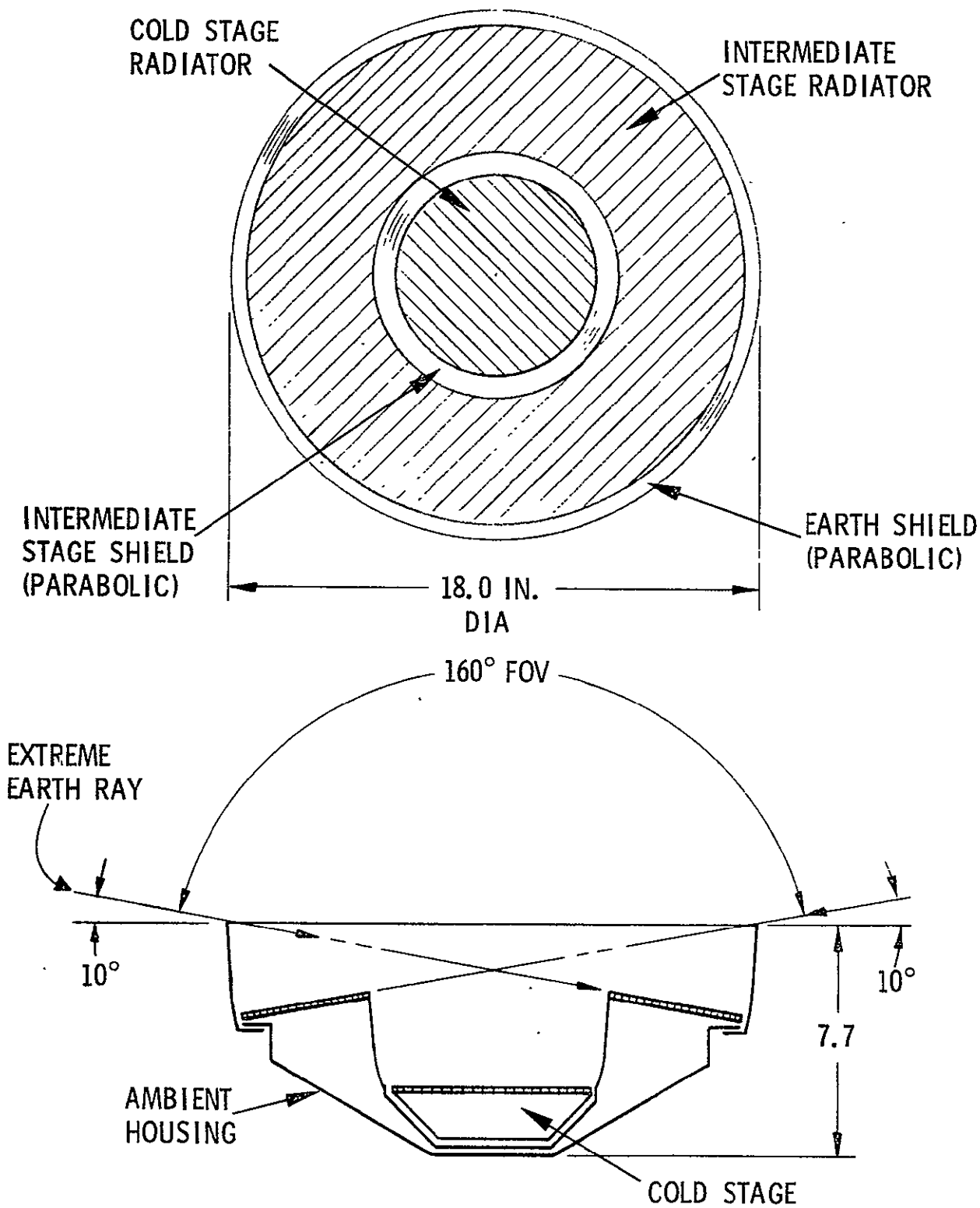


Figure 5-1. AASIR Cooler Schematic

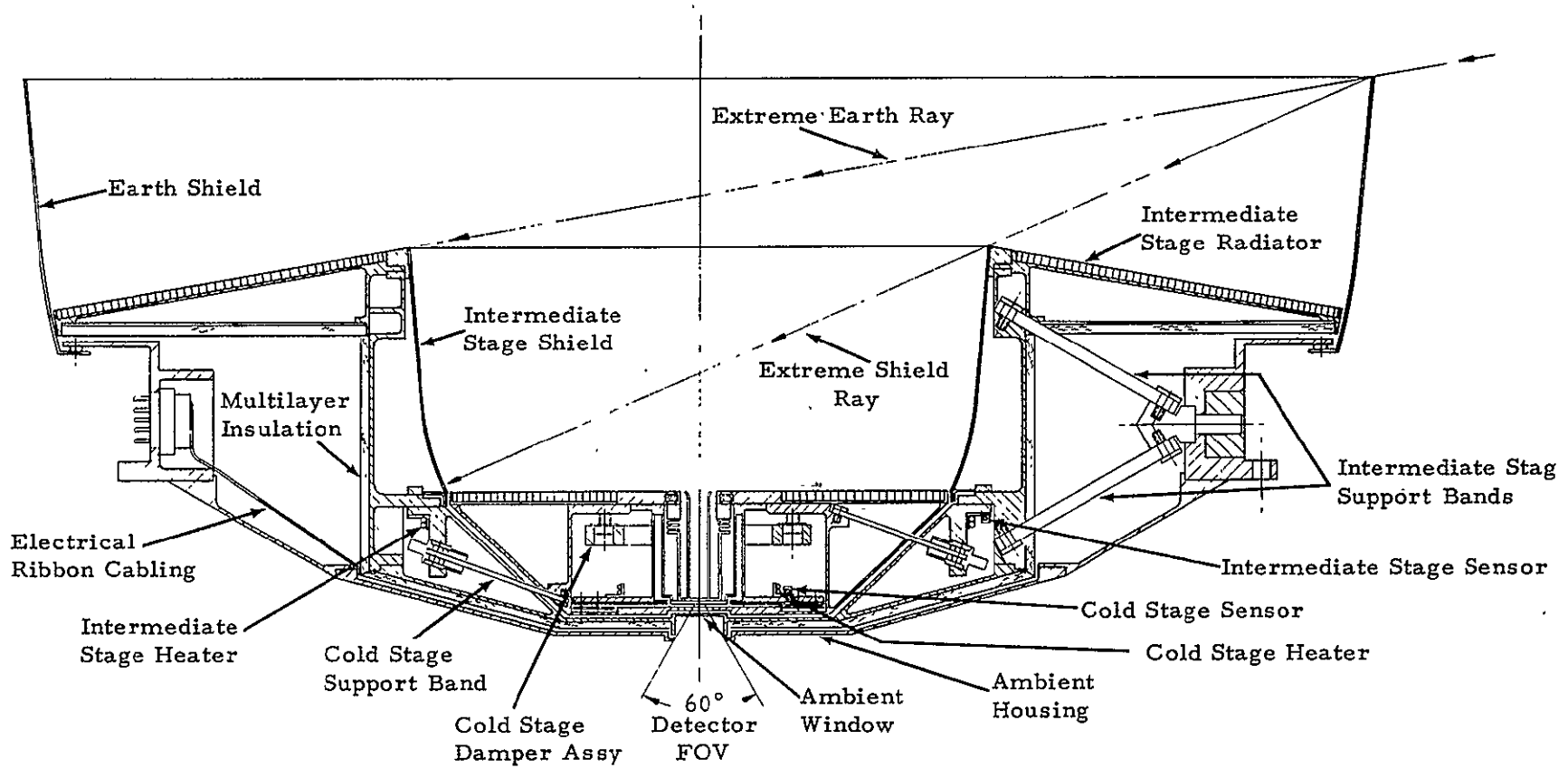


Figure 5-2. AASIR Radiation Cooler Layout Flight Configuration (Mod II)

The key features in the structural and thermal design of a typical multistage radiation cooler are itemized in Table 5-1, together with the particular design approach selected for the AASIR configuration. These approaches were preferred because of their successful implementation in the VISSR/VAS coolers. Two relatively new approaches are particularly noteworthy. A recent development in the VAS cooler program utilizing more sophisticated shield configurations has lead to dramatic improvements in cooler performance. Improvements in electro-forming techniques have made it possible to design radiation coolers having shields conforming to a curved shape rather than the straight conical type presently in use. A more effective cooler thermal design can be achieved using this variable shape shield as its mechanism for energy rejection is more efficient. The result is a larger cold-stage radiating area for the same overall cooler dimension. This state-of-the-art technology has been incorporated into the AASIR shield design. The AASIR design also uses the "pumpable" dewar concept which permits modular-type replacement for the array components as well as greatly simplified dewar maintainability. This new concept was not used on either the VISSR or VAS radiation coolers. The "parabolic" shields and pumpable dewar are shown in Figure 5-2 mounted in the radiation cooler assembly. Other design features carried over from the VISSR/VAS Programs are the highly successful and sophisticated design concepts of the interstage supports, tuned dampers, and flat ribbon cabling, also depicted in Figure 5-2.

#### DESIGN DESCRIPTION

The key components of the two-stage AASIR cooler are shown in Figure 5-2. The earth and intermediate stage shields specularly reflect to space energy from warm temperature surroundings. The high-emittance intermediate and cold-stage radiators radiate energy to space, thereby cooling their respective stages. The inner stages are thermally isolated from each other, and from the ambient housing, by low conductivity fiberglass support bands. Six support bands extend symmetrically from both the intermediate and cold-stage assemblies. The bands are located in three

pairs for each stage, and each pair is aligned in a vertical plane 120° from the next pair. This symmetry is necessary; for vibrational or dynamic stability, and for static alignment stability of the detector array during cool-down of the radiation cooler.

Table 5-1. AASIR Cooler Design Features

FEATURE	DESIGN
Interstage Supports	Continuous Wound Fiberglass Bands
Vibration Control	Viscoelastic, Tuned Rubber Dampers
Temperature Sensors	Platinum Resistance 1000 Ω at 0°C
Outgassing Heaters	Intermediate and Cold Stage
Specular Shields (Parabolic)	Electroformed Nickel Coated with VDA
Multilayered Insulation	Intermediate Stage Only
Detector Cooling - Bench Test	Joule-Thomson Liquid Nitrogen Cryostat
Dewar/Detector Assembly	Re-pumpable, Temporary Vacuum
Electrical Conductors	Flat "Ribbon" Cabling

Viscoelastic vibration dampers are used on the cold-stage assembly to reduce amplitudes of oscillation during vibration. The location of these dampers are shown in Figure 5-2. These dampers along with the fiberglass support bands have proven to be highly successful on other coolers in satisfying the stringent vibration and structural requirements.

Outgassing heaters are mounted on both stages to provide inflight decontamination capabilities for the critical thermal surfaces and optical windows. Other components include platinum temperature sensors for monitoring stage temperatures, and multilayered insulation is attached to the external surfaces of the intermediate stage for thermal isolation and additional contamination control.

A layout of the cold-stage assembly is shown in Figure 5-3. The assembly consists of a housing, radiator, heater, heat transfer bellows, and dewar subassembly. The housing is the primary structure of the cold stage and is the attachment point for the interstage support bands. The radiator is of open-faced honeycomb construction coated on the exterior side with a high emittance paint. The outgassing heater is mounted to the dewar housing. The heat transfer bellows (Figure 5-3) is required to provide a thermal short between the detector substrate and the radiator surface. The bellows during flight operation, conducts the bias power (dissipated at the detector substrate) to the radiator, minimizing the thermal gradient in the cold stage. All surfaces of the cold stage viewing the warm surfaces of the intermediate stage are coated with low-emittance electro-deposited gold.

The dewar subassembly, a critical component of the cold stage, is also shown in Figure 5-3. This unit contains the thermal detector array and associated electronics, detector leads, and "feedthrough" circuit board. The dewar can be evacuated during bench-test cooling of the array, but will be vented (through a filter) to the laboratory atmosphere during assembly and storage. The principal advantage of the pumpable dewar concept is the ease of dewar disassembly and maintainability. With the cooler removed from the scanner, the detector array is accessible by removing the cold-stage aperture plate, and the intermediate and ambient covers. It is intended that in this way, minor repairs can be performed on the substrate without removing the dewar assembly from the cooler. The cold-stage assembly is deeper than in previous designs to provide improved thermal isolation of the array during bench testing.

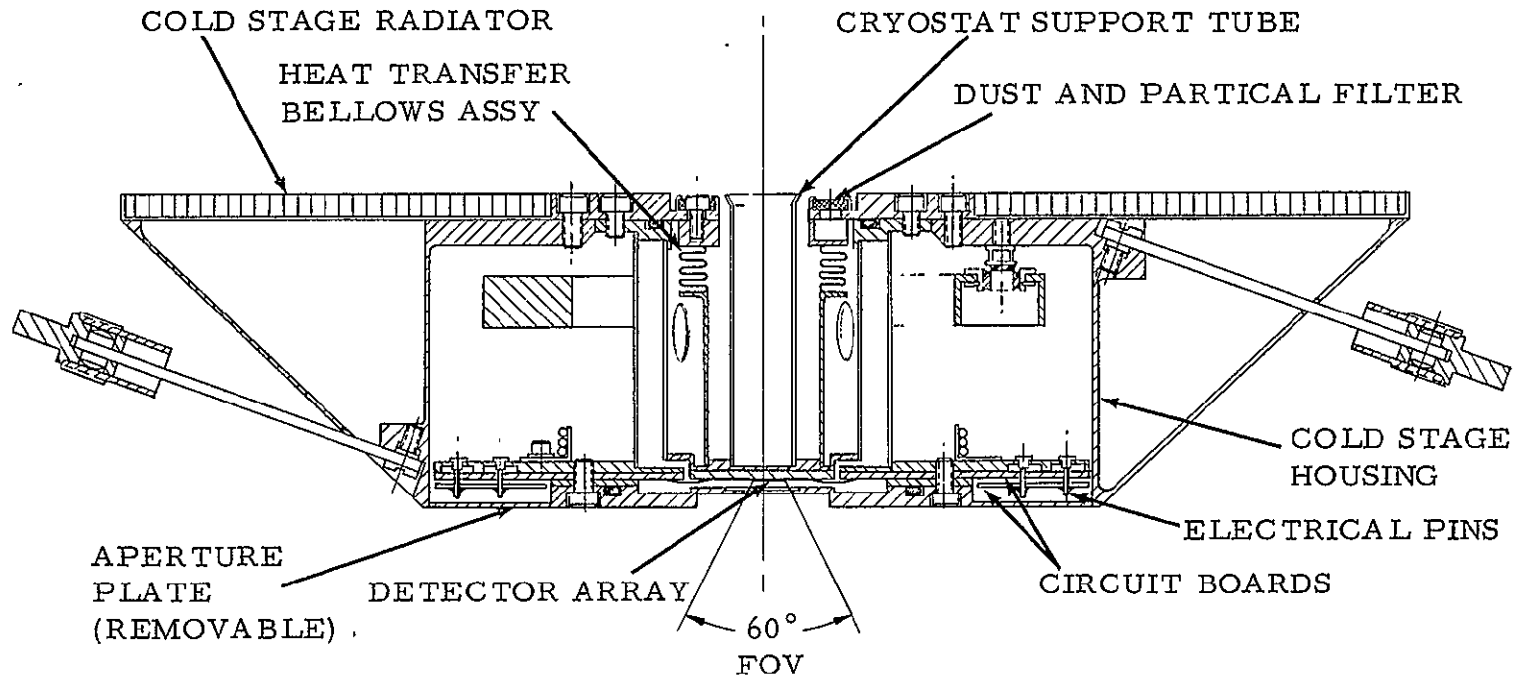


Figure 5-3. AASIR Cooler Flight Configuration Cold Stage Layout (Mod II)

Another important design feature utilized in the AASIR design is the "flat ribbon" type cable for electrical connections, rather than the cumbersome twisted lead construction used in the original VISSR coolers. The large number of terminations necessary at the cold-stage detector array requires a highly compact, and thermally efficient cable design. The ribbon cable concept satisfies this criteria, and because of workmanship factors, will increase the overall interconnection reliability; rather than decrease because of the additional connections.

## ANALYSIS AND PREDICTED PERFORMANCE

The AASIR cooler thermal and structural design follows a close parallel with the VISSR/VAS design. For comparative purposes a chart of the physical and thermal characteristics of the two designs is shown in Table 5-2. The AASIR cooler has less depth primarily because of the absence of solar energy in the cooler FOV. This factor together with the improved parabolic shield configuration allows considerably larger intermediate and cold-stage radiators, necessary to dissipate the large AASIR substrate heat loads. The steady-state operating temperatures of the intermediate and cold stages are comparable to those achieved with the VISSR design. A discussion of the thermal and structural characteristics and performance is outlined in the following pages.

### Thermal

The thermal analysis of the AASIR cooler shows the intermediate and cold-stage heat-load distribution listed in Table 5-3. The corresponding heat-load budgets for the VISSR and VAS coolers are included for reference. The chart shows that the higher AASIR loads on the cold stage reflect the general increase in size of the cold-stage radiator, detector array, and aperture size. The largest percentage heat load increases over the VAS design are in the support band and electrical lead conduction paths as these are most directly influenced by the larger radiator and array.

Table 5-2. Radiation Coolers, Physical and Thermal Characteristics

	<u>AASIR</u>	<u>VISSR</u>
Size (Inches)	18.0 Dia. × 7.5	18 Dia. × 13
Weight (Pounds)	5.5 (EST)	6.9
Radiating Area (Intermediate Stage) (Inches <sup>2</sup> )	188.9	76.0
Radiating Area (Cold Stage) (Inches <sup>2</sup> )	35.8	7.1
Ambient Stage Temperature (°K)	300	300
Intermediate Stage Temperature (°K)	136	136
Cold Stage Temperature (°K)	81	80
Array Stability (X and Y Axes) (Inch)	±0.0005	±0.0005

Table 5-3. AASIR Radiation Cooler, Nominal Heat Load Comparison

	AASIR (mw)	(%)	VAS (mw)	(%)	VISSR (mw)	(%)
<u>INTERMEDIATE STAGE</u>						
CONE RADIATION	634	(27)	315	(30)	315	(32)
INTERSTAGE RADIATION	1408	(60)	630	(59)	593	(61)
BAND CONDUCTION	210	(9)	49	(5)	49	(5)
LEAD CONDUCTION	96	(4)	70	(6)	22	(2)
TOTAL	2348	(100)	1064	(100)	979	(100)
<u>COLD STAGE</u>						
CONE RADIATION	6.3	(11)	1.9	(12)	1.9	(18)
INTERSTAGE RADIATION	6.4	(12)	1.6	(10)	1.7	(16)
APERTURE RADIATION	10.7	(20)	3.4	(21)	0.7	(7)
DETECTOR BIAS	10.0	(18)	4.6	(28)	2.0	(19)
PENETRATIONS	1.9	(4)	1.3	(8)	1.3	(12)
BAND CONDUCTION	7.1	(13)	1.1	(7)	1.4	(14)
WIRE CONDUCTION	12.0	(22)	2.4	(14)	1.4	(14)
TOTAL	54.4	(100)	16.3	(100)	10.4	(100)

The bias energy dissipated at the detector array will vary in magnitude depending on the characteristics of the individual detectors selected for the assembly. Therefore, it is of interest to project cooler performance with bias energy as a variable. Figure 5-4 shows such a curve with the probable operating range for the AASIR detector array. The predicted minimum cold-stage steady-state temperature is 80.7°K with an intermediate and ambient stage temperature of 136° and 300°K respectively, using a nominal bias load of 10 mw. If it becomes necessary to increase the detector bias to 25 mw, the cold-stage temperature would degrade to 86.6°K.

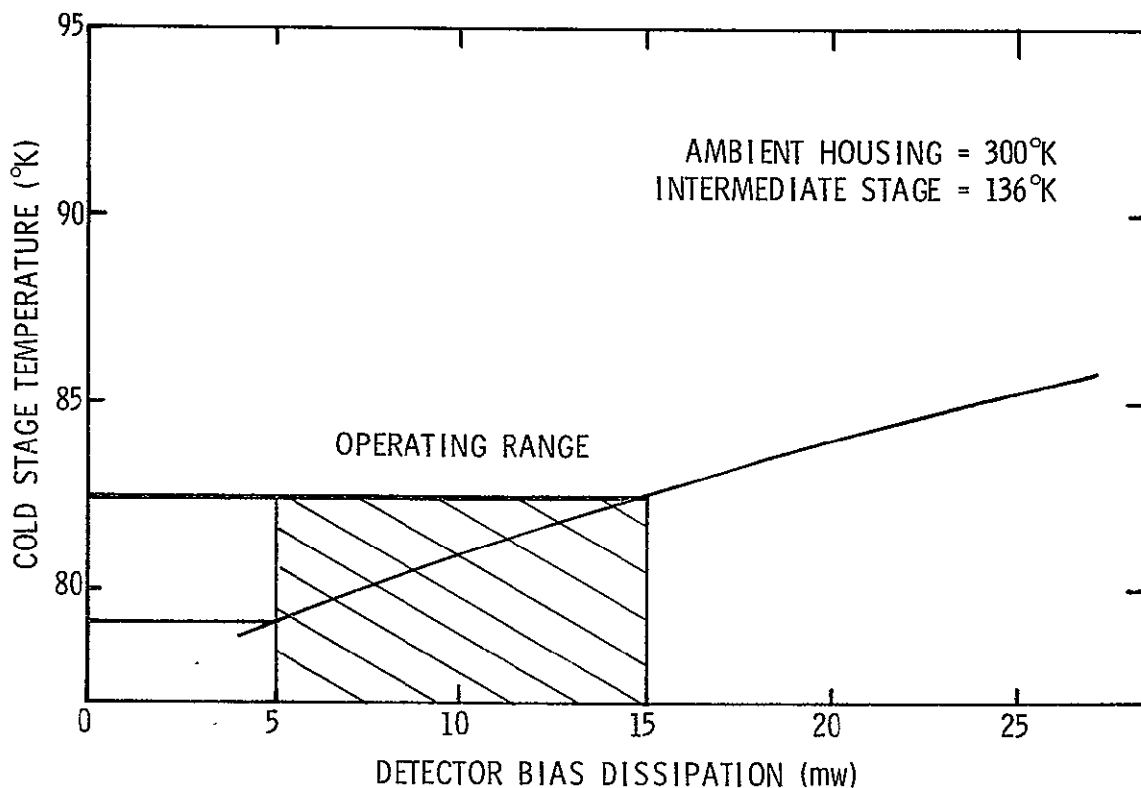


Figure 5-4. AASIR Radiation Cooler, Cold Stage Temperature Versus Bias Dissipation

The values presented so far have been based on an ambient housing and shield temperature of 300°K. However, several variables influencing this temperature such as spacecraft configuration, seasonal variations, and undefined thermal surface characteristics result in surface temperature

perturbations. The effects of these small changes in cooler ambient housing and shield temperatures on the cold-stage temperature are shown in Figure 5-5. A 10° change in ambient stage temperature results in a detector substrate temperature change of approximately 1.0°K.

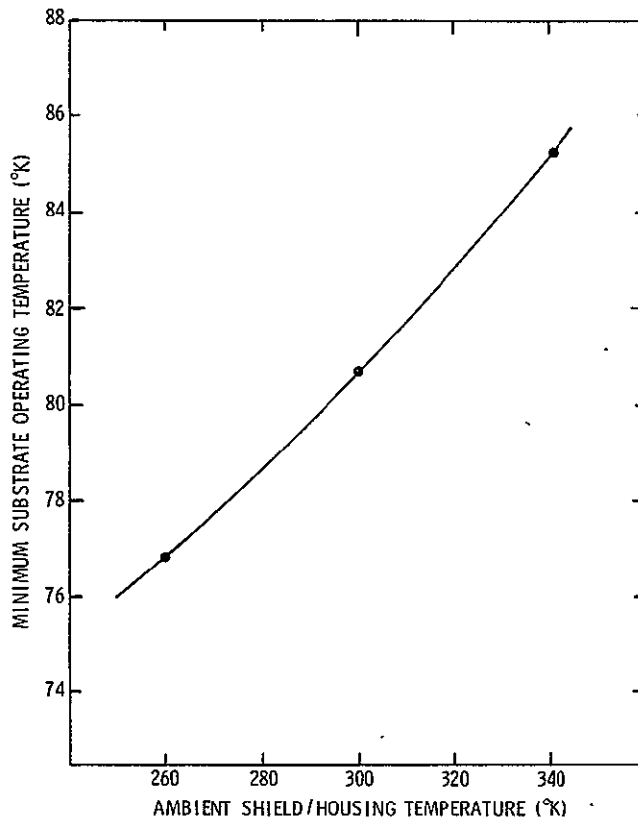


Figure 5-5. Cooler Performance Versus Shield Temperature

### STRUCTURAL ANALYSES

Structural analyses were conducted on both the earlier cooler configuration of the November '75 Design Review Report, and the later configuration of this report (Figure 5-2). From a structural dynamics viewpoint the two configurations differ primarily in the stage suspended masses, and in the angular orientation of the interstage support members (fiberglass bands).

Preliminary weight analyses were conducted on both configurations. The total weight of the earlier cooler configuration was found to be slightly greater (10.50 lb) than the configuration of this report (10.31 lb). A detailed stress analysis of all cooler structural parts would probably justify a weight reduction of 10% to 20%. Such an analysis was not conducted for this report.

For both configurations, the interstage support bands were sized such that the computed dynamic response of the cooler along its thrust axis (axis of symmetry) was similar to the VISSR cooler measured response.

Using interstage support bands sized in this manner, and using the input vibration qualification test levels of the VISSR cooler, a dynamics analysis indicated that the alternating stresses in these bands were of acceptable value, when compared with published fatigue data for unidirectional fiberglass.

This was determined by formulating a three degree-of-freedom dynamical model to determine thrust axis response. The response was calculated by the STARDYNE computer program for sinusoidal base (ambient housing) excitation. Modal damping of value similar to that measured on the VISSR cooler was assumed for all three modes.

#### Vibration Design

The radiative cooler design contains several important features which significantly quiet the response of the suspended stages to vibration excitation.

The stages of the cooler are symmetrical about the cooler optical axis. The mass center of each stage lies on the symmetrical axis. Aligning the mass centers of each stage with the lateral and axial elastic axes minimizes coupling between the lateral, axial, and rotational modes during vibration. This is done by selectively adjusting the stiffness of each symmetrical band group so that the elastic axes pass through the mass centers.

The use of pretensioned fiberglass bands permits a high support system stiffness without excessive heat leaks. The unusually high stiffness-to-conductivity ratio afforded by unidirectional fiberglass permits a relatively stiff interstage support system with natural frequencies similar to the VISSR cooler.

The addition of a viscoelastic damper to the cold stage reduces the system response. The damper design is modeled after that used on the VISSR cooler; the mass ratios, and the viscoelastic elements supporting the damper mass are identical to VISSR. The number of elements used has been increased from 3 to 9-10. These viscoelastic elements have equal spring rates and rubber shear strains in all three axes, imparting an isotropic quality to the assembled damper. Lateral, axial, and rotational modes (if any) are all effectively damped.

#### Alignment Stability

From creep data on unidirectional fiberglass at ambient conditions, it is known that band creep will not be a problem, particularly at the in-orbit operational temperatures. The alignment of the system during launch and in orbit will remain within close tolerances because the precision elastic limits are not exceeded.

#### Sizing the Interstage Support Bands

Two AASIR cooler configurations, Mod I (November '75 Design Review) and Mod II (this report) were analyzed to determine band sizes.

The objective of these analyses was primarily to determine the cross-sectional area of the suspension bands based solely on structural dynamics considerations. The basic approach was to scale the AASIR band stiffnesses such that the individual stage thrust axis resonant frequencies matched those of the successful VISSR cooler.

Table 5-4 shows the stiffness to weight ratios of the VISSR cooler and the scaled values for both AASIR Mod I and Mod II coolers. The band stiffness values shown are total thrust axis stiffness of the six bands supporting

each stage. Note that the damper mass has also been scaled upward to retain the same cold-stage mass to damper mass ratio.

Table 5-4. VISSR - AASIR Thrust Axis Stiffness-To-Weight Summary  
Values given as Stiffness (lb/in. )/Weight (lb)

	VISSR	AASIR Mod I	AASIR Mod II	Frequency
Intermediate Stage	101000/2.3	172400/3.923	158400/3.605	655 Hz
Cold Stage	2900/0.23	8540/0.677	9800/0.776	351 Hz
Damper Mass	400/0.10	1180/0.294	1350/0.337	198 Hz

The cross-sectional area of each leg of an individual band can then be calculated from the relation

$$A = \frac{K_z L}{12E \sin^2 \theta}$$

where  $K_z$  = thrust axis stiffness, lb/in

L = band length, in.

E = band modulus of elasticity = 8.5E6 psi

$\theta$  = band angle. See Figure 5-6

The cross sectional area values are then:

Mod I

Stage 1:  $A = 0.01866 \text{ inch}^2$

Stage 2:  $A = 0.00144 \text{ inch}^2$

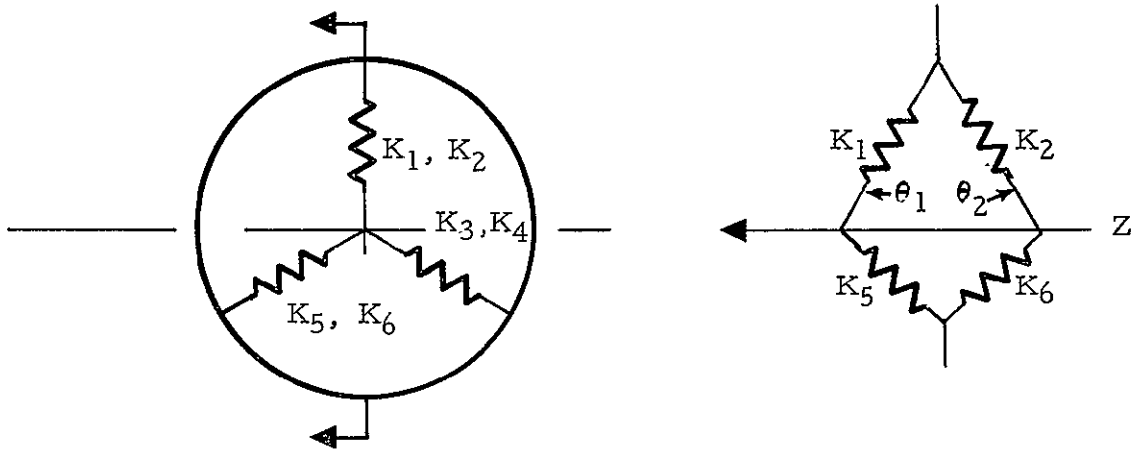


Figure 5-6. Combined Spring Rate for 6 Bands, Either Stage

Spring Rates for Symmetric Systems,

where  $k_1 = k_2 = k_n$ ,  $\theta_1 = \theta_2 = \theta_n$

$$(1) K_Z = 6(k \sin^2 \theta) = 6\left(\frac{AE}{L} \sin^2 \theta\right)$$

$$(2) K_{X,Y} = 3(k \cos^2 \theta) = 3\left(\frac{AE}{L} \cos^2 \theta\right)$$

Spring Rates for Non-Symmetric Systems,

where  $k_1 \neq k_2$ , but  $k_1 = k_3 = k_5$  and  $k_2 = k_4 = k_6$

$$(3) K_Z = 3(k_1 \sin^2 \theta_1 + k_2 \sin^2 \theta_2)$$

$$(4) K_{X,Y} = \frac{3}{2} (k_1 \cos^2 \theta_1 + k_2 \cos^2 \theta_2)$$

Where A = Combined cross section of both legs of a band

L = Band length, center-to-center

E = Band tensile modulus

Mod II

Stage 1:  $A = 0.01714 \text{ inch}^2$

Stage 2:  $A = 0.00170 \text{ inch}^2$

Lateral Stiffness

For  $\theta_1 = \theta_2$  and  $k_1 = k_2$  as in AASIR (see Figure 5-6) the lateral stiffness can be calculated as

$$K_x = 0.5K_z / \tan^2 \theta$$

If it is assumed that the mass center of each stage lies in the lateral elastic axis plane, an indication of the change in lateral resonant frequency (from VISSR) can be made as shown in Table 5-5.

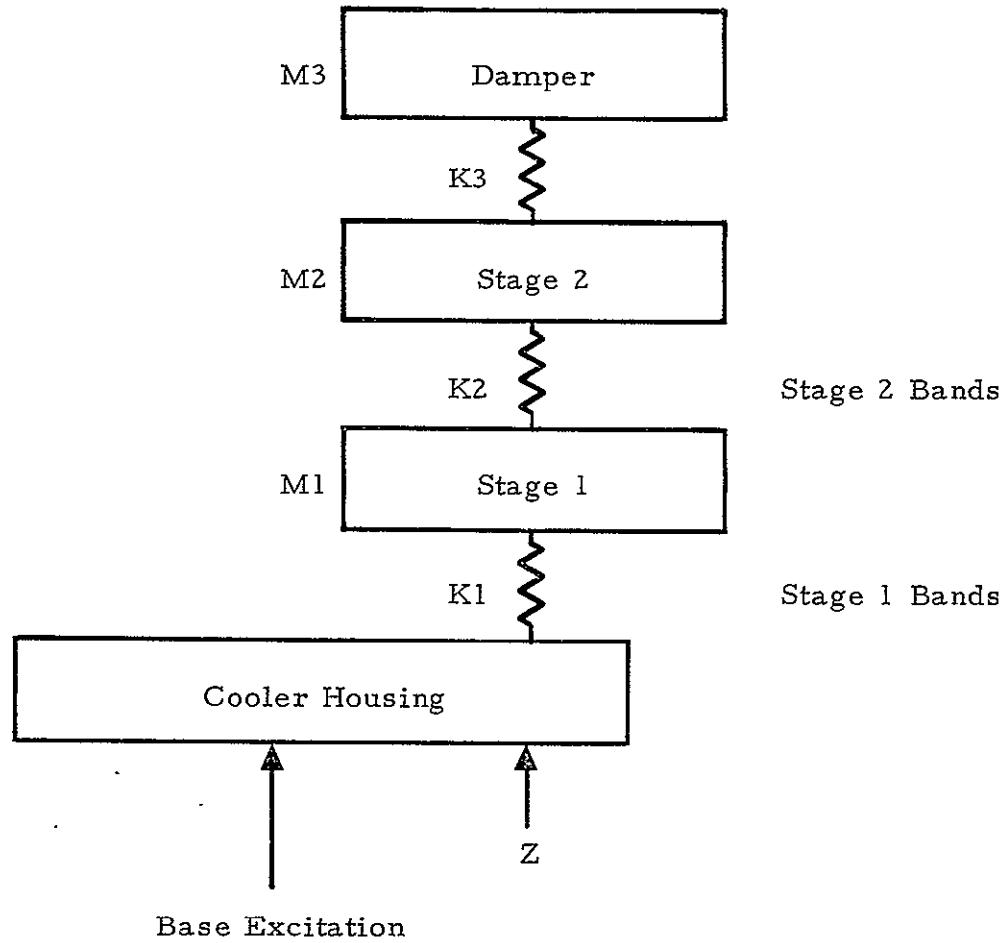
Table 5-5. VISSR - AASIR Lateral Stiffness and Resonant Frequency

Lateral Stiffness (lb/in)/Frequency (Hz)			
	VISSR	AASIR Mod I	AASIR Mod II
Intermediate Stage	21359/301	258600/803	237600/803
Cold Stage	7888/579	59473/927	41330/722

Note the significant increase in lateral resonant frequency for both Mod I and Mod II relative to VISSR. This results from the reduced band angles and the enforcement of equal thrust axis resonant frequencies.

Dynamic Response of Cooler Model

A three degree of freedom model of the AASIR cooler was formulated to determine thrust axis response. Figure 5-7 gives the details of the model. The STARDYNE finite element program was used to determine the response to 1g sinusoidal base motion from 20 to 1200 Hz. (The "base" was assumed to be the cooler housing). The mode shapes and frequencies found were as follows:



Mass and Spring Stiffnesses Used for Mod I and Mod II Models<sup>m</sup>

	M1	M2	M3	K1	K2	K3
Mod I	3.923	0.677	0.294	172400	8540	1180
Mod II	3.605	0.776	0.337	158400	9800	1350

Figure 5-7. Thrust Axis Lumped Mass Model of AASIR Cooler

	<u>Mode</u>	<u>Frequency</u>	<u>Stage 1</u>	<u>Stage 2</u>	<u>Damper</u>
Mod I	1	181	0.0085	0.1680	1.0
	2	373	0.0682	1.0	-0.3946
	3	678	1.0	-0.3887	0.0363
Mod II	1	180	0.0106	0.1699	1.0
	2	370	0.0831	1.0	-0.4006
	3	683	1.0	-0.3800	0.0348

Based on previous VISSR low level sine sweep response data a conservative value of 1% modal damping was assumed for the initial response calculation. The computed peak response of the Mod I and Mod II designs to 1g sinusoidal base (ambient housing) motion is summarized in Table 5-6.

Table 5-6. Peak Response to 1g Sinusoidal Base Motion  
(Thrust Axis)

	Intermediate Stage (g)	Frequency (Hz)	Cold Stage (g)	Frequency (Hz)
Mod I	46	678	56	373
Mod II	45	683	55	370

The stress in the bands due to these acceleration loads can be calculated as

$$\sigma = \frac{F}{12A \sin \theta} = \frac{WG}{12A \sin \theta}$$

The maximum stresses in the bands are then as shown in Table 5-7.

Table 5-7. Maximum Alternating Band Stress Due to 1g Base Motion

	Intermediate Stage, psi	Cold Stage, psi
Mod I	1600	8500
Mod II	1600	6400

(Note: Band ultimate tensile strength = 180000 psi)

Since an AASIR cooler qualification vibration test specification does not yet exist, cooler survival of qualification testing cannot be inferred from these results. However, a few observations can be made.

First, if the AASIR test specification is similar to VISSR, no sine vibration occurs above 200 Hz. At this frequency the response of both stages (both Mod I and Mod II) to 1g base excitation is less than 1.13g, i. e. , less than 2.5% of the values given in Table 5-6.

Second, if the AASIR random vibration test specification is similar to VISSR, at 0.02  $g^2/Hz$ , the grms accelerations of the stages would be approximately 25.6 for the cold stage and 31.4 grms for the intermediate stage. These levels indicate both acceptable  $3\sigma$  peak stresses and low fatigue damage.

Third, both the natural damping in the cooler structure and the damping due to the discrete dampers can be expected to increase with input level to about 2% total, as was measured on VISSR during qualification testing. This effect will result in lower band stresses during qualification vibration than would be expected from extrapolation of low level response.

Fourth, it must be noted that the adapter plate on which the VISSR cooler was mounted provided some vibration isolation for the intermediate and cold stages above a certain critical frequency. The use of similar isolation on AASIR should be considered even though the above analysis indicates that this isolation is not necessary.

## BENCH TEST COOLING

### Design/Operation

For ease of assembly, disassembly, and maintainability the pumpable dewar concept was integrated into the AASIR cooler design. That is, the dewar is evacuated only during flight, thermal-vacuum tests, and cryostat bench tests. Otherwise, the dewar is vented through a particle filter to the environment and ambient pressure.

The dewar must be evacuated during cryostat bench testing to minimize the convective heat losses to the dewar cold finger and detector substrate. Consequently, the bench test setup includes a vacuum pump line as well as a Joule-Thomson Cryostat (open loop). A schematic of this concept is shown in Figure 5-8. The ground test cover is attached to the cooler housing using the latches shown. The cryostat is located inside a pump tube mounted to the ground test cover. Flexible bellows are used to reduce residual forces on the cooler cold stage during bench-test cooling. A heat transfer bellows assembly (Figure 5-8 and 5-9) thermally shorts the cold-stage radiator to the detector substrate during flight operation. However, during bench testing, this assembly is detached from the radiator to allow the substrate to be thermally isolated and, ultimately, be cooled by the cryostat.

The details of the interface between the cold stage and vacuum/cryostat tube is shown in Figure 5-9. After the thermal bellows screws have been removed (the assembly is self-retracting), the open-loop cryostat is inserted into the cryostat sleeve mounted to the dewar stem. The cryostat tip will interface with the dewar as the pump tube mates (and seals) with the cold-stage radiator.

The dewar is then evacuated and the cryostat begins cooling the detector substrate. The dewar is sealed with three "O" rings which remain at or near room temperature throughout the test (Figure 5-8). The nitrogen gas exiting from the cryostat is exhausted outside the test cover, away from the critical cooler components.

When bench testing of the cooler is completed, the pump line and cryostat are removed and the heat transfer bellows is extended back to the radiator assembly. The bellows attachment screws are then replaced, providing good thermal contact between the bellows and radiator for maximum cooling during thermal-vacuum testing or flight operation.

Co

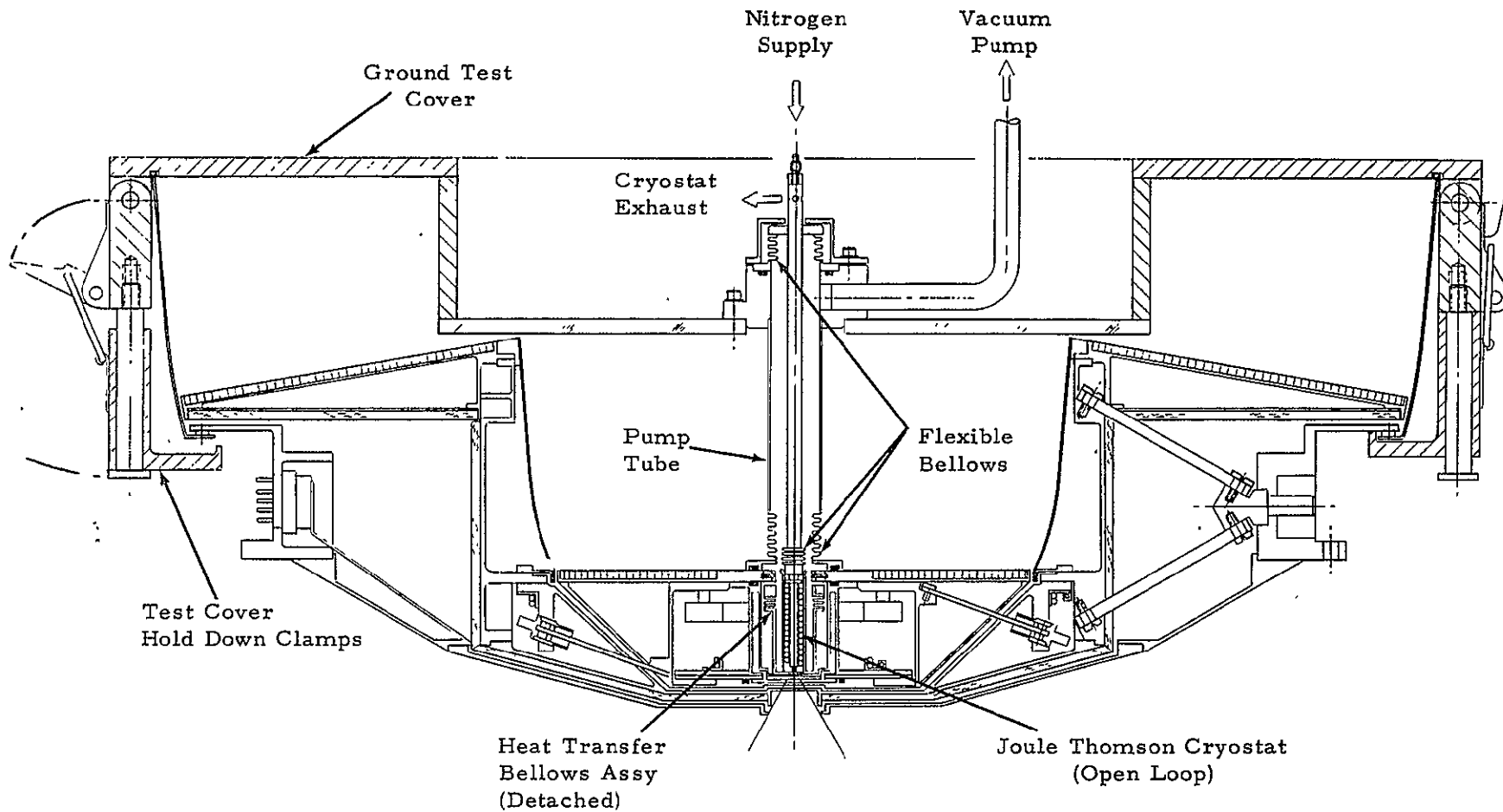


Figure 5-8. AASIR Radiation Cooler Layout Bench Test Configuration (Mod II)

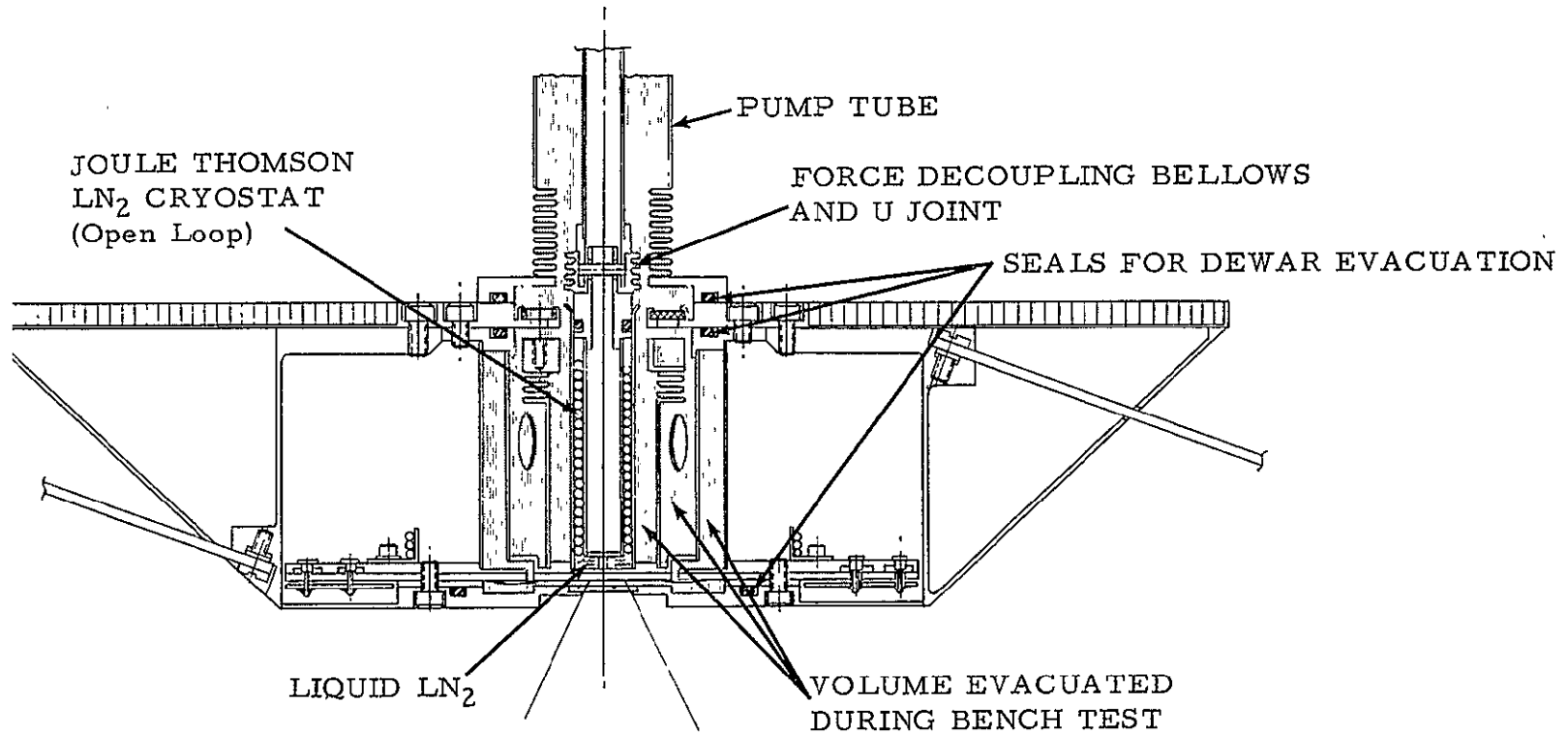


Figure 5-9. AASIR Cooler Bench Test Configuration Cold Stage Layout (Mod II)

### Breadboard Testing

The initial dewar design (Mod I), configured in the AASIR Design Review Report, November 1975, was constructed as a feasibility model to develop the pumpable dewar concept. The drawing of this dewar test assembly is shown in Figure 5-10.

The purposes of these tests were threefold: 1) to verify that the pumpable dewar concept was indeed practical and achievable; 2) to determine the substrate cooldown temperature with the J-T cryostat; and 3) to determine the "flight"  $\Delta T$  between the detector substrate and the cold-stage radiator.

Testing on the breadboard dewar was initiated in late 1976. The dewar was successfully evacuated but the substrate was cooled to only 128°K. The test dewar was then modified to reduce the thermal impedance between the substrate and liquid nitrogen. The substrate mounting surface was changed from Invar 36 to sapphire to reduce thermal gradients on same. Also, the cross-sectional area of the substrate support tube was decreased by 65% for improved thermal isolation. As a result the cryostat cooled the substrate to approximately 100°K. Using this test data together with analyses indicates that the substrate could be cooled to as low as of 90°K with further design refinements. At this point the cryostat testing was terminated and alternate design approaches were evaluated to provide the 80° to 85°K substrate test temperature.

The test dewar was returned to its "in orbit" configuration. With the heat transfer bellows attached, the dewar assembly was placed inside a 6-inch diameter calibrator and evacuated. The radiator temperature was held at 80°K. Simulated detector joule heating was applied to the detector substrate to determine the radiator to substrate  $\Delta T$ . The results showed a 1°K difference for 25-mw bias and approximately 1.75°K for 50-mw bias. As it is desirable to operate at less than 1°K differential at 10-mw, the tests indicate the design to be satisfactory.

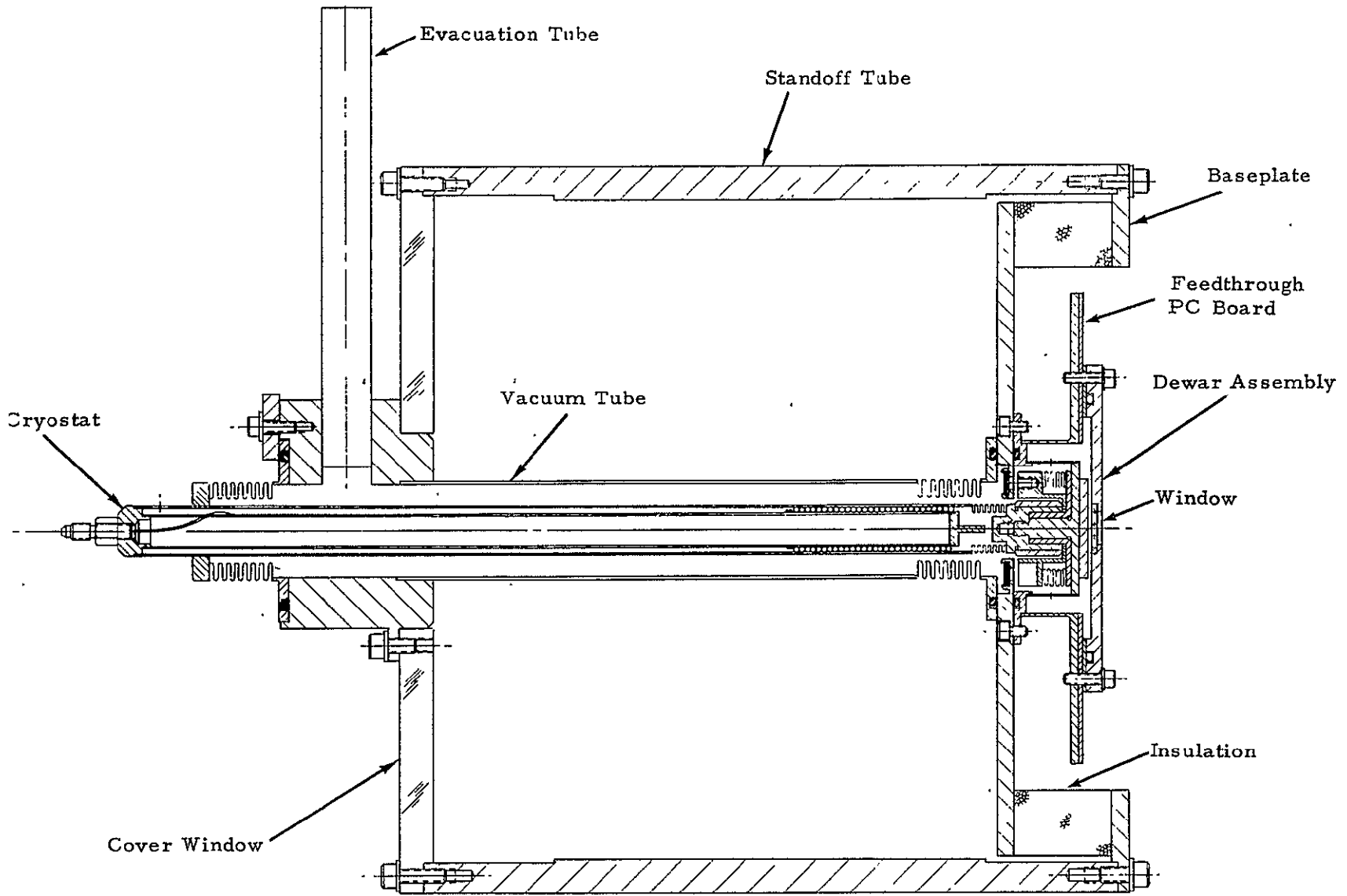


Figure 5-10. AASIR Dewar Test Assembly

In summation, the breadboard tests showed the pumpable dewar concept to be practical and the radiator-to-substrate temperature gradient to be less than the maximum allowable, and therefore acceptable. However, the design of the cryostat/dewar interface for this breadboard model was unacceptable and better thermal isolation of the detector substrate was required. Consequently this particular interface area was redesigned to yield the required cooldown temperatures. However, no tests have been accomplished to verify the new bench test performance.

Appendix A

AASIR SPECIFICATION

Appendix A  
AASIR SPECIFICATION

In this Appendix the original GSFC AASIR Specification (with changes indicated by W. Raskin, 7 February 1975) is reviewed, and suggested changes to the specification are presented. Where appropriate, the AASIR specifications are compared with the performance characteristics of the VISSR Atmospheric Sounder (VAS). Since this instrument is well along in its fabrication cycle at SBRC, its performance properties are either already known or can be accurately predicted.

Where changes have been made to the original specification, a vertical line has been placed in the right margin covering the extent of the change.

CONTENTS

		<u>Page</u>
1.0	SCOPE . . . . .	A-4
1.1	Introduction . . . . .	A-4
1.2	Instrument, General Aspects . . . . .	A-4
1.3	Overall Task Definition . . . . .	A-5
2.0	APPLICABLE DOCUMENTS . . . . .	A-6
2.1	Specifications . . . . .	A-6
2.1.1	AASIR Calibration and Acceptance Test Plan . . . . .	A-6
2.1.2	AASIR Interface Specification . . . . .	A-6
2.1.3	AASIR Scanner Interface Control Drawing . . . . .	A-6
	AASIR Electronics Module Interface Control Drawing . . . . .	A-6
2.2	Reference Documents . . . . .	A-6
2.2.1	NASA Specifications . . . . .	A-6
2.2.2	NASA Drawings . . . . .	A-6
2.3	Specifications for Contractor . . . . .	A-6
3.0	REQUIREMENTS . . . . .	A-6
3.1	Functional . . . . .	A-6
3.1.1	General . . . . .	A-6
3.1.2	Configuration . . . . .	A-6
3.1.2.1	Outline and Mounting . . . . .	A-6
3.1.2.2	Composition . . . . .	A-7
3.1.3	Radiometric Channels . . . . .	A-7
3.1.3.1	Type . . . . .	A-7
3.1.3.2	Relative Field-of-View Position and Orientation . . . . .	A-8
3.1.3.3	Signal Amplification, Voltage Range, and Linearity . . . . .	A-8
3.1.3.4	Infrared Channels Sun Saturation . . . . .	A-9
3.1.3.5	Detectors . . . . .	A-9
3.1.4	Scan Motion and Spectral Separation . . . . .	A-10
3.1.4.1	Scan Method . . . . .	A-10
3.1.4.2	Scan Angle Offset Pointing . . . . .	A-10
3.1.4.3	Scan Frame . . . . .	A-10
3.1.4.4	Scan Mirror Stow . . . . .	A-11
3.1.4.5	Scan Mirror Position Identification . . . . .	A-11
3.1.4.6	Spectral Separation . . . . .	A-11
3.1.5	Spatial Registration . . . . .	A-11
3.1.6	Inflight Calibration . . . . .	A-12
3.1.6.1	Reflectance Channel Radiometric Calibration . . . . .	A-12
3.1.6.2	Infrared Channels Radiometric Calibration . . . . .	A-12
3.1.6.3	Electrical Calibration . . . . .	A-13
3.1.7	Optical Focus Adjustment . . . . .	A-13
3.1.7.1	Reflectance Channel Focus Adjust . . . . .	A-13
3.1.8	Detector Cooler . . . . .	A-14
3.1.8.1	Inflight Alignment . . . . .	A-14
3.1.8.2	Decontamination Heaters . . . . .	A-14

CONTENTS (Cont)

	<u>Page</u>
3.1.8.3 Windows . . . . .	A-14
3.1.9 Command Processing . . . . .	A-14
3.1.10 Telemetry Monitoring . . . . .	A-14
3.1.11 Test Points . . . . .	A-14
3.1.12 Power and Grounding . . . . .	A-15
3.1.12.1 Power . . . . .	A-15
3.1.12.2 Ground Isolation . . . . .	A-15
3.1.13 Special Test Provisions . . . . .	A-15
3.1.13.1 Cryostat Cooling of Infrared Detectors . . . . .	A-16
3.1.13.2 Purge Ports . . . . .	A-16
3.1.13.3 Dust Covers . . . . .	A-16
3.1.13.4 Alignment "Bench Marks" . . . . .	A-16
3.1.13.5 Scan Mirror Stow, Mechanical . . . . .	A-16
3.2 Interface . . . . .	A-16
3.3 Performance . . . . .	A-16
3.3.1 General . . . . .	A-16
3.3.2 General Operating Conditions . . . . .	A-16
3.3.2.1 Radiative Cooler FOV . . . . .	A-16
3.3.2.2 Temperature . . . . .	A-16
3.3.3 Requirements . . . . .	A-17
3.3.3.1 Radiative Cooler . . . . .	A-17
3.3.3.2 Radiometric . . . . .	A-17
3.3.3.3 Optical . . . . .	A-18
3.3.3.4 Electrical . . . . .	A-18

AASIR SPECIFICATION

1.0 SCOPE

1.1 Introduction

The Advanced Atmospheric Sounder and Imaging Radiometer is intended to enhance the temporal and spatial aspect of the atmospheric sounding and imaging from geosynchronous altitude. A stable platform will be employed to provide longer dwell times (relative to a spinning sounder) to improve measurement accuracy. Two modes of operation will be available: (1) a full frame mode and (2) a reduced frame mode. Concentration on targets of opportunity in the reduced frame mode will reduce the spatial extent required for full quality sounding. The program identifies the critical technology for investigation and solution prior to the integration of a full AASIR system. Laboratory testing with well-controlled sources will verify the instrument performance, making it a candidate for orbital flight. Orbital data will enhance geosynchronous sounding and imaging from AASIR, establishing an optimized design for future geosynchronous meteorological instrumentation such as SEOS.

1.2 Instrument, General Aspects

This specification describes the requirements for developing an instrument called the Advanced Atmospheric Sounder and Imaging Radiometer (AASIR). The instrument is intended for use from synchronous altitude, and shall measure reflected energy and emitted infrared radiation for both sounding and imaging data. This instrument shall utilize as many of the basic components of the VISSR program (Contract NAS 5-21139) as possible. These shall include but not be limited to the following:

- 16-inch telescope
- Radiative cooler design
- Object plane scanner with one degree of freedom
- Ground test equipment
- Portions of the aft optics
- Sounder studies by University of Wisconsin

The overall aspects of the AASIR include the following:

- A 40.6-cm (16-inch) telescope is scanned in the object plane.
- High efficiency scanning modes provide full earth disc coverage as well as selected portions of the earth disc.
- Offset pointing enabling sectors to be chosen anywhere within the full disc.
- 12 channels of infrared sounding measurements.
- Imagery in 0.55- to 1.1-micrometer reflected band (0.75-km resolution).
- Thermal band relative measurement accuracy  $0.25 \text{ erg/sec cm}^2 \text{ sr cm}^{-1}$ .

Multielement HgCdTe and InSb detectors for thermal band detection.  
Radiative cooler.  
Silicon diode detectors in the reflectance band.  
Framing by a two degree gimbal object plane mirror - DELETED.  
Interface with three-axis stabilized platform.

The AASIR is intended to provide: three-dimensional atmospheric temperatures in the 13- to 15- and 4.3-micrometer CO<sub>2</sub> band (13.5-km maximum spatial resolution), infrared imagery in the 11- and 3.7-micrometer windows (4.5-km resolution) and several water vapor bands down to 3.7 micrometers (13.5-km maximum resolution).

1.3

### Overall Task Definition

The contractor shall provide an engineering model of a spaceflight instrument. It shall be capable of successfully meeting all specifications set forth below. The contractor shall perform complete instrument testing, to prove that all specifications have been met.

The program shall proceed in three phases.

Phase I - System Study and Instrument Design

Phase II - Breadboarding of Critical Components

(To be selected and approved by GSFC)

(a) Scanning mechanism

(b) Aft optics assembly

(c) Video processor and control circuitry

Phase III - Development and complete testing of Engineering Model

This shall include all new components and subsystem required. In addition, detailed methods shall be devised in order to prove the adequacy of the designs.

During Phase II, breadboards of the new components shall be fabricated, and the described tests shall be carried out. Phase II will include any redesign necessary to assure that all new designs meet the requirements. Life tests of the scanning mechanism shall be included in this phase.

Phase III shall be the development of a complete engineering model and complete system testing. It is the intent that the engineering model shall be fabricated from components, all of which have been previously proven. Phase III shall, therefore, consist of fabrication, testing, and engineering.

A design review shall be held at GSFC after the completion of each phase.

2.0 APPLICABLE DOCUMENTS

2.1 Specifications

- 2.1.1 SBRC: To be developed AASIR Calibration and Acceptance Test Plan
- 2.1.2 NASA, SBRC: To be developed AASIR Interface Specification
- 2.1.3 SBRC: AASIR Scanner Interface Control Drawing  
AASIR Electronics Module Interface Control Drawing

2.2 Reference Documents

2.2.1 NASA Specifications:

73-15035, Rev. A Visible and Infrared Spin-Scan Radiometer Interface Specification

SBRC: 19644, Rev. A VISSR Calibration and Acceptance Test Specification for GOES B&C Application

2.2.2 NASA Drawings:

G1314103, Rev. E VISSR Scanner Interface Control Drawing

G1314104, Rev. B VISSR Electronics Module Interface Control Drawing

G1314112, Rev. A VISSR Interconnect Harness Interface Control Drawing

2.3 Specifications for Contractor - S-250-P-1A, Prepared Monthly Periodic and Final Reports, May 1969.

3.0 REQUIREMENTS

3.1 Functional

3.1.1 General

The AASIR shall be a complete electro-optical instrument, designed to measure radiation in a reflectance band (0.55 to 1.1 micrometers), and infrared (3.7- to 15-micrometer) bands.

3.1.2 Configuration

3.1.2.1 Outline and Mounting

The AASIR shall consist of a Scanner and an Electronics Module. The scanner shall generally conform to the outline and mounting dimensions defined in NASA Drawing G1314103.

SBRC Remarks: The VISSR drawing above is N/A

### 3.1.2.2 Composition

The AASIR Scanner and Electronics Module shall contain the following:

#### 3.1.2.2.1 Scanner

- (1) A one-axis object-space scan mirror subassembly.
- (2) A Ritchey-Chretien primary collecting optics subassembly.
- (3) Disperser Assembly - a set of filters for the spectral separation of channels.
- (4) Reflectance and IR detectors and preamplifiers.
  - A set of secondary optics.
  - A two-stage radiative cooler for passively cooling the infrared channel detectors.
  - An optical focus drive subassembly for the reflectance channel.
  - An optical focus drive subassembly for the infrared channels.
  - An optical subassembly with reduced size aperture to permit an inflight radiometric check of calibration of the reflectance channels on the sun.
  - A calibration system to permit an inflight radiometric check of calibration of the infrared channels is required.
  - A scan mirror stow (magnetic latch) subassembly.
  - A structural system capable of supporting the above subassemblies to an alignment accuracy consistent with overall requirements.

#### 3.1.2.2.2 Electronics Module

- (1) Reflectance and infrared channel amplifiers.
- (2) Reflectance channel amplifier inflight gain control circuits.
- (3) Reflectance and infrared channel optical focus drive circuits.
- (4) Primary and redundant scan mirror drive servo controls and timing circuits.
- (5) Inflight calibration control and timing circuits.
- (6) Telemetry channel circuits.
- (7) Gain control circuitry.
- (8) An Electronics Module temperature sensor.
- (9) Command processing circuits.
- (10) Primary and redundant dc/dc converters.
- (11) Logic for sounder frame control.

### 3.1.3 Radiometric Channels

#### 3.1.3.1 Type

The AASIR shall have one reflective channel and twelve infrared channels. The number of detectors required for each channel shall be determined by the requirements for resolution, accuracy, etc.

3.1.3.2 Relative Field-of-View (FOV) Position and Orientation

The relative field-of-view position and orientation shall be determined during the study phase. It will be dependent on the form of spectral separation utilized.

3.1.3.3 Signal Amplification, Voltage Range and Linearity

3.1.3.3.1 Reflectance Channels

The nominal output voltage range of each reflectance channel, corresponding to an earth albedo range of 0% to 100% shall be 0.30 vdc to 4.75 vdc. The reflectance channels shall be designed to have a systems input/output linearity of  $\pm 1\%$  over the nominal output voltage range. The reflectance channel IFOV shall be 0.21 milliradian.

3.1.3.3.2 Infrared Channels

The nominal output voltage range of each sounding channel, corresponding to a blackbody target scene temperature range of 0°K to 320°K shall be 0.250 vdc to 4.75 vdc. The nominal output voltage range of the thermal imaging channels (see 3.1.4.6.1.1) corresponding to a blackbody target scene temperature range of 0°K to 340°K shall be 0.250 vdc to 4.75 vdc. The infrared channels shall have a system input/output linearity over the entire dynamic range of  $\pm 1\%$ .

The design goal NER of each channel is specified in Table 3.1.3.3.1. The NER shall be determined from the digital data output for a target which is at least 10 IFOVs wide and for at least 50 scan lines long. The frame times associated with these NERs shall be as shown in 3.1.4.3.2.

The output signal of each channel shall be independent of scan angle, for constant input radiance, to within the NERs as shown in Table 3.1.3.3.1.

The exact center wavelength values and tolerances of the channels will be decided by mutual agreement between the contractor and the technical officer.

Table 3.1.3.3.1 AASIR Thermal Channel Performance

Band	$\nu$ ( $\text{cm}^{-1}$ )	$\lambda$ ( $\mu\text{m}$ )	$\Delta\nu$ ( $\text{cm}^{-1}$ )	NER $20^\circ \times 20^\circ$ ( $\text{ergs/sec cm}^2 \text{ sr cm}^{-1}$ )	NER $1.2^\circ \times 1.2^\circ$ ( $\text{ergs/sec cm}^2 \text{ sr cm}^{-1}$ )
1	668.5	14.96	5	3.2	0.78
2	680	14.71	10	1.6	0.39
3	690	14.49	16	0.74	0.18
4	703	14.22	16	0.70	0.17
5	716	12.97	20	0.48	0.12
6	733	13.64	20	0.50	0.12
7	749	13.35	20	0.50	0.12
8	900	11.11	140	0.076	0.019
9	1225	8.16	60	0.43	0.11
10	1490	6.71	140	0.19	0.047
11	2360	4.24	50	0.019	0.0047
12	2700	3.70	440	0.0023	0.00056

SBRC Remarks: The table below represents the current AASIR spectral channel assignments and required NER values.

Band	$\nu$ ( $\text{cm}^{-1}$ )	$\lambda$ ( $\mu\text{m}$ )	$\Delta\nu$ ( $\text{cm}^{-1}$ )	IFOV ( $\mu\text{rad}$ )	NER $20^\circ \times 20^\circ$ ( $\text{ergs/sec cm}^2 \text{ sr cm}^{-1}$ )	NER $1.2^\circ \times 1.2^\circ$ ( $\text{ergs/sec cm}^2 \text{ sr cm}^{-1}$ )
1	668.5	14.96	5	375x375	Not Specified	2.45
2	680	14.71	15	375x375		0.25
3	690	14.50	16	375x375		0.25
4	703	14.22	16	375x375		0.25
5	716	13.97	20	375x375		0.25
6	733	13.64	20	375x375		0.25
7	750	13.33	20	375x375		0.25
7a	800	12.50	40	375x375		0.25
8	900	11.11	140	125x125		0.10
9a	1380	7.25	60	375x375		0.06
10	1490	6.71	140	375x375		0.05
11	2360	4.24	50	375x375		0.005
11a	2275	4.39	35	375x375		0.004
11b	2250	4.44	40	375x375		0.004
11c	2210	4.52	40	375x375		0.004
11d	2190	4.57	40	375x375		0.004
12	2535	3.94	140	375x375		0.004
*	2700	3.7	440	125x125		0.004

3.1.3.3.3 Option 1

The contractor shall propose as an option, the following added capabilities while retaining all other requirements of this specification. This option shall be the addition of five channels in the 4.2- to 4.6-micrometer range, operated in a high accuracy mode. In this mode a  $1.2^\circ$  scan frame shall be covered in less than twenty minutes as opposed to 1.2 minutes in the normal mode. This frame may be located anywhere within the earth's disc. The bandwidth of the channels shall be less than  $15 \text{ cm}^{-1}$ . The NER required for all five channels is less than  $0.001 \text{ ergs/cm}^2 \text{ sr cm}^{-1}$ .

The exact center values and tolerances of the channels will be decided by mutual agreement between the Technical Officer and the contractor, if the option is accepted.

SBRC Remarks: The 4.2- to 4.6- $\mu\text{m}$  sounding channels have been added. See Table 3.1.3.3.1.

3.1.3.3.4 Option 2 - Pointable Spectral Scanner - DELETED.

3.1.3.4 Infrared Channel Sun Saturation

The infrared channels shall be protected from saturation (due to sun exposure) in order to avoid long-time recovery periods of circuits following the illumination of the infrared channels IFOVs by the sun.

3.1.3.5 Detectors

The reflectance channels shall use silicon detectors for the purpose of detecting visible and near IR radiation. The infrared channels shall

use HgCdTe and/or InSb detectors for the purpose of detecting infra-red radiation.

3.1.3.5.1 Detector Measurements

Detector Characterization - The thermal detectors shall be well characterized. Data shall be taken and recorded for each detector element which will characterize responsivity, spectral response, noise spectrum, specific detectivity, and linearity as well as the dependence of these parameters on bias and temperature. In addition, each detector amplifier combination shall be accurately measured.

3.1.4 Scan Motion and Spectral Separation

3.1.4.1 Scan Method

The AASIR shall utilize a one-axis gimbaled scan mirror to provide pointing and scanning. The mirror shall be rotated by means of servo controlled torque motors, which utilize digital position-angle optical encoders for completing the feedback loops.

SBRC Remarks: The position encoder may be an optical encoder, a resolver/RDC, or a laser interferometer transducer.

3.1.4.2 Scan Angle Offset Pointing

The scan mirror shall be capable of pointing the IFOV anywhere within a  $\pm 10^\circ$  square, centered on the Z-Z axis, to an absolute accuracy of  $\pm 0.05^\circ$ . A command signal (or signals) shall be capable of driving the scan mirror to position the IFOV.

3.1.4.3 Scan Frame

A raster type scan frame shall be available. This will be accomplished by holding the east-west AASIR position fixed, and scanning the mirror in a north-south plane. The AASIR is then stepped, and another north-south scan is taken. A frame is completed when a square has been completed. At the end of the frame the AASIR shall be returned to its starting position. It shall be possible to initiate a frame from any initial mirror position but limited by the overall  $\pm 10^\circ$  scan angle maximum.

3.1.4.3.1 Scan Form

The scan shall be sinusoidal or linear.

3.1.4.3.2 Scan Frame Modes

There shall be four automatic scan frame modes available by command. These are as follows:

<u>Frame Size in degrees</u>	<u>Earth's Coverage/km</u>	<u>Time/seconds</u>
20x20	12500	1422
4x4	2500	284
1.2x1.2	750	85

These frames may start anywhere within the  $\pm 10^\circ$  scan angle capability. A start command shall be used to initiate the scan. If a particular scan frame is being limited by the  $\pm 10^\circ$  angle, a telemetry signal shall be used to indicate this condition. It may be desirable to include additional coverages between those indicated. The actual number and values shall be determined by agreement between the Technical Officer and the contractor.

#### 3.1.4.4 Scan Mirror Stow

The AASIR shall incorporate a provision for restricting the motion of the scan mirror to a fixed (stow) position when the scan mirror servo drive is not being operated (i.e., normal power OFF condition). The stow mechanism shall be of an electromagnetic "latch" design which shall permit repeated use and testing of the stow operation by command.

#### 3.1.4.5 Scan Mirror Position Identification

Each step position of the scan mirror shall be identified by parallel-signal word that is derived from the angle position encoder used in the scan drive servo loop.

#### 3.1.4.6 Spectral Separation

The spectral separation method shall be a filter wheel containing the spectral channels shown in Table 3.1.3.3.1.

##### 3.1.4.6.1 Filter Wheel Method - DELETED.

##### 3.1.4.6.1.1 Thermal Imaging

A means shall be provided for producing thermal imaging in the 3.7- and 11.1-micrometer bands at a resolution (IFOV) of 0.125 milliradian.

##### 3.1.4.6.1.2 Reflectance Channel Imaging

Reflectance channel imaging in the 0.55- to 1.1-micrometer channel shall be provided at a resolution (IFOV) of 0.021 milliradian or smaller.

##### 3.1.4.6.2 Spectroscope Method - DELETED.

#### 3.1.5 Spatial Registration

For purposes of this specification, two channels shall be said to be in perfect registration when the following conditions exist:

- a. The two IFOVs are identical in size and shape geometrically.
- b. The two areas overlap each other perfectly.
- c. The system relative response to the same points within each IFOV are equal.
- d. The readings are taken simultaneously.

A large detector IFOV may be in perfect registration with a set of small detector IFOVs if the latter has a total IFOV which perfectly matches the large detector IFOV.

The IR (sounding) channels shall be spatially registered to within  $\pm 0.01$  IFOV.

It is desired that the registration between the reflectance channel, the thermal imaging channels, and the sounding channels be as accurate as possible. This shall be considered an important parameter during the design phase. The final specification shall be determined by agreement between the contractor and the Technical Officer.

SBRC Remarks: This requirement appears to be extremely difficult to meet, even on a single detector basis. Diffraction effects alone between the 14- $\mu\text{m}$  sounding channels and the 11- $\mu\text{m}$  window channels amount to about 5%.

### 3.1.6 Inflight Calibration

The AASIR shall incorporate provisions for performing an inflight radiometric check-of-calibration of the reflectance and an inflight radiometric calibration of the infrared channels and an electrical calibration of the reflectance and infrared channel amplifiers.

#### 3.1.6.1 Reflectance Channel Radiometric Calibration

The reflectance channel shall include an optical subassembly with a reduced-size collecting aperture to permit an inflight radiometric check-of-calibration to be performed using the sun as a source. The collecting aperture size shall be made to provide a signal equivalent of approximately a 50% albedo calibration point when the sun is viewed.

#### 3.1.6.2 Infrared Channel Radiometric Calibration

##### 3.1.6.2.1 A blackbody source and a view of deep space shall be provided for calibration.

##### 3.1.6.2.2 The blackbody shall have an emissivity greater than 0.99, and measured to within $\pm 0.005$ .

SBRC Remarks: A service recently started at the National Bureau of Standards is the characterization of industry blackbody sources. At the present time, NBS will measure the radiant emittance of the blackbody in the 8- to 14- $\mu\text{m}$  region with an accuracy of  $\pm 0.5^\circ\text{C}$ . This corresponds to  $\pm 0.5\%$  in the  $900\text{ cm}^{-1}$  channel. However,  $\pm 0.5^\circ\text{C}$  at 4.0  $\mu\text{m}$  would correspond to  $\pm 1.5\%$  but NBS does not measure blackbodies in this spectral range.

##### 3.1.6.2.3 The effective temperature of the blackbody shall be measured to within $\pm 0.05^\circ\text{K}$ .

SBRC Remarks: The VAS program uses Yellow Springs thermistors which have an accuracy traceable to  $\pm 0.05^\circ\text{C}$ . However, after incorporation into the VAS, the accuracy is estimated to be  $\pm 0.1^\circ\text{C}$ .

- 3.1.6.2.4 The channel-to-channel relative calibration accuracy shall be better than the NER as specified in Table 3.1.3.3.1.
- 3.1.6.2.5 The absolute accuracy of each channel shall be calibrated to  $\pm 0.5^\circ\text{K}$ .
- 3.1.6.2.6 The gain of each channel shall be stable to within  $\pm 0.1\%$  between calibrations.

SBRC Remarks: This is the present VAS requirement.

- 3.1.6.2.7 The reflectivity of each element which influences the radiometric response by their emissivity, shall be measured to  $\pm 0.1\%$ , and the temperature of each element shall be telemetered to an accuracy of  $\pm 0.25^\circ\text{K}$ .

SBRC Remarks: The current SBRC capability allows reflectance measurement to an accuracy of about  $\pm 1.0\%$ . Under the best possible conditions this could be reduced to about  $\pm 0.5\%$  using NBS calibrated reflectance standards. Another source of error arises because of the difference in reflectance between the witness mirror which is measured and the actual mirror which cannot be measured owing to its size or shape.

In addition, an operational amplifier which uses resistor components and a regulated supply, which is telemetered, shall be used to bias the sensing element and buffer its output for telemetering purposes.

### 3.1.6.3 Electrical Calibration

Electrical calibration of the reflectance and infrared channel amplifiers shall be performed at the beginning of each frame. This calibration voltage will be introduced to the front end of the preamplifier and have an amplitude granularity adequate for checking or correcting nonlinearities of processing circuits so as to guarantee accuracies consistent with the signal to noise specified. Calibration of the sample and hold circuit used for shutter calibration shall also be accomplished by injecting a time varying voltage into the shutter circuit during calibration.

### 3.1.7 Optical Focus Adjustment

The AASIR shall incorporate provisions for independent adjustment of the optical focus of the AASIR reflectance infrared channels by command.

#### 3.1.7.1 Reflectance Channel Focus Adjust

Focus adjustment of the reflectance channels shall be accomplished by movement of the position of the defining aperture of the reflectance channel detectors relative to the focal plane of the reflectance channel optics. Position indications of the adjustable elements shall be included throughout the full range of focus.

SBRC Remarks: In the current AASIR design, focus of the visible channels is accomplished by moving the detector package.

### 3.1.8 Detector Cooler

A two-stage radiative cooler shall be used in the AASIR to passively cool the infrared channel detectors. The infrared channel detectors shall be attached to the cooler second (coldest) stage.

The radiative cooler shall have cooling capacity (under load) adequate to achieve 92°K under simulated space conditions.

A cryostat cooling technique will be provided for bench testing and gain scaling of the infrared spectral bands. The cryostat system shall provide a temperature level at the detector elements equal to or lower than that provided by the radiative cooler in vacuum. The detector package will contain temperature sensing elements so that detector temperatures are accurately known during bench operation.

#### 3.1.8.1 Inflight Alignment

The required inflight alignment of the AASIR Z-Z axis to the earth north-south line for proper operation of the radiative cooler shall not exceed 1°.

#### 3.1.8.2 Decontamination Heaters

Electrical heaters shall be included on the first and second stages of the radiative cooler to facilitate decontamination of the first and second stage surfaces. Heating of the radiative cooler's first and second stages shall be initiated by command.

#### 3.1.8.3 Windows

A direct path between the interior of the AASIR Scanner housing and the interior of the radiative cooler (first and second stage area) shall be avoided by the use of a sealed infrared window at the entrance aperture (for collected target scene radiation) of the radiative cooler housing. In addition, an infrared window shall be located on the radiative cooler first stage and the optical path of the infrared channel radiation to restrict the migration of outgassed contaminants from the vicinity of the interior housing of the radiative cooler to the infrared channel detector package.

### 3.1.9 Command Processing

The AASIR command processing circuits shall be capable of receiving and executing separate commands necessary to fulfill the AASIR mission. A listing of these commands shall be determined and included.

### 3.1.10 Telemetry Monitoring

The AASIR telemetry circuits shall monitor and provide suitable electrical outputs for analog and digital telemetry channels. Telemetry necessary to fulfill the AASIR mission objectives shall be included.

### 3.1.11 Test Points

Test points shall be included in the AASIR to facilitate testing.

3.1.12 Power and Grounding

3.1.12.1 Power - The AASIR shall be designed to operate using the following sources of supplied power:

- (1) +29 VDC Primary Power
- (2) +26 VDC Command Power
- (3) +26 VDC Timing Power

3.1.12.1.1 Primary Power

The +29 VDC Primary Power shall be the source of power for all AASIR circuits that do not require being referenced to either Command Power Ground or Timing Power Ground.

3.1.12.1.1.1 DC/DC Converters - DC/DC converters shall be used to provide voltages to those AASIR circuits which are not suitable for direct +29 VDC Primary Power application or where ground isolation from Primary Power Ground is required.

3.1.12.1.1.2 Redundancy - The AASIR shall contain a primary and a completely redundant dc/dc converter subassembly. Selection of the dc/dc converter subassembly to be used shall be by command.

3.1.12.1.1.3 Regulation - The dc/dc converter voltages used for the following AASIR circuits shall be regulated for both line (+29 VDC Primary Power) and load variations:

- (1) All reflectance and infrared channel amplifiers
- (2) All optical encoder light sources
- (3) All optical encoder logic and amplifier circuits
- (4) All temperature telemetry monitor circuits

3.1.12.1.2 Command Power - The +26 VDC Command Power shall be used for those AASIR circuits requiring reference to a Command Power Ground.

3.1.12.1.3 Timing Power - The +26 VDC Timing Power shall be used for those AASIR circuits requiring reference to a Timing Power Ground.

3.1.12.2 Ground Isolation - The AASIR shall maintain electrical (dc) isolation between the following grounding systems:

- (1) +29 VDC Primary Power
- (2) +26 VDC Command Power
- (3) +26 VDC Timing Power
- (4) Reflectance and infrared channels (signal)
- (5) Chassis

3.1.13 Special Test Provisions

The following special test provisions shall be included as a part of each AASIR subsystem.

- 3.1.13.1 Cryostat Cooling of Infrared Detectors - The AASIR radiative cooler/detector subassembly shall be designed to permit cooling of the infrared channel detectors with a Joule-Thompson cryostat during ambient laboratory environment testing.
- 3.1.13.2 Purge Ports - Purge ports shall be provided on the AASIR Scanner to permit independent purging of the radiative cooler and the Scanner housing with N<sub>2</sub> gas.
- 3.1.13.3 Dust Covers - Detachable dust covers shall be provided for both the AASIR Scanner optical entrance aperture and the radiative cooler. A part of the optical entrance aperture dust cover shall be (partially) transparent to both reflectance (0.55 to 1.1 micrometers) and infrared (10.5 to 12.6 micrometers) radiation.
- 3.1.13.4 Alignment "Bench Marks" - "Bench marks" shall be provided in the AASIR Scanner to facilitate angular and lateral alignment of the nominal optical axis of the AASIR for test. The angular bench mark shall consist of a source of emitted light radiation located at each end of the defining visible channel detector aperture (field) array. The lateral bench mark shall be a cross target located on the AASIR Scanner secondary mirror support structure.
- 3.1.13.5 Scan Mirror Stow, Mechanical - The AASIR design shall include an arrangement for restricting the movement of the scan mirror to a fixed (stow) position by strictly mechanical means. The stow and unstow operation may be accomplished manually.
- 3.2 Interface

The interface requirements shall be determined by mutual consent between the contractor and the GSFC Technical Officer.
- 3.3 Performance
- 3.3.1 General

The AASIR subsystem shall be capable of meeting the performance requirements specified in paragraph 3.3.3 when the AASIR is operated under the conditions defined in paragraph 3.3.2. The overall requirements are summarized in Table 3.1.3.3.1.
- 3.3.2 General Operating Conditions
- 3.3.2.1 Radiative Cooler FOV - The radiative cooler FOV shall be viewing space or a simulated space background.
- 3.3.2.2 Temperature - Unless otherwise specified the average AASIR Scanner temperature shall be between 0°C and 35°C. The Electronics Module temperature shall be between 0°C and 45°C.

3.3.3 Requirements

3.3.3.1 Radiative Cooler

3.3.3.1.1 Cooldown Time - When the AASIR is operated in a vacuum environment of less than  $10^{-5}$  torr with the radiative cooler heaters OFF for a period of 60 hours the radiative cooler shall be down to operating temperature.

3.3.3.1.2 Cooler Operation

3.3.3.1.2.1 At least two methods of cooler operation shall be considered. These are the servo controlled method and the maximum cooldown method.

The servo controlled method utilizes a heater and servo temperature controller. The cooler is operated at a temperature at least  $10^{\circ}\text{K}$  warmer than the coldest temperature attainable by the cooler.

The maximum cooldown method allows the cooler to operate at the coldest temperature attainable. In order to hold the output constant, an automatic gain system would be included in the electronics.

When the advantages and disadvantages of the various methods have been studied, the system to utilize on this instrument will be decided by mutual agreement between the contractor and the Technical Officer.

3.3.3.2 Radiometric

3.3.3.2.1 Reflectance Channel Signal to Noise (S/N) - The S/N of each visible channel shall be greater than 2.5 for an extended target scene at a 0.5% albedo level

SBRC Remarks: The present AASIR design does not meet this requirement using silicon photodiodes. For the  $20^{\circ} \times 20^{\circ}$  frame the S/N will be 258 for albedo = 100% and 1.7 for albedo = 0.5%.

3.3.3.2.2 Special Test - The complete instrument shall be set up to view a suitable outdoor scene. The instrument shall be made to scan the scene in each frame size and the outputs used to produce a pictorial display. It is required that there be no visible coherent noise in a worst-case scene.

3.3.3.2.3 Infrared Channel Noise Equivalent Radiance (NER) - The NER of each infrared channel shall be less than the values specified by Table 3.1.3.3.1.

3.3.3.2.3.1 Special Test - The thermal imaging channel shall be used to view the scene utilized for paragraph 3.3.3.2.2. In addition, it shall be used to view a scene of constant magnitude of nominally 20% of saturation. The pictorial display shall show no visible coherent noise.

SBRC Remarks: This test appears to be unnecessarily difficult if only a measurement of coherent noise is desired. Coherent noise can be measured on a line-by-line basis while the instrument is viewing a uniform integrating sphere,

or in the case of the IR channels a uniform extended blackbody. Two-dimensional pictures would require a cross-scan (east-west) step gimbal and associated drive.

3.3.3.2.4 Modulation Transfer Function (MTF) - The minimum system MTF, measured against a bar pattern target shall be as follows:

<u>Bar Size</u>	<u>MTF</u>
1.0 IFOV	0.35
1.5 IFOV	0.70
2.0 IFOV	0.85
4.0 IFOV	0.95

The response shall be flat and equal to unity at large bar target sizes.

3.3.3.3 Optical

3.3.3.3.1 Relative Spectral Response - The lower cutoff wavelength and upper cutoff wavelength of a channel relative spectral response are defined as the wavelengths at which the channel response is equal to 0.5 of the peak spectral response.

3.3.3.3.1.1 Reflectance Channel - For each reflectance channel, the low cutoff wavelength shall be  $0.55 \pm 0.05$  micrometers and the upper cutoff shall be the response of the silicon detectors.

3.3.3.3.1.2 Infrared Channels - For each of the infrared channels, the spectral characteristics are presented in Table 3.1.3.3.1 when the radiative cooler's second stage temperature is at its operating temperature. System spectral response measurements will be made and data recorded for each spectral band.

3.3.3.3.2 Field of View (FOV) - The angular FOV of a channel in a given scan direction is defined as the angular distance between the two angles at which the channel response to a slit source of radiation, that is aligned perpendicular to the direction of scan, is 0.5 of the peak response of the channel during the scan.

3.3.3.3.2.1 The angular IFOV of each reflectance detector shall be nominally 0.025 milliradian.

3.3.3.3.2.2 Infrared Channel - The angular IFOV of each infrared channel shall be nominally 0.375 milliradian.

3.3.3.3.2.3 Infrared Imaging Channel - The angular IFOV of the thermal imaging channels shall be nominally 0.125 milliradian.

3.3.3.4 Electrical

3.3.3.4.1 Primary Power - The average steady-state primary power required by the AASIR for a nominal +29 vdc at the power connector shall be minimized.

3.3.3.4.2 Channel Electronics Gain Variation - The electronic gain variation of the reflectance and infrared channels as determined by the change in

amplitude of the electronic calibration signal at the output of each channel shall not exceed 2% for any change in AASIR temperature in the range from 0°C to 35°C.

- 3.3.3.4.3 Channel Electronics Overshoot
- 3.3.3.4.3.1 Reflectance Channel - For a radiation signal input into the reflectance channels that is generated by the reflectance channel fields of view scanning across a step change in scene albedo level, the overshoot of the voltage signal output of each visible channel shall not exceed 5% of the output signal level change resulting from the change in scene albedo level.
- 3.3.3.4.3.2 Infrared Channels - For a radiation signal input into the infrared channel that is generated by the infrared channel fields of view scanning across a step change in scene radiance level, the overshoot of the voltage signal output of each infrared channel shall not exceed 5% of the output signal level change resulting from the change in scene radiance level.
- 3.3.3.4.4 Command Line Immunity
- 3.3.3.4.4.1 Transient Noise - No false commands shall be executed in the AASIR as a result of  $\pm 0.5$  volt transient signal occurring on any of the command channels.
- 3.3.3.4.4.2 Crosstalk - The receipt of a command in any one of the command channels shall not result in the execution of a command in any other command channel.
- 3.3.3.4.5 Frequency Response and Droop - The frequency response and electronic droop shall be accurately measured for each channel, and included in the reports.